ศิลาวรรณา ธรณีเคมี และ ลักษณะเฉพาะทางอัญมณีของแหล่งพลอยทับทิมกำเนิดในหินอ่อน บริเวณโมโรโกโรและมาเฮนเก ประเทศแทนซาเนีย

ร้อยเอก วอร์เตอร์ เอเดรียน บอลเมอร์

วิทยานิพนธ์นี้เป็นส่วนหนึ่งของการศึกษาตามหลักสูตรปริญญาวิทยาศาสตรดุษฎีบัณฑิต
สาขาวิชาธรณีวิทยา ภาควิชาธรณีวิทยา
คณะวิทยาศาสตร์ จุฬาลงกรณ์มหาวิทยาลัย
ปีการศึกษา 2554

Petrology, Geochemistry, and Gemmological Characteristics of Marble-Hosted Ruby Deposits of Morogoro and Mahenge, Tanzania

Captain Walter Adrian Balmer

A Dissertation Submitted in Partial Fulfillment of the Requirements
for the Degree of Doctor of Philosophy Program in Geology
Department of Geology
Faculty of Science
Chulalongkorn University
Academic Year 2011

Thesis Title	PETROLOGY, GEOCHEMISTRY AND GEMMOLOGICAL CHARACTERISTICS OF MARBLE-HOSTED RUBY DEPOSITS OF MOROGORO AND MAHENGE, TANZANIA
By	Captain Walter Adrian Balmer
Field of Study	Geology
Thesis Advisor	Assistant Professor Chakkaphan Sutthirat, Ph.D.
Thesis Co-Advisor	Professor Thomas Pettke, Ph.D.
Thesis Co-Advisor	Associate Professor Christoph A. Hauzenberger, Ph.D.

Accepted by the Faculty of Science, Chulalongkorn University in Partial Fulfillment of the Requirements for the Doctoral Degree

…….. Dean of the Faculty of Science
(Professor Supot Hannongbua, Dr.rer.nat.)

THESIS COMMITTEE

…….. Chairman
(Pitsanupong Kanjanapayont, Dr.rer.nat.)

…….. Thesis Advisor
(Assistant Professor Chakkaphan Sutthirat, Ph.D.)

…….. Thesis Co-Advisor
(Professor Thomas Pettke, Ph.D.)

…….. Thesis Co-Advisor
(Associate Professor Christoph A. Hauzenberger, Ph.D.)

…….. Examiner
(Associate Professor Visut Pisutha-Arnond, Ph.D.)

…….. Examiner
(Assistant Professor Somchai Nakapadungrat, Ph.D.)

…….. External Examiner
(Associate Professor Theerapongs Thanasuthipitak, Ph.D.)

วอร์เตอร์ เอเดรียน บอลเมอร์: ศิลาวรรณา ธรณีเคมี และ ลักษณะเฉพาะทางอัญมณีของแหล่งพลอยทับทิมกำเนิดในหินอ่อน บริเวณโมโรโกโรและมาเฮนเก ประเทศแทนซาเนีย
อ.ที่ปรึกษาวิทยานิพนธ์หลัก: ผศ.ดร. จักรพันธ์ สุทธิรัตน์, อ.ที่ปรึกษาวิทยานิพนธ์ร่วม: ศ.ดร. โธมัส เพทท์เก, รศ.ดร. คริสทอบท์ ฮัวเซนเบอร์เจอร์, 185 หน้า.

ศิลาวิทยา ธรณีเคมี และอัญมณีวิทยาจากการศึกษาจากตัวอย่างหินจำนวน 17 ตัวอย่าง และตัวอย่างพลอยจำนวน 80 ตัวอย่างจากเหมืองพลอยทับทิมกำเนิดในหินอ่อนจำนวน 4 เหมือง ในบริเวณโมโรโกโร ประเทศแทนซาเนีย และตัวอย่างพลอยทับทิมจำนวน 46 ตัวอย่างจากแหล่งอื่นๆที่แตกต่างกัน 5 แหล่ง คือ แหล่งโมกก ประเทศพม่า แหล่งยูนนาน ประเทศจีน แหล่งเมอร์กับ ประเทศทาจิกิสถาน แหล่งลุคเยน ประเทศเวียดนาม และแหล่งมันการี ประเทศเคนยา โดยการวิเคราะห์องค์ประกอบของธาตุร่องรอยและลักษณะเฉพาะทางอัญมณี

การกำหนดแหล่งกำเนิดพลอยทับทิมในหินอ่อนนั้นต้องอาศัยองค์ประกอบของธาตุร่องรอยเช่น Li Mg Ti V Cr Fe Ga Ge Nb และ Sn ที่ได้จากวิเคราะห์โดยเครื่องมือ LA-ICP-MS องค์ประกอบธาตุร่องรอยเหล่านี้บ่งชี้ถึงลักษณะเฉพาะของพลอยทับทิมจากบริเวณโมโรโกโรมีเหล็ก (Fe) ค่อนข้างสูงเมื่อเทียบกับพลอยทับทิมจากแหล่งกำเนิดในหินอ่อนอื่นๆ ดังนั้นการใช้หลักเกณฑ์ใหม่ เช่น องค์ประกอบที่เด่นชัดของแต่ละพื้นที่ร่วมกับการวิเคราะห์ด้วยเครื่องตรวจสอบอัญมณีขั้นสูงสามารถกำหนดแหล่งกำเนิดของพลอยทับทิมได้ เฉพาะลักษณะมลทิน สเปกตรัม UV-Visและข้อมูลจาก FTIR

ธรณีวิทยาของแหล่งพลอยทับทิมเทือกเขาอูลูกูรูและมาเฮนเก ในโมโรโกโร สัมพันธ์กับหินอ่อนเป็นส่วนของแนวแกรนูไลต์ตะวันออกในประเทศแทนซาเนีย ทั้งสองพื้นที่แสดงลักษณะธรณีแปรสัณฐานมีการดันตัวเข้าหากันขึ้นไปบนหินฐานไนส์ในทิศตะวันตกเฉียงเหนือ ลักษณะธรณีเคมีบ่งชี้ว่าแหล่งอูลูกูรูอยู่ในหินอ่อนเนื้อแคลไซต์ในขณะที่แหล่งมาเฮนเกพบในหินอ่อนเนื้อโดโลไมต์ ลักษณะศิลาวรรณาของแหล่งอูลูกูรูแสดงองค์ประกอบ โฟลโกไปต์-แอมฟิโบล์-คาร์บอเนต-คอรันดัม-เพลจิโอเคลส-สปิเนล-ไมกาขาว±สคาโพไลต์ ทัวร์มาลีน คลอไรต์ ขณะที่แหล่งมาเฮนเกพบแร่โฟลโกไปต์-คาร์บอเนต-คอรันดัม-เพลจิโอเคลส-แซฟฟิรีน± แอมฟิโบล์ สฟีน ทัวร์มาลีน คลอไรต์ เป็นหลัก

การเกิดพลอยทับทิมทั้งสองพื้นที่นั้นมีลักษณะโครงสร้างเด่นชัดที่แตกต่างกันซึ่งอาจเป็นผลจาก การเปลี่ยนแปลงอุณหภูมิ-ความดันขเวลาในลักษณะทวนเข็มนาฬิกา การเย็นตัวลงเมื่อความดันคงที่เนื่องมาจากการการลดแรงดันขณะอุณหภูมิคงที่ทำให้เกิดคอรันดัมตามกระบวนการแปรสภาพไปข้างหน้า (M1) ทั้งจากปฏิกิริยาภายใต้สภาวะของแข็งจากไดแอสพอร์ หรือกระบวนการสลายของมาร์กาไรต์ไปเป็นคอรันดัมและเพลจิโอเคลส สภาวะสูงสุดของการแปรสภาพM1คืออุณหภูมิประมาณ 750 องศาเซลเซียสและความดัน 8-9 กิโลบาร์ ซึ่งเป็นการแปรสภาพขั้นแกรนูไลต์ สัมพันธ์กับกระบวนการเกิดเทือกเขาแนวตะวันออกของแอฟริกาเมื่อประมาณ 620 ล้านปี ปริมาณ CO_2 ในของไหลมีการเปลี่ยนแปลงอย่างรวดเร็วในองค์ประกอบของของไหลซึ่งสามารถทำให้เกิดคอรันดัมขึ้นอีกครั้งสัมพันธ์กับกระบวนการแปรสภาพครั้งที่สอง (M2) ในช่วงก่อน 580 ล้านปี ต่อจากนั้นพบลักษณะการแปรสภาพขั้นกรีนชีสต์สัมพันธ์กับกระบวนการแปรสภาพครั้งที่สาม (M3) ประมาณ 580 ล้านปี

ลักษณะโครงสร้างที่ควบคุมการเกิดปฏิกิริยาของไหลกับหินเหย้าที่เป็นอ่อนในบริเวณที่มีความสามารถในการไหลผ่านได้ดีไปจนถึงการเกิดพลอยทับทิมในส่วนหัวของแนวคดโค้งต่างๆ

ภาควิชา ธรณีวิทยา ..... ลายมือชื่อนิสิต .....
สาขาวิชา ธรณีวิทยา ..... ลายมือชื่อ อ.ที่ปรึกษาวิทยานิพนธ์หลัก .....
ปีการศึกษา 2554 ..... ลายมือชื่อ อ.ที่ปรึกษาวิทยานิพนธ์ร่วม .....
ลายมือชื่อ อ.ที่ปรึกษาวิทยานิพนธ์ร่วม .....

4973896023 : MAJOR GEOLOGY
KEYWORDS : Marble-Hosted Ruby Deposit/ Morogoro/ Nappe/ Eastern Granulites/ East African Orogeny/ FTIR/ UV-Vis/ LA-ICP-MS/ Origin Determination

WALTER ADRIAN BALMER: PETROLOGY, GEOCHEMISTRY, AND GEMMOLOGICAL CHARACTERISTICS OF MARBLE-HOSTED RUBY DEPOSITS OF MOROGORO AND MAHENGE, TANZANIA. ADVISOR: ASST. PROF. CHAKKAPHAN SUTTHIRAT, Ph.D., CO-ADVISORS: PROF. THOMAS PETTKE, Ph.D., ASSOC. PROF. CHRISTOPH A. HAUZENBERGER, Ph.D, 185 pp.

Petrological, geochemical and gemmological investigations were carried out on 17 rock samples and 80 loose ruby samples from 4 marble-hosted ruby mines in the Morogoro Region, Tanzania. In addition, 46 ruby samples from 5 different deposits including Mogok/ Myanmar, Yunnan/ China, Murgab/ Tajikistan, Luc Yen/ Vietnam, and Mangari/ Kenya were tested for their trace-element compositions and gemmological characteristics.

Origin determination for marble-hosted rubies based on their trace-element composition including Li, Mg, Ti, V, Cr, Fe, Ga, Ge, Nb, and Sn was proven feasible by the application of LA-ICP-MS. The detected trace-element compositions indicate that Morogoro rubies are characterized by a Fe-dominated chemical fingerprint compared to other marble-hosted rubies. Consequently, new criteria such as locality distinctive binary and ternary plots were defined and procedures for the application of advanced gemmological testing for origin determination based on inclusion features, UV-Vis spectrum analysis, and FTIR fingerprinting were refined.

Geologically, the ruby deposits of the Uluguru and Mahenge Mts in the Morogoro Region are related to marbles which represent the cover sequence of the Eastern Granulites in Tanzania. In both localities, the cover sequences define a tectonic unit which is present as a nappe structure thrusted onto the gneissic basement in a northwestern direction. Based on geochemistry, the Uluguru Mts deposits are located within calcite-marble whereas deposits in the Mahenge Mts are found in dolomite-marbles. Petrographically, the mineral assemblage found in the Uluguru Mts is characterized by Phlogopite-Amphibole-Carbonate-Corundum-Plagioclase-Spinel-White Mica +/- Scapolite, Tourmaline, Chlorite whereas the combination of Phlogopite-Carbonate-Corundum-Plagioclase-Sapphirine +/- Amphibole, Sphene, Tourmaline, Chlorite describes the mineral assemblage present in samples from the Mahenge Mts.

Thermodynamic calculations were carried out based on non-ideal mixing activities of essential minerals. Two ruby formations were distinguished by textural differences which may be the result of an anti-clockwise P-T-t trace where isobaric cooling is followed by isothermal decompression. The first formation appears to have formed during the prograde path (M1) either by a solid-state reaction from diaspore or by the breakdown of margarite into corundum and plagioclase. The peak conditions for M1 metamorphism at ~750°C and 8-9kbar, belonging to granulite facies, occur in relationship to the East African Orogeny at ~620Ma. A CO_2 dominated fluid experienced a rapid change in fluid composition which was responsible for the second corundum generation to form and is related to M2 metamorphism >580Ma. Subsequently, the examined units underwent a greenschist facies overprint related to M3 metamorphism at ~580Ma.

Finally, a structurally controlled genetic model was proposed where fluids interacted with the marble-host rocks in zones of higher permeability to form a saddle reef type ruby mineralization confined to fold hinges.

Department : Geology
Field of Study : Geology
Academic Year : 2011

Student's Signature .....
Advisor's Signature .....
Co-Advisor's Signature .....
Co-Advisor's Signature .....

Acknowledgements

First of all, I would like to express my gratitude to Mr. George Bosshart, Horgen, Switzerland who as my mentor and friend introduced me to the wonderful world of gemmology.

Second, and happy that I was accepted as his student in Thailand, I am grateful for the support of my thesis advisor Asst.Prof. Chakkaphan Sutthirat. It was a special honour to be the first international Ph.D. student at the Department of Geology at Chulalongkorn University. In this context I also would like to mention Mrs Wanida Muangnoicharoen who helped me in various administrative matters during the time I was studying in Thailand. Especially thankful for their help and guidance during my Ph.D., however, I am to my two co-advisors Assoc.Prof. Christoph A. Hauzenberger and Prof. Thomas Pettke. Their support and kind invitation to use the laboratories at their premises had a major impact on my work for which I would like to express my sincere gratitude.

Further, Assoc.Prof. Harald Fritz, University Graz, Austria and Assoc.Prof. Eugen Libowitzky, University of Vienna, Austria are thanked for their valuable suggestions and comments.

GIT, Bangkok, Thailand and SSEF, Basel, Switzerland supported me substantially with their generous offer to use their equipment for advanced gemmological testing for which I am very greatful.

Mr. Vincent Pardieu, GIA Bangkok, Thailand I would like to thank for sample material and shared field information. Mr. Prayoon Pongtrakul, Gramack (T) Ltd., Dar es Salaam, Tanzania is thanked for his help by providing crucial infrastructure and granting field access during my fieldwork. A special thank goes also to Prof. Abdulkarim H. Mruma, Geological Survey of Tanzania, and his team for their collaboration and field assistance. Also related to my fieldwork I would like to mention Dr. Michael Krzemnicki, Basel, Switzerland and Mr. Moses Sarakikya, Dar es Salaam, Tanzania who I shared happy moments and inspiring discussions in the field with. Father Alfred and the people of the Matombo Parish, Tanzania I would like to thank for their hospitality while being a guest in their beautiful country.

Prof. Henry Hänni, Basel, Switzerland is thanked for the skilled and highly appreciated preparation of thick and thin sections. In this regard also Mr. Mark Smith, Thai-Lanka Trading Ltd, Bangkok, Thailand has to be mentioned for his careful and swift sample polishing as well as for many inspiring discussions related to various gemmological topics. Mr. Arthur Birago, Freaking Cat, and Mr. Vlad Yavorkskyy, Yavorskyy both Bangkok, Thailand and Mr. Jaroslav Hyrsl, Prague, Czech Republic are thanked for the supply of important sample material.

A special thank has to be expressed also to Mr. Frank Lamezan and Mrs Elizabeta Stankovic both Unterseen, Switzerland who were a great help during the last stage of my thesis.

Finally, Mrs Wilawan Atichat, Mrs & Mr Chaniya and Adam Rochd-Somboon, Mr. Alex Chou, Mrs Bangon Konsuri, and Mrs Jaqueline Drysdale Laird who, as a small group of close friends, were responsible for my stay in Thailand to become a wonderful experience.

The last words of thank, however, go to my family, Mrs & Mr. Edith and Walter Balmer as well as Mrs & Mr. Stefanie and Bruno Schütz-Balmer, who I am especially indebted to. Trough all these years of study they never lost faith in me and allowed me to follow my passion for which I am sincerely grateful. With the time I was allowed to spend in Thailand they offered me a priceless gift and an experience for a lifetime.

CONTENTS

Page

LIST OF TABLES

Page

CHAPTER V GEMMOLOGY

CHAPTER VI TRACE-ELEMENT ANALYSIS

CHAPTER VII CONCLUSIONS

CHAPTER VIII RECOMMENDATIONS

LIST OF FIGURES

Page

CHAPTER I INTRODUCTION

CHAPTER II LITERATURE REVIEW

CHAPTER III GEOLOGY

CHAPTER IV PETROLOGY

CHAPTER V GEMMOLOGY

CHAPTER VI TRACE-ELEMENT ANALYSIS

CHAPTER VII CONCLUSIONS

CHAPTER VIII RECOMMENDATIONS

CHAPTER I

INTRODUCTION

1.1 General Statement

In contrast to a common assumption, the price of a gemstone does not depend on its beauty only but also on where it was found. Certain origins possess a captivating mystic, fascinating history or the reputation of producing legendary gems of rare beauty. This creates a romance which is highly esteemed by jewellers, gemmologists and final customers alike. A prestigious origin of a gemstone acts as a multiplying factor and is reflected in the high prices rubies from preferred deposits achieve. Hence, there is an urgent need by the global gem market for certificates which indicate a gems provenance.

In the past, this was not too difficult a task. Gem quality corundum was available from a very limited number of deposits only. Most of the rubies and sapphires which made their way into a piece of jewellery originated from a handful of mines located in Sri Lanka, Burma, Kashmir, or Thailand. Since the early 1990's, however, more and more new gem deposits have emerged with their products in the global gem market. Especially, the recent findings in Madagascar and East Africa (EA) have a major impact on the corundum market.

Since the number of deposits producing gem quality corundum is increasing as well as more advanced treatments are available, the need for reliable gemmological reports is more vital than ever. For gem laboratories on the other hand it is essential to have new analytical options available together with reliable criteria to be in the position to issue origin certificates on corundum with great confidence also in the future.

For origin determination in gemmology it is generally assumed that the geological and geochemical environment where gemstones grow have a direct influence on the gems' mineralogical and geochemical characteristics.

Therefore, it is believed that distinctive variations in the trace element composition, the spectrometric characteristics as well as the suite of mineral inclusions for rubies originating from different geological settings can be found (Gübelin, 1983; Gübelin Gem Lab, 2006a-c; Hänni, 1994; Hughes, 1997; Schubert, 1996; Krzemnicki, 2007; Gübelin & Koivula, 2008).

Whether it is possible to differentiate gemstones from similar geological environments, such as rubies deriving from various marble-hosted deposits, on the basis of their gemmological characteristics or their trace-element composition signatures still has to be examined.

1.2 Study Area

As seen in the today's gem market a large number of top quality rubies derive from mines related to marble-hosted deposits (e.g. Mogok, Myanmar). Trade evidence indicates that the finest gem quality corundum formed in such environments where geochemical and metamorphic conditions were ideal for the formation of top quality rubies.

Because of the economic importance, rubies from marble-hosted deposits had been chosen to be in the centre of this research project. As explained above, the study of petrology and genesis of marble-hosted ruby deposits is one of the main interests of this project. Comprehensive studies of petrological relationships however can be carried out on ruby bearing host rock samples from primary deposits only.

Additional to this pre-condition, the current market trend in terms of resources was taken into account as well.

Since 2008 there was a significant rise in ruby production in East Africa observed. Namely the mines in Winza, Central Tanzania (Schwarz et al., 2008) as well as Montepuez and Niassa in Northern Mozambique (Pardieu et al., 2009) became famous when their precious products emerged in the international gem market in recent years. Based on these new findings together with the fact that more traditional corundum producing countries suffered from political unrest the supply of the international ruby market shifted gradually from Myanmar (Burma) and Madagascar to East African sources in the immediate past.

Consequently, primary marble-hosted ruby deposits in EA were therefore defined as preferred targets for this study. Such a deposit was finally found in the Morogoro Region, Tanzania where fine rubies were produced in the 80's and early 90's once already (Hughes, 1997).

Until today, most studies on primary corundum deposits in EA however focused on none marble-hosted deposits from sources in the Mangari area, Kenya (Mercier et al., 1999) or from Longido (Keller, 1992), Umba (Solesbury, 1967), and Winza (Schwarz et al., 2008) the last three all in Tanzania. In contrast to these deposits, the marble-hosted ruby deposits in the Morogoro Region did not catch the attention of researchers and detailed studies were not carried out until present.

Conclusively, the marble-hosted ruby deposits in the Morogoro Region, Tanzania were chosen as a study area and to be in the focus of this research project.

1.3 Motivation

Up to present most studies which had been carried out on gem quality corundum deposits were focussing either on geology or gemmology. The key to a better understanding and correct interpretation of the characteristics found in gem quality

corundum, however, lies in the combination of these two fields. Therefore, it is one of this study's objectives to address geological information together with gemmological characteristics of gem-quality rubies originating from marble-hosted deposits.

An other objective was to close analytical gaps in the characterisation of rubies from the Morogoro Region as well as to improve or expand the application of analytical methods used in gemmology.

It was further the aim of this research to investigate for new criteria in origin determination on marble-hosted rubies by the application of latest technology in trace-element analysis.

Finally, it was a goal to evaluate the genesis of the ruby deposits in the Morogoro Region, Tanzania and to compare the characteristics found with other marble-hosted ruby deposits in the world.

1.4 Methodology

The methods and analytical techniques applied in this study were organised following the outline of a methodoly flow-chart as shown in Fig. 1.1.

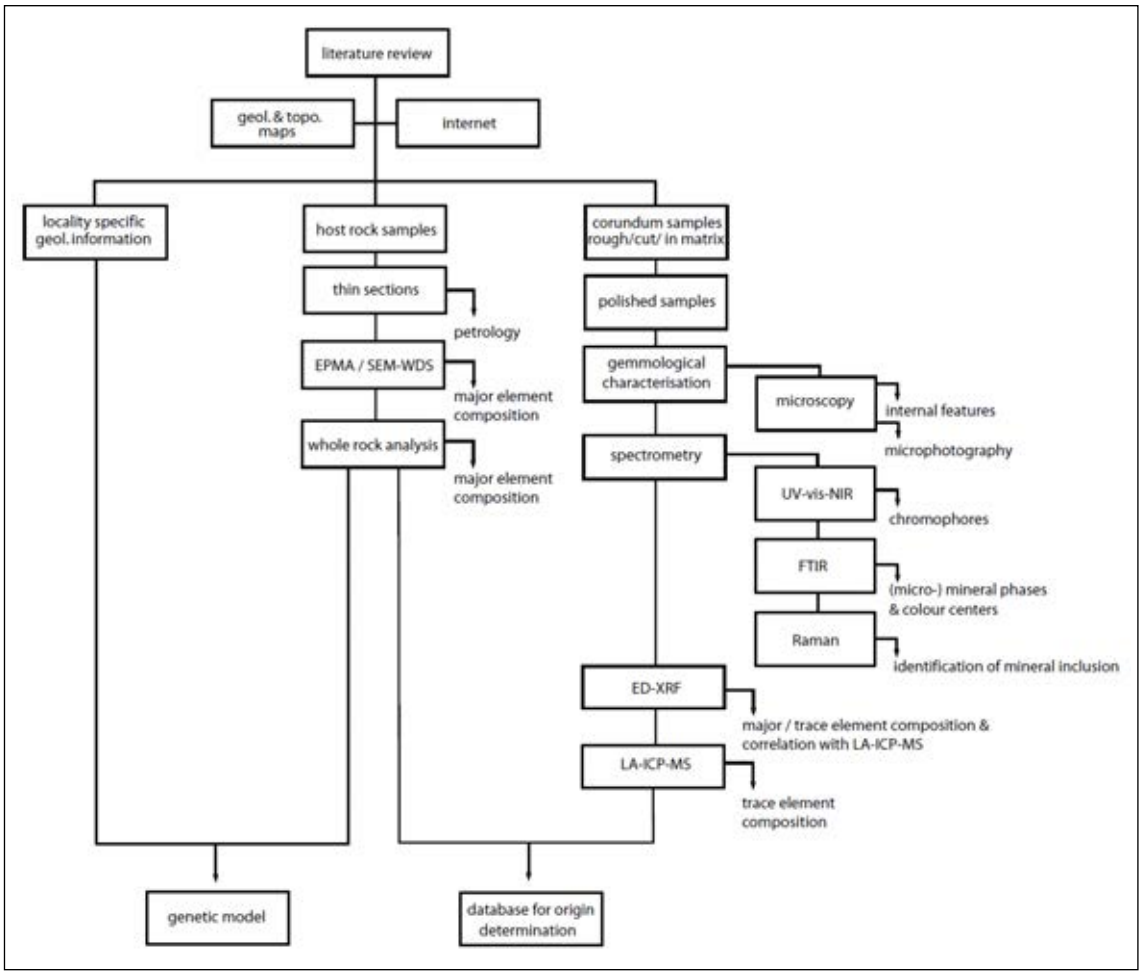

Fig. 1.1: Methodology flow-chart of techniques applied in the framework of this study.

1.4.1 Literature Review

As an initial step, literature and open source information available from libraries and the internet were consulted to search for information about previous gemmological studies on corundum from Tanzania, the deposits in terms of geology and production, the geography and history of the study area as well as to look for logistic infrastructure which a field campaign could base on.

Contacts to governmental organisations such as the Geological Survey of Tanzania in Dodoma, Tanzania, or academic institutions like the Department of Geology at the University of Dar es Salaam were established by the author during this stage. Key to a successful field campaign however were contacts to mining companies located both in Tanzania and Thailand granting access to the mines and to researchers who had specific knowledge of the targeted study area.

1.4.2 Fieldtrips and Sample Collection

The various fieldtrips which were undertaken in the framework of this study were crucial in terms of origin determination. Only if it was possible to collect sample material with secured origin a reference database for origin determination purposes could be built. Since it is very difficult to purchase samples with a high level of confidence in terms of origin from the gem trade, the only way to collect such samples is on-site at the mine and if possible by the researcher himself. Therefore, two fieldtrips to the areas of interest in EA and Tanzania in particular were planed.

Once in the field, a geological survey to examine the petrologic and structural setting of the marble-hosted ruby deposits in the Morogoro Region, Tanzania was carried out. Due to limited time in the field and tropic conditions (high weathering rate and dense vegetation) full scale geological mapping was not undertaken. Loose ruby samples for gemmological and trace-element analyses as well as host rock samples to determine the metamorphic conditions of the marble-hosted ruby deposits were collected at the same time however.

The first fieldtrip was carried out during summer 2007 and started with a two week fieldtrip organised by the International Coloured Gemstone Association. After this introductory excursion to gem producing areas in EA (Kenya & Tanzania) the author was spending another 4 weeks in the field to gather further first hand information about the geology, current mining situation, mine access, as well as to buy maps from the Geological Survey of Tanzania in Dododma. The author also took the opportunity to make personal contact with the local government organisations and to visit potential study areas. This trip was mainly funded by a sponsoring which was granted by the Gems and Jewelery Institute of Thailand (Public Organisation), Bangkok (GIT).

The second fieldtrip in summer 2009 was focusing on the defined study areas in the Morogoro Region specifically. During a stay of almost 3 months it was possible to visit several mining sites and to collect samples directly at the mines. At the end of this field season the 31st International Gemmological Conference in Arusha, Tanzania

was attended where a preliminary field report was delivered (Balmer et al., 2009). This second fieldtrip as well as the purchase of sample material was fully financed by the author himself.

In order to collect further reference material with high level of confidence in terms of origin additional fieldtrips to other marble-hosted ruby deposits were carried out. Accordingly, the marble-hosted ruby deposit in Luc Yen, Vietnam was visited in Winter 2008, Spring 2009 and Autumn 2010. Also the deposits near Yuan Jiang in Yunnan, China were visited twice in Autumn 2009 and Autumn 2010. Again, the fieldtrips as well as the purchase of sample material was funded by the author himself.

1.4.3 Sample Preparations

1.4.3.1 Rock Samples

Sample registration and selection as well as initial sawing of rock samples was carried out at the facilities of the Department of Geology at Chulalongkorn University, Bangkok, Thailand first.

A total of 17 thin- and thick sections were then produced from rock samples which had been collected during two field seasons in 2009 and 2010 in the Morogoro Region, Tanzania. These 17 samples included rock samples from the investigated mines as well as from the basement. After petrographic description samples had to be chosen for further investigations regarding mineral chemistry as well as thermodynamic calculations. To describe the mineral paragenesis in the two mines investigated in the Uluguru Mts sufficiently two thick sections each had been necessary. In the contrary, it was possible to find one characteristic sample for each of the two investigated mines in the Mahenge Mts which described the mineral assemblage satisfyingly.

The mentioned thin- and thick sections were obtained from both the Department of Geology, Chulalongkorn University, Bangkok, Thailand, the Institute of Earth Sciences, Karl-Franzens' University, Graz, Austria as well as the Institute of Geological Sciences, University of Bern, Switzerland.

After petrographic investigations the 6 samples which were chosen for mineral chemistry analysis were coated by a thin layer of carbon to allow the sample surface to become conductive. The carbon coating was added by a sputtering procedure carried out immediately before analysis.

In addition, whole rock analysis were carried out on samples from Mwalazi and Visakazi II Mine in the Uluguru Mts as well as Kitwaro and Ipangko Mine in the Mahenge Mts. For each of the four examined ruby mines there was a mineralised as well as a host rock sample tested, 8 whole rock samples in total. At the mines, all unmineralised host rock samples were collected in close proximity next to the mineralised rocks but about 20m away the furthest.

The samples had to be broken and grinded in order to receive a fine grained host-rock powder of a size not more than 200Mesh. This rock powder was then sent to DMR for further analysis. The result are disussed in chapter 4 as well.

The results from mineral chemistry investigations as well as thermodynamic calculations are discussed in further detail in chapter 4. Worksheets describing the petrography of all 17 samples can be found in Appendix A.2.

1.4.3.2 Loose Ruby Mineral Samples

During gemmological testing a total of 80 loose rubies (Uluguru Mts n=43, Mahenge Mts n=37) in the range of about 1ct size from the Morogoro Region were analysed. None of the samples had been subject to treatments and most of the samples had been collected in the field by the author himself. As Indicated in Appendix A.1, a few samples from the Morogoro Region however were kindly provided by Mr. Vincent Pardieu from his personal collection. Additionally, there were also some samples from other marble-hosted ruby deposits incorporated in the gemmological investigations. Samples from Yunnan, China (n=12) and as Luc Yen, Vietnam (n=8) as well as John Saul Mine, Kenya (n=3) had also been collected by the author where as the samples from Murgab, Tajikistan (n=6) were obtained from Mr. Vladislav Yavorskyy, Bangkok, Thailand. Samples from Mogok & Namyaseik, Myanmar (Burma) (n=17) were either received from Mr. George Bosshart's private collection, Horgen, Switzerland or on loan from the reference collection of GIT, Bangkok, Thailand. All these samples which hadn't been collected by the author himself still were confirmed to be collected at the deposit itself. Samples purchased from local markets had not been incorporated into this study unless indicated otherwise. This restrictive procedure was followed to maximise the level of credibility in terms of origin for the examined samples.

To prepare rough ruby samples for gemmological testing two parallel windows perpendicular to the c-axis had been polished on each sample. In the case of spectrometry, the parallel windows allowed the analysing beam to travel more readily which further improved the spectrum quality in the following. This step in sample preparation was carried out mainly by Thai-Lanka Trading Ltd. in Bangkok or with other companies of local cutting industry in Bangkok, Thailand.

In the suite of preparation steps the polished surfaces had been wiped by a lint-free cloth drenched in ethanol next. This simple procedure proofed to be efficient enough in removing traces of grease as well as dust and reduce contamination to acceptable levels.

For the examination of reference sample materials by FTIR, KBr pellets had to be pressed. Therefore, the sample material was crushed and powdered using an agate mortar and pistil first. Subsequently, the powdered samples were mixed with KBr powder in the weight ratio of 1:100 to receive a sample with a total weight of 1g. Finally, the KBr pellet was pressed in a simple screw-press device as seen in Fig.1.2. If spectra obtained from a pellet with a weight ratio of 1:100 showed too high ab-

sorptions the sample to KBr weight ratio was lowered to 1:500 and an additional KBr sample pellet was pressed in the following. Reference sample material was either purchased from the gem market in Bangkok by the author or donated by Mr. Jaroslav Hyrsl from Prague, Czech Republic in the case of gibbsite.

Sample preparation of rough samples for trace-element analysis is very important in the case of LA-ICP-MS. Due to the fact that not all gemmological samples are cut stones, undesired staining or dirt can be trapped in cavities and grooves on the surface or in cracks of a rough gemstone. To avoid such contaminations and to eliminate debris but also polishing remnants a cleaning procedure introduced by Balmer et al. (2009) was applied.

For polished samples a much easier approach could be followed. An easy two-step procedure is already sufficient enough to eliminate surface staining. The first step involves rubbing the polished or faceted gemstone surface where the ablation will be carried out against a clean sheet of paper. The second step is handled by wiping the surface with a lent-free paper cloth or tissue which is drenched in ethanol first. Working with rubber gloves and tweezers further decreases the potential of an unintended surface contamination that mostly relate to residues of human sweat and grease.

In the following the exact number of investigated samples for each analytical technique will be indicated individually in the appropriate chapters.

Fig. 1.2: Tools used to create KBr sample pellets. From left to right, an agate mortar and pistil to grind the sample material, a pressure cell with unscrewed top screw to create the translucent to transparent KBr pellets, and on the far right the sample holder with a Blu-Tack™ rim to allow fine positioning adjustments of the pressure cell when attached to the sample holder for FTIR measurements are displayed.

1.4.4 Analytical Techniques

1.4.4.1 Petrography

The relative genetic time relationships between metamorphism, alteration, and tectonics as well as the petrologic conditions under which the rubies grew were examined by microscopy on thin sections obtained from host rock samples. The microscopy examinations together with microphotography was carried out at the Department of Geology, Chulalongkorn University, Bangkok, Thailand.

1.4.4.2 Electron-Probe-Micro-Analysis (EPMA)

The chemical composition of minerals was determined using a JEOL JXA8100 EPMA unit at the Department of Geology at the Chulalongkorn University, Bangkok, Thailand (Fig. 1.3). Analyses were taken under the application of an accelerating voltage of 15kv and 10nA sample current. The measurements were taken under focused beam which resulted in a beam <1µm in diameter. The sample measuring time was set to 30 seconds and to 10 seconds for peak counts and background counts, respectively. As standards there were natural mineral standards used. Data correction was carried out by following a ZAF procedure.

Fig. 1.3: EPMA unit employed at the premises of the Department of Geology, Chulalongkorn University, Bangkok, Thailand.

1.4.4.3 Scanning-Electron-Microscope with Attached Wave-Dispersive X-Ray-Fluorescence Spectrometre (SEM Coupled WD-XRF)

Additional mineral analyses were carried out at the Department of Earth Sciences, Karl-Franzens University, Graz, Austria with a JEOL 6310 SEM equipped with a LINK ISIS energy dispersive system and a MICROSPEC wavelength dispersive system. Standard analytical conditions were set to an accelerating voltage of 15kV and 6nA sample current on PCD. The applied beam diameter was 1µm except for carbonates, Am, and Phl the beam size was changed to ~5µm to avoid damage of the mineral by the electron beam. The matrix corrections of silicates were made using the Phi-Roh-Z procedure. The following mineral standards were used: Si, K (EDS): Adular; Al (EDS): Andalusite; Fe (EDS), Mg (WDS): Garnet; Ca, Ti (EDS): Titanite; Mn (EDS): Tephroite; Zn (EDS): Gahnite; Cr (EDS); Mg-Chromite; Cl (EDS): Atacamite; F (WDS): F-Apatite, Na (WDS): Jadeite.

The practical detection limits in these routine analyses varies from ~0.05wt.% for the MICROSPEC wavelength dispersive system, and 0.1 to 0.2wt.% for the LINK ISIS energy dispersive system.

1.4.4.4 WD-XRF Whole Rock Analysis

According to the proposal of this research project, geochemical analysis of whole rock composition of marble host rock samples were not planned initially. During the conduct of this Ph.D. however a possibility emerged to have whole rock samples analysed by the Department of Mineral Resources (DMR), Bangkok, Thailand. Therefore, limited whole rock analysis was carried out anyhow.

Whole rock analysis by XRF analyses were carried out on fused glass disks at the Department of Mineral Resources (DMR) of Thailand using a PANalytical WD-XRF (Axios advanced) spectrometer. Each glass disk was made of 1 gram of a powdered sample fused with 5 grams of a fluxing agent, which is a 66:34 combination of di-lithium tetraborate and lithium metaborate. Two rock standards, including JB-1a (Basalt) and MRG-1 (Gabbro), were used for calibration. In addition, FeO contents were also acquired through a wet chemical task at DMR. Then, weight percent of Fe_2O_3 of each specimen were recalculated using the following equation:

$$Fe_2O_3 = Fe_2O_3^t - 1.1113 \times FeO$$

The detection limits in these routine tasks are 0.01wt.% for MnO, K_2O and P_2O_5; 0.02wt.% for TiO_2, $Fe_2O_3^t$ and CaO; 0.05wt.% for Al_2O_3; 0.1wt.% for SiO_2, MgO and Na_2O, respectively.

In order to analyse the collected ruby samples with most up-to-date analytical technique it was further possible to establish collaboration with the University of Bern. Prof. Thomas Pettke generously granted the author full access to his LA-ICP-MS laboratory while being in Switzerland (Winter 2007, Autumn 2008, Spring 2010). Travel

expenses to and within Europe were covered by the kind financial support of Kabelfernsehen Bödeli AG, Unterseen, Switzerland.

Finally, advanced gemmological testing, including spectrometric methods as well as ED-XRF trace-element analysis, were applied to characterise the examined sample material gemmologically. The majority of gemmological examinations were done at the premises of GIT (Spring 2011) but finalised with measurements taken at the gemmological laboratory of SSEF, Basel, Switzerland (Summer 2011).

1.4.4.5 Gem Testing Techniques

In the framework of this study there were traditional as well as advanced gem testing methods applied. Traditional gem testing included the determination of specific gravity by hydrostatic measurements as well as optical properties such as refractive index and birefringence by refractrometry. Pleochroism was tested by a hand-held dichroscope where as the reaction to short- (254nm) and long-wave (365nm) ultra-violet irradiation was examined by a 7W UV lamp. All gemmological instruments employed were products by System Eickhorst, Hamburg, Germany.

Beside the traditional gemmological examinations, advanced gem testing methods were applied during this study as well.

FTIR spectra were taken in condensed-beam mode on cut and polished samples by a Thermo Scientific, Nicolet 6700 unit. For the analysis of KBr reference samples the mode was changed to transmission and a simple sample holder was applied to position the sample perpendicular to the ray path, penetrating the sample right in its centre. For each measurement 124 scans at resolution 2 were accumulated. The spectra were taken in the range between 1500 and 5000cm^{-1}.

Polarised UV-vis spectra on the other hand were taken in the range between 200 and 860nm applying a Perkin Elmer, Lambda 950 photospectrometer. The instrument parameters were set to 102.5nm/min scanning speed, 0.5nm data spacing, 2nm slit width and the filter change to be executed at 319.2nm. An adapted sample holder for gem testing, basically an aperture plate with a counterbore of 4mm in diameter attached in front of the integration sphere of the UV-vis unit, was used to hold the samples in position during the measurements.

Selected mineral samples were further analysed by Raman spectrometry where a Renishaw InVia unit was applied to indentify mineral inclusions. For these examinations a ”green” Ar-Ar laser emitting coherent light of 25mW power at a wavelength of 514nm was employed. Scanning time was set to 10 seconds where as 20 accumulations for each measurement were sufficient to receive significant signals. Finally, the spectra were collected in the range between 2000 to 200cm^{-1} Raman Shift, and 100% laser power.

1.4.4.6 Energy-Dispersive X-Ray Fluorescence Spectrometry (ED-XRF)

ED-XRF measurements were carried out at the Gem and Jewelery Institute of Thailand (Public Organisation), Bangkok, Thailand (GIT). GIT houses an EDAX Eagle III unit which was purchased in 2009.

Since ED-XRF was not the main method applied during this study technical details are not reported here. Specific aspects will, however, be discussed during a performance comparison with LA-ICP-MS in chapter 6.1. Instrument parameters employed for analysis in this study are as follows. All measurements were made under vacuum conditions where 40kV tube voltage and 250µA tube current were reported respectively. The X-ray beam was 300µm in diameter. For calibration a routine of matrix-matched standards was setup by GIT using several rubies and sapphires of known composition. The actual calibration finally was made by a linear regression incorporating the data acquired from the mentioned ruby and sapphires standard samples.

The printouts of the individual ED-XRF spectra of the measurements carried out during this study are attached to the Appendix under chapter B.5.

1.4.4.7 Laser-Ablation Inductively-Coupled-Plasma Mass-Spectrometry (LA-ICP-MS)

Regarding LA-ICP-MS investigations, it was possible to establish a close collaboration with Prof. Thomas Pettke from the Earth Sciences Department of the University of Bern, Switzerland. Three lab sessions were carried out in the following where samples from various marble-hosted ruby deposits were analysed at the premises of Prof. Pettke's laboratory (Fig. 1.4). The University of Bern hosts a 193 nm ArF excimer laser ablation unit (GeoLas, Microlas, Germany) coupled to an Elan DRC-e quadrupole mass spectrometer (Perkin Elmer, Canada). For a general appraisal of modern LA-ICP-MS techniques and applications, the reader is referred to a recent Mineralogical Association of Canada Short Course compilation (Sylvester, 2008).

As it can be deducted from the name, three integral instrument components are involved in a LA-ICP-MS setup (Fig. 1.5).

The first component consists of an optical system including a pulsed UV-laser source, an optical beam homogeniser and finally a microscope. Prior to the microscope there is also an aperture blend and a CCD camera intercalated in the light path.

The various optical lenses and filters subsequent to the laser are responsible to homogenise the energy of the laser beam throughout its diameter. The flat-top laser beam (i.e., constant energy density across the ablation spot, irrespective of spot size) allows a homogenous ablation creating sharp edged and even bottomed laser pits. With variable aperture blend openings the pit size of the ablation can be changed from 200µm down to 5µm accordingly. By adjusting the distance between objective and sample the microscope finally focuses the laser beam on the sample's

Fig. 1.4: The LA-ICP-MS unit at the laboratory of Prof. Thomas Pettke, Earth Science Department, University of Bern, Switzerland.

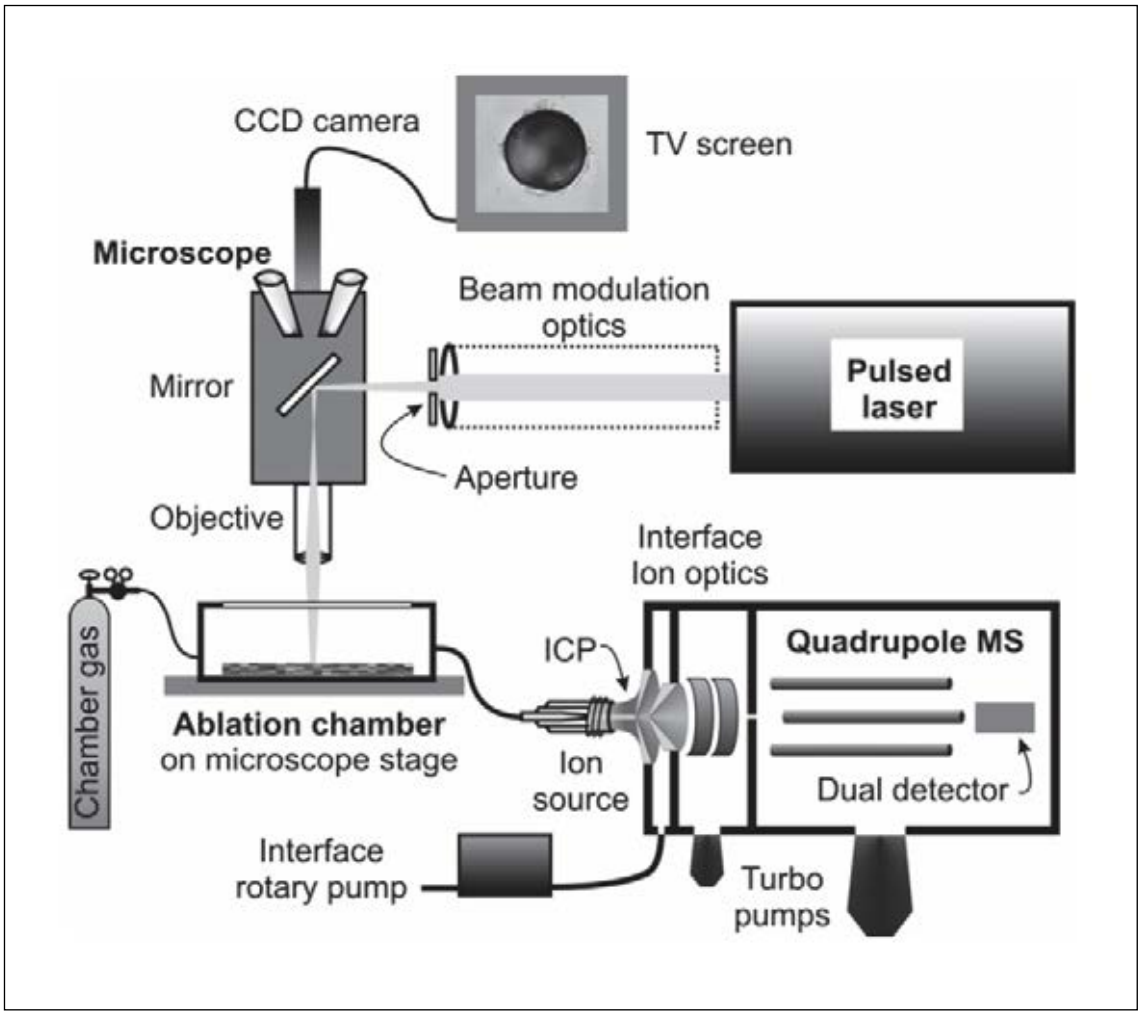

Fig. 1.5: Schematic layout of a Laser-Ablation Inductively-Coupled-Plasma Mass-Spectrometer with its three instrumental parts : Laser-optics, sample cell with carrier gas system attached to ICP, and finally the MS unit (modified after Heinrich et al., 2003)

surface whereas the precise positioning and online observation of the ablation process is facilitated by a CDD camera and screen.

Once the ablation took place the ablated sample particles are flushed in a stream of carrier He gas (or gas-mixture) into the plasma, the second part of the LA-ICP-MS. To allow an efficient sample transport from the ablation pit to the plasma the air-sealed sample chamber is connected by thin plastic tubes. When the aerosol reached the inductively coupled plasma the sub-microscopic sample particles (aerosol particle size 10 - 1000 nm) get atomized and ionised, at temperatures of 6000 - 9000 Kelvin.

After the ICP source, the ions are filtered according to their mass to charge ratio in a quadrupole, i.e., mass filtering is electrostatically. As a last and third part there is a mass-spectrometer attached to plasma which are usually combined to one unit. Here the analyte reaches the end of its journey and the isotopes deriving from the now ionised sample are detected according to specifications in the analytical routine.

Detailed instrument specifications of the LA-ICP-MS unit deployed at the Earth Sciences Department, University of Bern, Switzerland information are provided in Tab.1.1.

Laser Ablation Parameters

Laser : Lambda Physik, Complex-Pro, ArF Eximer Laser

Wavelength :	193nm
Pulse Rate :	10 Hz
Laser Output :	150mJ
Fluence :	23J/cm^2
Pit Size :	120µm
Background Time :	50sec.
Ablation Time :	60sec.

ICP-MS Parameters

ICP-MS : Perkin-Elmer, ELAN DRC-e, Quadrupole

Carrier Gas Flow :	1.000 l/min : He 0.007 l/min : H_2
Radio Frequency Power (RF) :	1450W
Nebulizer Ar Gas Flow :	0.67l/min
Auxilary Ar Gas Flow :	0.65l/min
Cooling Ar Gas Flow :	16.0l/min

Analysed Isotopes

^{7}Li	^{93}Nb
^{9}Be	^{95}Mo
^{11}B	^{118}Sn
^{23}Na	^{137}Ba
^{25}Mg	^{139}La
^{29}Si	^{140}Ce
^{31}P	^{141}Pr
^{39}K	^{146}Nd
^{44}Ca	^{147}Sm
^{49}Ti	^{153}Eu
^{51}V	^{157}Gd
^{53}Cr	^{159}Tb
^{55}Mn	^{163}Dy
^{57}Fe	^{165}Ho
^{59}Co	^{167}Er
^{62}Ni	^{169}Tm
^{65}Cu	^{173}Yb
^{66}Zn	^{175}Lu
^{71}Ga	^{178}Hf
^{73}Ge	^{181}Ta
^{75}As	^{182}W
^{85}Rb	^{208}Pb
^{88}Sr	^{232}Th
^{89}Y	^{238}U
^{90}Zr	

Tab. 1.1: LA-ICP-MS instrument parameters as reported during this study.

1.5 The History of Ruby Mining in the Morogoro Region, Tanzania

Tanzania had been a source for gem quality corundum since the early 1900 when ruby was first mined from an anyolite deposit near Longido, Northern Tanzania. In the late 1950's a next deposit located in the Umba River Valley started its production where fancy sapphires of various and fantastic colours were mined.

During the 1970's then rubies and spinels started to occur from the Morogoro Region, Central Tanzania (Dirlam et al, 1992).

The height of ruby production in the Uluguru Mts however was reached in the early 1980's after a ruby mine was discovered near the village of Ngong'horo in the south of Uluguru Mountains about 35km southeast of Morogoro City (Altherr et al., 1982). Encouraged by the first findings of fine rubies Mayote (T) Ltd., a Thai mining company based in Dar es Salaam, opened their mine nearby at Visakazi in 1984. Shortly after a mine called Mwalazi and located about 5km further to the north took up its operation in 1986 (pers.comm. V. Pardieu, GIA Bangkok, Thailand). Additionally to the ruby mining activities in the Uluguru Mts, the village of Matombo used to host a spinel mine during the same time. Mining was stopped in the late 1990's however due to a conflict of interest between the local community and the diocese in Morogoro who owns the land in the vicinity of Matombo (pers.comm. Father Alfred, Matombo parish).

Unlike the corundum found in the Umba Valley, the rubies mined in the Morogoro Region resembled the material known from more traditional sources such as Mogok, Myanmar (Burma). Because there were not many options regarding bright intense coloured rubies other than the stones from Mogok, Myanmar (Burma) during this time the new mines discovered in Central Tanzania were a welcome alternative and their rubies became soon highly sought after (Fig. 1.6). Due to a semi-mechanised mining style, the fact that the deposit was found in a primary source, and due to seasonal weather conditions the yield from the Morogoro ruby mines never reached big quantities however.

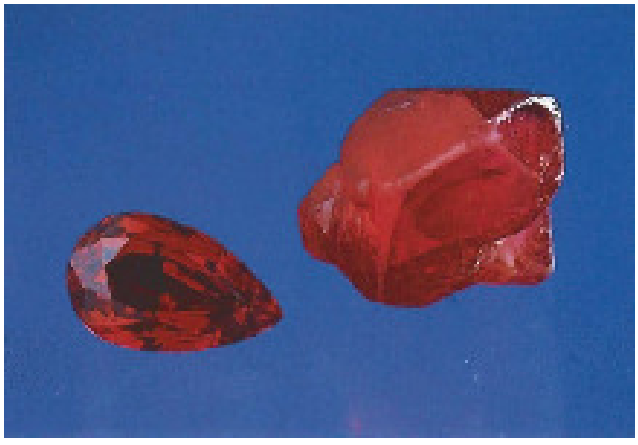

Fig. 1.6: The picture shows two samples of gem quality rubies produced from the Mwalazi Mine, Uluguru Mts, Morogoro Region, Tanzania in the early 1990's (from Dirlam, 1992). The pieces shown in the picture weigh 0.87ct for the pear-shaped faceted ruby and 5cts for the rough crystal respectively.

Then in late 1993 (Hamid et al., 1999) the discovery of an additional corundum deposit in Tunduru, Southern Tanzania was made and gem mining in Tanzania reached new levels as a whole. As a consequence and stimulated by this new find the Tanzanian government changed their mining policy. Combined with the fact that large quantities of rubies from Mong Hsu, Myanmar (Burma) started to emerge in the international gem market at that time the mines in the Morogoro Region could not compete in terms of productivity and quality any longer. In the following the industrial mining operations in the Morogoro Region came to a halt soon after and miners started to move further south to Tunduru where they found work in the newly opened mines at there. With one exception only small scale artisanal-style mining remained in the Morogoro Region and locals took care of the mining ever since. When visited by the author in 2007, the alluvial deposits which were mentioned by Dirlam et al. (1992) and located near the settlements of Mvuha and Magogoni further downstream in the Ruvu River plains, they were found no longer to be actively mined either.

The one exception for mechanised mining which was mentioned above is a new mining operation which started in early 2009 nearby the former mine at Visakazi. Since there was no name given to this mine yet the operation was called Visakazi II by the author. The current semi-mechanised mine is operated by Deutrex 818 Ltd. a company registered in Dar es Salaam which mainly caters the Indian gem trade with cabochon grade rubies (pers.comm. V. Pardieu, GIA Bangkok, Thailand).

In the Mahenge Mts. two main mining areas had been producing gem quality rubies in the past. Mining activities started in the plains east of the Mahenge Mts near the settlements of Lukande, Chipa and Mayote. The first discovery of rubies in the foothills of the Mahenge Mts is mentioned to have taken place by hunters in 1984 (Koivula et al., 1993). Afterward several Thai investors started mining operations in Lukande and Mayote in 1986 (pers.comm. V. Pardieu, GIA Bangkok, Thailand). A few years later in the late 1980’s mining started also in the Mahenge Mts itself. One of the first hillside mines was known as Kitwaro followed by the Ipangko ruby mine shortly after. Both mines were worked by the same Dar es Salaam based Thai company which was active in ruby mining also in the Uluguru Mts as well as in the plains near Mahenge at that time.

Mechanised mining activities diminished however after a series of incidents related to thefts happened in the mid 1990’s and mining became too difficult due to problems with the local authorities arising from these unfortunate events. Mining activities then shifted from Mahenge further southwest to Songea where corundum was produced since 1992 (pers.comm. V. Pardieu).

Recently, there were only a few locals left, maybe a dozen at each mine, taking care of the mining as seen when the author visited the deposit in the vicinity of Mahenge in 2007 and 2009. The people present at the mines were basically watchmen stationed there to look after the infrastructure which was left behind by the former mining companies and to make sure that nobody violates the right to mine. Mining in these mines seem to take place sporadically and on a small-scale, day to day bases only.

In 2005, the discovery of a vibrant neon-pink spinel deposit, just across the hill eastward from the former Ipangko ruby mine and near the town of Mahenge, blew new live into the mining activities in the Mahenge Mts. At the time of visit in 2009 there were several hundred miners working in a semi-mechanised mining style at the Ipangko spinel mine where explosives, excavators, water jets, jigs and diesel-driven water pumps and pneumatic hammers were applied to find the bright shining pink spinels in the white marble host rock. Where the gem-bearing marble is weathered to lateritic soil small box-type mining by local miners could be observed applying primitive tools only or diesel-engine driven water pumps the most. The mining licences are held by several companies and private investors today. There are however efforts taken by some of these licence holders to combine the concessions in order to control the production and therefore the supply to the market of these unique spinels coming from the Mahenge Mts.

Fig. 1.7: Sketch map showing the corundum occurrences in Tanzania (modified after a template by R. Hughes).

1.6 Thesis Report Organisation

In the suite of this research report the following topics will be covered.

Chapter 2 starts with a literature overview on the most relevant publications in geology, gemmology as well as trace-element analysis related to the topics of this study. The aim of the next chapter is therefore to provide the reader with the most significant back ground information on what was published in the fields of research which are going to be touched by this project.

Chapter 3 is focussing on the geology of the study area. By proceeding from large to small scale observations regional geology aspects are introduced first and field observations on a deposit scale will be discussed thereafter. Structural field observations will be covered. From stereoplots relationships to the regional structure the Uluguru Nappe are drawn. Finally, the observed tectonic events are tried to be linked to deformational phases mentioned in literature.

Chapter 4 is covering the petrological investigations regarding the ruby formation of the marble-hosted ruby deposits in the Morogoro Region, Tanzania. Mineral descriptions from microscopy as well as results from EPMA and WD-XRF investigations were considered. The chapter will be concluded with thermobarometric calculations and possible reactions which explain the observed ruby mineralisation.

Chapter 5 shades light on the gemmological characterisation of rubies from the Morogoro Region in comparison with rubies from other marble-hosted deposits. The main interest of this chapter is with new results and procedures obtained from advanced gemmological testing carried out during this study. Results from FTIR and UV-vis photospectrometry investigations will be presented and new procedures discussed.

Chapter 6 is dedicated to trace-element analysis by Laser-Ablation Inductively-Coupled-Plasma Mass-Spectrometry (LA-ICP-MS). From a performance comparison of the chosen analytical method with widely applied ED-XRF, and instrument characteristics, to improved sampling and data reduction procedures the reader is introduced to the application of LA-ICP-MS in gemmology step by step. The chapter finally concludes with distinctive plots and diagrams which are suitable for origin determination of marble-hosted rubies based on LA-ICP-MS analysis.

In Chapter 7 the attempt is made to set the information gained from previous chapters into relation with each other. A genetic model will be introduced subsequently and tired to put in a broader context by the comparison with other marble-hosted ruby deposits thereafter.

In Chapter 8 the opportunity is taken to summerise the findings of this research project as well as taking new knowledge from this study into account and projecting it on to new research targets. Analytical recommendations will be made, areas for new mining activities suggested and new research topics indicated.

Chapter 9 is giving reference to publications which had been taken into account during this study.

The Appendix section finally, adds the data and further detailed information which did not find its way into the main text but still has to be mentioned to give full reference on which data the here presented research was based on.

CHAPTER II

LITERATURE REVIEW

2.1 Ruby

A long standing reference is "Gems" by Webster (1994) where gemmological characteristics and general information about gemstones and their origins are covered.

More detailed information on corundum is available in "Ruby & Sapphire", Hughes (1997). This publication gives a comprehensive overview of the different corundum occurrences of the world in terms of geography and gemmology. Although many new mines opened their production since the book was published, it is still considered a standard work on corundum deposits and corundum in general.

2.2 Ruby Deposits

More related to the genesis of corundum deposits the publications of Hunstiger (1990); and Giuliani et al. (2007) have to be mentioned. They give a detailed overview including a deposit classification by Giuliani et al. (2007) which allows addressing corundum deposits systematically.

2.2.1 East African Corundum Deposits

Regarding gem deposits located in East Africa a few publications giving a general overview of the occurrences in East Africa can be found (Keller, 1992; Dirlam et al., 1992; Schlüter, 1997). Mainly the more traditional sources had been covered during the past by more detailed studies whereas for the newer deposits hardly any publications can be found.

In Kenya, the John Saul Mine has been in the focus of previous studies in particular. Starting with early, more regional geology studies by Pohl and Niedermayr (1979), Pohl and Horkel (1980), and Key and Ochieng (1991) the deposit had been examined more in detail recently by Mercier et al. (1999) and Simonet (2000). It was found that the deposit is located at the contact between graphitic gneisses and an intruding ultramafic body where the rubies are restricted to be found in an alteration zone of the graphitic gneisses right in the contact zone.

On the Tanzanian side a traditional occurrence also related to an alteration involving desilification is the deposit of Umba. Already in the late 60's Umba had been recognised as a primary deposit involving pegmatites intruding an ultramafic body (Solesbury, 1967). Later research concentrated on the gemmological properties of the material produced from this occurrence both found in primary as well as secondary deposits (Zwaan, 1974; Hänni, 1986; Hänni, 1987).

Further to the north the occurrence of Longido as a traditional source of gem material has to be mentioned. Meixner (1977) and Keller (1992) described this special deposit of rubies in zoisite.

The recent discovery of the Winza ruby mine near Mpwapwa in the Dodoma Region was discussed in detail by Schwarz et al. (2008).

All these sources of rubies from EA are not of a marble related mineralisation type however.

2.2.2 Marble-Hosted Ruby Deposits

Marble-hosted ruby deposits in particular had been the topic for a large number of publications in the field of gemmology already. Gemmological research on specific localities was carried out for the deposits of Mogok, Myanmar (Kane and Kammerling, 1992; Kammerling et al., 1994; Schlüssel, 2002), Mong Hsu, Myanmar (Peretti et al., 1995; Peretti et al., 1996; Smith and Surdez, 1994; Siripaisarnpipat et al., 2002), Hunza, Pakistan (Gübelin, 1982), Murgab, Tajikistan (Smith, 1998; Pardieu et al., 2009), Jegdalek, Afghanistan (Bowersox et al., 2000), Chumar & Ruyil, Nepal (Smith et al., 1997), and Luc Yen, Vietnam (Kane et al., 1991; Long et al., 2004) in the past already.

The deposits in Yuan Yiang, Yunnan, China (Balmer et al., 2010) as well as Hunza, Pakistan (Okrusch et al., 1976) and especially the deposits of Luc Yen, Vietnam (Garnier et al., 2002; Garnier et al., 2005) were also examined under geological aspects. Garnier et al., (2008) further published a comprehensive report on the petrology of Himalayan marble-hosted ruby deposits concerning the formation of gem quality ruby.

2.2.2.1 The Marble-Hosted Ruby Deposits of the Uluguru and Mahenge Mts, Morogoro Region, Tanzania

The marble-hosted ruby deposits of the Uluguru and Mahenge Mts in the Morogoro Region, Tanzania are the subject of this research project, and had been studied by a few researchers in the past only. Malisa and Muhongo (1990) published a very general study focusing on regional tectonics related to the Pan African and the possible connection to the genesis of gem deposits in the Mozambique Belt. Hänni and Schmetzer (1991) as well as Msolo (1992) worked specifically on ruby occurrences in the Morogoro Region, Tanzania. Whereas Hänni and Schmetzer (1991) focused on the gemmological aspects of the rubies produced from this region, Msolo (1992) was concentrating on the geology of one particular deposit in the Uluguru Mts, the Visakazi Mine. A short, more exploration orientated work about the ruby occurrences in the Uluguru Mts, Tanzania was then published by Muhongo and Errera (1993).

Finally, it can be said that not enough literature was found to sufficiently characterise the ruby deposits of the Uluguru and Mahenge Mts, Morogoro Region, Tanzania. Furthermore, detailed trace-element analysis data for the gem material of the examined

region is not available until today. The lack of information was one of the reasons why it was decided to select these deposits as the target area of this research project.

2.3 Regional Geology of the Morogoro Region, Tanzania

First references considered in this research project were the geological maps issued by the Geological Survey of Tanzania, Dodoma, Tanzania (GST). There were three Quarter Degree Sheets (QDS) published still during the British colonial time in the late 1950's and early 1960's. For the Uluguru Mts this were the QDS 183 and 201 published by Sampson & Wright (1961) as well as Sampson & Spence (1959) respectively. The Mahenge Mts were covered in just one sheet QDS 251 published by Birch & Stephenson (1962). Theses maps included already very detailed geological information regarding the lithology and some structural information. Cross-Sections revealed the complex fold structures of the two study areas. The three QDS also indicated similarities of the two areas the Mahenge and the Uluguru Mts. Large fold structures consisting of meta-carbonates mainly which were thrusted on to a granulite basement and cut in their root zones by major fault structures are recognisable in these maps. Further a northwest trending shear sense is displayed by the trace of these regional structures.

Following the geological mapping campaign in the Uluguru Mts a detailed report was published by the GST which included besides a compiled geological also a first structural map. Further information on potential resources of the area was provided in the mentioned GST Bulletin No.37 as well (Sampson & Wright, 1964). However already mentioned, ruby was not yet recognised as to be of economical importance.

Collins & Pisarevski (2005) introduced a possible scenario for the amalgamation of eastern Gondwana and the larger picture to explain the geologic development of the Eastern Granulites in Tanzania. Major geodynamic events are postulated for 630-570Ma when the East African Orogeny (EAO) or formerly known as Mozambique Belt was formed. A second event for the final assemblage of Gondwana is mentioned to have happened at 530Ma.

At the same time Fritz et al. (2005) were studying the regional structures of the area east of Dodoma in further detail. They also investigated the regional geological developments in terms of metamorphism and drew a connection to large scale tectonic developments responsible for the formation of granulite belts east to the Tanzania Craton. Nappe structures are mentioned to be present in both cases the Uluguru as well as the Mahenge Mts as well as Beta-shaped P-T paths were followed during the progress of metamorphic history.

Rossetti et al. (2008) focused more on the time constraints of structural features in the Uluguru Mts. Late tectonic events in the Uluguru Mts are related to the Kuunga-Malagasy orogeny and ages of ca. 550Ma. Ar-Ar dating was carried out on structure penetrating intrusions of post-deformational age.

With a numerical model applied to the tectonic framework of Central Tanzania it was possible for Fritz et al. (2009) to explain the divergent metamorphic histories which were observed by petrologic examinations for the Western and Eastern Granulites previously. Also the intense folding and final nappe stacking of the Eastern Granulite cover units onto the basement of the Eastern Granulites were possible to be described by this model.

Finally, the age of an anorthosite body found in the northwest of the Uluguru Mts was discussed by Tenczer et al. (2006). By U-Pb dating it was determined that the emplacement of this ultramafic unit took place prior to the EAO between 880 and 820Ma. A major metamorphic event was recorded in metamorphic rims on tested zircons which showed ages of 650-640Ma.

It also has to be mentioned that no deposit specific literature was found. Further details on the geology of the marble-hosted ruby deposits of the Morogoro Region will be discussed in chapter 3.

2.4 Origin Determination of Corundum

At the beginning of its history, origin determination on corundum was based on traditional gem testing criteria which, due to locality specific characteristics, allowed a separation between minerals from different deposits. With an increasing number of gem quality corundum producing deposits over the last 20 years, origin determination became progressively difficult. The reason for this is an increasing overlap of the criteria origin determination is traditionally based on. In order to receive more distinctive information for origin determination the techniques applied gradually changed from simple gem testing determining mineralogical parameters (refractometer, hydrostatic balance, etc.) to the examination of characteristic mineral inclusion associations (microscopy, Raman) (Gübelin, 1973; Gübelin, 1983; Gübelin & Koivula, 1986; Schubert, 1996, Gübelin & Koivula, 2008) and more advanced methods such as spectrometry (UV-vis-NIR, FTIR) (Bosshart, 1982), trace element composition analysis (ED-XRF) (Hänni, 1994; Gübelin Gem Lab, 2006a-c, Mc Clure, 2006).

2.5 LA-ICP-MS in Gemmology

Aside from a few ED-XRF measurements detailed trace-element geochemistry for most of the marble-hosted deposits had not been published until today. Therefore, a comprehensive comparison of marble-hosted ruby trace-element compositions is not known of either.

In contrast, LA-ICP-MS has become more and more popular for origin determination in gemmology and a few first publications had been made already (Guillong and Günther, 2001; Rankin et al., 2003; Abduriyim and Kitawaki, 2006a-c). However an in-depth study on ruby samples of different marble-hosted localities and the Morogoro Region, Tanzania in particular had not been carried out yet.

CHAPTER III

GEOLOGY

Since 2008 there was a significant rise in the production of high quality rubies from East Africa was observed. Namely the mines in Winza, Central Tanzania (Schwarz et al., 2008) as well as Montepuez and Niassa in Northern Mozambique (Pardieu et al., 2009) became famous when their precious products emerged in the international gem market in recent years. In the 80's and early 90's however a source for beautiful rubies was mined in the Morogoro Region, Tanzania once already. Although there was gem quality rubies found, the Morogoro rubies never reached the level of importance of their counterparts in Burma.

One reason to put the spot light on to the nowadays not much noticed and rather extensively worked deposits in the Uluguru and Mahenge Mts., Morogoro Region, Tanzania was that they are not yet fully exploited and still possess a potential for future developments. It was therefore one of the aims of this study to gain further knowledge about the geologic environment and processes which were responsible for the formation of rubies in the Morogoro Region, Tanzania.

3.1 Geography and Production of the Marble-Hosted Ruby Deposits in the Morogoro Region, Tanzania

The way from Dar es Salaam to the Uluguru Mts leads first to the city of Morogoro, a medium sized town located about 180km west of Dar es Salaam in Central Tanzania. From Morogoro city the mostly unpaved road towards the Selous Game Reserve has to be followed in southern direction to reach the Uluguru Mts.

To get access to the still active ruby mines in the Uluguru Mts a 4WD vehicle is inevitable. The marble-hosted rubies are mined in four areas in the Uluguru Mts. Following the road leading from Morogoro city towards Matombo and then further south into to the floodplains of Ruvu River the mining areas are known as Msombizi, Mwalazi, followed by Mingo and Visakazi. The Mingo mine is very likely to be the same occurrence which was previously mentioned by Altherr et al. (1982). A nearby settlement called Ngorong'horo as well as similar geological setting as mentioned by Altherr et al. (1982) give further evidence towards such an assumption. Visakazi was a mining center of regional importance in the past. Due to coordinates given by Msolo (1992) it was possible to unambiguously locate the former mine in the field. Less than 2km apart there is the latest gem mining operation in the Uluguru Mts taking place in the semi-mechanised Visakazi II mine where rubies are mined both in a open pit as well as in an inclined drift operation of about 20m depth (Fig. 3.1).

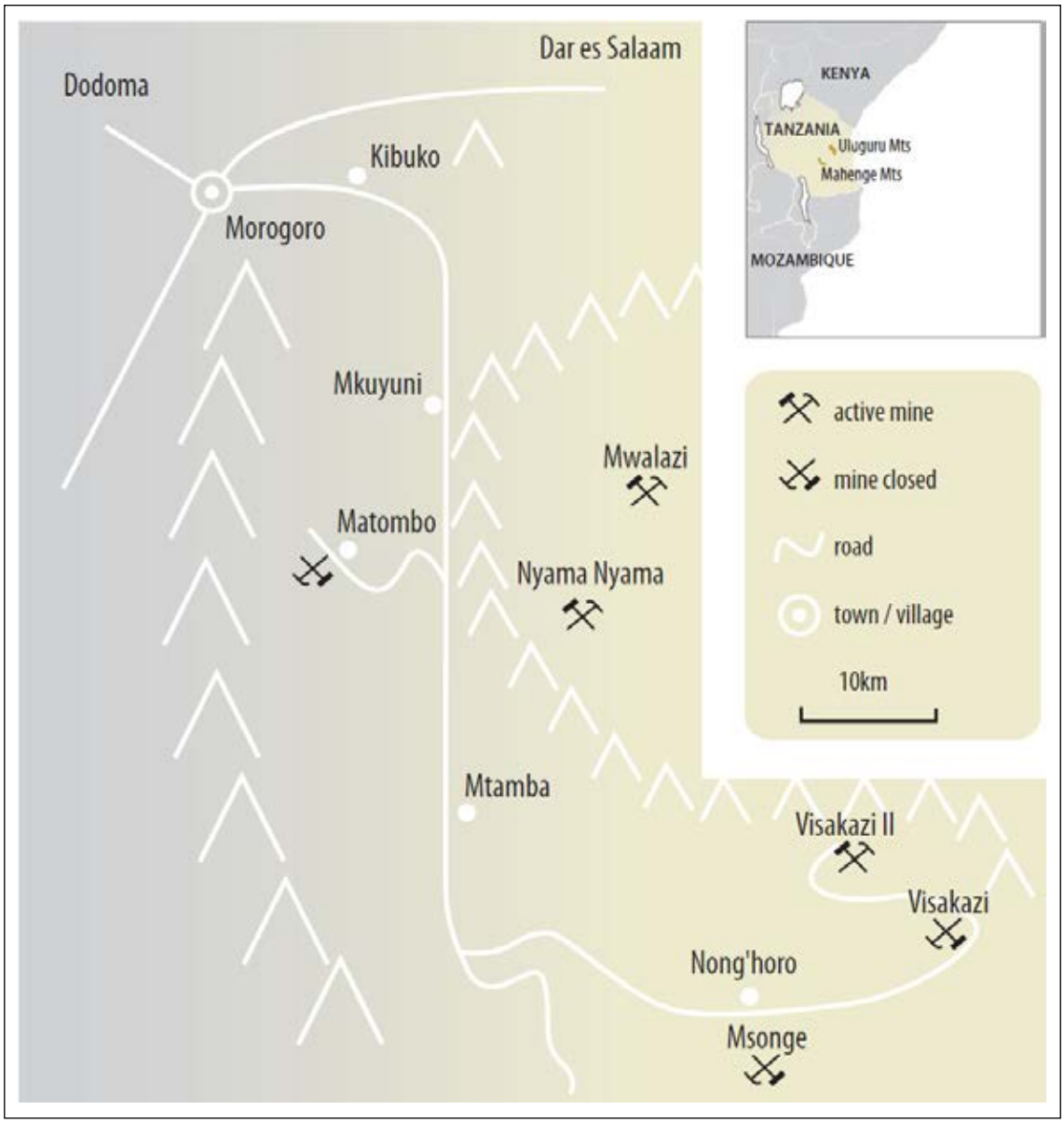

Fig. 3.1: The sketch maps indicate the locations of the mines in the Uluguru Mts, Morogoro Region, Central Tanzania.

In Mkuyuni, a small village on the way to Matombo, gemstones from the area are traded in a local market. Brokers sell brown to dark orange as well as bright green Cr-containing tourmaline, orangy brown zircon together with attractive purple coloured rhodolite garnets, pale pink and hazy spinels along with cabochon grade rubies. The quality of the goods is medium to low grade in general. Gem quality rough had been seen as well, this on a rare occasion however only. Still intact, nicely euhedrally crystallised specimens as well as stones exceeding 5cts are rare.

To reach the second marble-hosted ruby deposit in the Morogoro Region one has to go back to Morogoro City and travel ca. 200km further south west to Mahenge town. The journey from the Uluguru to the Mahenge Mts by a 4WD vehicle can be covered within one day.

Fig. 3.2: A small selection of rough and cut rubies from the Uluguru Mts collected and bought by the author in Visakzi Mine and the Mkuyuni market respectively (Photo: courtesy by Thai-Lanka Trading Ltd., Bangkok, Thailand).

Mahenge town is located on the northern slopes of a mountain range bearing the same name as the town. As in the Uluguru Mts the ruby deposit in the Mahenge Mts is also rather width spread and can be found in an area which covers about 25 x 20km. One of the marble-hosted ruby mining areas within the Mahenge Mts deposit can be reached by taking the path through the hills leading towards the settlement of Ipangko. This mining area lays about 10km southwest of Mahenge town in the karstic mountains and became famous recently for their spectacular neon-pink coloured spinels. On the way a former ruby mining area known as Kitwaro is passed after about 5km on a steep slope towards the west. From Kitwaro following the north-south striking valley for another 7-8km Ipangko village can be reached where another previously mined ruby mine is located. Towards the east, and just on the other side of the hill the most recent and active mining site, the Ipangko Spinel Mine, can be reached by a short hike.

Taking the road in the other direction from Mahenge town leading southward towards the plains one passes by the spinel mine of Mbarbanga after about 25km. The mine is located within the southern foothills of the Mahenge Mts and produces small quantities of attractive violet, blue and purple coloured spinels. The mine can be accessed from the road at Mzelezi village after a short hike through tropical forest. Following the main road further towards the plains and southeast of Mahenge town the villages Lukande and Chipa, two alluvial mining sites, are reached after another 15km. Following the same road a combined alluvial as well as primary marble-hosted occurrence is then reached at Mayote. The last stretch of about 5km from Lukande towards Mayote however it is not accessible by car and the distance has to be covered either by bicycle crossing several small rivers or by foot (Fig. 3.3)

In Mahenge town which is the trading center for the gem stones found in the area, the highly sought after neon-pink spinels from the Ipangko Spinel Mine dominate the market nowadays. Although, there are still spinels in various colours other than neon-pink along with small parcels of rubies sold in the market as well. Again large top quality stones are usually not seen in the local market however.

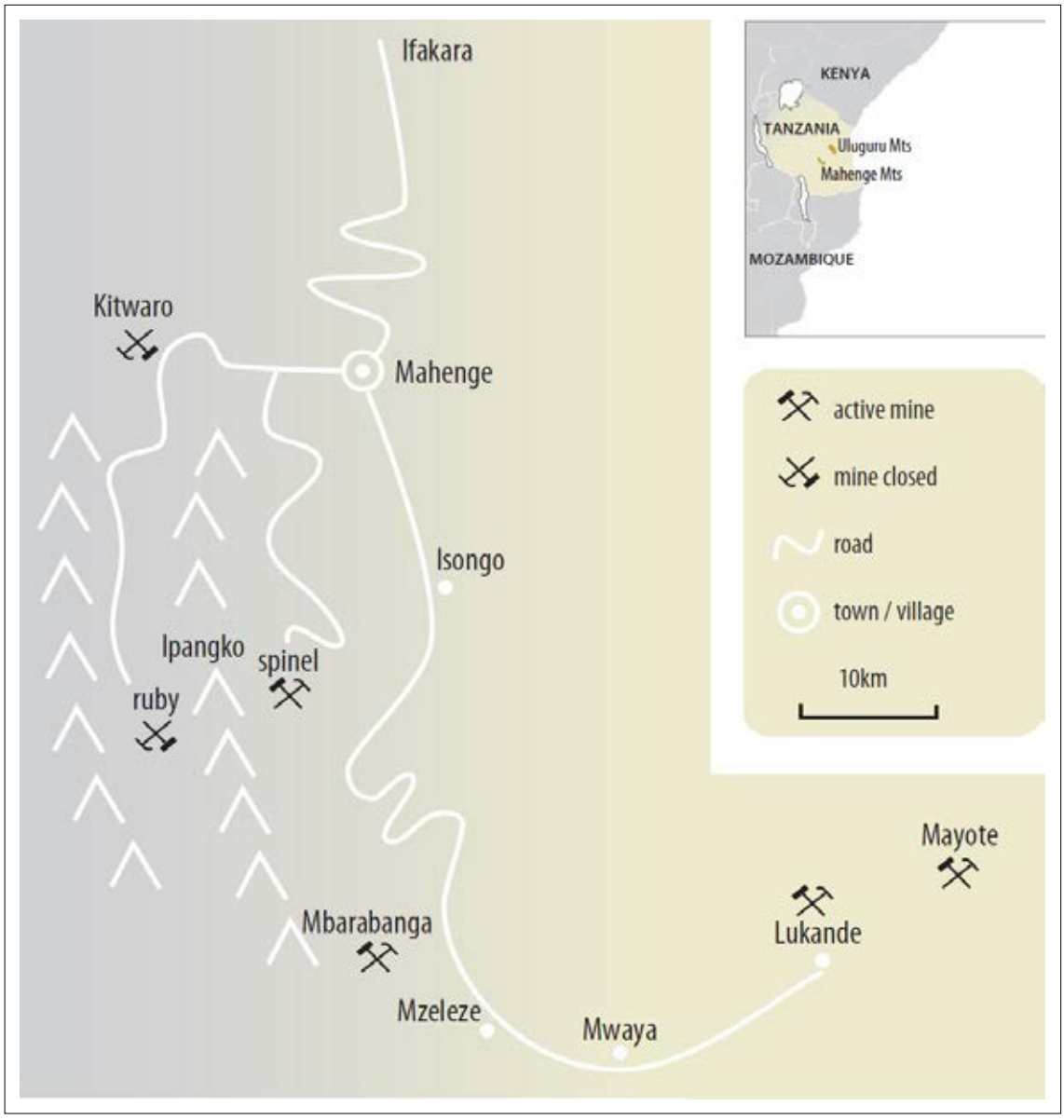

Fig. 3.3: The sketch maps indicate the locations of the mines in the Mahenge Mts, Morogoro Region, Central Tanzania.

Finally, the marble-hosted rubies from the Morogoro Region, Tanzania had been addressed in the past as to derive form one deposit only (Hänni & Schmetzer, 1991). Which criteria there are, in addition to the fact that the two deposits in the Morogoro Region are found to be located about 200km apart, to allow a separation of the rubies originating from the Uluguru and Mahenge Moutains, Morogoro Region, Central Tanzania was examined in the framework of this Ph.D. project.

3.2 Genetic Classification of Gem Corundum Deposits

Primary corundum deposits can generally be divided into two major groups in respect to their geological environments (Fig. 3.4).

Magmatic or igneous deposits are predominantly found in relationship with alkaline basalt volcanism such as the ruby and sapphire deposits in Thailand and Cambodia, or the sapphire deposits in Australia for example. Only in rare cases, corundum is found in plutonic rocks e.g. syenites in Garba Tula, Kenya (Giuliani et al., 2007). In deposits where an alkaline basalt type is involved, the volcanism itself was not the cause for the corundum formation but the vehicle for corundum being transported to the earth's surface either as xenocrysts or included in xenoliths. The exact genetic process, however, is still matter of an ongoing and controversial debate (Levinson & Cook, 1994; Guo et al., 1996; Sutherland et al., 1998a & b, Sutthirat et al., 2001). Further, it is to mention that two different types within the basalt related occurrences are distinguished. In a first one, sapphires are found in the colour varieties of blue, green, and yellow which lead to the category of so-called BGY-sapphire deposits. In a second case, there are rubies instead of sapphires found in alkaline-basalts. If the two types occur in the same deposit they are referred to as bi-modal deposits (Sutherland et al., 1998a).

Where corundum derives from a metamorphic environment the situation is a bit more diverse. Major deposit types are deposits related to desilification processes in alteration zones of contact metamorphism (e.g. pegmatites in ultramafics or (ultra-)mafic intrusions in felsic rocks), deposits in high-grade Al-rich meta-sedimentary rocks, deposits related to granulites (metamorphism sensus strictus) and finally deposits based on metasomatic fluid-rock interactions and marble-hosted corundum deposits. The metamorphic types of deposits are often related to orogenic processes where high metamorphic grades were present and if geo-chemical pre-conditions were favourable and phase conditions were reached where corundum is stable, the formation of corundum was possible.

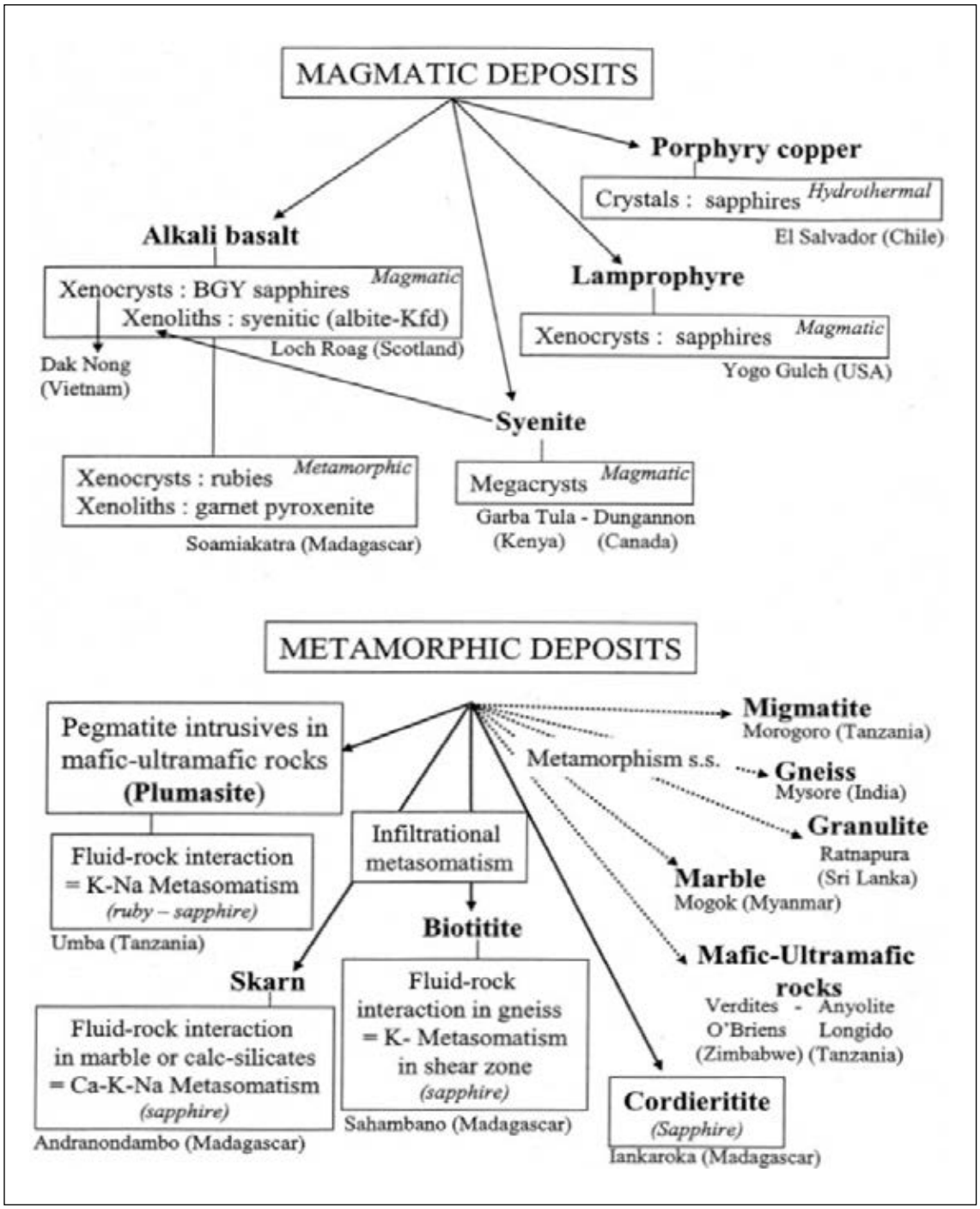

Fig. 3.4: Classification of corundum deposits from Guiliani et al. (2007)

3.2.1 Marble-hosted Ruby Deposits of the World

Marble hosted ruby deposits are known to produce some of the finest rubies in the world. A glance on Fig. 3.5 reveals that marble-hosted ruby deposits are found in many countries around the globe. It is interesting to see however that, with the exception of the deposits in the Morogoro Region, Tanzania, all marble-hosted ruby deposits are confined to young orogens only. Namely these are the Rocky Mountains, the Alps and the Himalayan mountain range. Of economic importance however are the deposits in the Himalayan as well as the Morogoro Region only.

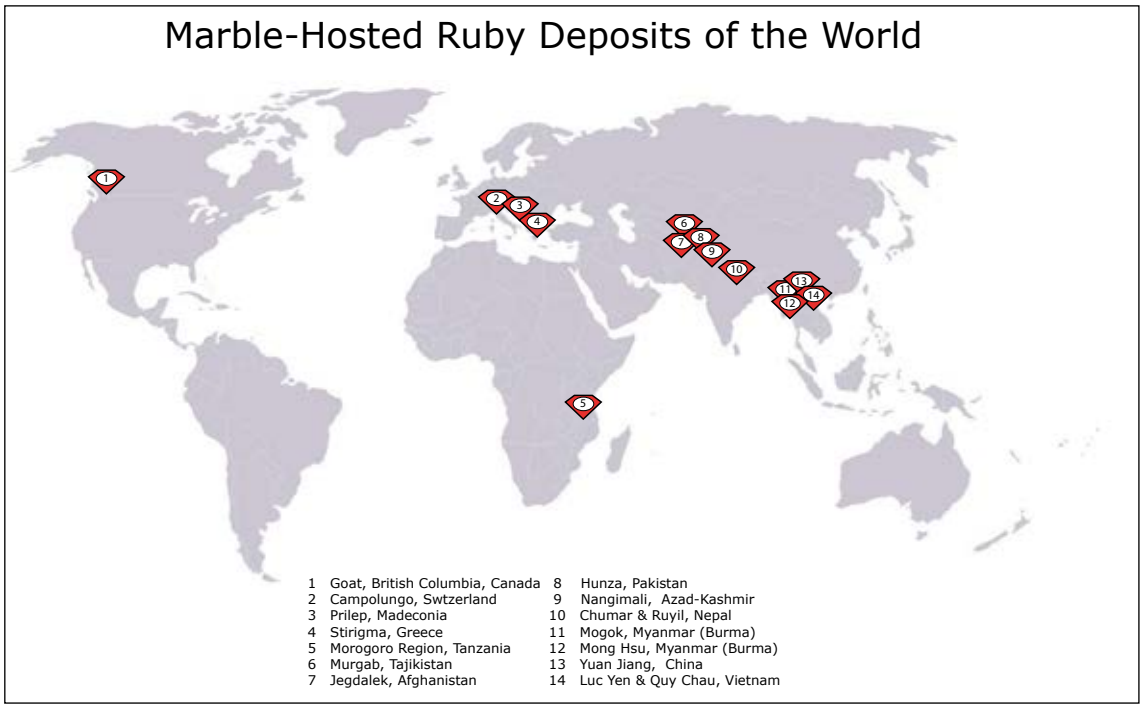

Fig. 3.5: Marble-hosted ruby deposits are found around the world but always related to orogenic belts. The deposits in the Morogoro Region are the only marble-hosted ruby deposits in Africa of economic importance up to present.

3.3 Geology

3.3.1 Regional Geology

From west to east the study area spreads from Dodoma to the Indian Sea including the Uluguru Mts. in the vicinity of Morogoro. To the south the area of interest is limited by the Mahenge Mts. This perimeter is almost identical with the area studied by Fritz et al. (2005). Therefore, their publication had been used as a main source of information for a short introduction into the regional geology of the study area.

Transecting the geology from Dodoma eastward one finds the eastern margin of the Archean Tanzanian Shield exposed first then followed by the triangular shaped Usagaran Belt, before passing through the Precambrian units of Western and Eastern Granulites. Finally, the mainly Mesozoic sedimentary formations of Karoo Group and the Indian Sea are reached (Fig. 3.6).

The focus during this study lays on the units of the Eastern Granulites where nowadays most of the important gem deposits of Tanzania are found.

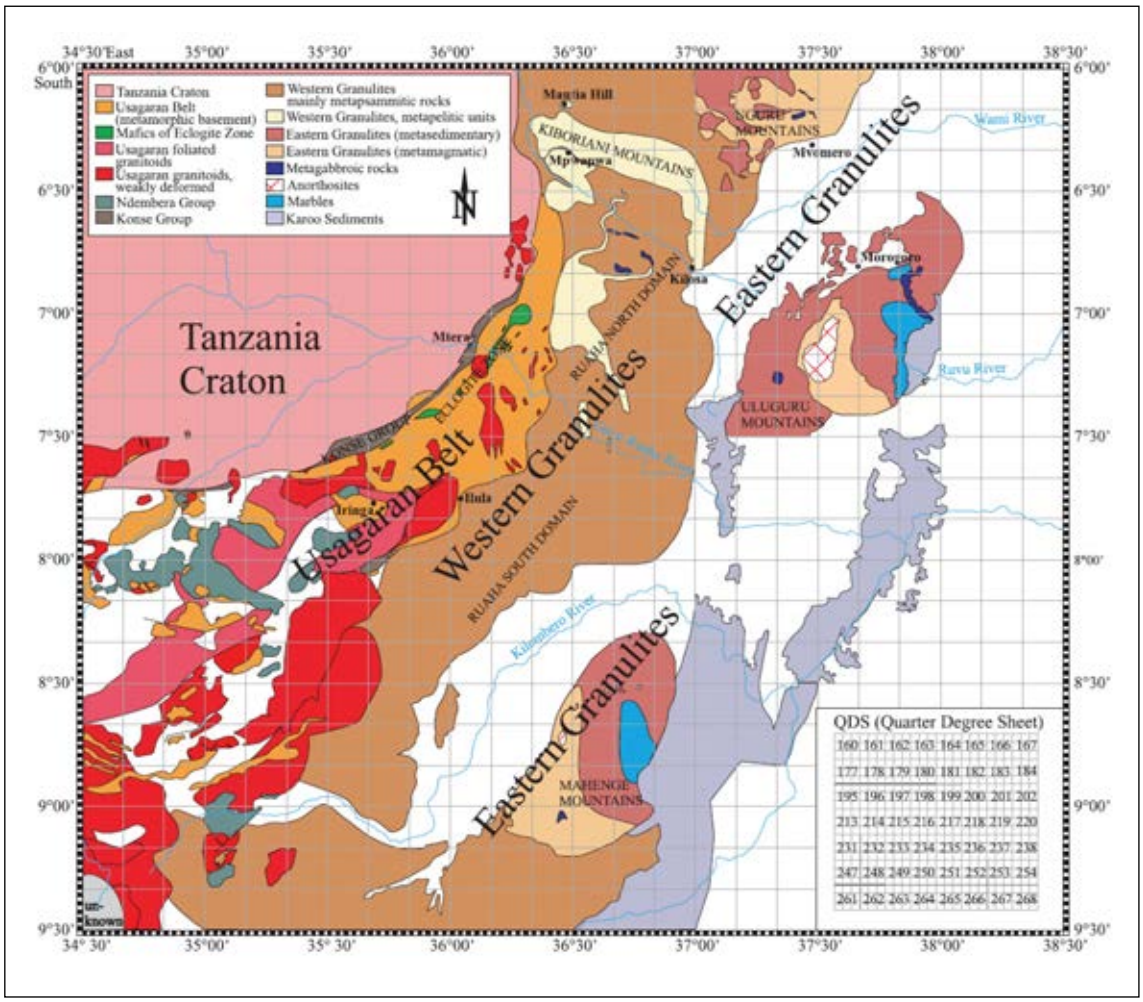

Fig. 3.6: Lithological units of Central Tanzania (from Fritz et al., 2005).

3.3.1.1 The Precambrian Basement (after Fritz et al., 2005)

Within the study area the effects of two orogenic periods seem to have overlapped. In the western part an early orogen at about 2.0-1.8Ga known as the Usagaran Orogeny is documented in rocks of the Usagaran Belt as well as the westernmost part of the Western Granulites. During this period an active continental margin including continent-continent collision in the north, island arc magmatism in the centre and strike-slip tectonics in the south had established. The basement is then unconformably overlain by the ~1.9Ga weakly metamorphosed Ndembera Group, which indicates the Usagaran Orogeny to be 1.9Ga or older.

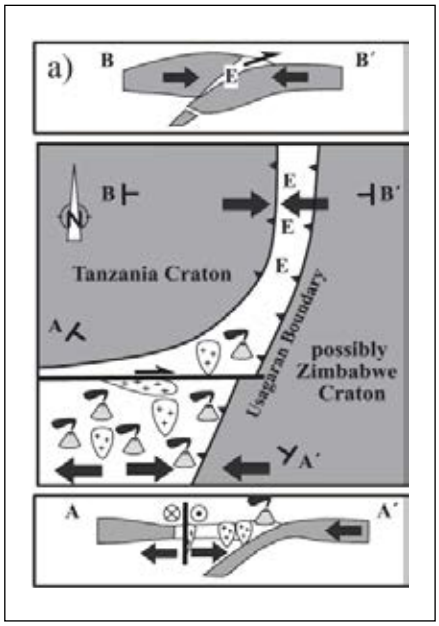

Fig. 3.7: Tectonic situation during the Palaeoproterozoic Usagaran orogeny, ca. 1.9Ga. The northern part was dominated by continent-continent collision leading to eclogite facies metamorphism whereas in the central and southern part by oblique convergent tectonics a major dextral strike-slip fault and subduction zone with active island arc magmatism developed (from Fritz et al., 2005).

The second and younger orogen is known as the East-African Orogeny (EAO) representing an episode lasting from 650 to 540Ma marking the major thermotectonic event of the EAO which was also referred to as the Mozambique Belt in the past.

The EAO is characterised by general westward thrusting due to oblique continent-continent collision of East and West Gondwana. As mentioned earlier, there had been a partial overprint of the first orogenic event, the Usagaran Orogeny, by the younger EAO.

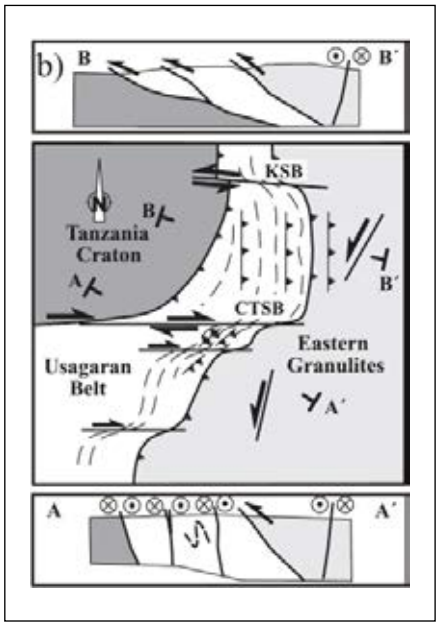

Fig. 3.8: Due to the oblique collision of East Gondwana (Eastern Granulites) and West Gondwana fragments (Tanzanian Craton, Usagaran Belt, and Western Granulites) major shear zones established. The Kiboriani Shear Belt (KSB) and Central Tanzanian Shear Belt (CTSB) mark the limits of orthogonal collision where nappe tectonics pushed Usangarn Belt units onto the Tanzanian Craton. South of the CTSB lateral shear along the boundary of the Tanzania Craton led to sinistral strike-slip zones (from Fritz et al., 2005).

The geometry of the Tanzania Craton plaid a major role during the compressive tectonics related to continent-continent collision and the accretion of Gondwana. The Tanzania Craton acted as a rigid indenter where orthogonal thrusting resulted along its eastern flank and pronounced strike-slip displacement developed along the craton margin to the South.

3.3.1.2 The Eastern Granulites

The Eastern Granulites consist mainly of juvenile crust with meta-igneous rocks indicating formation ages of 986-800Ma (Fritz et al., 2005; Tenczer et al., 2006). As a particularity of the Eastern Granulites underlaying orthogneisses of granitoid composition include anorthosites with intrusion ages between 880-820Ma for the Uluguru Mts (Tenczer et al., 2006). Metasedimentary rocks with basal paragneisses, metapelites, and schists followed by thick marbles overlay the igneous dominated basement. The marbles seem to have Neoproterozoic sedimentation ages taken the Xixano Complex in northern Mozambique into account which also shows a comparable geological setting in the Cabo Delgado Nappe Complex. The marbles in the Cabo Delgado Nappe Complex had been affected by a granulite facies metamorphic event which dates between 735+/-4Ma to 607+/-11Ma (Bingen et al., 2011). A similar age is therefore postulated for the marbles found in the Eastern Granulites of the Morogoro Region. Finally, there are two generations of pegmatites found in the Mahenge and the Uluguru Mts.

The absence of Usagaran ages along with the presence of marbles and metapelites found in Eastern Granulite cover sequences which represent shallow water sediments lead to the postulation of a continent east of the previously described suture zone in the Usagaran Belt (Fritz et al., 2005). This again implies an affiliation of the Eastern Granulites to a former part of East Gondwana most probably (Fig. 3.9).

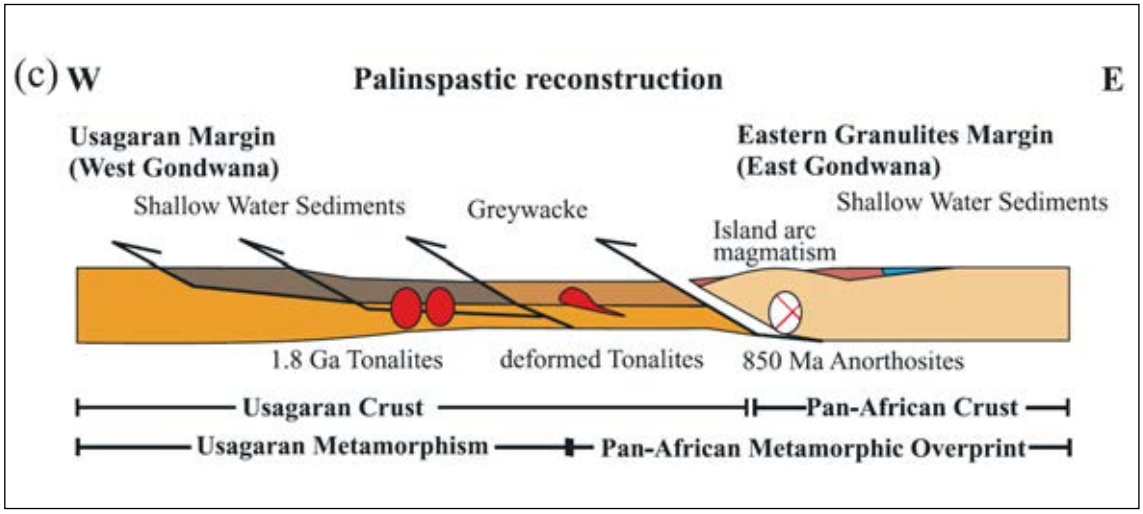

Fig. 3.9: Palinspatic reconstruction of the study-area and its adjacent terranes (from Fritz et al., 2005).

The tectonic and metamorphic evolution in the study area is complex and shows four distinguishable deformations accompanied by two metamorphic events.

A first deformation D1 in the Eastern Granulites is directly related to the EAO and being almost contemporaneous with the peak metamorphism M1 (~850°C and 10-12 kbar) at about 640Ma (Fritz et al., 2005; Tenczer et al., 2006). Isoclinal fold structures related to D1 can be linked to flat shear zones and strike-slip zones in the Uluguru Mts (Fritz et al., 2005).

D2 at about 640-580Ma (~620Ma after Fritz et al., 2009) is represented by a westward nappe tectonic with major thrust faulting, as well as stacking of Eastern Granulite units at lower crustal levels onto each other and against the Western Granulites. Also during this time, a second syn-deformation amphibolite facies metamorphism M2 with the character of isobaric from M1 cooling established (Fritz et al., 2005; Fritz et al., 2009). A first generation of concordant intrusions which can be related to a migmatisation of the basement emplaced in this period as well (Fritz et al., 2005).

As an analogon, the Helvetic Nappes in the Alps of Central Europe can be mentioned where a similar development was recorded (Fig. 3.10).

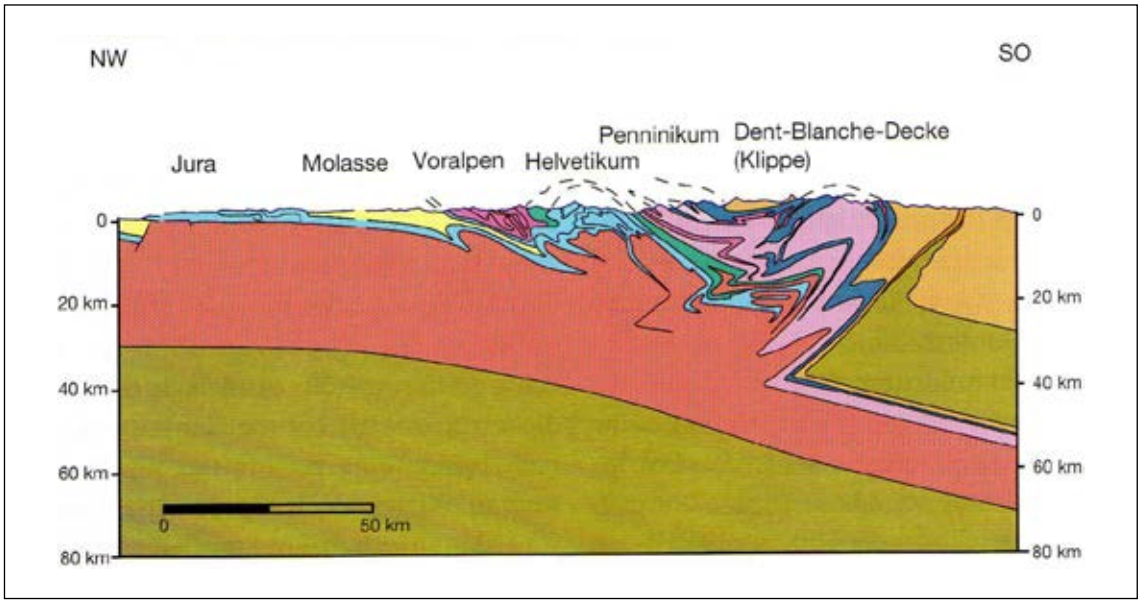

Fig. 3.10: Similar tectonic development as recognised in the Eastern Granulites of Central Tanzania is found in the Alps of Central Europe where the Helvetic Nappes were thrusted over an autochthonous crystalline basement (from Marthaler, 2005).

Final thrusting during D3 followed by extension was dominant in the Eastern Granulites from 580-550Ma and characterised by isothermal cooling (Fritz et al., 2005; Fritz et al., 2009). This period has a lower time limit by late, discordant dykes of tonalitic composition in the Uluguru Mts which show semi-brittle D3 deformation after their emplacement (579+/-4Ma, Rossetti et al., 2008). Along with D3 there is also a last metamorphism M3 encountered which are recorded by a slight Greenschist facies overprint (Fritz et al., 2005).

D4, <550Ma, is characterised by strike-slip movements along the southern margin of the Tanzanian Craton. This stage is late to post-orogenic and is related to further cooling throughout all units (Fritz et al., 2005). This period of cooling and exhumation took place during a long period of time and lasted until ~380Ma (Rossetti et al., 2008).

The main features described above are basically found in both the Mahenge and the Uluguru Mts Mts. The exact orientation of structures and pegmatites may be different in the two locations however (Fig. 3.11, from Fritz et al., 2005).

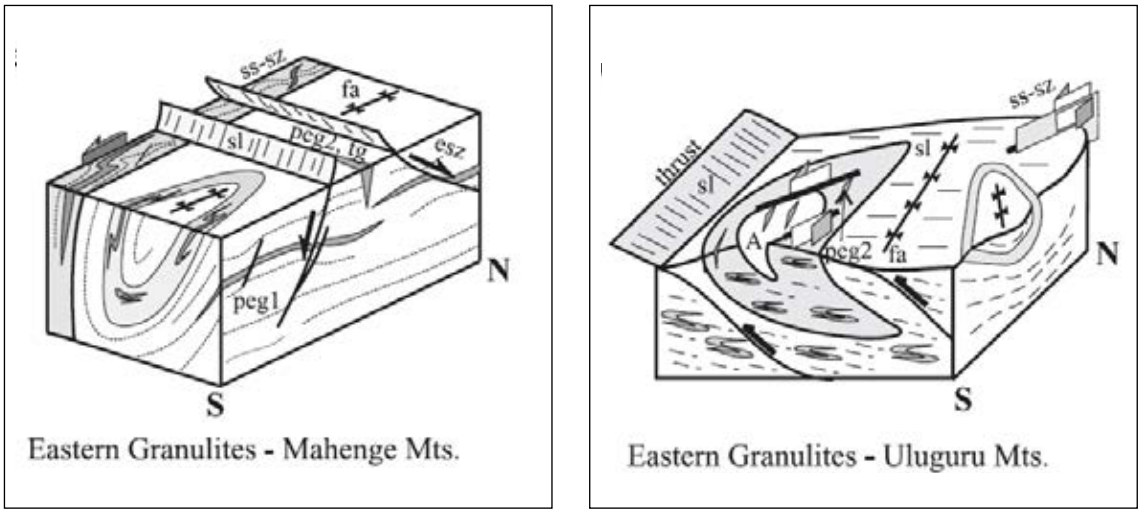

Fig. 3.11: Most prominent structural features of the Mahenge and Uluguru Mts in the Eastern Granulites are isoclinal folds related to deformation D1 during a compressional regime caused by continent-continent collision in the East African Orogen (~640Ma, Fritz et al., 2005). These are followed by nappe-stack structures related to trusting during deformation D2 (~620Ma, Fritz et al., 2009). Both deformations are accompanied by a metamorphism M1 at peak conditions of granulite grade and retro-grade amphibolite facies metamorphism M2 related to isobaric cooling respectively (Fritz et al., 2005). Finally, the nappe structures of the Uluguru and Mahenge Mts experience isothermal decompression and extention leading to a semi-brittle deformtion D3 which went along with a last metamorphism M3 at greenschist grade (Fritz et al., 2005; Rossetti et al., 2008). After ~580Ma (Rossetti et al., 2008) general cooling and brittle deformation D4 is dominant in all rock units of the Easter Granulites. Drawings from Fritz et al. (2005).

3.3.1.3 Differences between Western and Eastern Granulites

Although they share similarities, the Eastern Granulites are still quite different from their Western counterparts. Characteristic for the Eastern Granulites, for example, is the lack of quartzites and the presence of anorthosites compared to the Western Granulites.

Western and Eastern Granulites are further distinguished mainly by their different history in terms of metamorphism. In particular, there are two different PT-paths recorded in the rocks of the two granulite terranes. During the EAO, the Usagaran Belt as well as the Western Granulites took a clockwise retrograde evolution where thrusting followed exhumation. In the Eastern Granulites, however, an anti-clockwise PT-path is observed. Isobaric cooling after a metamorphic peak (M1 & M2) is followed by isothermal decompression (M3) and final exhumation (Fig. 3.12).

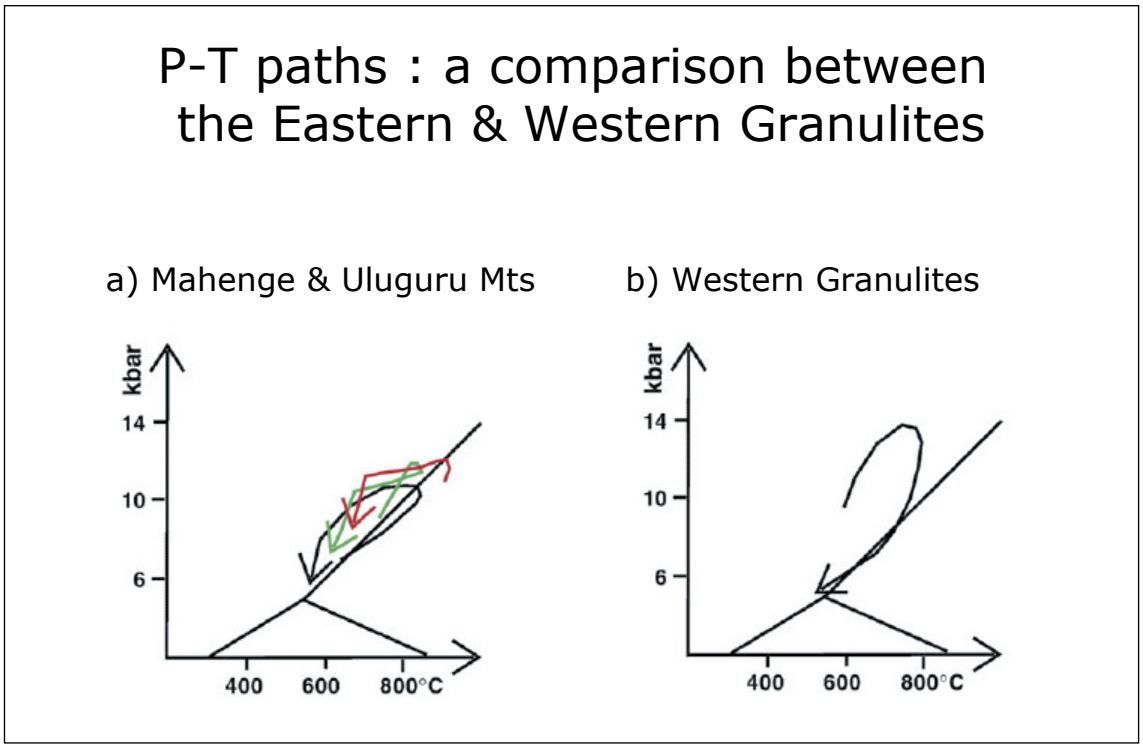

Fig. 3.12: Compared to the P-T path observed in the Western Granulites an anti-clockwise course is recorded in the rocks of the Mahenge & Uluguru Mts. They indicate isobaric cooling from peak metamorphism followed by isothermal decompression during exhumation (from Fritz et al., 2009)

3.3.1.4 Hot Granulite Nappe Model

Fritz et al. (2009) were able to visualise a possible tectonic scenario for the tectonic development of Eastern Granulites in Central Tanzania by applying a finite element "hot fold nappe model" after Beaumont et al., 2006. The proposed model was also capable to explain the different histories of metamorphism found in the Eastern and Western Granulites respectively.

The model included a subduction to the east as postulated previously (Fritz et al., 2005). Initiated by this eastward subduction a crustal thickening was caused by collisional tectonics first. Due to the increased gravitational load a thermal disequilibrium established and a hot, ductile zone at lower crust levels was created. Accompanied by migmatisation this lower crust which is interpreted to be the basement of the Eastern Granulites was mobilised. Simultaneously to lateral flow along a décollement the mobilised unit caused intense shearing in the overlaying formation which was recorded in a stacked nappe structure. The mobilsed zone itself experienced thining under isobaric cooling conditions. In the meanwhile the Western Granulites experienced isothermal decompression when thrusted as a wedge against the Tanzanian Craton which itself acted as a rigid indenter. As a final stage isothermal cooling and extentional tectonics are described for the cover sequences of the Eastern Granulites by the proposed model (Fig. 3.13).

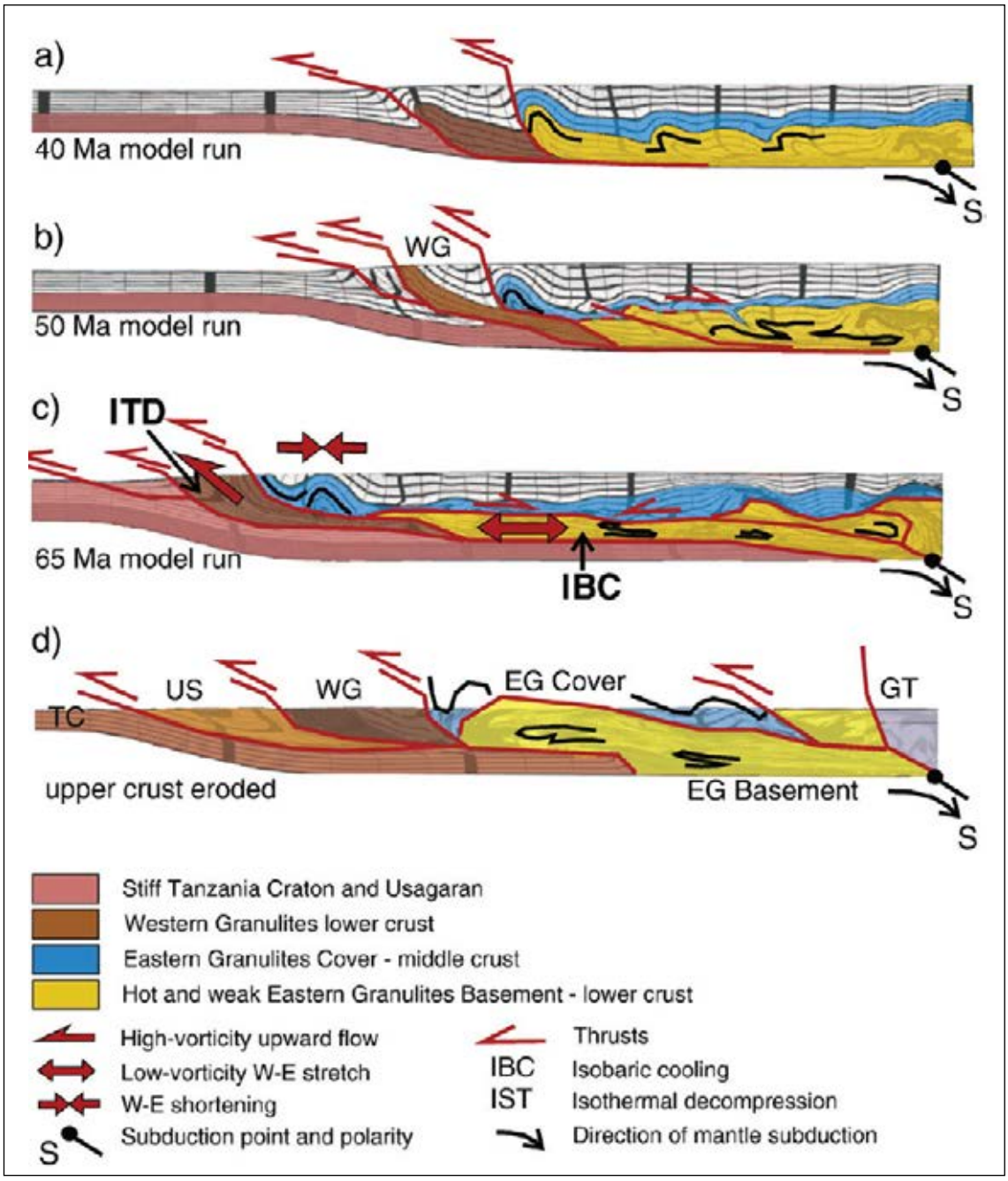

Fig. 3.13: The finite element model introduced by Fritz et al. (2009) allows to explain isobaric cooling of Eastern Granulite basement and intense folding of its cover while the Western Granulites experienced isothermic decompression (from Fritz et al., 2009).

3.3.1.5 The Sedimentary Units

After the EAO and during Paleozoic ages uplift and erosion was dominant. From Carboniferous up to Tertiary times major erosion is documented in the deposition of the Karoo Group sediments. It was in Jurassic times (~165Ma) when the breaking apart of Gondwana set Madagascar apart from East Africa and the sedimentary basin got separated. The Karoo Group shows a change in its composition northward from continental to marine sediments. The Costal areas are dominated by Miocene to recent sediments (Schlüter, 1997).

3.3.1.6 Neogene Volcanism

The most recent development is a Neogene volcanism related to the East African Rift which is still active today (e.g. Mount Kilimanjaro). Early tholeiitic eruptions evolved towards a more alkaline basaltic magmatism (Schlüter, 1997). Whether the kimberlites of Eocene age found in craton areas can be linked as a triggering mantle-plume event for the East African Rift is not yet clear.

3.3.2 Deposit Geology – Field Observations

As it was explained in chapter 3.4.1.2 the Uluguru and the Mahenge Mts share most of their geological characteristics. Due to better infrastructure available in the Uluguru Mts where the Parish of Matombo was available to be used as a base camp combined with a larger number of accessible outcrops and prominent geological features it was decided after the first field season to choose the Uluguru Mts to be the target of further geological investigations. Therefore, exemplary and detailed geological work was carried out in the Uluguru Mts only.

3.3.2.1 Field Examinations

In the following the east to west trending Ruvu Syncline (Sampson & Wright, 1961) was studied by transecting the nappe structure from north to south following the road leading from Morogoro City to the Selous Game Reserve. Along a west to east section several ruby and spinel mines were visited through out the Uluguru Nappe which allowed to receive a comprehensive picture of this tectonic unit.

During two field campaigns geological measurements such as the strike and dip of foliation planes, lineations or orientations of ruby mineralised boudins were taken as well as specimens of host and mineralised rock along with loose ruby samples collected. All outcrops were referenced by a GPS device for exact positioning (Appendix A.1 & Appendix A.3).

Structural data were visualised by the open source software OpenStereo by C.H. Grohmann and G.A.C. Campanha from the University of São Paulo, Brazil, using the lower hemisphere projection of a the Lambert-Net.

3.3.2.2 Basement

The basement which is underlaying the Uluguru Nappe is exposed in three outcrops in the field.

A first occurence was found at a small pass connecting Kiroka, a village in the north of the Uluguru Mts, with Morogoro City. This outcrop was recognised to be the same location where a discordant tonalite intrudes an highly foliated enderbitic gneiss as described by Rossetti et al. (2008) (Fig. 3.14).

Fig. 3.14: The tonalitic pegmatite intruding an enderbitic gneiss as described by Rossetti et al. (2008) was found near a pass connecting Kiroka with Morogoro City.

In Kiroka graphitised gneisses are commonly found on the foothill of Mt Bondwa. This unit is located just below the contact to the overlaying tectonic unit, the Uluguru Nappe System. Accordingly, Mt Bondwa consists of marble as observed in the field.

Another outcrop exposing basement rocks was found near Mwalazi Mine located southeast of Mkuyuni village on the northern banks of Ruvu River. At this location the Ruvu River cuts through the overlaying marble coverage and exposes a garnet rich gneiss.

In the Msuvizi River near Matombo dark tumbled rocks were found in the river bed which were most likely transported from further west of the Uluguru Mts. The rocks contained a gneissic texture and typically included large garnet crystals. In the field, this rock type was recognised to be the host rock of rubellite garnets which are found as pebbles in the Msuvizi and Ruvu River.

Further description of the Basement units can be found in Appendix A.2.

3.3.2.3 Host Rock

As introduced in chapter 3.4.1.2 the marble-hosted ruby deposits in both the Uluguru and the Mahenge Mts are found to be within the cover sequence of the Eastern Granulites. Accordingly the host rock of the ruby mines was found in coarse grained calcite marbles in the Uluguru and dolomite marbles in the Mahenge Mts, respectively. Beside a few pyrite crystals there were no other phases found in the unmineralised marble units (Fig. 3.15).

Fig. 3.15: In a marble quarry near Mkuyuni in the Uluguru Mts very pure, unmineralised marble can be seen which shows very dark weathering colours on the surface.

3.3.2.4 Ruby Mineralisation

Rubies were found in localised zones related to fold structures only. The ruby mineralisation is confined to boudinaged biotite-rich layers. The mineralised boudin-like lenses have widths between 5 to 20cm and consisted of a biotite-rich rim encapsulating ruby crystals in their interior (Fig. 3.16). Additionally, green amphibole as well as calcite and sometimes plagioclase and pyrite are associated with the ruby crystals.

Fig. 3.16: Boudin-like lense with ruby mineralisation found at Mwalazi Mine.

3.3.2.5 Structural Geology

Although the term nappe was not used yet Sampson & Spence (1959) already recognised the Uluguru Nappe as a large overthrown fold structure which was covering the basement. To further investigate the relationship between this major regional structure and the marble-hosted ruby deposits which are contained in this tectonic unit, several locations were considered (Fig. 3.17).

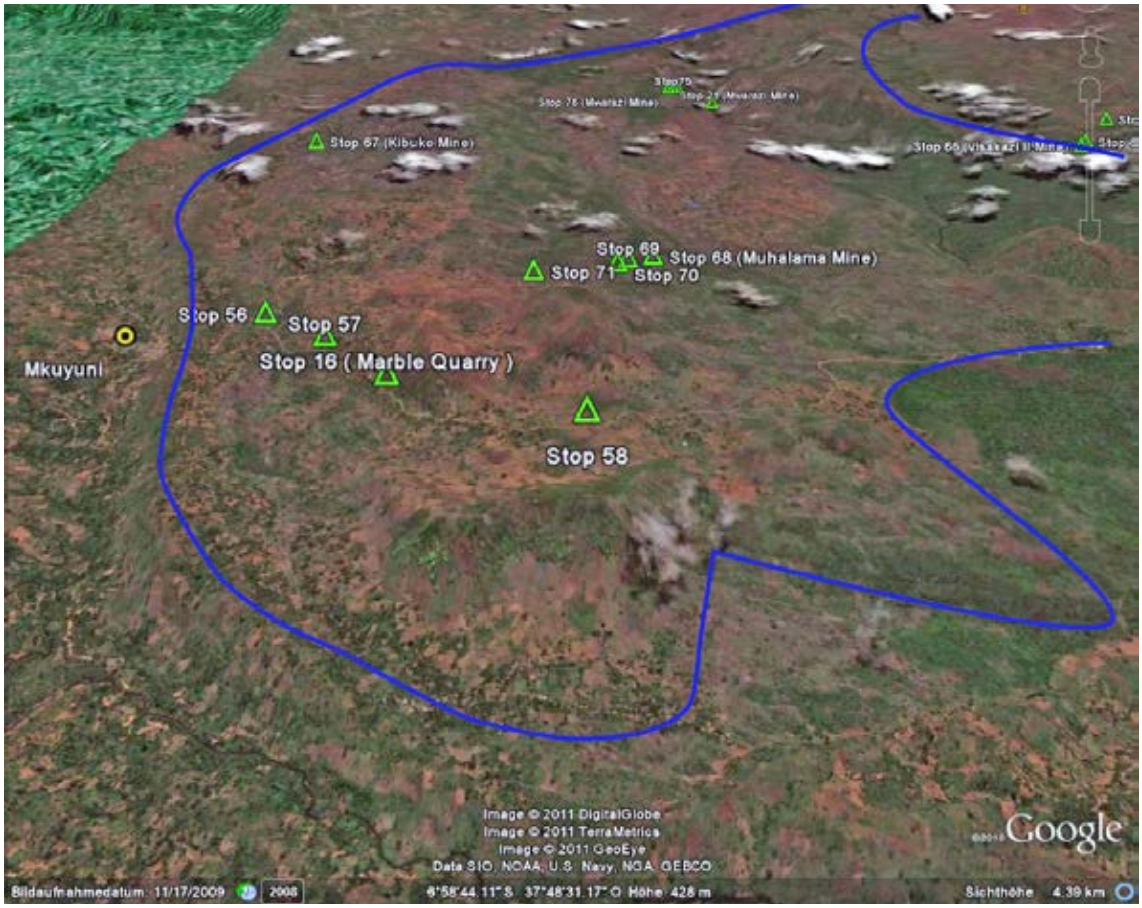

Fig. 3.17: Overview of the Uluguru Nappe seen from a western direction. Outcrops which were examined within the Uluguru Nappe during this study are marked by green triangles where as the intrinsic surface of the nappe is coloured in blue. Exact coordinates of the stops or outcrops can be found in Appendix A.3.

In total 6 localities were vistited (in clockwise order starting in the north of the nappe structure: outcrop#58, Kibuko Mine, Mwarazi Mine, Msonge Mine, Visakazi Mine, and Muhalama Mine) and structural data collected. Three localities with especially clear and well exposed structures will be discussed in detail.

The Mwalazi Mine (outcrops #21, 75 & 76) is located on a small hill which represents an antiform fold structure which strikes nearly north to south. Following the crest of the hill smaller subsidiary folds were found in which the ruby mineralisation was concentrated. These subsidiary folds showed diameters of about 5-10m (Fig. 3.18).

Fig. 3.18: Subsidiary fold structures at Mwalazi Mine contain mineralised lenses which are parallel to the strike of the fold axis at this mine. The ruby nodules are found usually near the fold axial hinges whereas the fold limbs do not contain any ruby mineralisation. The picture on the right shows a mine at the top of the hill which had been mined until recently. Along the crest of the hill there are several other pits found which were mined for ruby before (left). The relationship between mineralisation and structural features were found to be similar in all pits.

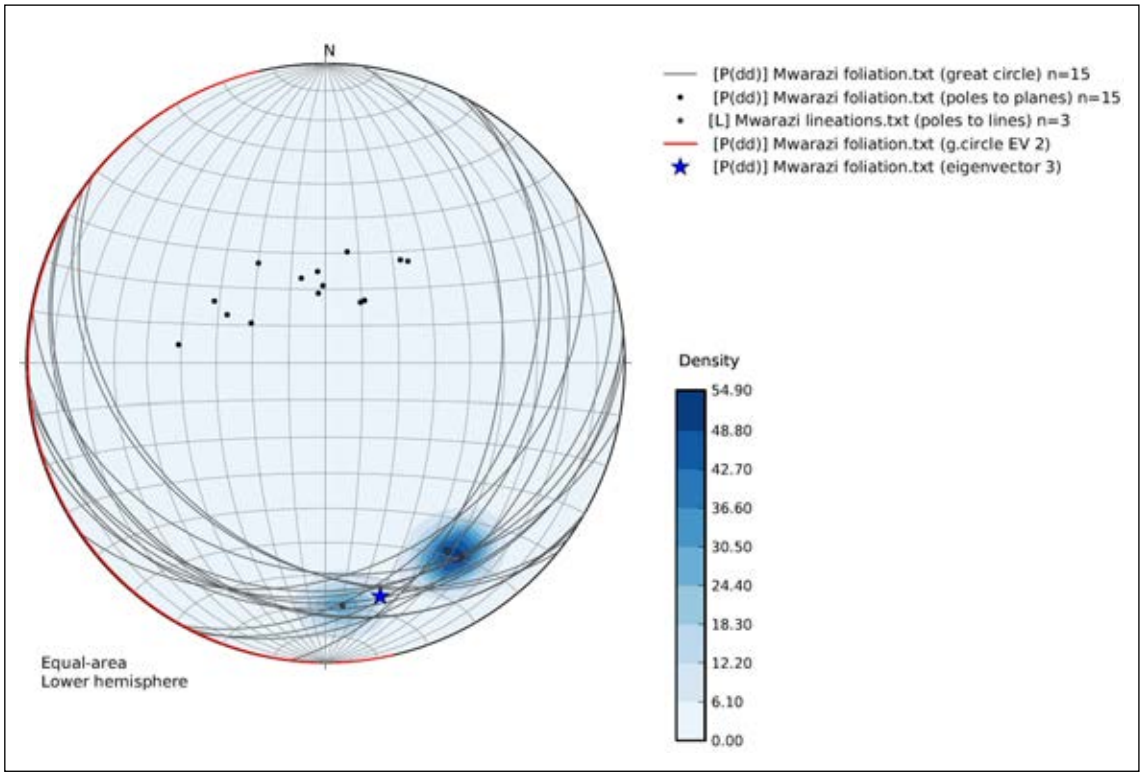

Fig. 3.19: A stereographic plot of foliation planes measured at Mwalazi Mine describes a fold structure with a corresponding fold axis at 168/21 (blue star). Additionally, the orientation of three mineralised boudin-like lenses was measured and found to be aligned in the same direction (blue contours in the steroplot).

Foliation plane measurements which were taken at the mine site describe a fold axis at 168/21 (Fig. 3.19). The ruby mineralisation was always confined to close proximity to fold hinges and contained in biotite-rich lense-shaped nodules. Additionally, these boudin-like structures showed parallel orientation to the fold axis as shown in Fig. 3.18 (see also Fig. 3.16). In the fold limbs there were no rubies observed, however.

The second location is outcrop#58 near Mkuyuni which is close to the nappe front of the cover sequence. The nappe front is basically a large overturned fold where the upper limb is partly missing. The large scale fold (nappe front) is refolded and an anticline structure where the central part is eroded is seen in Fig. 3.20. These observations were confirmed by a fold axis at 084/27 which is described by foliation planes measured in this area (Fig. 3.21).

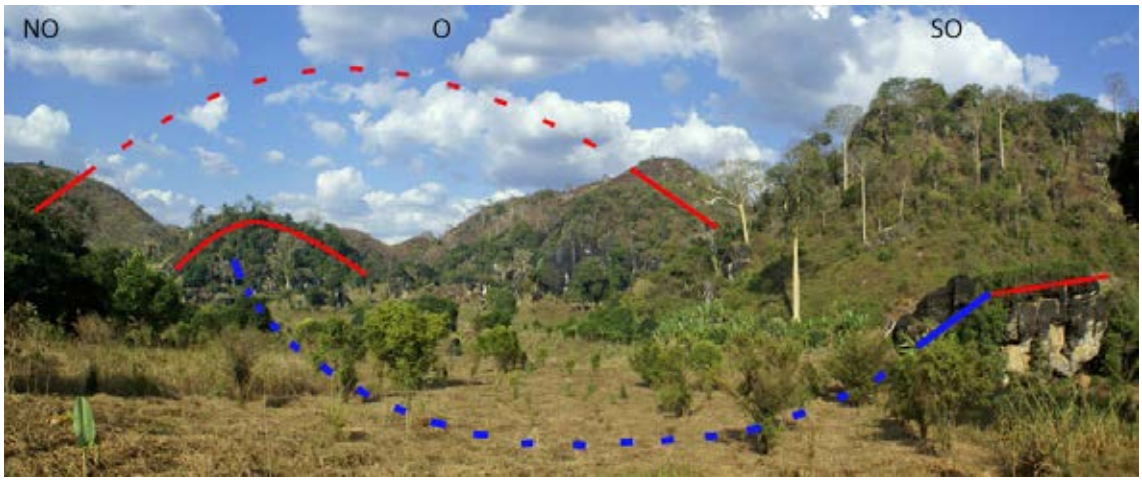

Fig. 3.20: A view in eastern direction from outcrop #58 reveals an anticlinal valley of a antiform syncline (red). The core of this overturned fold structure is missing. The block visible in the front is solid and the orientation of foliation planes correspond with the surrounding structures describing a synform anticlinal at the front zone of the Uluguru Nappe (blue). The observed structural features at outcrop #58 indicate a complex pattern of superimposed folding phases (Photo: courtesy of Michael Krzemnicki).

Visakazi II ruby mine (outcrops #66 & 67) is located at the lower limb of the examined nappe front related fold structure. This position within the nappe is also in close proximity to the basement thrust over which the Uluguru Nappe was dislocated. In the area near Visakazi II the nappe front is characterised by smaller folds with increased frequency but decreased amplitude (Fig. 3.17). Foliation planes define a fold axis for this mine at 043/32 (Fig. 3.22). This marks a different orientation compared to what was encountered for Mwalazi Mine.

In Fig. 3.23 all fold structures examined in the Uluguru Mts are included in one stereographic plot. It can be seen that the fold axis found in the Uluguru Mts plot on a great circle which dips towards the southeast (116/17). The fold structures in the Uluguru Mts are therefore oriented in a fan-like pattern which points in a southeastern direction (Fig. 3.23). This indicates that the fold axes are folded themselves which implies more than one folding phase.

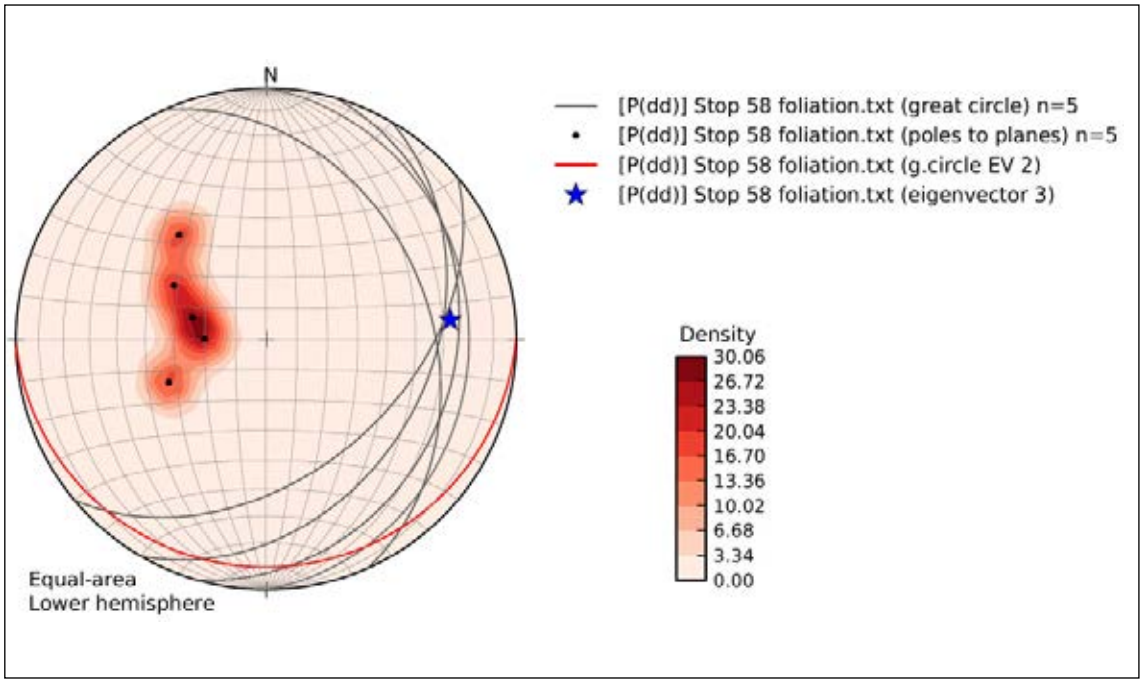

Fig. 3.21: The foliation planes and corresponding poles of the antiform syncline measured at outcrop #58, which in Fig. 3.20 are marked red, describe a fold with corresponding fold axis at 084/27 (blue star).

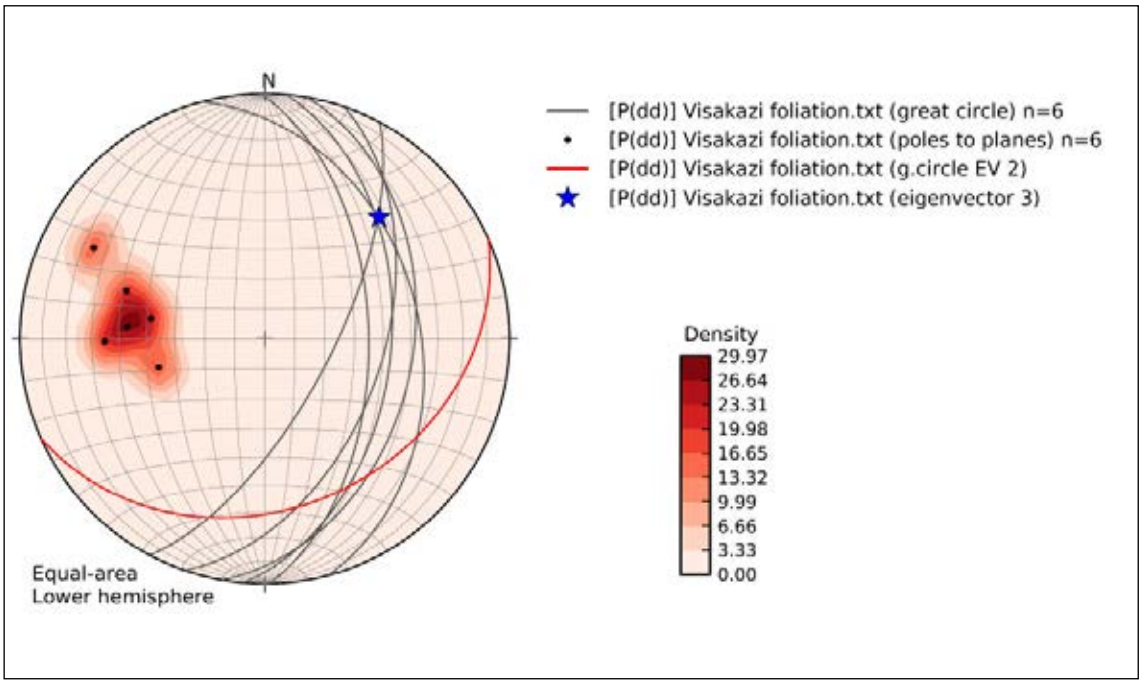

Fig. 3.22: Visakazi II Mine is located at the lower side at the intrinsic surface of the Uluguru Nappe close to the basement thrust over which the Uluguru Nappe was transported onto the basement. Foliation planes measured at Visakazi II Mine indicate a fold axis at 043/32 (blue star).

Besides the nappe structure late fault structures can be recognised in the field. The most prominent was a dextral strike-slip fault which was observed immediately south of outcrop#58 as well as in the area close to Mwalazi Mine. By applying a digital elevation model using a SRMT90 data set available online from http://srtm.csi.cgiar.org/

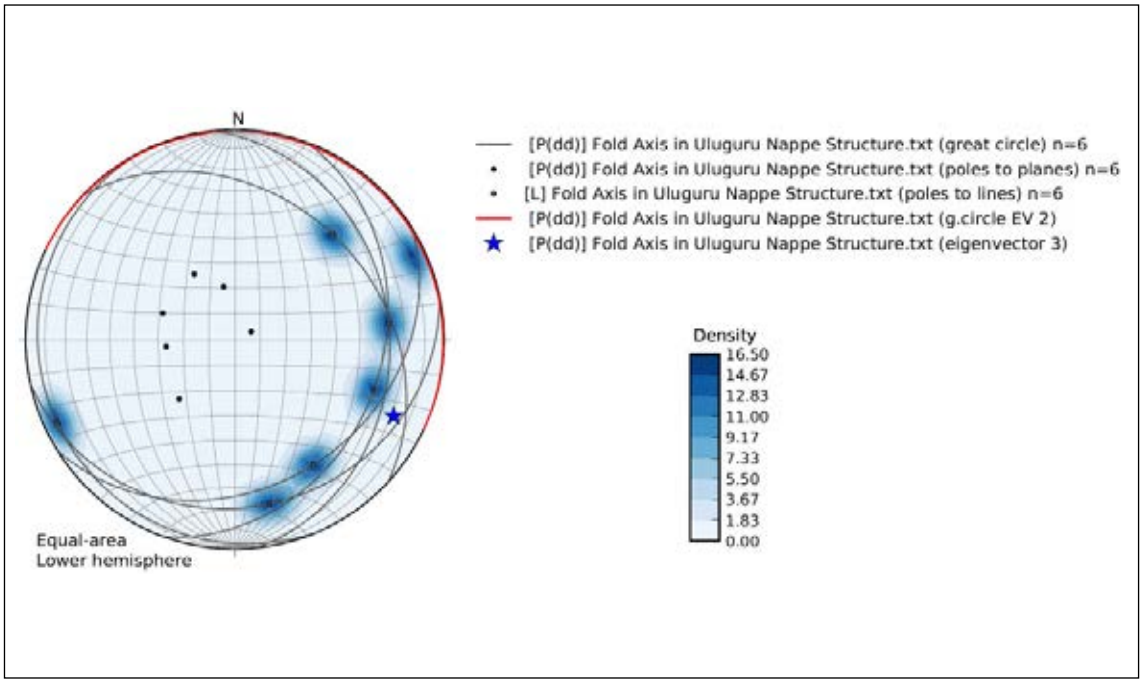

Fig. 3.23: The stereographic projection of all fold axis of the examined 6 locations indicate a fan of folds within the Uluguru Nappe. The folds are oriented a great circle which points towards the southeast with a dip of about 20° (blue star).

and the GIS software package "Global Mapper", this structural feature is clearly visible. The fault can be found just beneath the westward buldge of the Uluguru Nappe and is marked by the flow patterns of Ruvu and Msumbizi River (Fig. 3.26). A clear linear structure can be recognised in Fig. 3.24 which cuts through the Uluguru Nappe in an eastnortheastern strike. The offset along the fault further confirms a dextral shear sense as observed in the field. It can also be recognised that the fold style exposed south to the fault shows a different pattern in terms of orientation, frequency and amplitude than compared to what is observed in the northern part. Finally, in respect to the two rivers which follow the trace of this fault the name Ruvu-Msumbizi Fault is suggested by the author.

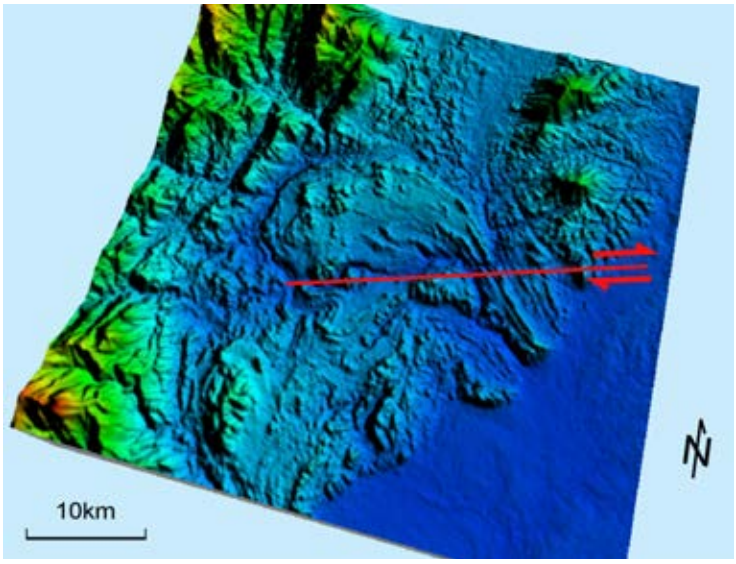

Fig. 3.24: The digital elevation model image illustrates the Uluguru Nappe structure which can be found in the centre of the picture. The red line indicates the trend of the dextral strike-slip fault which was recognised in the field by the author and mentioned by Sampson & Spence (1959) as individual segments. In this digital image, however, the structure can be recognised as a continuous fault cutting through the Uluguru Nappe (immediately above the red line). The lower left corner of the digital image is located at 7°8'3''S/ 37°41'51''E.

3.4 Discussion

As recognised in the field, the complex fold pattern in outcrop#58 indicates the presence of at least two folding phases responsible for the formation of the Uluguru Nappe. Such an assumption was confirmed later on by the stereographic plotting of fold axis recorded in the Uluguru Nappe (Fig. 3.23). The folded pattern of fold axis implies a superimposed folding phase D2 after an initial folding phase during D1. A general trend in southeastern direction for the fold axis in the Uluguru Nappe was measured. Because the dip direction of the fold axis plots in a southeastern direction it can be assumed that the underlaying basement is slightly tilted towards the east. This again would still allow a thrusting with a northwestern vergence during D3 as proposed by other researchers before. Whether the basement was tilted before or after D3 can not be determined clearly.

The schematic development of the Uluguru Nappe as shown in the Fig. 3.25 is not only in accordance to field observations made in this study but also to tectonic models introduced by Fritz et al. (2005), Rossetti et al. (2008), and Fritz et al. (2009).

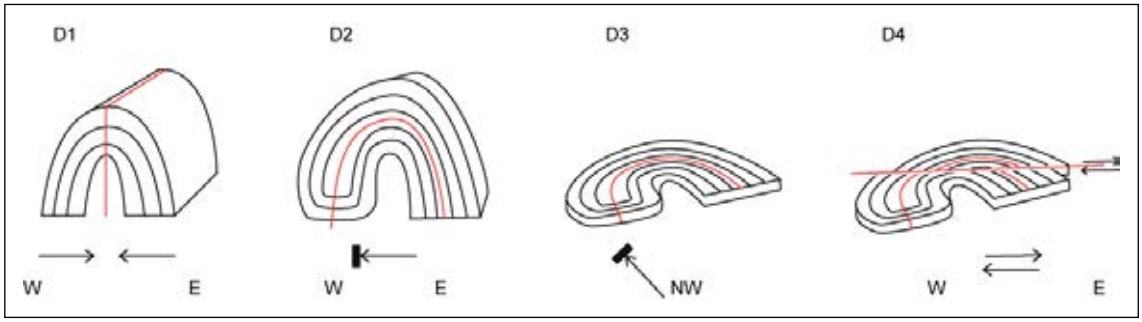

Fig. 3.25: The observed fold style of the Uluguru Nappe can be explained by four deformation phases. A first deformation D1 was related to isoclinal folding. During D2 the fold was overturned and dumped onto the basement. During D3 a stacking due to further thrusting onto the basement in a northwestern direction occurred. Finally, in D4 during a period of exhumation and cooling, brittle deformation penetrated the nappe structure by strike-slip faults such as the Ruvu-Msumbizi Fault, recording a dextral shear sense.

Finally, the Ruvu-Msumbizi Fault which had been described in this study as a continous fault, marks a brittle event during the last tectonic phase recorded in the Uluguru Mts known as deformation D4. This tectonic event caused a dextral strike-slip fault to develop, penetrating the southern half of the Uluguru Nappe from west to east. In the field, the fault was mainly recognised due to the fact that the rivers Ruvu and Msumbizi follow the trace of this tectonic structure. In the case of Msumbizi River the fault even crosscut the root zone of the Uluguru Nappe (Fig. 3.26).

The exposure of different fold patterns on the northern and the southern part of the fault are further interpreted as an indication for a mainly vertical dislocation component for this fault. Consequently, this led to different parts of the nappe structure to be exposed at the surface. South from the Ruvu-Msumbizi fault there is a change to higher a fold frequency but smaller amplitudes observed, in particular. This again is interpreted as a pattern representing higher friction on the lower limb of the nappe structure exposed to high shear strain when thrusted on to the basement. This would reflect the deformation D3 when stacking of the already overturned fold structure on to the basement took place. Also the complex fold structure exposed at outcrop#58

could be interpreted as an interference pattern of superimposed folds generated by D2 and D3 folding phases. In contrast, fragments of the upper limb of the overturned fold structure at the front of the Uluguru Nappe are exposed to the north of the Ruvu-Msumbizi Fault. There, being further away from the basement thrust D3 structures are less prominent.

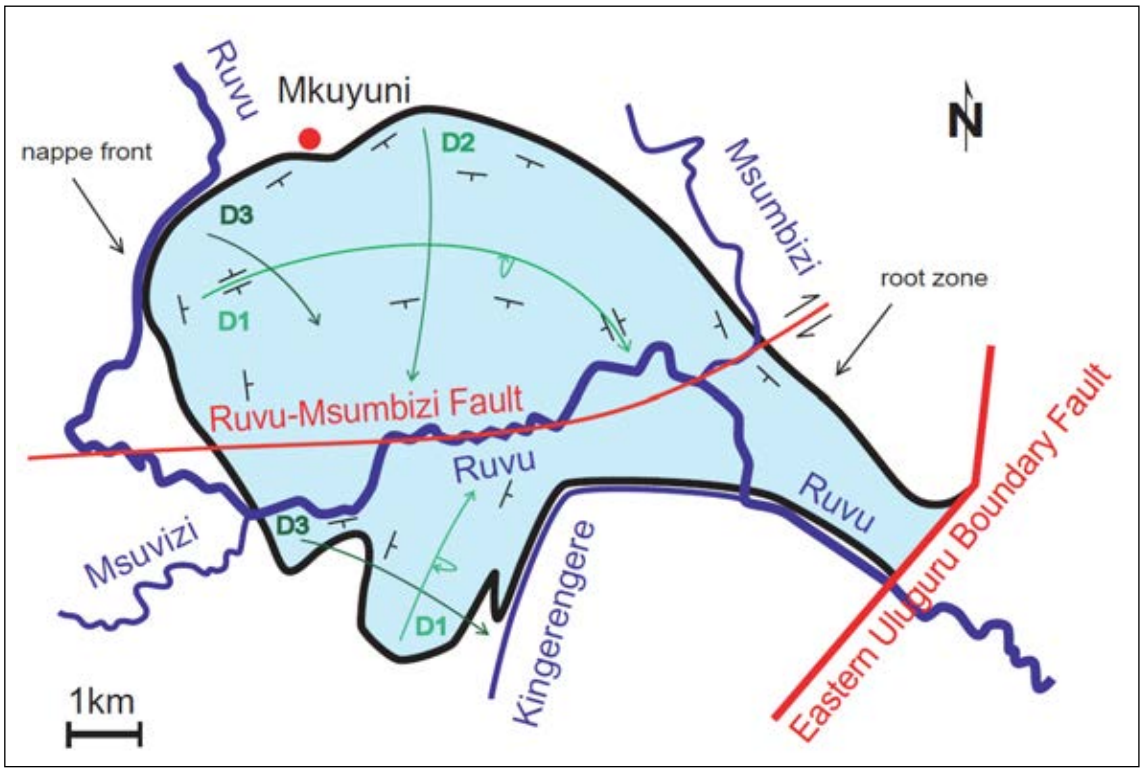

Fig. 3.26: This sketch map shows the most important structural features within the Uluguru Nappe. The Uluguru Nappe itself is displayed blue where as the intrinsic surface of the nappe structure is marked by a black line. Faults are coloured in red, fold structures are marked in green shades. Finally, strike and dip are indicated by black markers. The nappe front and the root zone of Uluguru Nappe are indicated by arrows pointing out the according areas within the nappe structure.

Finally, it was found that the ruby mineralisation in the Uluguru Nappe is structurally controlled. Ruby mineralised nodules are oriented parallel in respect to the measured fold axis (Fig. 3.19). Furthermore, these mineralised boudin-like lenses were found always in close position to fold hinges and never in the fold limbs similar to what is as known for saddle reefs. This indicates a mineralisation which took place after iso-clinal folds developed during deformation D1. Because the mineralisation was under tectonic stress as the observed boudin-like structure indicates it can be assumed that the mineralisation took place prior or at least simultaneously with D3 deformation. D4 deformation can be ruled out since the ruby bearing fold structures are cut by late faults as seen in Mwalazi Mine which is close to the Ruvu-Msumbizi Fault.

CHAPTER IV

PETROLOGY

Selected samples from four ruby mines in the Morogoro Region, Tanzania were investigated by petrographic, petrologic and thermodynamic methods (see chapter 1).

The sampled mines are located in the Uluguru Mts. (Mwalazi and Visakazi II Mine) and in the Mahenge Mts (Kitwaro and Ipanko Mine), both in the Morogoro Region, Tanzania (see Fig. 3.1 & Fig. 3.3).

4.1 Sample Material

Besides petrographic examinations on 17 thick- and thin sections, whole rock analysis were carried out on one mineralised and one host rock samples for each of the investigate mines (8 whole rock samples in total).

4.1.1 Sample Preparation

Sample preparation regarding petrologic samples was carried out as addressed in chapter 1.4.3.

4.1.2 Sample Description

In the following section selected samples are macroscopically described. The samples were selected on the basis of observed mineral paragenesis after petrographic examinations were carried out. In contrast to the Kitwaro and Ipangko Mine, Mahenge Mts, two samples were necessary to cover the mineral assemblages encountered in Mwalazi as well as Visakazi II Mine, Uluguru Mts.

Where applicable mineral abbreviations are used as suggested by Kretz (1983).

4.1.2.1 Mwalazi Mine

Sample TZM04 was collected from a mineralised zone close to the fold hinge. It represents one of the ruby mineralised nodules which were mentioned in chapter 3 before. Sample TZM04 shows a dark green core consisting of amphibole together with intense purplish rubies in the center. White patches were identified as carbonate phases calcite and dolomite. The core is surrounded by a dark brownish rim of biotite. There is no foliation visible but the dark brown biotite rim is clearly following the outline of the nodule (Fig. 4.1).

Sample TZM08 represents an inner core of a mineralised boudin-shaped lense only. A dark green nodule which consists of amphibole and corundum mainly contains

Fig. 4.1: Sample TZM04 (left) and TZM08 (right) from Mwalazi Mine in the Uluguru Mts represent both ruby mineralised boudins where as in TZM08 mainly the ruby bearing core of such a boudin is present.

further calcite and dolomite as well as flakes of biotite. There is no foliation visible in this specimen (Fig. 4.1).

4.1.2.2 Visakazi II Mine

Sample WB1 was collected in the open pit area of Visakazi II mine. It consist mainly white calcite with a brownish band of biotite and amphibole. A few ruby phenocrysts can be found in this sample as well. The sample was collected from the neck zone of a mineralised nodule. (Fig. 4.2).

Sample WB6 was collected from an underground operation at Visakazi II Mine where an inclined drift with a length of about 20m is lowered into the ground. The sample shows a strong mineralisation in the core where intense, dark green amphibole and purplish corundum can be found. The mineralised zone contains further plagioclase and is surrounded by a thick layer of white calcite. In this mineralised boudin-shaped lense the normally pronounced biotite rim is missing however biotite flakes can still be found through out the sample. Again there is no foliation visible (Fig. 4.2).

Fig. 4.2: The two samples from Visakazi II Mine represent two different zones in terms of production site as well as in terms of mineralisation. Sample WB1 is taken in the open pit operation of Visakazi II Mine and represents the neck of a mineralised boudin-shaped lense where as sample WB6 contains a core of such a lense which was collected in the drift operation at Visakazi II Mine.

4.1.2.3 Kitwaro Mine

At Kitwaro Mine sample TZG03 was collected from an already abandoned open pit. The mine showed several zones of mineralisation which were confined to a fold hinge. Along the strike of the fold axes the mine operation was carried out. The sample consists of the mostly unmineralised dolomite and biotite bearing host rock but includes a small ruby bearing zone. The ruby mineralisation is again encapsulated in a thick rim of dark biotite. The core is characterised by dark green amphibole, and intense purplish red corundum as well as white spots of calcite and dolomite as well as plagioclase. Dark violet crystals are indentified to be sapphirine which is found in association with corundum. No foliation is visible either in this specimen (Fig. 4.3)

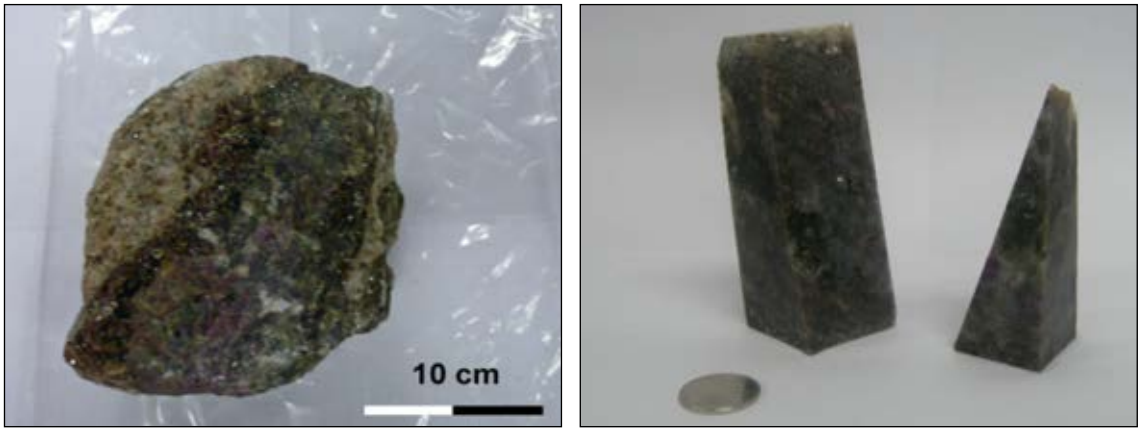

Fig. 4.3: Also in sample TZG03 a mineralised boudin-shaped lense including the center and the neck zone was contained. In comparison to the samples from the Uluguru Mts sapphirine was oberved in association with the ruby mineralisation. Again a biotite rich rim is found encapsulating the mineralisation of this nodule.

4.1.2.4 Ipangko Mine

Sample TZH08 was taken from an open pit of the former Ipangko Ruby Mine. This mine is situated in the same marble unit as the Kitwaro Mine however located about 6km further to the south. Sample TZH08 represents a rather large mineralised zone compared to the other mineralised nodules investigated before. Also in this sample the typical biotite-rich rim can be found. Sapphirine is however much more prominent than in sample TZG03. In contrast to the other samples so far there was no amphibole observed in this sample. Together with sapphirine there is also purplish red corundum found, accompanied by dolomite and plagioclase. Again there is no clear foliation visible in this specimen (Fig. 4.4).

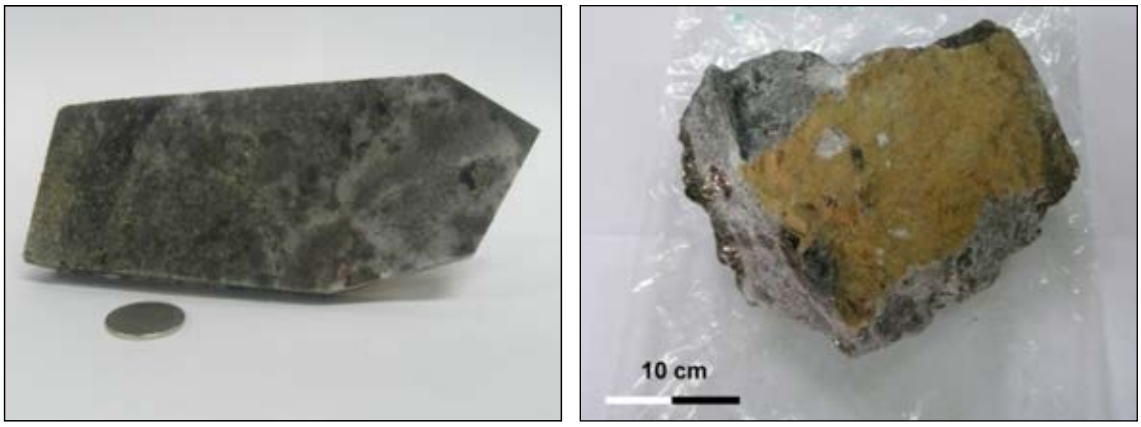

Fig. 4.4: In sample TZH08 a rather large mineralised boudin-shaped lense can be examined where the biotite-rich rim can be seen in the picture to the left followed by a mineralised zone with sapphirine, dolomite, plagioclase and corundum. The weathered surface which is seen in the picture to the right shows a brownish-yellowish colour.

4.2 Whole Rock Chemistry

Comparing unmineralised host rocks and ruby bearing samples the following characteristics can be found: Marbles consist mainly of CaO and MgO with only small amounts of other oxides, depending on their silicate or oxide mineral content. An increase in SiO_2, Al_2O_3, K_2O, and Na_2O is obvious for the silicate (amphibole and biotite) and oxide rich ruby mineralised samples (Tab. 4.1).

Further, it has to be mentioned that a difference in host rock composition was observed from the Uluguru to the Mahenge Mts as well. In the Uluguru Mts calcite-marbles are present where as for the Mahenge Mts dolomite-marbles were found to be the host rock for the investigated ruby mineralisations (Fig. 4.5).

Three of the selected mineralised samples were big enough to have thick sections polished as well as powder samples created from the same rock sample. The following samples therefore correspond with each other (powder sample/ thick section): RUTZM-22_E/ WB10, RUTZH-18_E/ TZG03, RUTZH-19_E/ TZH08.

The results collected in this investigation are displayed as a summary in Tab. 4.1.

Fig. 4.5: Two host rock samples, a dolomite-marble from the Kitwaro Mine, Mahenge Mts (left, ROTZH-09_E) and a partially graphitised calcite-marble from the Mwalazi Mine (right, RUTZM-40_E).

Sample	locality	description	SiO_2	TiO_2	Al_2O_3	Fe_2O_3	FeO	MnO	MgO	CaO	Na_2O	K_2O	P_2O_5	SO_3	LOI.	H_2O^-	Total
RUTZM-40/ E	Mwarazi	Cal-marble	0.28	<0.02	0.06	0.25	nil	0.02	0.80	54.34	<0.10	0.01	0.01	0.01	43.92	0.11	99.81
RUTZM-38/ E	Mwarazi	mineralised nodule	33.58	0.62	21.55	0.71	1.14	0.04	11.10	18.44	1.75	1.43	2.13	0.02	7.02	0.22	99.72
ROTZM-14/ E	Visakazi II	Cal-marble	0.15	<0.02	0.06	0.03	nil	0.02	2.41	52.87	<0.10	<0.01	0.03	0.03	44.02	0.19	99.81
RUTZM-22/ E	Visakazi II	mineralised marble	25.48	0.79	17.94	3.05	5.74	0.01	12.30	15.23	0.91	0.91	0.56	11.04	5.15	0.19	99.30
ROTZH-09/ E	Kitwaro	Dol-marble	4.28	<0.02	0.05	0.05	nil	<0.01	21.14	30.87	<0.10	<0.01	0.03	0.08	43.14	0.24	99.86
RUTZH-18/ E	Kitwaro	mineralised marble	29.37	2.65	23.70	0.29	nil	<0.01	9.81	19.82	0.89	2.26	4.96	0.16	5.74	0.21	99.85
ROTZH-11/ E	Ipangko (ruby)	Dol-marble	2.35	<0.02	0.11	0.29	0.36	0.03	20.61	30.63	<0.10	0.09	0.08	0.45	44.64	0.17	99.81
RUTZH-19/ E	Ipangko (ruby)	mineralised marble	37.99	3.63	29.46	0.73	0.45	<0.01	6.12	16.51	0.43	1.75	0.89	0.30	1.40	0.15	99.80

Tab. 4.1: Whole rock investigations indicate an increase in the oxides SiO_2, TiO_2, FeO/Fe_2O_3, Na_2O, K_2O, P_2O_5 and in one case SO_3 from host rock to mineralised samples. Increases in composition compared to the unmineralised host rock are coloured in green where as decreases are marked in red.

4.3 Petrography and Mineral Chemistry

Again samples from the Uluguru Mts as well as the Mahenge Mts were examined. Minerals were identified by petrographic and mineral chemical means. In particular, optic characteristics were used during microscopic investigations whereas Back-Scatter Electron images (BSE images) and EDX signatures were used to identify individual phases prior to quantitative analysis.

After mineral chemistry data had been collected the data was processed by PET an open source Mathematica based software package developed by Edgar Dachs, University of Salzburg, Austria and available from http://www.unisalzburg.at/portal/page?_pageid=805,259394&_dad=portal&_schema=PORTAL to calculate mineral compositions (Dachs, 1998). The compositions of the following minerals were calculated on basis of predefined oxygen numbers (given in parentheses):

amphibole (23 O), apatite (12.5 O), mica (11 O), calcite (1 O), chlorite (14 O), dolomite (2 O), corundum/rutile (3 O), kali-feldspar (8 O), plagioclase (8 O), sapphirine (20 O), sphene (5 O), spinel (4 O), and tourmaline (24.5 O).

Fe^{3+} was calculated following Droop (1987), except amphibole where calculations were based on Leake et al. (1997).

Representatives of the most important mineral phases (amphibole, calcite, chlorite, dolomite, feldspar, phlogopite, sapphirine, scapolite, spinel, tourmaline, and white mica) which were analyised by EPMA and SEM coupled WD-XRF are summerised in Tab.4.2 - Tab.4.12. Regarding the mineral chemistry of apatite, corundum, rutile, and sphene, it was neglected to create specific tables however. The mineral chemistry of apatite will be discussed in further detail in chapter 4.3.3. where as the mineral chemistry of corundum will be addressed on the basis of an in-depth LA-ICP-MS investigation in chapter 5.

Further, there is a complete data compilation of all measurements taken by EPMA and SEM coupled WD-XRF included in Appendix A.4. Regarding instrument specifications further information is given in chapter 1.4.4.

Amphibole, mineral composition calculated on the basis of 23(O,OH,F)

Deposit	Uluguru Mts						Mahenge Mts		
Mine	Mwalazi Mine			Visakazi Mine			Kitwaro Mine		
Sample	TZM04_53	TZM04_78	TZM04_81	WB1_11	WB6_25	WB6_37	TZG03_1	TZG03_6	TZG03_28
SiO2	42.06	41.67	41.50	44.55	43.01	42.38	42.11	41.46	42.55
TiO2	0.94	1.13	1.06	0.63	1.01	0.62	1.96	1.93	0.52
P2O5	bdl	bdl	bdl	bdl	bdl	bdl	bdl	bdl	bdl
Al2O3	17.67	18.19	17.81	17.83	18.40	18.23	17.54	17.86	18.89
Cr2O3	0.46	0.55	0.56	bdl	0.54	0.41	bdl	bdl	bdl
Fe2O3	bdl	bdl	bdl	bdl	bdl	bdl	bdl	bdl	bdl
FeO	1.79	1.86	1.89	0.26	0.61	0.48	0.76	0.64	0.71
MnO	bdl	bdl	bdl	bdl	bdl	bdl	bdl	bdl	bdl
MgO	17.35	16.46	16.57	18.50	17.68	17.17	17.55	17.79	17.99
CaO	13.41	13.51	13.21	12.33	12.27	12.27	13.07	13.03	13.17
K2O	1.29	1.24	1.14	1.10	1.25	0.95	1.72	1.28	0.53
Na2O	1.79	1.85	1.86	2.38	2.39	2.70	2.58	2.95	3.54
Cl	bdl	bdl	bdl	bdl	bdl	bdl	0.25	0.22	0.22
F	bdl	0.53	0.60	1.35	1.08	1.02	0.88	0.98	0.92
Total	96.87	96.99	96.20	98.93	98.38	96.36	98.42	98.14	99.04
Si	5.907	5.849	5.906	6.186	6.033	6.060	5.957	5.880	5.941
Ti	0.099	0.119	0.113	0.066	0.106	0.067	0.209	0.206	0.055
P	-	-	-	-	-	-	-	-	-
Al	2.925	3.009	2.987	2.918	3.042	3.071	2.925	2.985	3.109
Cr	0.051	0.061	0.063	-	0.060	0.046	-	-	-
Fe3	-	-	-	-	-	-	-	-	-
Fe2	0.611	0.802	0.543	0.015	0.036	0.028	0.090	0.049	0.041
Mn	-	-	-	-	-	-	-	-	-
Mg	3.632	3.444	3.515	3.830	3.697	3.659	3.701	3.761	3.745
Ca	2.018	2.032	2.014	1.834	1.845	1.880	1.981	1.980	1.970
K	0.231	0.222	0.207	0.195	0.224	0.173	0.310	0.232	0.094
Na	0.487	0.503	0.513	0.641	0.650	0.747	0.708	0.811	0.958
Cl	-	-	-	-	-	-	0.060	0.053	0.052
F	-	0.235	0.270	0.593	0.481	0.459	0.394	0.440	0.406
Sum	15.961	16.276	16.131	16.278	16.174	16.190	16.335	16.397	16.371

Tab. 4.2: Mineral chemistry of selected amphibole samples

Calcite, mineral composition calculated on the basis of 1(O)

Deposit	Uluguru Mts					Mahenge Mts					
Mine	Mwalazi Mine		Visakazi Mine			Kitwaro Mine			Ipangko Mine		
Sample	TZM04_61	TZM04_66	WB1_7	WB1_26	WB1_33	TZG03_15	TZG03_33	TZG03_43	TZH08_53	TZH08_57	TZH08_60
SiO2	bdl	bdl	bdl	bdl	bdl	bdl	bdl	bdl	bdl	bdl	bdl
TiO2	bdl	bdl	bdl	bdl	bdl	bdl	bdl	bdl	bdl	bdl	bdl
P2O5	bdl	bdl	bdl	bdl	bdl	bdl	bdl	bdl	bdl	bdl	bdl
Al2O3	bdl	bdl	bdl	bdl	bdl	bdl	bdl	bdl	bdl	bdl	bdl
Cr2O3	bdl	bdl	bdl	bdl	bdl	bdl	bdl	bdl	bdl	bdl	bdl
Fe2O3	bdl	bdl	bdl	bdl	bdl	bdl	bdl	bdl	bdl	bdl	bdl
FeO	bdl	bdl	bdl	bdl	bdl	bdl	bdl	0.04	bdl	0.26	bdl
MnO	bdl	bdl	bdl	bdl	bdl	bdl	bdl	bdl	bdl	bdl	bdl
MgO	1.63	1.53	0.44	2.26	1.49	1.80	1.16	1.90	1.27	2.35	2.25
CaO	55.02	56.57	52.28	51.51	52.77	52.39	52.36	53.38	54.5	51.80	54.12
K2O	bdl	bdl	bdl	bdl	bdl	bdl	bdl	bdl	bdl	bdl	bdl
Na2O	bdl	bdl	bdl	bdl	bdl	bdl	bdl	bdl	bdl	bdl	bdl
Cl	bdl	bdl	bdl	bdl	bdl	bdl	bdl	bdl	bdl	bdl	bdl
F	bdl	bdl	bdl	bdl	bdl	bdl	bdl	bdl	bdl	bdl	bdl
Total	56.65	58.28	52.72	53.77	54.59	54.19	53.52	55.32	55.77	54.41	56.37
Si	-	-	-	-	-	-	-	-	-	-	-
Ti	-	-	-	-	-	-	-	-	-	-	-
P	-	-	-	-	-	-	-	-	-	-	-
Al	-	-	-	-	-	-	-	-	-	-	-
Cr	-	-	-	-	-	-	-	-	-	-	-
Fe3	-	-	-	-	-	-	-	-	-	-	-
Fe2	-	-	-	-	-	-	-	0.001	-	0.004	-
Mn	-	-	-	-	-	-	-	-	-	-	-
Mg	0.040	0.039	0.012	0.058	0.041	0.046	0.030	0.047	0.031	0.059	0.055
Ca	0.960	0.961	0.988	0.942	0.959	0.954	0.970	0.952	0.969	0.937	0.945
K	-	-	-	-	-	-	-	-	-	-	-
Na	-	-	-	-	-	-	-	-	-	-	-
Cl	-	-	-	-	-	-	-	-	-	-	-
F	-	-	-	-	-	-	-	-	-	-	-
Sum	1.000	1.000	1.000	1.000	1.000	1.000	1.000	1.000	1.000	1.000	1.000

Tab. 4.3: Mineral chemistry of selected calcite samples

Chlorite, mineral composition calculated on the basis of 14(O,OH)

Deposit	Uluguru Mts					
Mine	Mwalazi Mine			Visakazi Mine		
Sample	TZM08_52	TZM08_66	TZM08_67	WB1_36	WB6_16	WB6_23
SiO2	27.30	27.61	27.58	27.36	29.11	29.60
TiO2	0.02	bdl	0.02	bdl	bdl	bdl
P2O5	bdl	bdl	bdl	bdl	bdl	bdl
Al2O3	23.58	23.85	24.21	27.55	21.40	22.06
Cr2O3	1.88	1.40	1.42	bdl	1.12	0.73
V2O3	0.13	0.12	0.13	n.a.	n.a.	n.a.
Fe2O3	bdl	bdl	bdl	bdl	bdl	bdl
FeO	3.21	3.11	3.24	1.15	0.84	0.80
MnO	bdl	bdl	bdl	bdl	bdl	bdl
MgO	28.76	29.09	28.84	27.45	31.51	31.61
CaO	bdl	bdl	0.03	0.09	bdl	0.09
K2O	bdl	bdl	0.03	bdl	bdl	bdl
Na2O	0.02	bdl	0.05	bdl	bdl	0.06
Cl	bdl	bdl	0.01	0.10	bdl	bdl
F	bdl	bdl	bdl	0.46	0.24	0.28
Total	84.92	85.19	85.57	84.16	84.22	85.22
Si	2.649	2.662	2.651	2.634	2.810	2.819
Ti	0.002	-	0.001	-	-	-
P	-	-	-	-	-	-
Al	2.696	2.711	2.743	3.126	2.434	2.476
Cr	0.144	0.107	0.108	-	0.086	0.055
V	0.010	0.009	0.010	n.a.	n.a.	n.a.
Fe3	-	-	-	-	-	-
Fe2	0.260	0.251	0.261	0.093	0.067	0.063
Mn	-	-	-	-	-	-
Mg	4.160	4.182	4.133	3.940	4.533	4.488
Ca	-	-	0.003	0.009	-	0.009
K	-	-	0.004	-	-	-
Na	0.003	-	0.010	-	-	0.010
Cl	-	-	0.001	0.016	-	-
F	-	-	-	0.140	0.073	0.083
Sum	9.924	9.922	9.925	9.958	10.003	10.003

Tab. 4.4: Mineral chemistry of selected chlorite samples

Dolomite, mineral composition calculated on the basis of 2(O)

Deposit	Uluguru Mts						Mahenge Mts	
Mine	Mwalazi Mine			Visakazi Mine			Kitwaro Mine	
Sample	TZM04_58	TZM04_80	TZM08_85	WB1_6	WB1_9	WB1_10	TZG03_10	TZG03_25
SiO2	bdl	bdl	bdl	bdl	bdl	bdl	bdl	bdl
TiO2	bdl	bdl	bdl	bdl	bdl	bdl	bdl	bdl
P2O5	bdl	bdl	bdl	bdl	bdl	bdl	bdl	bdl
Al2O3	bdl	bdl	bdl	bdl	bdl	bdl	bdl	bdl
Cr2O3	bdl	bdl	bdl	bdl	bdl	bdl	bdl	bdl
Fe2O3	bdl	bdl	bdl	bdl	bdl	bdl	bdl	bdl
FeO	0.84	0.84	1.12	0.27	bdl	bdl	0.18	0.33
MnO	bdl	bdl	bdl	bdl	bdl	bdl	bdl	bdl
MgO	20.67	19.27	19.93	20.80	20.88	20.55	20.65	20.59
CaO	32.09	31.53	30.74	30.47	30.60	30.78	31.36	31.80
K2O	bdl	bdl	bdl	bdl	bdl	bdl	bdl	bdl
Na2O	bdl	bdl	bdl	bdl	bdl	bdl	bdl	bdl
Cl	bdl	bdl	bdl	bdl	bdl	bdl	bdl	bdl
F	bdl	bdl	bdl	bdl	bdl	bdl	bdl	bdl
Total	53.60	51.64	51.79	51.54	51.48	51.33	52.19	52.72
Si	-	-	-	-	-	-	-	-
Ti	-	-	-	-	-	-	-	-
P	-	-	-	-	-	-	-	-
Al	-	-	-	-	-	-	-	-
Cr	-	-	-	-	-	-	-	-
Fe3	-	-	-	-	-	-	-	-
Fe2	0.021	0.022	0.029	0.007	-	-	0.005	0.008
Mn	-	-	-	-	-	-	-	-
Mg	0.935	0.909	0.935	0.971	0.974	0.963	0.954	0.944
Ca	1.043	1.069	1.036	1.022	1.026	1.037	1.041	1.048
K	-	-	-	-	-	-	-	-
Na	-	-	-	-	-	-	-	-
Cl	-	-	-	-	-	-	-	-
F	-	-	-	-	-	-	-	-
Sum	1.999	2.000	2.000	2.000	2.000	2.000	2.000	2.000

Tab. 4.5: Mineral chemistry of selected dolomite samples

Feldspar, mineral composition calculated on the basis of 8(O)

Deposit	Uluguru Mts						Mahenge Mts					
Mine	Mwalazi Mine			Visakazi Mine			Kitwaro Mine			Ipangko Mine		
Sample	TZM08_40	TZM08_41	TZM08_44	WB1_17	WB6_4	WB6_63	TZG03_30	TZG03_36	TZG03_41	TZH08_38	TZH08_39	TZH08_42
SiO2	56.68	56.78	58.53	45.75	44.79	43.85	44.23	43.90	40.71	42.58	43.05	43.35
TiO2	bdl	bdl	bdl	bdl	bdl	bdl	bdl	bdl	bdl	bdl	bdl	bdl
P2O5	bdl	bdl	bdl	bdl	bdl	bdl	bdl	bdl	bdl	bdl	bdl	bdl
Al2O3	25.80	25.72	27.62	34.86	35.41	35.30	34.84	34.50	35.98	35.83	35.66	35.34
Cr2O3	bdl	bdl	bdl	bdl	bdl	bdl	bdl	bdl	bdl	bdl	bdl	bdl
Fe2O3	bdl	bdl	bdl	bdl	bdl	bdl	bdl	bdl	bdl	bdl	bdl	bdl
FeO	bdl	bdl	bdl	bdl	bdl	bdl	bdl	bdl	bdl	bdl	bdl	bdl
MnO	bdl	bdl	bdl	bdl	bdl	bdl	bdl	bdl	bdl	bdl	bdl	bdl
MgO	bdl	bdl	bdl	bdl	bdl	bdl	bdl	bdl	bdl	bdl	bdl	bdl
CaO	8.17	8.01	2.76	18.50	18.83	19.59	19.86	19.68	19.90	20.13	20.10	20.13
K2O	bdl	bdl	2.65	bdl	bdl	bdl	bdl	bdl	bdl	bdl	bdl	bdl
Na2O	6.45	6.59	6.07	0.66	0.44	0.49	0.51	0.49	0.44	0.32	0.37	0.32
Cl	bdl	bdl	bdl	bdl	bdl	bdl	bdl	bdl	bdl	bdl	bdl	bdl
F	bdl	bdl	bdl	bdl	bdl	bdl	bdl	bdl	bdl	bdl	bdl	bdl
Total	97.17	97.13	97.63	99.77	99.47	99.23	99.44	98.57	97.04	98.85	99.18	99.15
Si	2.606	2.610	2.654	2.108	2.074	2.045	2.059	2.062	1.953	1.999	2.014	2.027
Ti	-	-	-	-	-	-	-	-	-	-	-	-
P	-	-	-	-	-	-	-	-	-	-	-	-
Al	1.398	1.393	1.476	1.893	1.932	1.940	1.912	1.909	2.034	1.983	1.966	1.948
Cr	-	-	-	-	-	-	-	-	-	-	-	-
Fe3	-	-	-	-	-	-	-	-	-	-	-	-
Fe2	-	-	-	-	-	-	-	-	-	-	-	-
Mn	-	-	-	-	-	-	-	-	-	-	-	-
Mg	-	-	-	-	-	-	-	-	-	-	-	-
Ca	0.403	0.394	0.134	0.913	0.934	0.979	0.991	0.990	1.023	1.013	1.007	1.009
K	-	-	0.153	-	-	-	-	-	-	-	-	-
Na	0.575	0.587	0.533	0.059	0.039	0.044	0.046	0.045	0.041	0.029	0.034	0.029
Cl	-	-	-	-	-	-	-	-	-	-	-	-
F	-	-	-	-	-	-	-	-	-	-	-	-
Sum	4.982	4.986	4.950	4.973	4.979	5.008	5.008	5.006	5.051	5.024	5.021	5.013
Xan	0.41	0.40	0.16	0.94	0.96	0.96	0.96	0.96	0.96	0.97	0.97	0.97
Xab	0.59	0.60	0.65	0.06	0.04	0.04	0.04	0.04	0.04	0.03	0.03	0.03
Xor	0.00	0.00	0.19	0.00	0.00	0.00	0.00	0.00	0.00	0.00	0.00	0.00

Tab. 4.6: Mineral chemistry of selected feldspar samples

Phlogopite, mineral composition calculated on the basis of 11(O,OH,F)

Deposit	Uluguru Mts						Mahenge Mts					
Mine	Mwalazi Mine			Visakazi Mine			Kitwaro Mine			Ipangko Mine		
Sample	TZM04_77	TZM04_82	TZM08_83	WB1_22	WB1_23	WB6_8	TZG03_14	TZG03_19	TZG03_22	TZH08_51	TZH08_54	TZH08_56
SiO2	39.22	38.99	38.14	40.79	41.56	39.83	39.58	39.61	39.10	38.06	37.44	37.76
TiO2	0.97	1.08	1.29	1.46	1.61	1.24	1.13	0.83	0.69	1.05	1.07	0.93
P2O5	bdl	bdl	bdl	bdl	bdl	bdl	bdl	bdl	bdl	bdl	bdl	bdl
Al2O3	17.72	17.65	20.12	16.00	16.20	17.89	17.12	17.12	18.56	18.82	19.57	19.12
Cr2O3	0.31	0.26	1.28	0.19	bdl	0.50	bdl	0.15	0.15	0.28	0.28	0.45
Fe2O3	bdl	bdl	bdl	bdl	bdl	bdl	bdl	bdl	bdl	bdl	bdl	bdl
FeO	1.70	1.67	2.36	0.37	0.45	0.48	0.49	0.56	0.53	1.85	1.73	1.36
MnO	bdl	bdl	bdl	bdl	bdl	bdl	bdl	bdl	bdl	bdl	bdl	bdl
MgO	24.52	24.16	20.15	25.17	24.79	24.39	25.54	25.60	25.32	23.61	23.43	24.42
CaO	0.15	0.11	0.12	0.12	bdl	0.11	0.14	0.17	0.17	bdl	bdl	bdl
K2O	9.94	10.08	9.79	10.37	10.21	9.32	9.57	9.65	9.57	9.49	9.50	9.77
Na2O	0.39	0.60	0.59	0.25	0.21	0.77	0.86	0.71	0.71	0.31	bdl	0.33
Cl	bdl	bdl	bdl	bdl	bdl	bdl	bdl	bdl	bdl	bdl	bdl	bdl
F	1.00	0.71	0.10	1.97	2.05	1.54	1.16	1.20	0.91	0.99	0.81	1.00
Total	95.92	95.59	93.94	96.69	97.08	96.15	95.59	95.60	95.71	94.46	93.83	95.14
Si	2.758	2.749	2.720	2.856	2.889	2.785	2.778	2.783	2.733	2.712	2.677	2.674
Ti	0.051	0.057	0.069	0.077	0.084	0.065	0.060	0.044	0.036	0.056	0.058	0.050
P	-	-	-	-	-	-	-	-	-	-	-	-
Al	1.468	1.467	1.691	1.320	1.327	1.474	1.416	1.418	1.529	1.580	1.649	1.596
Cr	0.017	0.014	0.072	0.011	-	0.027	-	0.008	0.008	0.016	0.016	0.025
Fe3	-	-	-	-	-	-	-	-	-	-	-	-
Fe2	0.100	0.098	0.141	0.022	0.026	0.028	0.029	0.033	0.031	0.110	0.103	0.081
Mn	-	-	-	-	-	-	-	-	-	-	-	-
Mg	2.570	2.540	2.142	2.627	2.569	2.543	2.673	2.681	2.638	2.508	2.497	2.578
Ca	0.011	0.008	0.009	0.009	-	0.008	0.011	0.013	0.013	-	-	-
K	0.892	0.907	0.891	0.926	0.906	0.832	0.857	0.865	0.853	0.863	0.867	0.883
Na	0.053	0.082	0.082	0.034	0.028	0.104	0.117	0.097	0.096	0.043	-	0.045
Cl	-	-	-	-	-	-	-	-	-	-	-	-
F	0.222	0.158	0.022	0.436	0.451	0.340	0.258	0.267	0.201	0.223	0.183	0.224
Sum	8.142	8.080	7.839	8.318	8.280	8.206	8.199	8.209	8.138	8.111	8.050	8.156
Xmg	0.96	0.96	0.94	0.99	0.99	0.99	0.99	0.99	0.99	0.96	0.96	0.97

Tab. 4.7: Mineral chemistry of selected phlogopite samples

Sapphirine, mineral composition calculated on the basis of 20(O)

Deposit	Mahenge Mts					
Mine	Kitwaro Mine			Ipangko Mine		
Sample	TZG03_14	TZG03_19	TZG03_22	TZH08_19	TZH08_21	TZH08_55
SiO2	12.59	12.27	12.63	10.25	10.86	11.50
TiO2	bdl	0.13	bdl	bdl	bdl	bdl
P2O5	bdl	bdl	bdl	bdl	bdl	bdl
Al2O3	64.44	64.15	64.83	66.76	65.59	67.17
Cr2O3	0.39	0.28	0.34	0.73	0.66	0.57
Fe2O3	bdl	bdl	bdl	bdl	bdl	bdl
FeO	0.54	0.49	0.55	0.76	0.82	0.75
MnO	bdl	bdl	bdl	bdl	bdl	bdl
MgO	20.41	20.39	20.79	19.12	19.37	19.74
CaO	bdl	bdl	0.20	0.01	0.03	bdl
K2O	bdl	bdl	bdl	bdl	bdl	bdl
Na2O	bdl	bdl	bdl	bdl	bdl	bdl
Cl	bdl	bdl	bdl	bdl	bdl	bdl
F	bdl	bdl	bdl	bdl	bdl	bdl
Total	98.37	97.71	99.34	97.63	97.31	99.73
Si	1.472	1.444	1.462	1.209	1.285	1.329
Ti	-	0.012	-	-	-	-
P	-	-	-	-	-	-
Al	8.881	8.895	8.842	9.284	9.153	9.147
Cr	0.036	0.026	0.031	0.068	0.062	0.052
Fe3	-	-	-	-	-	-
Fe2	0.053	0.048	0.053	0.075	0.081	0.072
Mn	-	-	-	-	-	-
Mg	3.558	3.576	3.587	3.364	3.419	3.400
Ca	-	-	0.025	-	-	-
K	-	-	-	-	-	-
Na	-	-	-	-	-	-
Cl	-	-	-	-	-	-
F	-	-	-	-	-	-
Sum	14.000	14.001	14.000	14.000	14.000	14.000
Xmg	0.99	0.99	0.99	0.98	0.98	0.98

Tab. 4.8: Mineral chemistry of selected sapphirine samples

Scapolite, mineral composition calculated on the basis of 12(Si,Al)

Deposit	Uluguru Mts		
Mine	Visakazi Mine		
Sample	WB1_8	WB1_43	WB1_45
SiO2	47.47	45.99	46.76
TiO2	0.00	0.00	0.00
P2O5	0.00	0.00	0.00
Al2O3	26.32	26.74	27.20
Cr2O3	0.00	0.00	0.00
Fe2O3	0.00	0.00	0.00
FeO	0.00	0.00	0.00
MnO	0.00	0.00	0.00
MgO	0.00	0.00	0.00
CaO	16.27	17.53	17.20
K2O	0.25	0.17	0.18
Na2O	4.15	3.28	3.53
Cl	0.62	0.38	0.44
F	0.00	0.00	0.21
Total	95.08	94.09	95.52
Si	6.986	6.842	6.861
Ti	0.000	0.000	0.000
P	0.000	0.000	0.000
Al	4.565	4.688	4.704
Cr	0.000	0.000	0.000
Fe3	0.000	0.000	0.000
Fe2	0.000	0.000	0.000
Mn	0.000	0.000	0.000
Mg	0.000	0.000	0.000
Ca	2.565	2.794	2.704
K	0.047	0.032	0.034
Na	1.184	0.946	1.004
Cl	0.155	0.096	0.109
F	0.000	0.000	0.097
Sum	15.502	15.398	15.513
Xca	0.68	0.74	0.72

Tab. 4.9: Mineral chemistry of selected scapolite samples

Spinel, mineral composition calculated on the basis of 4(O)

Deposit	Uluguru Mts					
Mine	Mwalazi Mine			Visakazi Mine		
Sample	TZM04_57	TZM04_59	TZM04_64	WB1_30	WB6_45	WB6_51
SiO2	bdl	bdl	bdl	bdl	bdl	bdl
TiO2	bdl	bdl	bdl	bdl	bdl	bdl
Al2O3	61.93	58.51	61.33	67.08	24.51	23.68
Cr2O3	4.37	7.60	4.65	0.38	44.35	43.34
Fe2O3	bdl	bdl	bdl	bdl	bdl	bdl
FeO	5.78	6.87	6.39	1.00	8.33	11.40
MnO	0.20	bdl	bdl	bdl	bdl	bdl
MgO	19.34	17.47	18.94	26.40	13.29	10.83
ZnO	7.60	8.81	8.80	4.19	7.46	7.35
CaO	bdl	bdl	bdl	bdl	bdl	bdl
K2O	bdl	bdl	bdl	bdl	bdl	bdl
Na2O	bdl	bdl	bdl	bdl	bdl	0.34
Cl	bdl	bdl	bdl	bdl	bdl	bdl
F	bdl	bdl	bdl	bdl	bdl	bdl
Total	99.22	99.26	100.11	99.05	98.18	96.94
Si	-	-	-	-	-	-
Ti	-	-	-	-	-	-
Al	1.889	1.827	1.869	1.934	0.898	0.891
Cr	0.089	0.159	0.095	0.007	1.090	1.094
Fe3	0.021	0.014	0.036	0.020	0.006	0.035
Fe2	0.104	0.138	0.102	-	0.211	0.269
Mn	0.004	-	-	-	-	-
Mg	0.746	0.690	0.730	0.963	0.616	0.516
Zn	0.145	0.172	0.168	0.076	0.171	0.173
Ca	-	-	-	-	-	-
K	-	-	-	-	-	-
Na	-	-	-	-	-	0.021
Cl	-	-	-	-	-	-
F	-	-	-	-	-	-
Sum	2.998	3.000	3.000	3.000	2.992	2.999
Xmg	0.73	0.68	0.70	0.91	0.61	0.52

Tab. 4.10: Mineral chemistry of selected spinel samples

Tourmaline, mineral composition calculated on the basis of 24.5 (O,OH,F), B2O3 was not measured

Deposit	Uluguru Mts						Mahenge Mts		
Mine	Mwalazi Mine			Visakazi Mine			Kitwaro Mine		
Sample	TZM08_34	TZM08_78	TZM08_79	WB6_6	WB6_12	WB6_20	TZG03_27	TZG03_37	TZG03_44
SiO2	35.11	35.80	36.25	37.11	36.59	37.13	36.70	36.83	33.31
TiO2	0.82	0.97	0.74	0.97	0.89	0.36	0.55	0.59	0.52
P2O5	bdl	bdl	bdl	bdl	bdl	bdl	bdl	bdl	bdl
Al2O3	31.05	32.70	31.92	30.82	30.33	30.47	30.48	30.67	32.51
Cr2O3	2.04	0.55	2.04	0.96	1.55	2.33	1.56	1.43	1.64
V2O3	n.a.	0.15	0.17	n.a.	n.a.	n.a.	n.a.	n.a.	bdl
Fe2O3	bdl	bdl	bdl	bdl	bdl	bdl	bdl	bdl	bdl
FeO	0.63	0.66	0.53	0.18	0.21	0.24	bdl	0.19	0.21
MnO	bdl	bdl	bdl	bdl	bdl	bdl	bdl	bdl	n.a.
MgO	10.05	10.50	10.24	11.38	10.95	11.27	11.02	11.79	11.33
CaO	2.09	2.78	2.03	2.33	2.29	2.06	2.66	2.68	2.54
K2O	0.02	0.03	0.03	bdl	bdl	bdl	bdl	bdl	0.03
Na2O	1.65	2.35	2.96	1.72	1.82	1.77	1.70	1.76	2.54
Cl	n.a.	bdl	bdl	bdl	bdl	bdl	bdl	bdl	bdl
F	n.a.	bdl	bdl	0.59	0.59	0.56	0.58	0.59	0.22
Total	83.45	86.49	86.91	86.05	85.22	86.18	85.25	86.53	84.85
Si	5.807	5.725	5.788	5.959	5.948	5.971	5.959	5.906	5.474
Ti	0.102	0.116	0.089	0.117	0.109	0.044	0.067	0.071	0.064
P	-	-	-	-	-	-	-	-	-
Al	6.054	6.164	6.007	5.833	5.812	5.774	5.833	5.797	6.296
Cr	0.267	0.069	0.258	0.121	0.199	0.296	0.200	0.181	0.213
V	n.a.	0.019	0.021	n.a.	n.a.	n.a.	n.a.	n.a.	-
Fe3	-	-	-	-	-	-	-	-	-
Fe2	0.087	0.088	0.071	0.024	0.029	0.032	-	0.025	0.028
Mn	-	-	-	-	-	-	-	-	n.a.
Mg	2.478	2.504	2.437	2.723	2.654	2.702	2.668	2.819	2.777
Ca	0.370	0.476	0.347	0.401	0.399	0.355	0.463	0.460	0.448
K	0.005	0.007	0.007	-	-	-	-	-	0.006
Na	0.529	0.728	0.916	0.534	0.572	0.551	0.535	0.547	0.810
Cl	n.a.	-	-	-	-	-	-	-	-
F	n.a.	-	-	0.298	0.303	0.283	0.298	0.299	0.116
Sum	15.699	15.896	15.941	16.010	16.025	16.008	16.023	16.105	16.232

Tab. 4.11: Mineral chemistry of selected tourmaline samples

White Mica, mineral composition calculated on the basis of 11(O,OH)

Deposit	Uluguru Mts					
Mine	Mwalazi Mine			Visakazi Mine		
Sample	TZM08_62	TZM08_77	TZM08_86	WB6_18	WB6_38	WB6_59
SiO2	44.98	46.11	44.97	30.30	48.33	48.93
TiO2	0.09	0.15	0.17	bdl	0.33	0.25
Al2O3	40.29	40.07	39.80	49.59	37.62	38.33
Cr2O3	0.81	0.58	0.74	0.63	bdl	bdl
V2O3	0.17	0.08	bdl	n.a.	n.a.	n.a.
Fe2O3	bdl	bdl	bdl	bdl	bdl	bdl
FeO	0.08	0.03	bdl	bdl	bdl	0.12
MnO	n.a.	n.a.	bdl	bdl	bdl	bdl
MgO	0.71	0.33	1.09	0.58	0.55	0.32
CaO	0.54	0.41	0.46	11.73	1.63	1.28
K2O	1.69	1.32	0.72	bdl	2.45	2.54
Na2O	6.09	5.98	6.06	1.06	3.30	1.49
Cl	bdl	bdl	bdl	bdl	bdl	bdl
F	bdl	bdl	bdl	bdl	bdl	bdl
Total	95.45	95.09	94.03	93.89	94.19	93.26
Si	2.891	2.954	2.912	2.039	3.109	3.147
Ti	0.004	0.007	0.008	-	0.016	0.012
Al	3.051	3.025	3.038	3.933	2.853	2.906
Cr	0.041	0.029	0.038	0.034	-	-
V	0.009	0.004	-			
Fe3	-	-	-	-	-	-
Fe2	0.004	0.002	-	-	-	0.006
Mn	n.a.	n.a.	-	-	-	-
Mg	0.068	0.032	0.106	0.058	0.053	0.031
Ca	0.037	0.028	0.032	0.846	0.112	0.088
K	0.139	0.108	0.059	-	0.201	0.208
Na	0.758	0.743	0.761	0.138	0.411	0.186
Cl	-	-	-	-	-	-
F	-	-	-	-	-	-
Sum	7.002	6.934	6.961	7.048	6.755	6.584
Xk	0.15	0.12	0.07	-	0.28	0.43
Xna	0.81	0.85	0.89	0.14	0.57	0.39
Xca	0.04	0.03	0.04	0.86	0.15	0.18

Tab. 4.12: Mineral chemistry of selected white mica samples

4.3.1 Uluguru Mts

4.3.1.1 Mwalazi Mine

Sample TZM04 is characterised by a mineral assemblage of phlogopite-amphibole-calcite/dolomite-corundum-plagioclase-chlorite +/-apatite, rutile. The texture is heterogranular granoblastic where euhedral grains of corundum, phlogopite and apatite

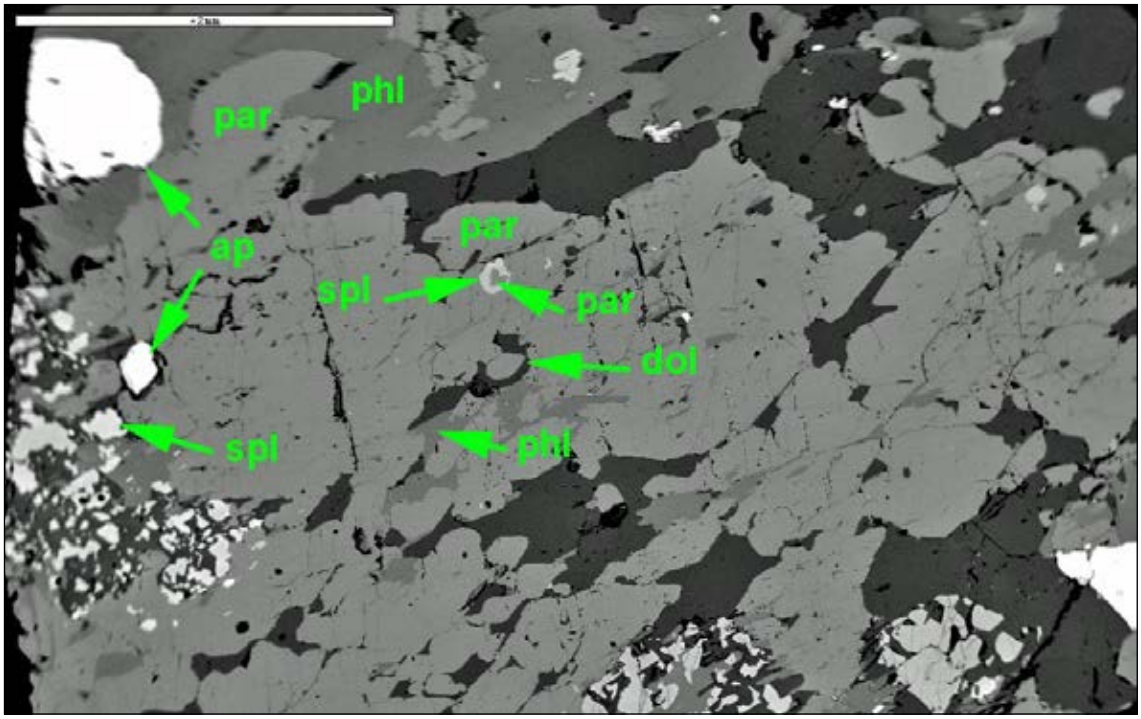

Fig. 4.6: It can be observed that pargasite and spinel are replacing each other in sample TZM04. A pargasite grain is encapsulated by spinel in the middle of the upper half of the picture. On the other hand there is spinel grains found in pargasite on the far left as well as towards the bottom side of the BSE picture displayed.

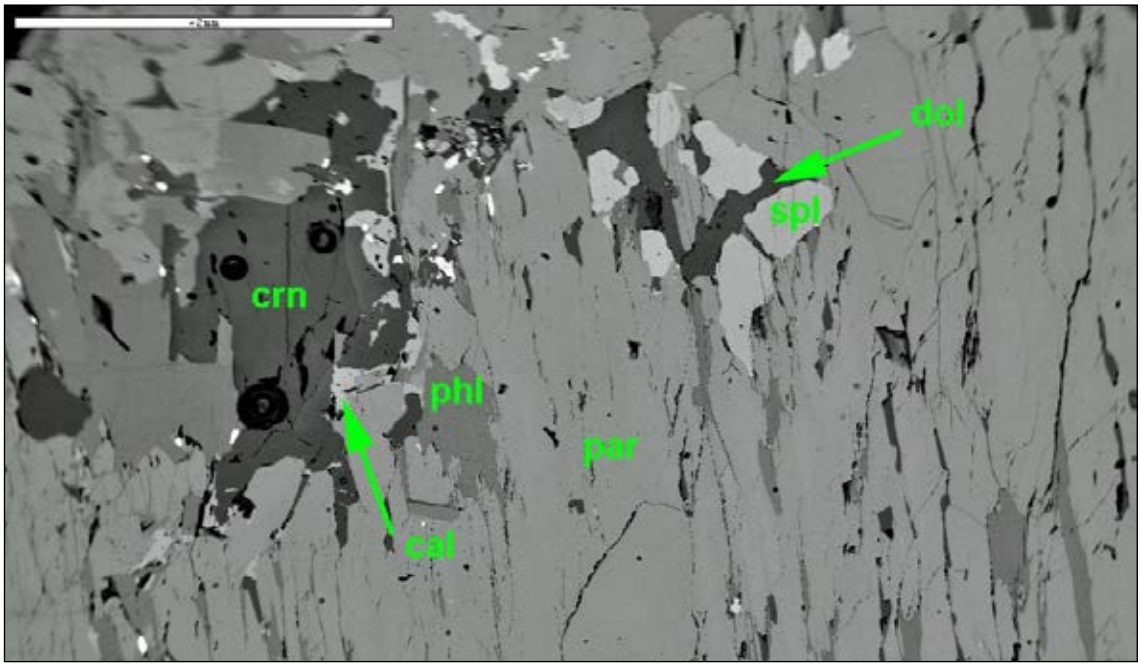

Fig. 4.7: Spinel and corundum occur close to each other in this BSE image. Together with corundum and spinel there is also calcite and dolomite associated. Aditionally, if pargasite is taken into account a similar assemblage as described in Fig. 4.6 can be observed.

can be found in a fine grained matrix of calcite/dolomite, phlogopite, apatite, and plagioclase crystals. Corundum is present as porphyroblastic grains. In apatite and corundum a poikiloblastic texture can be found where inclusions are common. Except in the rim of the examined mineralised nodule where a thick layer of phlogopite is present no structural features are preserved due to strong re-crystallisation. The average grain size is between 5-10mm where as corunudm porphyroblasts measure 1-5mm in diameter (Appendix A.2).

Reactions between pargasite, dolomite, corundum and spinel can be observed. As seen in Fig. 4.6, spinel is replacing pargasite as well as being encapsulated by spinel. However the reaction where corundum, and pargasite replace spinel seems to be more common in sample TZM04. Further, there is also dolomite, corundum, calcite and spinel found to be stable next to each other (Fig. 4.7). Combined with pargasite a similar assemblage as described for Fig. 4.6 with pargasite, corundum, and dolomite can be observed.

	TZM04_58	TZM04_61	TZM04_64	TZM04_77	TZM04_81	TZM04_78
Mineral	dolomite	calcite	spinel	phlogopite	pargasite	Al-pargasite
SiO2	bdl	bdl	bdl	39.22	41.50	41.67
TiO2	bdl	bdl	bdl	0.97	1.06	1.13
P2O5	bdl	bdl	bdl	bdl	bdl	bdl
Al2O3	bdl	bdl	61.33	17.72	17.81	18.19
Cr2O3	bdl	bdl	4.65	0.31	0.56	0.55
Fe2O3	bdl	bdl	bdl	bdl	bdl	bdl
FeO	0.84	bdl	6.39	1.7	1.89	1.86
MnO	bdl	bdl	bdl	bdl	bdl	bdl
MgO	20.67	1.63	18.94	24.52	16.57	16.46
ZnO	bdl	bdl	8.80	bdl	bdl	bdl
CaO	32.09	55.02	bdl	0.15	13.21	13.51
K2O	bdl	bdl	bdl	9.94	1.14	1.24
Na2O	bdl	bdl	bdl	0.39	1.86	1.85
Cl	bdl	bdl	bdl	bdl	bdl	bdl
F	bdl	bdl	bdl	1.00	0.60	0.53
Total	53.60	56.65	100.11	95.92	96.20	96.99
Si	-	-	-	2.758	5.906	5.849
Ti	-	-	-	0.051	0.113	0.119
P	-	-	-	-	-	-
Al	-	-	1.869	1.468	2.987	3.009
Cr	-	-	0.095	0.017	0.063	0.061
Fe3	-	-	0.036	-	0.543	0.802
Fe2	0.021	-	0.102	0.100	-	-
Mn	-	-	-	-	-	-
Mg	0.935	0.040	0.730	2.570	3.515	3.444
Zn	-	-	0.168	-	-	-
Ca	1.043	0.960	-	0.011	2.014	2.032
K	-	-	-	0.892	0.207	0.222
Na	-	-	-	0.053	0.513	0.503
Cl	-	-	-	-	-	-
F	-	-	-	0.222	0.270	0.235
Sum	1.999	1.000	3.000	8.142	16.131	16.276
Xmg			0.70	0.96		

Tab. 4.13: Mineral chemistry for selected minerals as measured for sample TZM04.

The chemical composition of selected minerals is given in Tab. 4.13. The carbonate phases dolomite and calcite occur as nearly pure endmembers. Dolomite however contains low amounts of FeO (0.84wt%). Calcite on the other hand has with 1.63wt% MgO a small dolomite component but no FeO was measured. Spinel on the other hand showed a X_{Mg} value of 0.70 in combination with a high ZnO value of 8.80wt% as well as 4.65wt% Cr_2O_3. This indicates considerable component of chromite and gahnite for this particular spinel. The analysed mica is with a X_{Mg} 0.96 close in composition to a pure phlogopite endmember. With the content of 1wt% this phlogopite is rather rich in F however. The measured amphibole phases were identified as pargasite and Al-pargasite with contents of volatile components of about 0.5wt%.

In sample TZM08 the mineral paragenesis consists of calcite/dolomite-corundum-phlogopite-white mica-amphibole. Rutile, spinel, tourmaline, plagioclase, chlorite as well as sulphide ore minerals are contained as accessories. Plagioclase, apatite, and calcite/dolomite are present together with corundum as euhedral crystals in the core of the mineralised zone. Corundum itself shows a porphyroblastic texture where two generations can be recognised based on textural evidence. An early generation shows more angular bulky crystals which are often fractured. A second generation is characterised by smaller more granular almost round crystals which mostly look intact. They often occur also as small aggregates of several roundish crystals resembling a bunch of grapes. Poikiloblastic texture is observed in apatite and corundum grains due to inclusions again. Phlogopite is present in a granoblastic texture throughout the sample. In connection with corundum phlogopite often shows a lepidoblastic texture however. The carbonate phases calcite and dolomite are found in a saccharoidal texture in the matrix and as large euhedral crystals elsewhere. Structural information was not preserved due to high degree of recrystallisation. Average grain size is between 2-5mm whereas corundum granoblasts may reach a bit larger dimensions and matrix minerals sometime smaller than 1mm (Appendix A.2).

In Fig. 4.8 a partial replacement of corundum by spinel can be observed. Further there are two corundum generations distinguishable due to textural differences. Be-

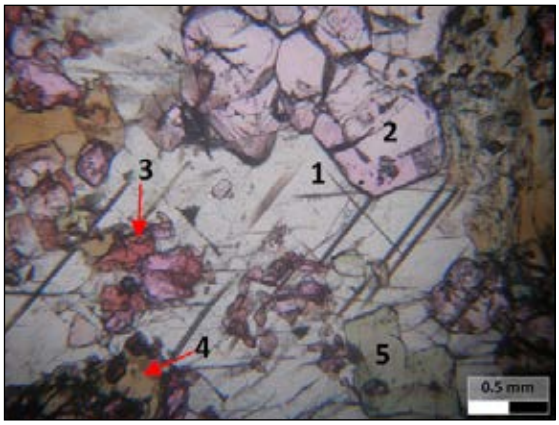

Fig. 4.8: This microphotograph had been taken in unpolarised light. The several minerals visible are 1) a carbonate phase, 2) corundum, 1st generation, 3) corundum, 2nd generation with partial replacement by spinel, 4) phlogopite, and 5) was described as amphibole however wasn't confirmed by EPMA or SEM coupled WD-XRF.

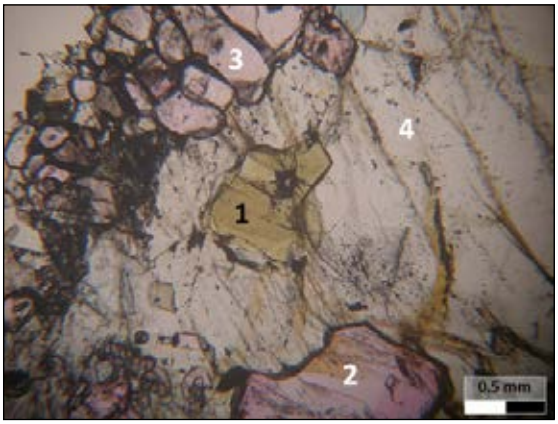

Fig. 4.9: Two texturally different corundum generations (2&3) as well as a tourmaline (1) crystals in the center of this unpolarised microphotograph are visible. The matrix consists of a carbonate phase (4) in this part of the examined thick section.

side 2nd generation corundum there was tourmaline recognised as a late phase in sample TZM08 as well (Fig. 4.9).

The BSE image Fig. 4.10 displays a greenish white mica which was observed throughout sample TZM08. Surprisingly, this mineral proofed not to be chromian muscovite (fuchsite) but to be of paragonite composition. Also two corundum generations are clearly visible in Fig. 4.10 which are usually in close relastionship with Paragonite. Further, chlorite is partially replacing phlogopite during a late stage metamorphic overprint.

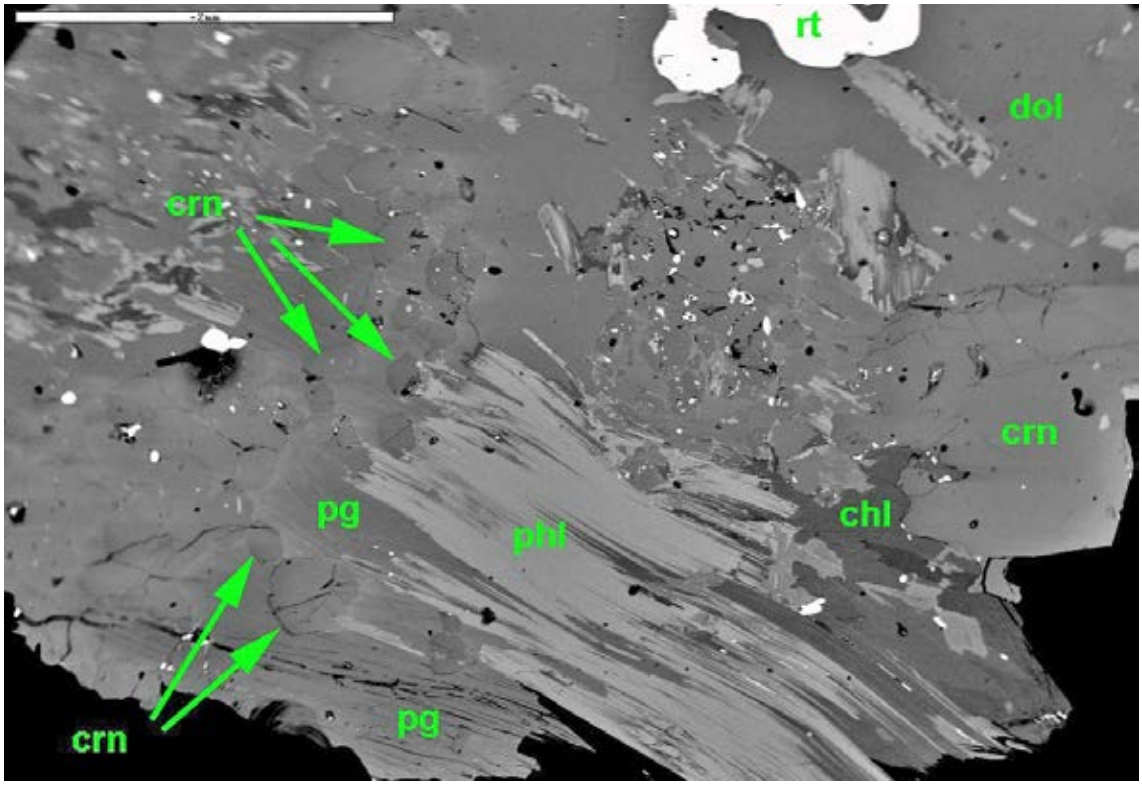

Fig. 4.10: In this BSE image mainly the occurrence of paragonite, corundum, and dolomite are of importance. Then it is also interesting to see that there are two corundum generations preserved. A first one with the large crystal to the right as well as a second generation with smaller, rounded crystals to the left of the image. Finally, chlorite represents a late overprint in this assemblage.

Dolomite is the only carbonate phase found in this sample. Plagioclase has a composition of An_{40} which corresponds to andesine. Euhedral spinel was identified by qualitative EDX analysis only. Phlogopite shows a high X_{Mg} value of 0.94 and a rather low F-content was below detection limit of <0.2 wt%. Paragonite contains about 1.5wt% K_2O which corresponds to a considerable muscovite component of 15 mol%. The composition of the tourmaline measured in this sample has a signature which indicates mainly a dravite and uvite component as well as a subordinate schorl component due to small amounts of FeO. Because B_2O_3 could not be measured by the instruments applied in this study further calculations regarding the mineral chemistry of tourmaline was not carried out (Tab. 4.14).

Mineral	TZM08_85 dolomite	TZM08_41 plagioclase	TZM08_83 phlogopite	TZM08_62 paragonite	TZM08_52 chlorite	TZM08_79 tourmaline
SiO2	bdl	56.78	38.14	44.98	27.30	36.25
TiO2	bdl	bdl	1.29	0.09	bdl	0.74
P2O5	bdl	bdl	bdl	bdl	bdl	bdl
Al2O3	bdl	25.72	20.12	40.29	23.58	31.92
Cr2O3	bdl	bdl	1.28	0.81	1.88	2.04
V2O3	bdl	n.a.	bdl	0.17	0.13	0.17
Fe2O3	bdl	bdl	bdl	bdl	bdl	bdl
FeO	1.12	bdl	2.36	0.08	3.21	0.53
MnO	bdl	bdl	bdl	n.a.	n.a.	n.a.
MgO	19.93	bdl	20.15	0.71	28.76	10.24
CaO	30.74	8.01	0.12	0.54	bdl	2.03
K2O	bdl	0.04	9.79	1.69	bdl	0.03
Na2O	bdl	6.59	0.59	6.09	bdl	2.96
Cl	bdl	n.a.	bdl	bdl	bdl	bdl
F	bdl	n.a.	bdl	bdl	bdl	bdl
Total	51.79	97.13	93.94	95.45	84.92	86.91
Si	-	2.610	2.720	2.891	2.649	5.788
Ti	-	-	0.069	0.004	-	0.089
P	-	-	-	-	-	-
Al	-	1.393	1.691	3.051	2.696	6.007
Cr	-	-	0.072	0.041	0.144	0.258
V	-	n.a.	-	0.009	0.010	0.021
Fe3	-	-	-	-	-	-
Fe2	0.029	-	0.141	0.004	0.260	0.071
Mn	-	-	-	n.a.	n.a.	n.a.
Mg	0.935	-	2.142	0.068	4.160	2.437
Ca	1.036	0.394	0.009	0.037	0.001	0.347
K	-	0.002	0.891	0.139	0.001	0.007
Na	-	0.587	0.082	0.758	0.003	0.916
Cl	-	n.a.	-	-	0.001	-
F	-	n.a.	-	-	-	-
Sum	2.000	4.986	7.817	7.002	94.845	15.941
Xmg			0.94		0.94	
Xk				0.15		
Xna				0.85		
Xan		0.40				
Xor		0.00				

Tab. 4.14: Mineral chemistry for selected minerals as measured for sample TZM08.

4.3.1.2 Visakazi II Mine

In thin section WB6 the mineral assemblage is phlogopite-amphibole-corundum-plagioclase-calcite/dolomite-sulphides. As accessories apatite, tourmaline, white mica, and chlorite were identified. In general a heterogranular granoblastic texture developed in sample WB6 where grains of plagioclase, apatite, calcite/dolomite, corundum, white mica, tourmaline as well as ore minerals are found. Corunudm and ap atite occur as porphyroblastic grains with often poikiloblastic texture due to inclusions. A polygonal, mosaic texture is found where amphibole, corundum and phlogopite or phlogopite, calcite/dolomite, and amphibole grains form triple junctions. A vermicular

texture of symplectitic growth of phlogopite and corundum completes the textures recorded in sample WB6. The sulphide ore minerals were identified by ore microscopy in reflectance light mode to be mainly pyrite with small amounts of pyrrhotite and chalcopyrite. Spinel was identified as inclusions in corundum. No structural information is preserved due to high degree of re-crystallisation. The grain sizes found are between 1-7mm whereas the bigger crystals occur among corundum. The matrix shows typical grain sizes of 1-3mm (Appendix A.2).

As a reaction in WB6 the symplectitic growth of phlogopite and corundum can be observed (Fig. 4.11). This event marks a rapid and drastic change in conditions which forced an instant crystal growth due to the changing conditions. Another replacement reaction is visible where white mica is growing at the expense of corunudm and phlogopite (Fig. 4.12). A third reaction in WB6 is the replacement of corundum by margarite (Fig. 4.13). In some places phlogopite and anorthite is replaced by corundum, dolomite, and paragonite.

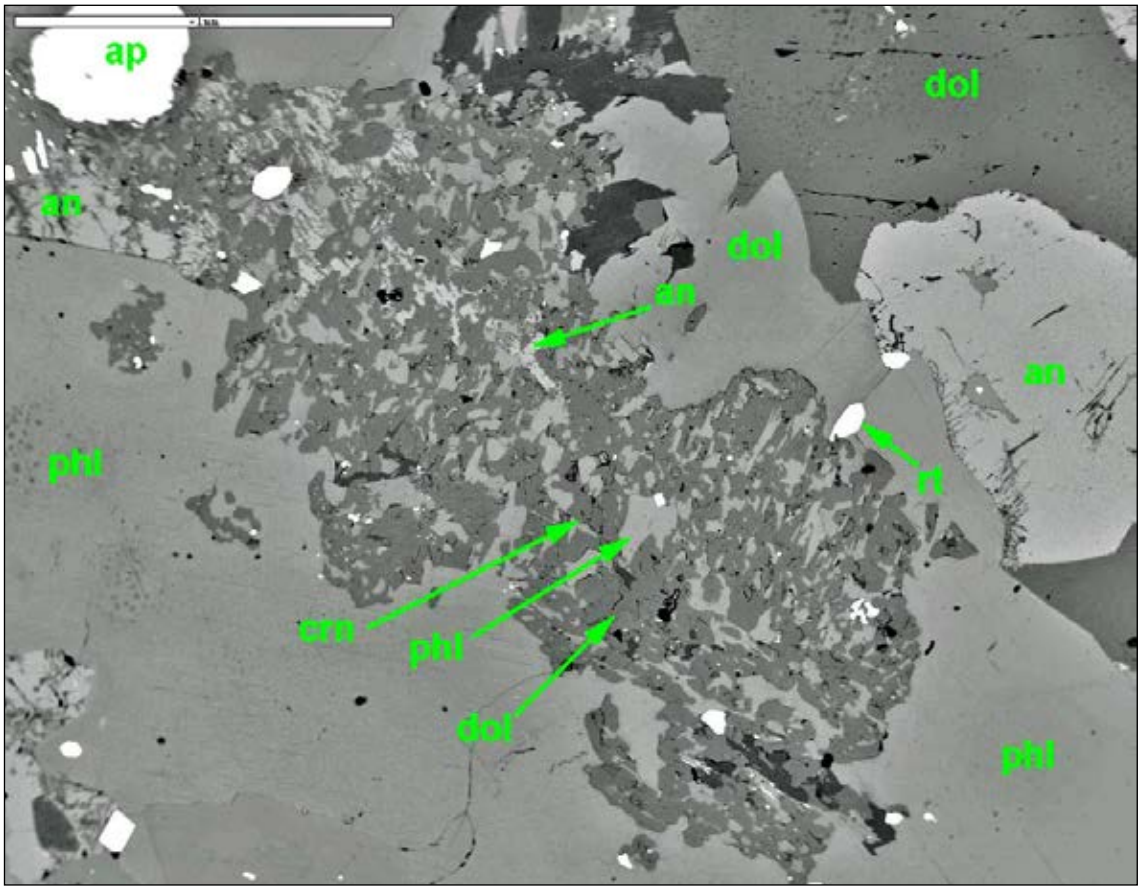

Fig. 4.11: As a main reaction a symplectitic replacement of dolomite by phlogopite, and corundum is visible in the middle of this BSE image.

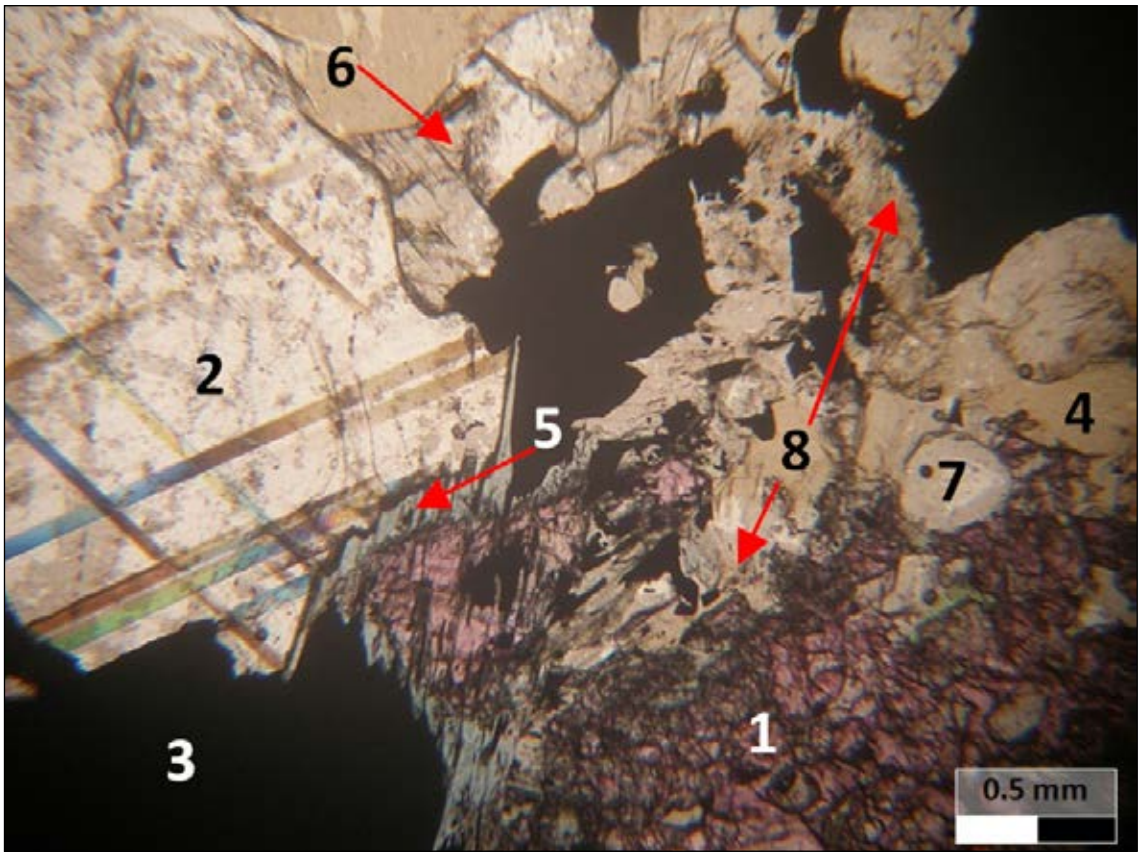

Fig. 4.12: In this microphotograph taken under crossed polarisers 1st generation corundum (1) is visible which is partially replaced by white mica (5). Additionally there is a carbonate phase (2), sulphide ore minerals (3), phlogopite (4), apatite (6) and chlorite (8) as well as staining (6) observed in this thick section.

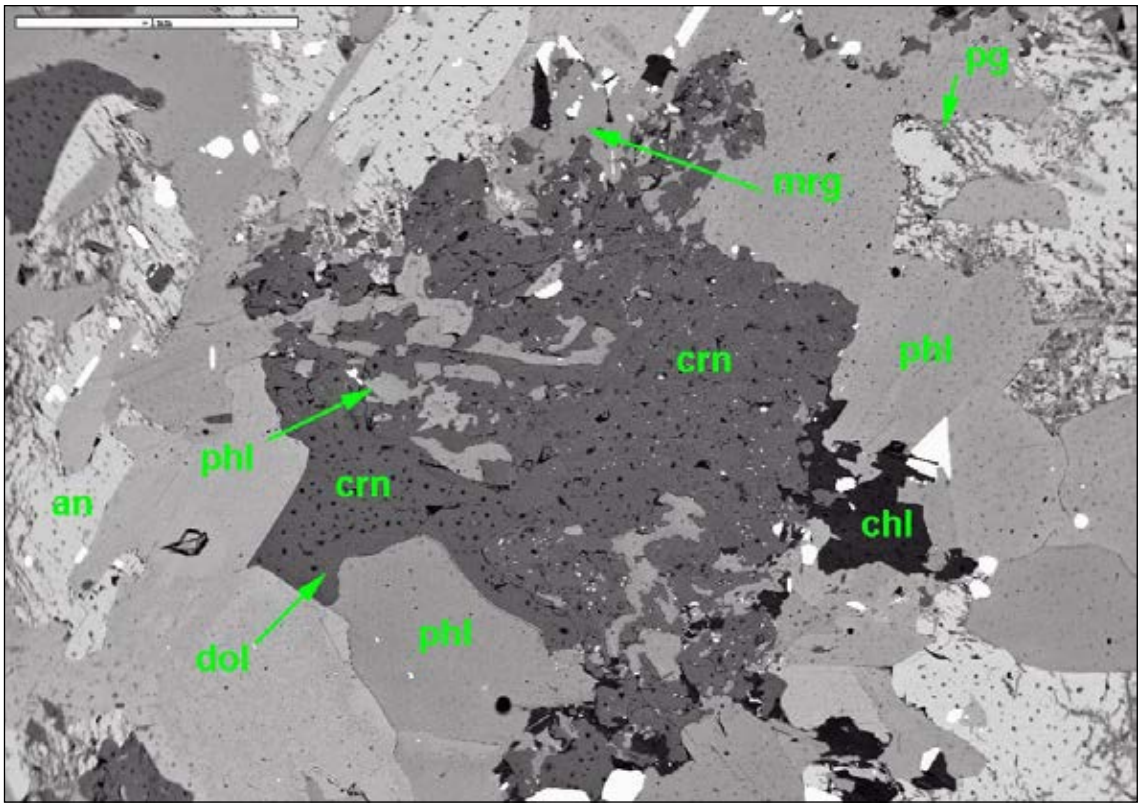

Fig. 4.13: In a second BSE image of the same sample there was the replacement of corundum by margarite and anorthite by paragonite documented. There is further a reaction rim of dolomite around corundum to be noted.

Mineral chemical data are summarised in Tab. 4.4. The carbonate phase was indentified as dolomite with a small siderite component only. Plagioclase is almost pure anorthite endmember measured as An_{96}. Due to the very high Cr_2O_3 content a spinel inclusion in corundum proofed to be of chromite composition with a X_{Mg} 0.52 and a high ZnO content of 7.35wt% (gahnite component). The analysed amphibole shows Al-pargasite composition with elevated F-content of 1.08wt%. Two different white micas are present: margarite with X_{Ca} 0.86 and a paragonite component of 14mol%. Paragonite grains were found as well which have a X_{Na} of 0.79. For the two white micas F and Cl were not analysed. Phl again is present as almost a pure Mg endmember with X_{Mg} 0.99 but elevated F-contents of more than 1.5wt%. Tourmaline was measured in this sample as well however B_2O_3 content could not be analysed with the instruments applied in this study. Mainly a mineral composition dominated by uvite and dravite endmembers was found. Small amounts of FeO further indicate the presence of a sub-ordinate schorl component (Tab.4.15).

	WB6_53	WB6_4	WB6_51	WB6_8	WB6_38	WB6_18	WB6_25	WB6_16	WB6_20
Mineral	dolomite	plagioclase	spinel	phlogopite	paragonite	margarite	Al-pargasite	chlorite	tourmaline
SiO2	bdl	44.79	bdl	39.83	48.33	30.30	43.01	29.11	37.13
TiO2	bdl	bdl	bdl	1.24	0.33	bdl	1.01	bdl	0.36
P2O5	bdl	bdl	bdl	bdl	bdl	bdl	bdl	bdl	bdl
Al2O3	bdl	35.41	23.68	17.89	37.62	49.59	18.40	21.40	30.47
Cr2O3	bdl	bdl	43.34	0.50	bdl	0.63	0.54	1.12	2.33
Fe2O3	bdl	bdl	bdl	bdl	bdl	bdl	bdl	bdl	bdl
FeO	0.30	bdl	11.40	0.48	bdl	bdl	0.61	0.84	0.24
MnO	bdl	bdl	bdl	bdl	bdl	bdl	bdl	bdl	bdl
MgO	21.20	bdl	10.83	24.39	0.55	0.58	17.68	31.51	11.27
ZnO	bdl	bdl	7.35	bdl	bdl	bdl	bdl	bdl	bdl
CaO	32.42	18.83	bdl	0.11	1.63	11.73	12.27	bdl	2.06
K2O	bdl	bdl	bdl	9.32	2.45	bdl	1.25	bdl	bdl
Na2O	bdl	0.44	0.34	0.77	3.30	1.06	2.39	bdl	1.77
Cl	bdl	bdl	bdl	bdl	bdl	bdl	bdl	bdl	bdl
F	bdl	bdl	bdl	1.54	bdl	bdl	1.08	0.24	0.56
Total	53.92	99.47	96.94	96.15	94.19	93.89	98.38	84.22	86.18
Si	-	2.074	-	2.785	3.109	2.039	6.033	2.810	5.971
Ti	-	-	-	0.065	0.016	-	0.106	-	0.044
P	-	-	-	-	-	-	-	-	-
Al	-	1.932	0.891	1.474	2.853	3.933	3.042	2.434	5.774
Cr	-	-	1.094	0.027	-	0.034	0.060	0.086	0.296
Fe3	-	-	0.035	-	-	-	0.036	-	-
Fe2	0.008	-	0.269	0.028	-	-	0.036	0.067	0.032
Mn	-	-	-	-	-	-	-	-	-
Mg	0.949	-	0.516	2.543	0.053	0.058	3.697	4.533	2.702
Zn	-	-	0.173	-	-	-	-	-	-
Ca	1.043	0.934	-	0.008	0.112	0.846	1.845	-	0.355
K	-	-	-	0.832	0.201	-	0.224	-	-
Na	-	0.039	0.021	0.104	0.411	0.138	0.650	-	0.551
Cl	-	-	-	-	-	-	bdl	-	-
F	-	-	-	0.340	-	-	0.481	0.073	0.283
Sum	2.000	4.979	2.999	8.206	6.755	7.048	16.210	10.003	16.008
Xmg			0.52	0.99				0.99	
Xan		0.96							
Xca					0.21	0.86			
Xna					0.79	0.14			

Tab. 4.15: Mineral chemistry for selected minerals as measured for sample WB6.

In sample WB1 the mineral assemblage is characterised by calcite/dolomite-phlogopite-amphibole-plagiclase-scapolite-corundum-spinel +/- apatite, chlorite, sulphide ore minerals. The main phases however were calcite/dolomite and phlogopite. A vermicular texture was recorded where corundum was overgrown by scapolite. Corundum forms as porphyroblastic grains with poikiloblastic texture due to numerous inclusions. Phlogopite and white mica occur usually within foliation planes. Phlogopite mostly in lepidoblastic texture and in close contact with Corundum. Sulphide ore minerals had been identified by ore microscopy as mainly pyrite as well as small contents of pyrrhotite and chalcopyrite. The degree of re-crystallisation is high resulting in grain sizes between 1 and 5mm in average (Appendix A.2).

Spinel inclusions in corundum indicated a former assemblage of calcite and spinel which is replaced now by dolomite and corundum (Fig. 4.14). A next reaction seen in the same figure is a symplectitic growth of corundum and scapolite. Fig. 4.14 also shows that there are two corundum generation present. Large porphyroblastic grains represent the 1st generation whereas the 2nd generation is present only within the symplectitic overgrowth. Further, there are also small remnants of pargasite in scapolite and dolomite (Fig. 4.14). The same reaction texture is seen in Fig. 4.15 where pargasite is surrounded by a reaction rim of scapolite followed by dolomite.

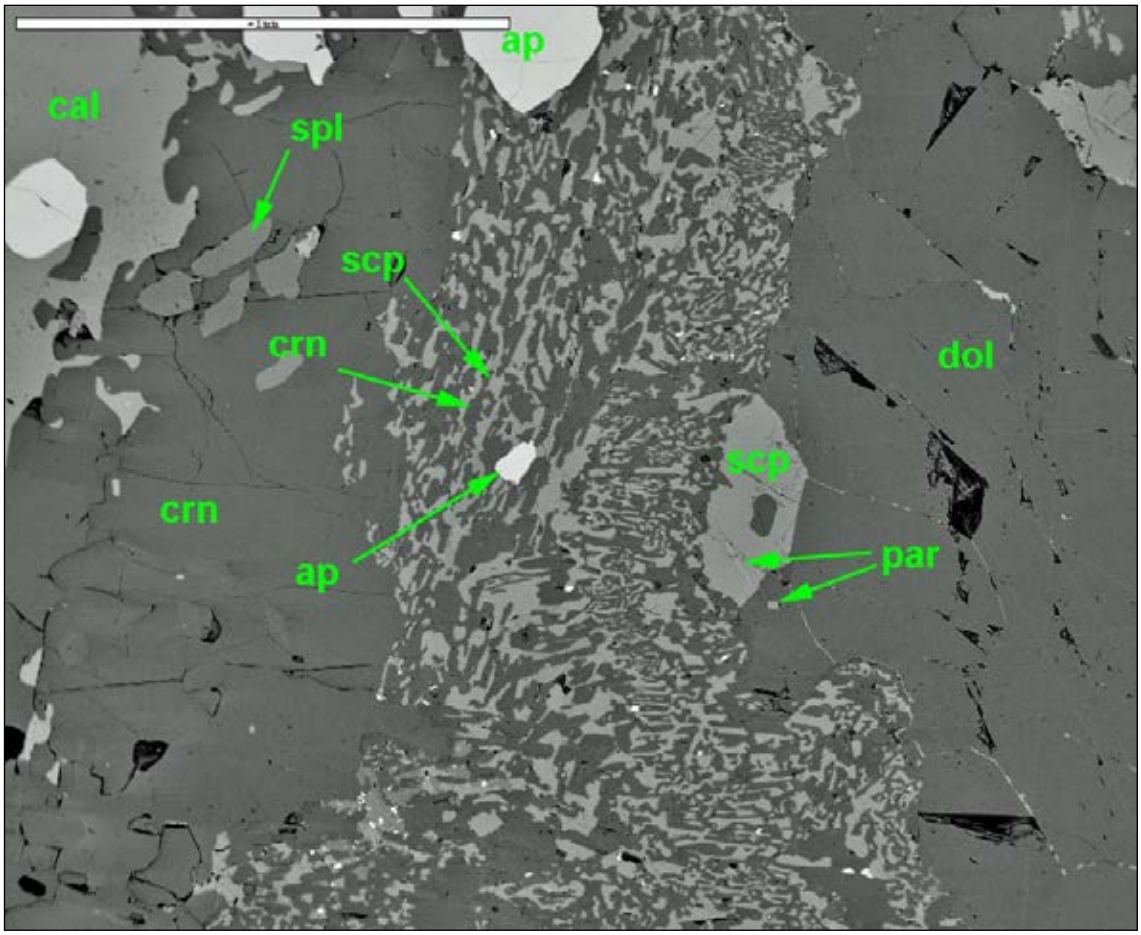

Fig. 4.14: Spinel as an inclusion in corundum represents a former assemblage in connection with calcite. A symplectitic overgrowth of scapolite and corundum indicates rapid change in conditions.

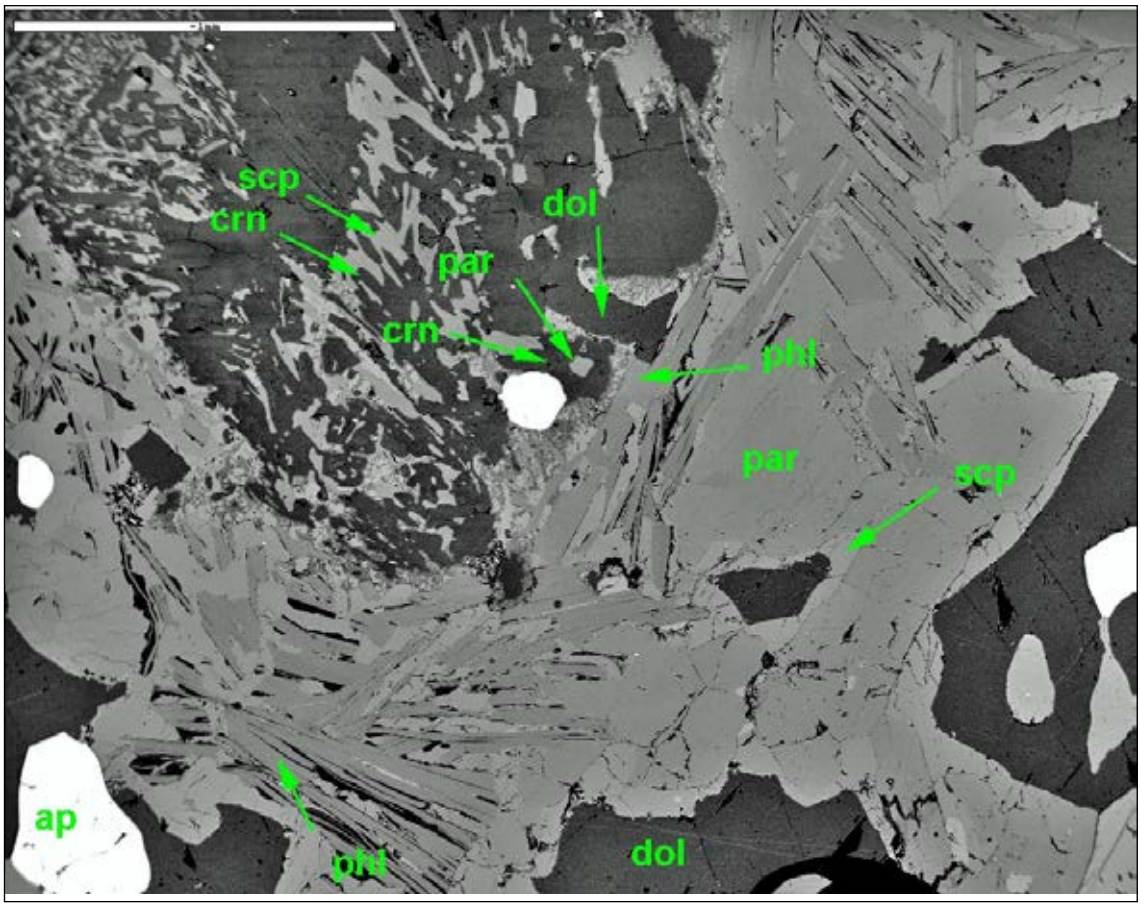

Fig. 4.15: In this BSE image a reaction rim of scapolite and dolomite around pargasite is most prominent. Further, there is symplectitic overgrowth by scapolite and corundum documented.

Tab. 4.16 displays a summary of selected minerals analysed in sample WB1. Carbonate phases were nearly pure and only a small dolomite component for calcite was measured. Plagioclase showed a high An-content with a value of An_{94}. Spinel on the other hand, had an FeO content of 1wt% and containing high values for ZnO of 4.19wt% which indicates a certain gahnite component to be present in the analysed spinel. Cr_2O_3 content with less then 0.5wt% was unusually low however. Scapolite was found to be Ca-rich. As a volatile component Cl was measured and the total composition corresponds to a value of $X_{Meionite}$ 0.74. The amphibole phase present in WB1 was identified as Al-pargasite and was with 1.35wt% high in F-content. Phlogopite is again almost a pure Mg endmember with X_{Mg} 0.99 but high in F-content with almost 2wt% (Tab. 4.16).

Mineral	WB1_9 dolomite	WB1_26 calcite	WB1_17 plagioclase	WB1_30 spinel	WB1_43 scapolite	WB1_22 phlogopite	WB1_11 Al-pargasite	WB1_36 chlorite
SiO2	bdl	bdl	45.75	bdl	45.99	40.79	44.55	27.36
TiO2	bdl	bdl	bdl	bdl	bdl	1.46	0.63	bdl
P2O5	bdl	bdl	bdl	bdl	bdl	bdl	bdl	bdl
Al2O3	bdl	bdl	34.86	67.08	26.74	16.00	17.83	27.55
Cr2O3	bdl	bdl	bdl	0.38	bdl	bdl	bdl	bdl
Fe2O3	bdl	bdl	bdl	bdl	bdl	bdl	bdl	bdl
FeO	bdl	bdl	bdl	1.00	bdl	0.37	0.26	1.15
MnO	bdl	bdl	bdl	bdl	bdl	bdl	bdl	bdl
MgO	20.88	2.26	bdl	26.40	bdl	25.17	18.50	27.45
ZnO	bdl	bdl	bdl	4.19	bdl	bdl	bdl	bdl
CaO	30.60	51.51	18.50	bdl	17.53	bdl	12.33	bdl
K2O	bdl	bdl	bdl	bdl	0.17	10.37	1.10	bdl
Na2O	bdl	bdl	0.66	bdl	3.28	0.25	2.38	bdl
Cl	bdl	bdl	bdl	bdl	0.38	bdl	bdl	bdl
F	bdl	bdl	bdl	bdl	bdl	1.97	1.35	0.46
Total	51.48	53.77	99.77	99.05	94.09	96.69	98.93	84.16
Si	-	-	2.108	-	6.842	2.856	6.186	2.634
Ti	-	-	-	-	-	0.077	0.066	-
P	-	-	-	-	-	-	-	-
Al	-	-	1.893	1.934	4.688	1.320	2.918	3.126
Cr	-	-	-	0.007	-	-	-	-
Fe3	-	-	-	0.020	-	-	0.015	-
Fe2	-	-	-	-	-	0.022	0.015	0.093
Mn	-	-	-	-	-	-	-	-
Mg	0.974	0.058	-	0.963	-	2.627	3.830	3.940
Zn	-	-	-	0.076	-	-	-	-
Ca	1.026	0.942	0.913	-	2.794	-	1.834	-
K	-	-	-	-	0.032	0.926	0.195	-
Na	-	-	0.059	-	0.946	0.034	0.641	-
Cl	-	-	-	-	0.096	-	-	-
F	-	-	-	-	-	0.436	0.593	0.140
Sum	2.000	1.000	4.973	3.000	15.398	8.298	16.293	9.933
Xmg				0.91		0.99		
Xan			0.94					
Xmeionite					0.74			

Tab. 4.16: Mineral chemistry for selected minerals as measured for sample WB1.

4.3.2 Mahenge Mts

4.3.2.1 Kitwaro Mine

The mineral assemblage in sample TZG03 is phlogopite-calcite/dolomite-amphibole-plagioclase-corundum-sapphirine including accessory minerals rutile, chlorite, and tourmaline. A granoblastic texture is dominant in sample TZG03 where grains of amphibole, plagioclase, apatite, sapphirine, corundum and phlogopite are most common. Corundum and sapphirine occur as porphyroblastic grains whereas sapphirine and apatite are poikiloblastic. Grain sizes range from 1-5mm with porphroblasts of about 1-3mm in size. (Appendix A.2).

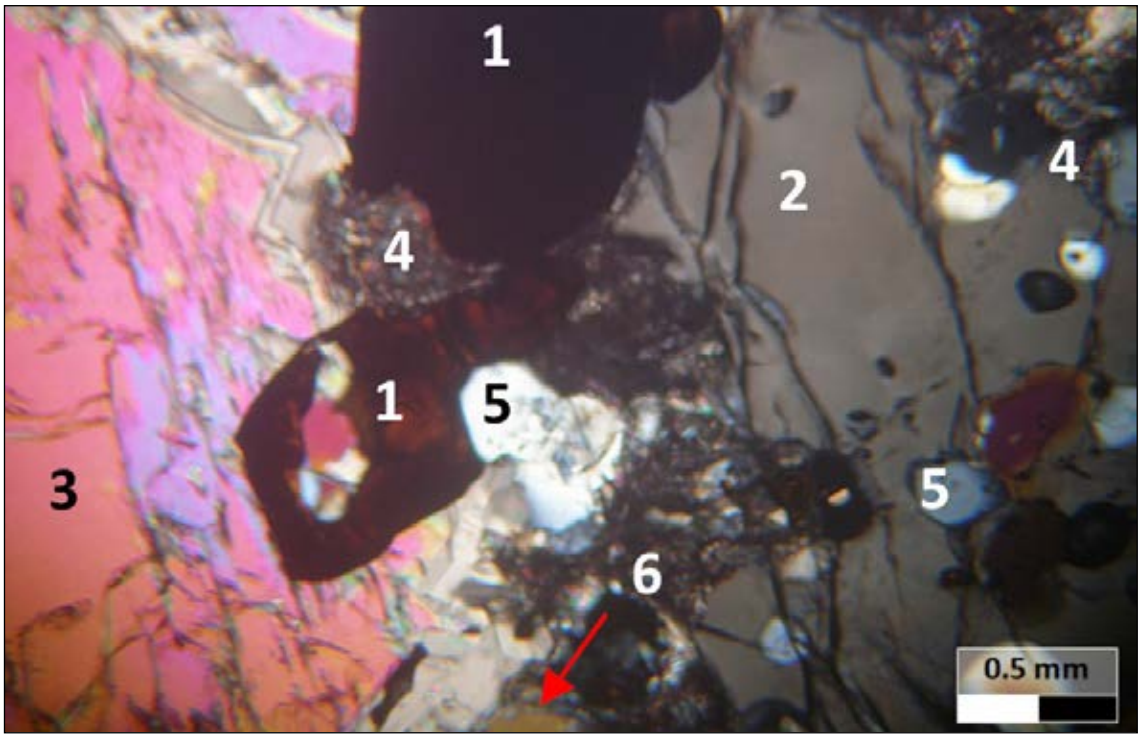

Fig. 4.16: Sapphirine (2) appears as a large grey crystal on the right of the microphotograph which was taken under crossed polarisers. A symplectitic overgrowth (4) can be recognised to the left of the sapphirine crystal. Apatite (5) and rutile (1) are accessory minerals being present in this sample. To the left there is a large amphibole (3) crystal to be seen whereas the very tip of a phlogopite (6) crytstal is captured on the bottom end of this picture.

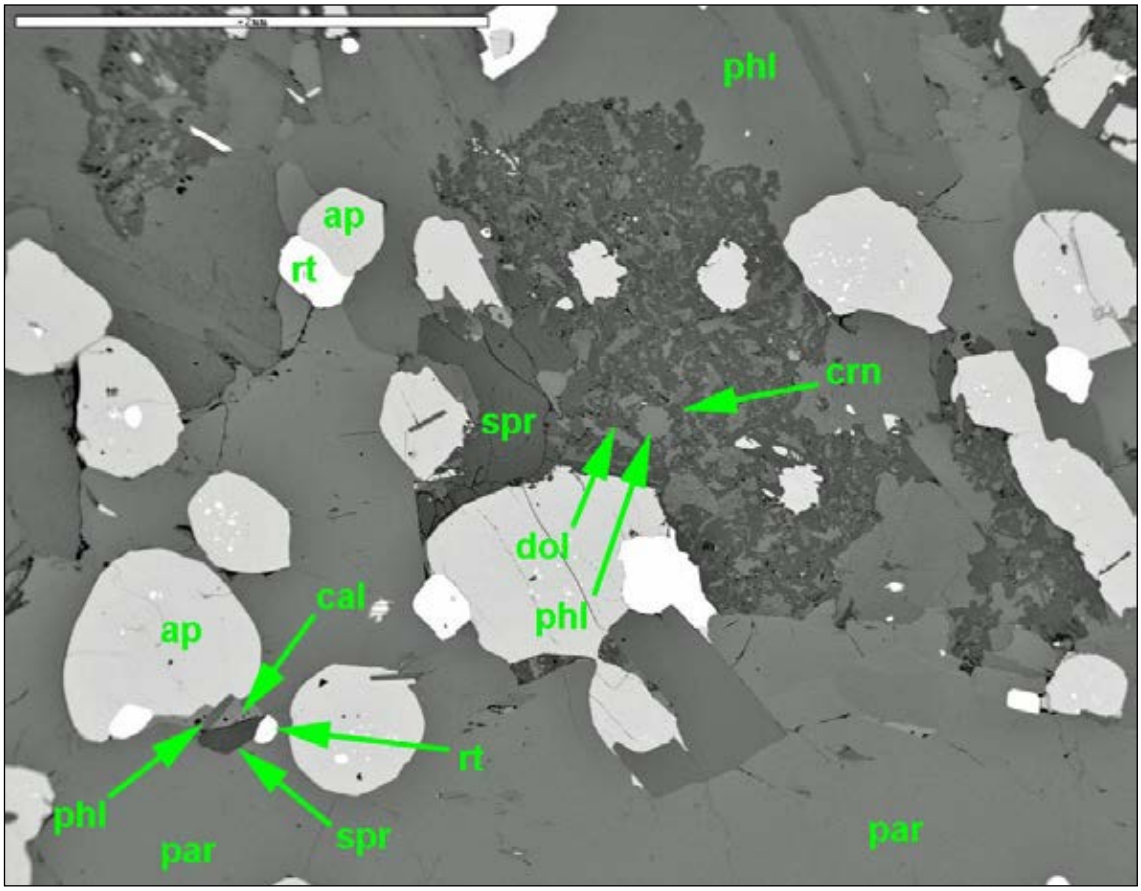

Fig. 4.17: In this BSE image two separate mineral assemblages can be observed. In the lower left corner there is sapphirine with calcite still intact surrounded by pargasite. In the center of the picture then there is corundum and dolomite observed to replace sapphirine in symplectitic reaction.

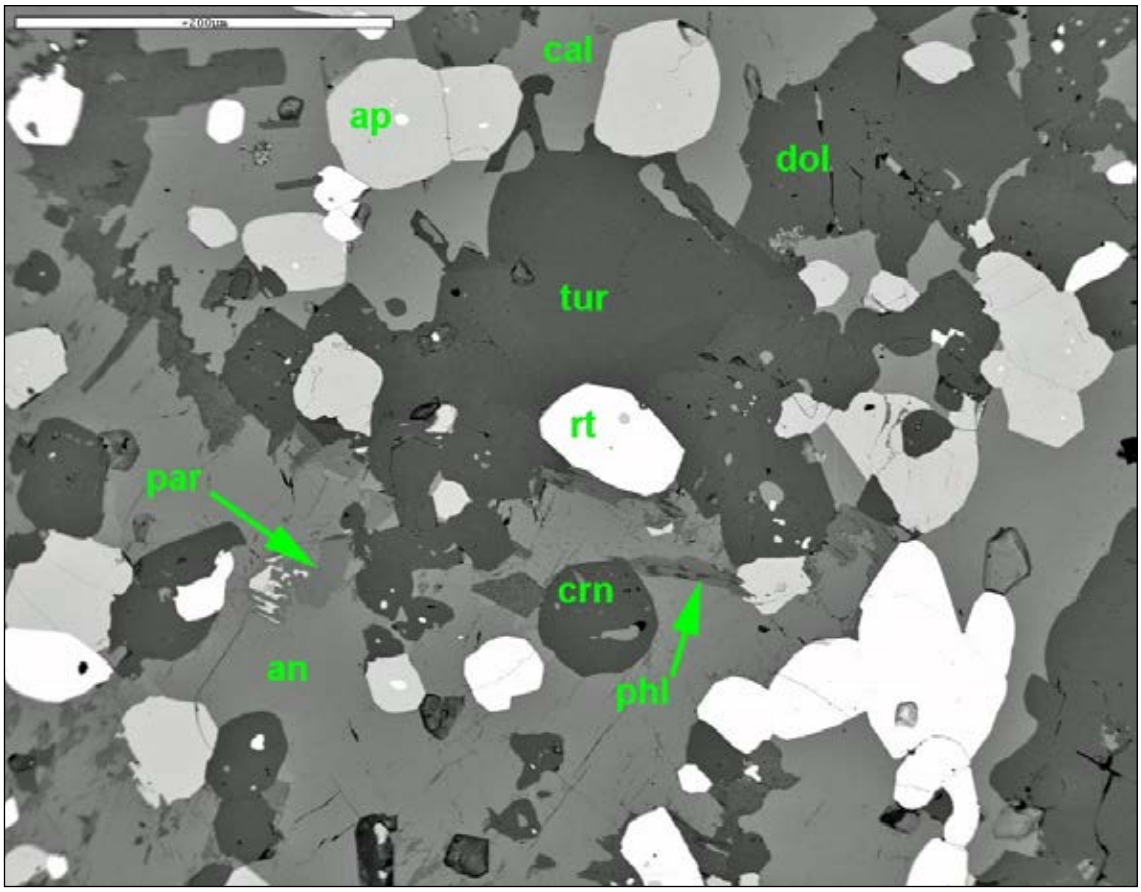

Fig. 4.18: Plagioclase with dolomite and corundum as well as pargasite with dolomite and corundum describe two assemblages present in this BSE image. As a peculiarity there is also tourmaline contained along with rutile and apatite which are accessory minerals in Sample TZG03.

A symplectitic replacement of sapphirine is most prominent (Fig. 4.16). In Fig. 4.17 the symplectite is consisting of dolomite, corundum and phlogopite. Sapphirine is also visible to co-exist with calcite in the same figure. Dolomite, pargasite, corundum, and plagioclase are are seen in Fig. 4.18. Some tourmaline grains were identified in this sample.

Mineral chemistry data for sample TZG03 is summarised in Tab. 4.17. Calcite and dolomite are almost ideal endmembers with only a small dolomite component in calcite. Plagioclase was identified to be of An_{96} composition. No spinel was found in this sample, however. The measured amphibole were identified as pargasite and Al-pargasite and show elevated F-content of nearly 1wt%. Phlogopite reaches almost endmember values with a X_{Mg} of 0.99. F-content for phlogopite is high with 1.2wt%. Finally, there is tourmaline to be mentioned which shows a composition between dravite and uvite (Tab. 4.17).

Mineral	TZG03_10 dolomite	TZG03_15 calcite	TZG03_30 plagioclase	TZG03_14 sapphirine	TZG03_8 phlogopite	TZG03_6 pargasite	TZG03_28 Al-pargasite	TZG03_32 tourmaline
SiO2	bdl	bdl	44.23	12.59	39.61	41.46	42.55	36.48
TiO2	bdl	bdl	bdl	bdl	0.83	1.93	0.52	0.61
P2O5	bdl	bdl	bdl	bdl	bdl	bdl	bdl	bdl
Al2O3	bdl	bdl	34.84	64.44	17.12	17.86	18.89	30.83
Cr2O3	bdl	bdl	bdl	0.39	bdl	bdl	bdl	1.62
Fe2O3	bdl	bdl	bdl	bdl	bdl	bdl	bdl	bdl
FeO	0.18	bdl	bdl	0.54	0.56	0.64	0.71	0.18
MnO	bdl	bdl	bdl	bdl	bdl	bdl	bdl	bdl
MgO	20.65	1.80	bdl	20.41	25.60	17.79	17.99	11.20
ZnO	bdl	bdl	bdl	bdl	bdl	bdl	bdl	bdl
CaO	31.36	52.39	19.86	bdl	bdl	13.03	13.17	2.72
K2O	bdl	bdl	bdl	bdl	9.65	1.28	0.53	bdl
Na2O	bdl	bdl	0.51	bdl	0.71	2.95	3.54	1.70
Cl	bdl	bdl	bdl	bdl	bdl	0.22	0.22	bdl
F	bdl	bdl	bdl	bdl	1.20	0.98	0.92	0.50
Total	52.19	54.19	99.44	98.37	95.28	98.14	99.04	85.84
Si	-	-	2.059	1.472	2.783	5.880	5.941	5.891
Ti	-	-	-	-	0.044	0.206	0.055	0.074
P	-	-	-	-	-	-	-	-
Al	-	-	1.912	8.881	1.418	2.985	3.109	5.868
Cr	-	-	-	0.036	-	-	-	0.207
Fe3	-	-	-	0.053	-	-	-	-
Fe2	0.005	-	-	-	0.033	0.049	0.041	0.024
Mn	-	-	-	-	-	-	-	-
Mg	0.954	0.046	-	3.558	2.681	3.761	3.745	2.696
Zn	-	-	-	-	-	-	-	-
Ca	1.041	0.954	0.991	-	-	1.980	1.970	0.471
K	-	-	-	-	0.865	0.232	0.094	-
Na	-	-	0.046	-	0.097	0.811	0.958	0.532
Cl	-	-	-	-	-	0.053	0.052	-
F	-	-	-	-	0.267	0.440	0.406	0.255
Sum	2.000	1.000	5.008	14.000	8.188	16.397	16.371	16.018
Xmg					0.99			
xan			0.96					

Tab. 4.17: Mineral chemistry for selected minerals as measured for sample TZG03.

4.3.2.2 Ipangko Mine

Sample TZH08 contains the mineral assemblage phlogopite-calcite/dolomite-phlogopite-sapphirine-corundum. As accessories apatite, rutile and ore minerals are observed. Plagioclase, apatite, calcite/dolomite, phlogopite and amphibole occur sometimes as euhedral crystals. Corundum and sapphirine are present as porphyroblastic grains with some inclusions. A polygonal, moisaic texture is found when plagioclase, calcite/dolomite, and apatite grains build triple junctions. A saccharoidal texture however is found typically in the calcite/dolomite-rich matrix. Sapphirine shows a symplectitic overgrowth with vermicular texture. Amphibole and tourmaline are absent in this sample however. Grain sizes were found to be in the range from 1-10mm where as porphyroblasts showed sizes of 5-10mm. (Appendix A.2).

Sapphirine shows a corona structure which represents a reaction rim of sapphirine with corundum and phlogopite. Corundum further occurs in two generations. A first generation shows euhedral texture whereas the second generation is present as very fine crystals together with phlogopite in a symplectite overgrowing sapphirine (Fig. 4.19). There is no spinel found in sample TZH08. In Fig. 4.20 calcite occurs typically close either to sapphirine or anorthite.

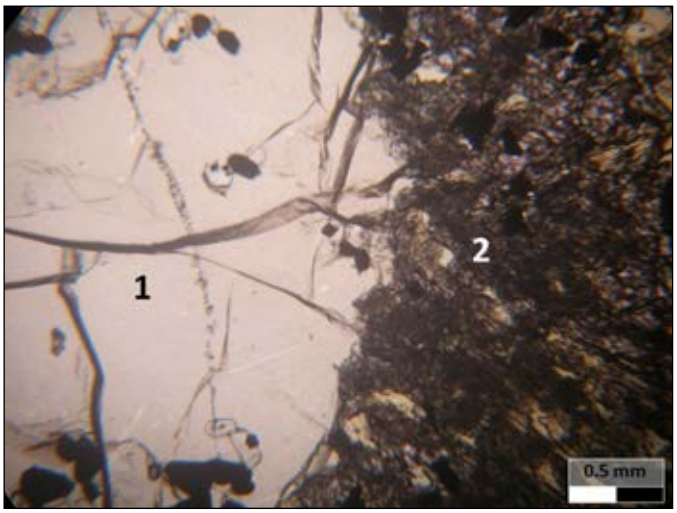

Fig. 4.19: In this microphotograph which was taken under unpolarised light conditions a large broken sapphirine (1) crystal is visible which is overgrown by a symplectite of phlogopite and corundum (2).

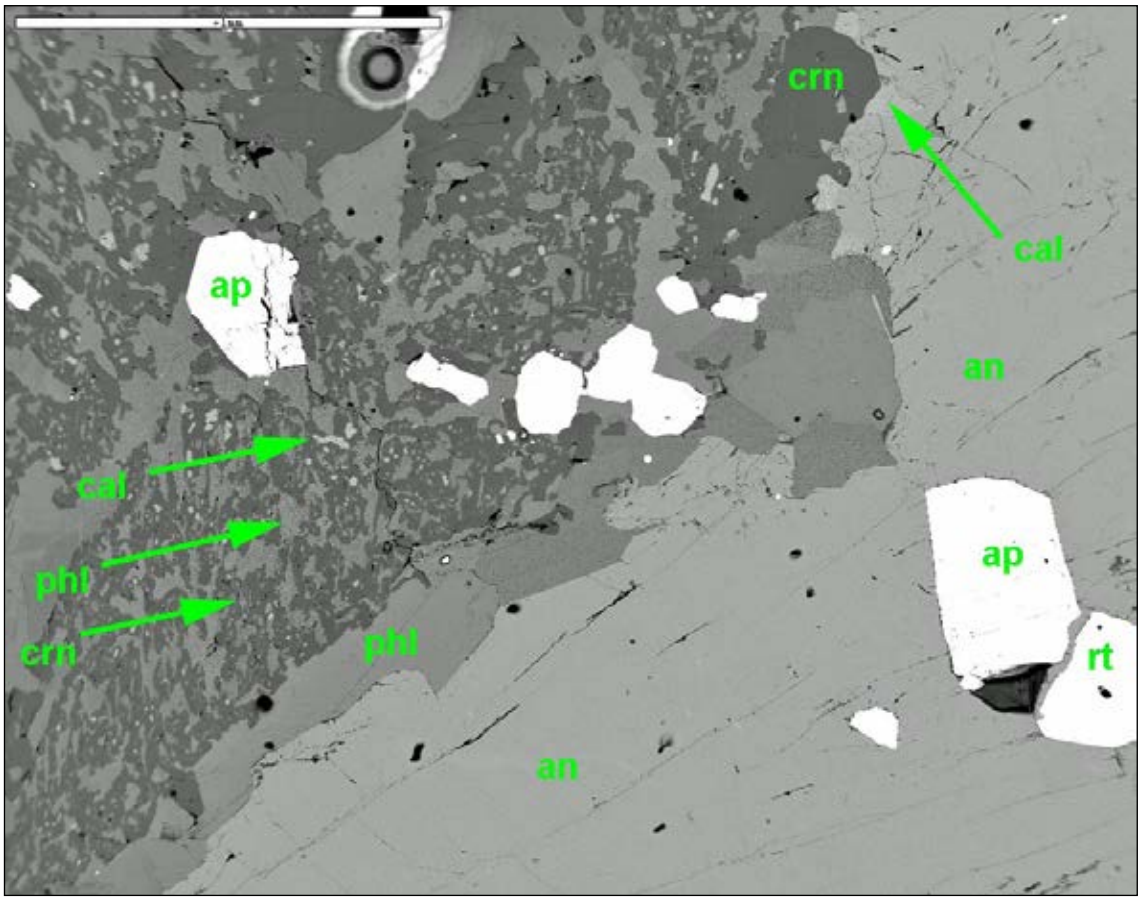

Fig. 4.20: While corundum with calcite and anorthite co-exist is sapphirine overgrown by a vermicular symplectite of corundum and phlogopite.

The results of mineral chemistry analysis for selected minerals of sample TZH08 are summarised in Tab. 4.18. In sample TZH08 no dolomite is observed. Calcite however contains a small dolomite component. Phlogopite has a high X_{Mg} value of 0.96 and an elevated F-content of 0.99wt%. Plagioclase is anorthite rich with An_{97}.

	TZH08_53	TZH08_42	TZH08_55	TZH08_51
Mineral	calcite	plagioclase	sapphirine	phlogopite
SiO2	bdl	43.35	11.50	38.06
TiO2	bdl	bdl	bdl	1.050
P2O5	bdl	bdl	bdl	bdl
Al2O3	bdl	35.34	67.17	18.82
Cr2O3	bdl	bdl	0.57	0.28
V2O3	n.a.	bdl	n.a.	n.a.
Fe2O3	bdl	bdl	bdl	bdl
FeO	bdl	bdl	0.75	1.85
MnO	bdl	n.a.	bdl	bdl
MgO	1.27	bdl	19.74	23.61
ZnO	bdl	n.a.	bdl	bdl
CaO	54.5	20.13	bdl	bdl
K2O	bdl	bdl	bdl	9.49
Na2O	bdl	0.32	bdl	0.31
Cl	bdl	bdl	bdl	bdl
F	bdl	bdl	bdl	0.99
Total	55.77	99.15	99.73	94.46
Si	-	2.027	1.329	2.712
Ti	-	-	-	0.056
P	-	-	-	-
Al	-	1.948	9.147	1.580
Cr	-	-	0.052	0.016
V	n.a.	-	n.a.	n.a.
Fe3	-	-	0.072	-
Fe2	-	-	-	0.110
Mn	-	n.a.	-	-
Mg	0.031	-	3.400	2.508
Zn	-	n.a.	-	-
Ca	0.969	1.009	-	-
K	-	-	-	0.863
Na	-	0.029	-	0.043
Cl	-	-	-	-
F	-	-	-	0.223
Sum	1.000	5.013	14.000	8.111
Xmg				0.96
Xan		0.97		

Tab. 4.18: Mineral chemistry for selected minerals as measured for sample TZH08.

4.3.3 Apatite Mineral Chemistry

Apatite was included in the mineral chemistry investigations carried out in this study as well. The results would like to be discussed not by locality but as a group instead. The main differences in the mineral chemistry of apatite was found in the content of F, Cl, and OH. Fig. 4.21 shows the composition of the apatites in terms of endmembers. The apatite from the Mahenge Mts have generally higher values of Cl compared to the apatite from the Uluguru Mts. Further was the variation in OH and F bigger for apatite from the Uluguru Mts than for the samples measured from the Mahenge Mts. The apatite from the Uluguru Mts where plotted in a very narrow range in respect to Cl however. On the other side, apatite from the Mahenge Mts showed only little variation in the OH content.

Finally, it can be said that it was possible to separate apatite from the Mahenge and the Uluguru Mts based on the analysis of volatile components.

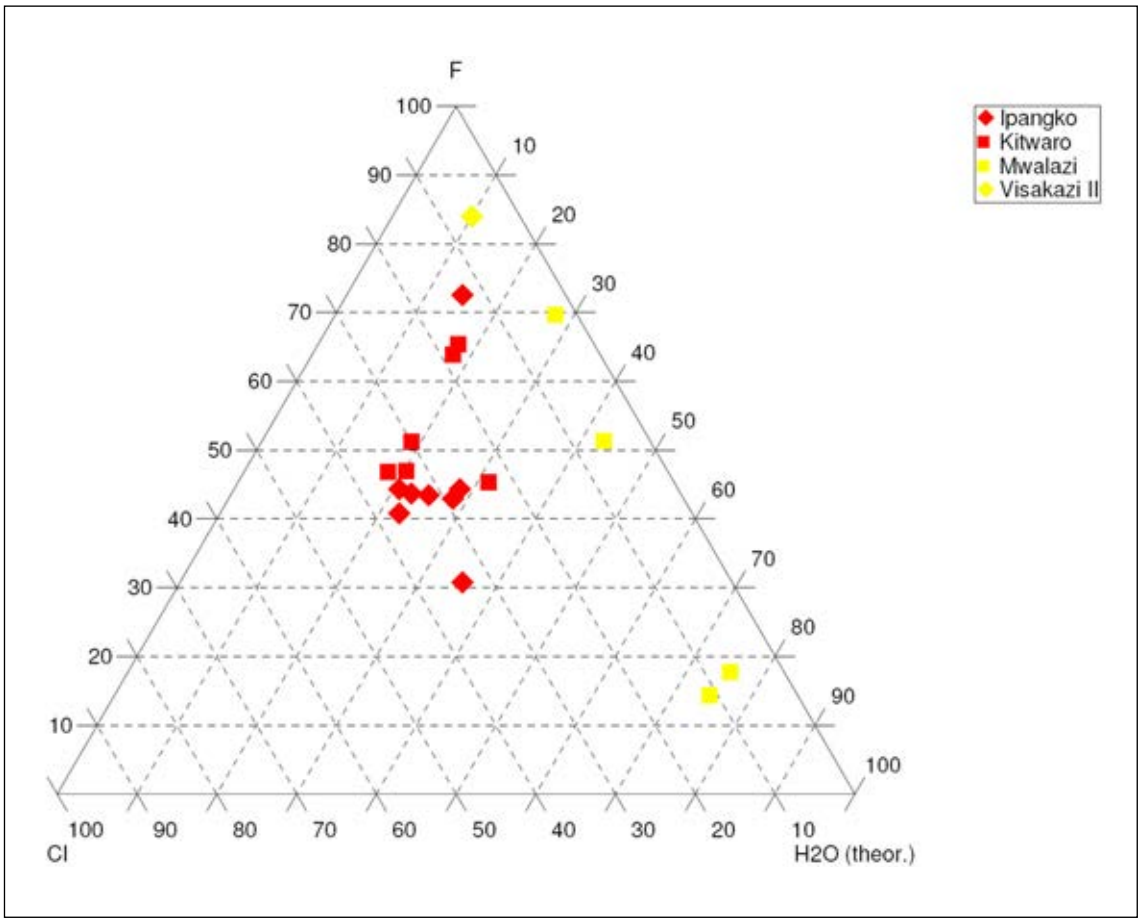

Fig. 4.21: The ternary plot of apatite from the Uluguru Mts (yellow) and the Mahenge Mts (red) display two populations which are clearly distinguishable. The two populations (n=20) appear to differ the most in the Cl component.

4.4 Thermodynamic Calculations

In order to obtain information about the P-T-X_{CO2} evolution of the rock samples and mineral reactions involved with the corundum formation, thermodynamic phase diagram calculations were performed with the Perplex software package by J.A.D. Connolly, Eidgenössisch Technische Hochschule Zürich, Switzerland available form http://www.perplex.ethz.ch/ was applied (Connolly, 1990). In the following, P-T as well as T-X_{CO2} Schreinemakers phase diagrams were created. Calculations by PerpleX were based on a thermodynamic database after Holland & Powell (1998) and according updates.

Thermodynamic phase diagram calculations were carried out for the 6 thick sections which were discussed in chapter 4.3. For the selection of these specific mineral chemistry data sets criteria such as data quality and how representative they were for a given samples were considered.

The non-ideal behaviour of solid solutions had to be taken into account prior to phase diagram calculations. Mineral activities were calculated using activity models proposed by Holland & Powell (1998). The activity of selected mineral phases was calculated using AX2, a freeware program by T. Holland, Cambridge University, Great Britain, available from http://www.esc.cam.ac.uk/research/research-groups/holland. As indicated by geology related literature (chapter 3) peak metamorphic conditions in the Morogoro Region are described to be at granulite facies. Activities were calculated for near peak PT conditions, which are about 9kbar and ~700°C therefore. For spinel and margarite an ideal ionic mixing on site model was chosen, while for scapolite the activity model of Baker & Newton (1995) was applied.

Carbonate phases are close to pure endmember composition and thus activity was set to 1. Also corundum was found to be nearly pure in mineral composition with minor contents of Cr_2O_3 of up to 1wt% only. Conclusively, the activity of corundum was assumed to be 1.

As mentioned the metamorphic peak conditions were described as to be at granulite facies conditions. According to mineral activity calculations a pressure of 9kbar was applied to calculate T-X_{CO2} Schreinemakers phase diagrams. Observed mineral assemblages plot usually in the CO_2 fluid rich side of the T-X_{CO2} diagram and thus a X_{CO2} of 0.8 was used to calculate the P-T Schreinmarkers phase diagrams.

4.4.1 Uluguru Mts

4.4.1.1 Mwalazi Mine

TZM04

For sample TZM04 thermodynamic phase diagram calculations were made for the chemical system CaO-MgO-Al_2O_3-SiO_2-H_2O-CO_2 (CMASH+CO_2).

For thermodynamic calculations mineral activities had been calculated by AX2. In order to stay in the CMASH+CO_2 system the Ca-rich component of the endmember tremolite was used for amphibole instead of the measured pargasite. The resulting mineral activities are, spinel: 0.34, tremolite: 0.22. All other used minerals were considered pure endmembers.

The observed mineral assemblage dolomite + corundum + spinel shown in Fig. 4.7 indicate that the reaction (1) must have been reached on a prograde path at some point. Anorthite is missing which rules out reaction (2) to be responsible for the formation of Spl.

dolomite + corundum = calcite + spinel (1)

tremolite + dolomite + corundum = anorthite + spinel (2)

In Fig. 4.6 as well as Fig. 4.7 the retrograde assemblage of reaction (2) can be seen. An amphibole inclusion in a spinel crystal surrounded by amphibole again (Fig. 4.6) indicates that reaction (2) must have been overstept on the pro- as well as on a retrograde path. Margarite was not encountered in this sample which marks the lower limit of the recorded thermodynamic conditions by reaction (3). On the other hand the reaction (4) was not reached in this sample which gives an upper limit for thermodynamic conditions to be encountered by sample TZM04.

margarite = anorthite + corundum (3)

anorthite + dolomite = amphibole + calcite + spinel (4)

There are two possibilities for corundum forming reactions responsible for the 1st generation of ruby to be created in sample TZM04. At lower temperature and usually pressure conditions a possible diaspore phase which was included as detritic fraction in the marble could be transformed into corundum by a solid state reaction (5). Another possibility is that reaction (3) could be responsible for corundum formation. The two reactions have therefore be seen as two possibilities how 1st generation corundum may have formed in the investigated marbles.

diaspore = corundum (5)

Taking the displayed T-X_{CO2} phase diagram in Fig. 4.22 and the limiting reaction (1) into account the following minimum conditions for a M1 metamorphic event can be estimated: X_{CO2} 0.24 and T 650°C. This indicates a minimum value due to the stability fields indicated in Fig. 4.22 only. Especially X_{CO2} may actually occur at considerably higher values. M2 on the retrograde path didn’t overstep the reaction (3) as a lower limit.

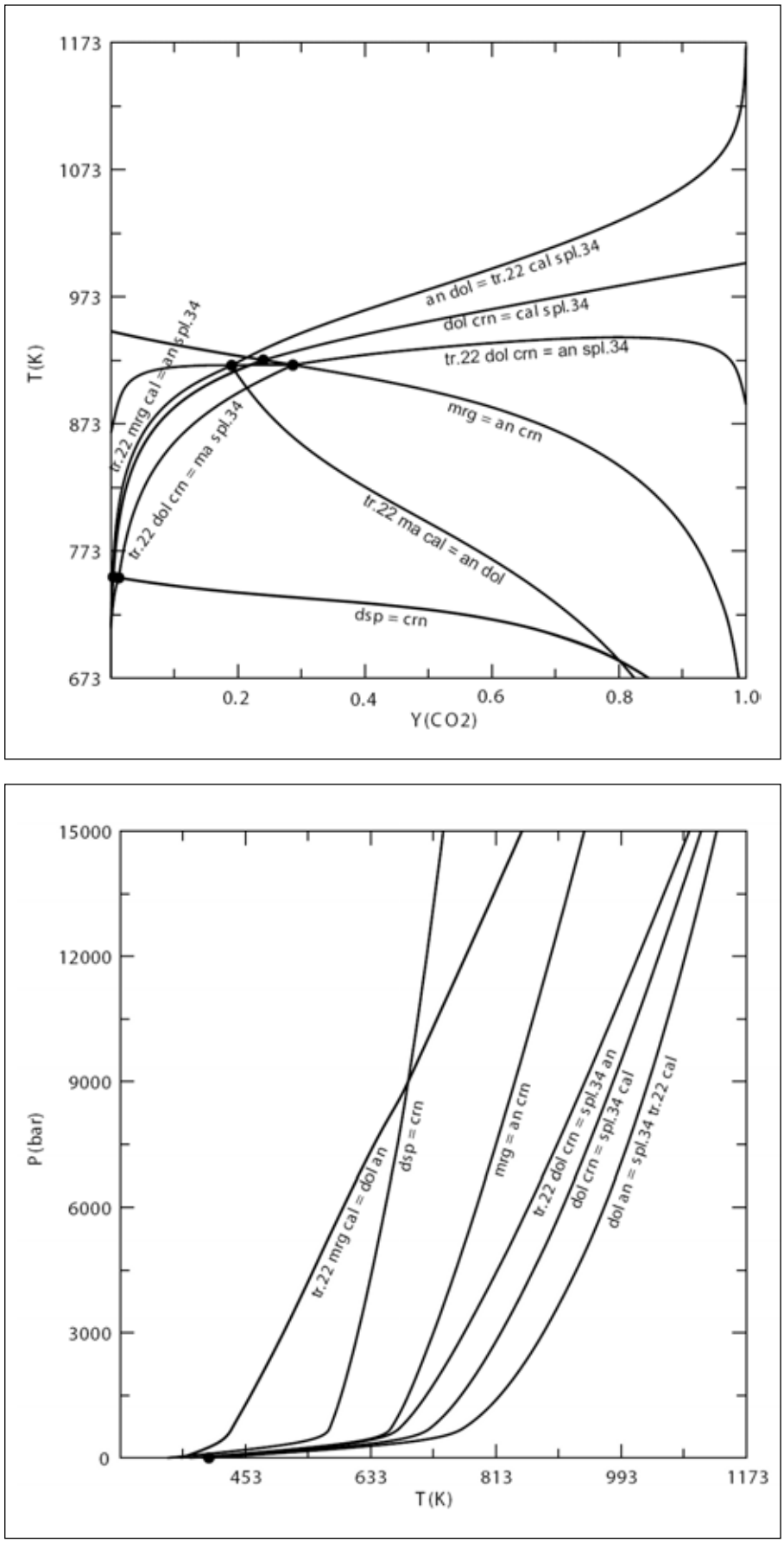

Fig. 4.22: Phase diagrams for sample TZM04 calculated based on activity corrected thermodynamic mineral data as well general conditions chosen as P=9kbar and X_{CO2} =0.8 respectively.

TZM08

For sample TZM08 the chemical system K_2O-CaO-MgO-Al_2O_3-SiO_2-H_2O-CO_2 (KCMASH+CO_2) was used.

Mineral activities were calculated by AX2 for anorthite, phlogopite, and paragonite. The measured composition of anorthite resulted in an activity of 0.56. For phlogophite an activity of 0.36 was calculated. In the case of paragonite the muscovite component was chosen to be considered in order to allow K_2O to be included in further calculations defining a KCMASH+CO_2 system. The activity for muscovite was calculated to be 0.71.

In Fig. 4.8 a replacement reaction of corunudm by spinel was observed. This indicates that reaction (1) was reached during prograde metamorphism. On the other hand there is also corundum and dolomite seen in Fig. 4.10 which indicates the overstepping of this reaction in retrograde direction after peak metamorphism. Further on a retrograde path the assemblage phlogopite and corunudm can be seen in Fig. 4.10. The presence of white mica finally states that reaction (6) was crossed during the retrograde path.

dolomite + white mica = phlogopite + corundum + calcite (6)

As seen in Fig. 4.8 and Fig. 4.9 there are two corundum generations present in sample TZM08. Possible reactions for a 1st generation on a prograde path would be again reactions (3) and (5) as well as in the case of TZM08 also reaction (6). This indicates that several prograde corundum forming reactions during prograde M1 metamorphism are possible. Along the retrograde path the calculated diagram allows only one possible reaction: reaction (1) is crossed towards lower temperatures and spinel is replaced by corundum. This explains why ruby crystals of 1st generation are usually much bigger than the crystals formed during a 2nd generation.

As a minimum condition for M1 reaction (1) must have been crossed in TZM08. This again implies that a temperature of at least 610°C was realised. Regarding the fluid composition almost the entire range from 0 to 1 would be possible as indicated by the T-X_{CO2} phase diagram (minimum X_{CO2} at 0.03). It can be assumed however that X_{CO2} was at higher levels. Temperatures would be higher in this case also most probably around 700-800°C or even above. As a maximum condition for M2 reaction (6) was overstepped during the retrograde path but since there is no Mrg observed in sample TZM08 reaction (3) was not reached yet (Fig. 4.23).

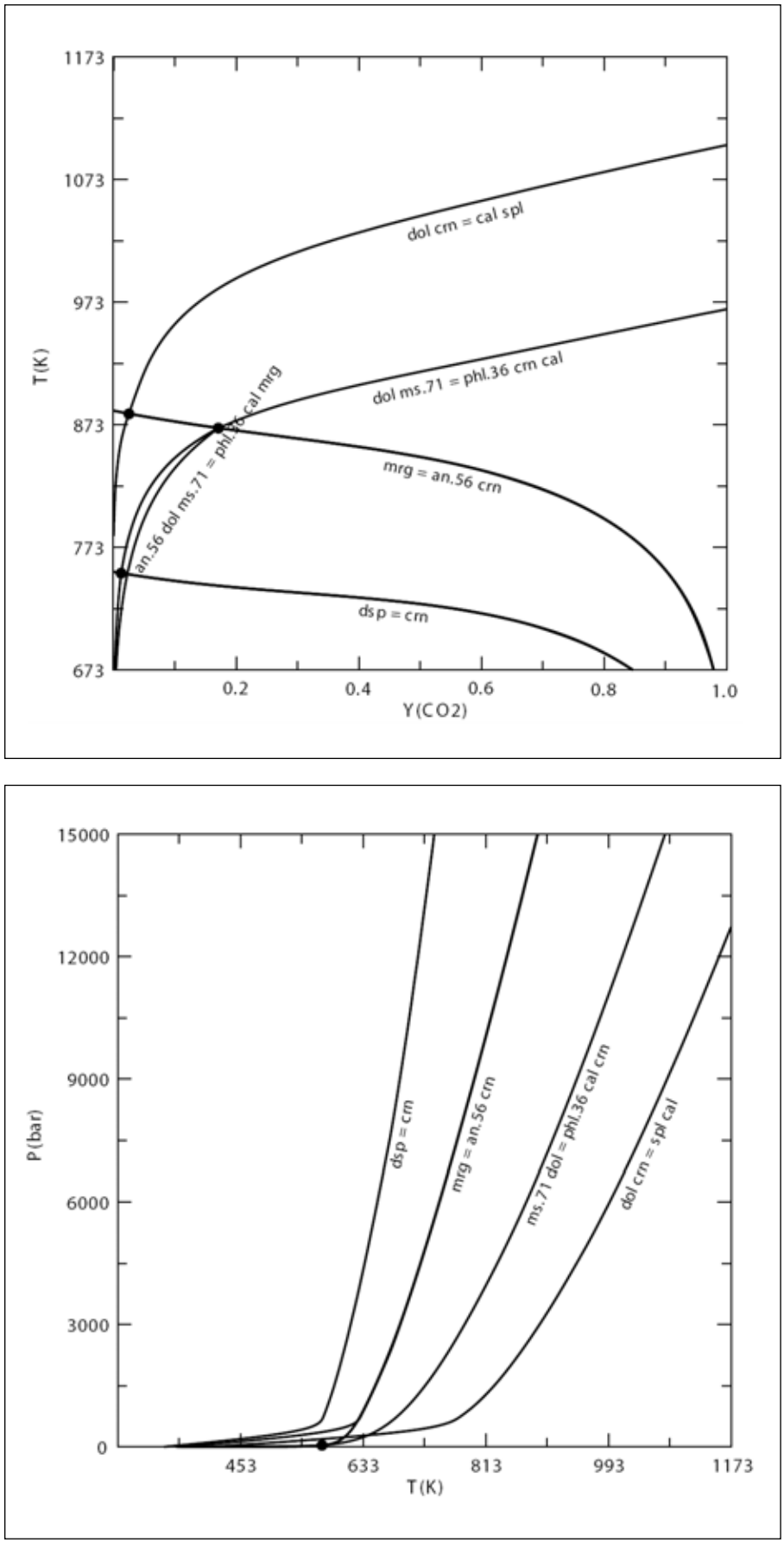

Fig. 4.23: Phase diagrams for sample TZM08 calculated based on activity corrected thermodynamic mineral data as well general conditions to be set at P=9kbar and X_{CO2} =0.8 respectively.

4.4.1.2 Visakazi II Mine

WB6

Thermodynamic phase diagrams were calculated for sample WB6 in the chemical system K_2O-CaO-MgO-Al_2O_3-SiO_2-H_2O-CO_2 (KCMASH+CO_2).

Mineral activities were calculated by AX2 for anorthite, pargasite, phlogopite and paragonite whereas the activity for margarite was calculated using an ideal mixing on site model. Accordingly the activity for margarite was evaluated to be 0.67. For the analysed chemical compositions an activity for anorthite of 0.96 and for phlogopite of 0.52 was calculated. The tremolite activity in amphibole was calculated to be 0.20. The muscovite component in the paragonite rich white mica was used which was evaluated with 0.60.

In Fig. 4.11 a symplectitic overgrowth of phlogopite and corundum over dolomite and a replaced mineral which does no longer exist describes reaction (6). Because there is no spinel observed in sample WB6 all reactions including spinle can be neglected as potential reactions to have taken place. On the other hand there is white mica observed to replace corundum in Fig. 4.12 which represents the retrograde part of reaction (6). Also in Fig. 4.13 a dolomite reaction rim with corundum and the occurrence of white mica indicates a retrograde crossing of reaction (6) and possibly reaction (7).

amphibole + dolomite + white mica = phlogopite + anorthite + calcite (7)

Margarite can be seen in Fig. 4.13 which gives evidence that reaction (3) was crossed during retrograde cooling.

The formation of symplectite which is considered to indicate disequilibrium due to rapid change in P, T, or fluid chemistry can be used to constrain the metamorphic evolutionary history. Near isobaric cooling as well as slow cooling history was obtained for the granulite facies rocks in East Africa (Appel et al., 1998; Moeller et al., 2000; Hauzenberger et al., 2005; Tenczer et al., 2011). As seen in the T-X_{CO2} phase diagram a rapid change in fluid composition is therefore the only possibility to overstep reaction (6). An influx of a H_20 rich fluid phase would drive the reaction towards lower X_{CO2} values. Peak conditions for M1 are likely to have been on the CO_2 rich side as indicated in other samples. Accordingly, maximum condition for M1 is defined by reaction (6). Minimum conditions on the other hand are limited by the intersection of reaction (6) and (3) at 660°C and X_{CO2}>0.5. For M2 is related to the formation of the symplectite when reaction (6) is overstept due to a rapid change in fluid composition towards lower X_{CO2} values, the minimum condition is defined by reaction (6) itself. Because Spl can not be found it can be assumed that reaction (2) was never reached. This is in agreement with M2 to be on a retrograde path after M1. This again emphasises mainly a change in fluid composition rather than in temperature or pressure compared to the peak conditions which were present during M1. In general, a slightly lower temperature for M2 compared to M1 can be assumed however. Finally,

there is a late stage metamorphic overprint documented in sample WB6 when reaction (3) was crossed during retrogression. This represents the metamorphic event M3 which is mainly documented by the presence of margarite and chlorite in sample WB6. As corundum forming reactions again reaction (3) and (5) are possible but reaction (3) due to the occurrence of margarite in Fig. 4.13 seems more likely. On a retrograde path there are also two reactions possible for a 2nd corundum generation to be formed. First reaction (6) is most likely. However if X_{CO2} was higher than 0.7 reaction (8) would be possible as well (Fig. 4.24).

amphibole + corundum + dolomite + white mica = phlogopite + anorthite (8)

Corundum crystal growth during M1 is however more prominent than during M2 in sample WB6. Regarding the P-T phase diagram the metamorphic textures further imply that a minimum pressure and temperature conditions had not fallen below 6.2kbar and 540°C respectively.

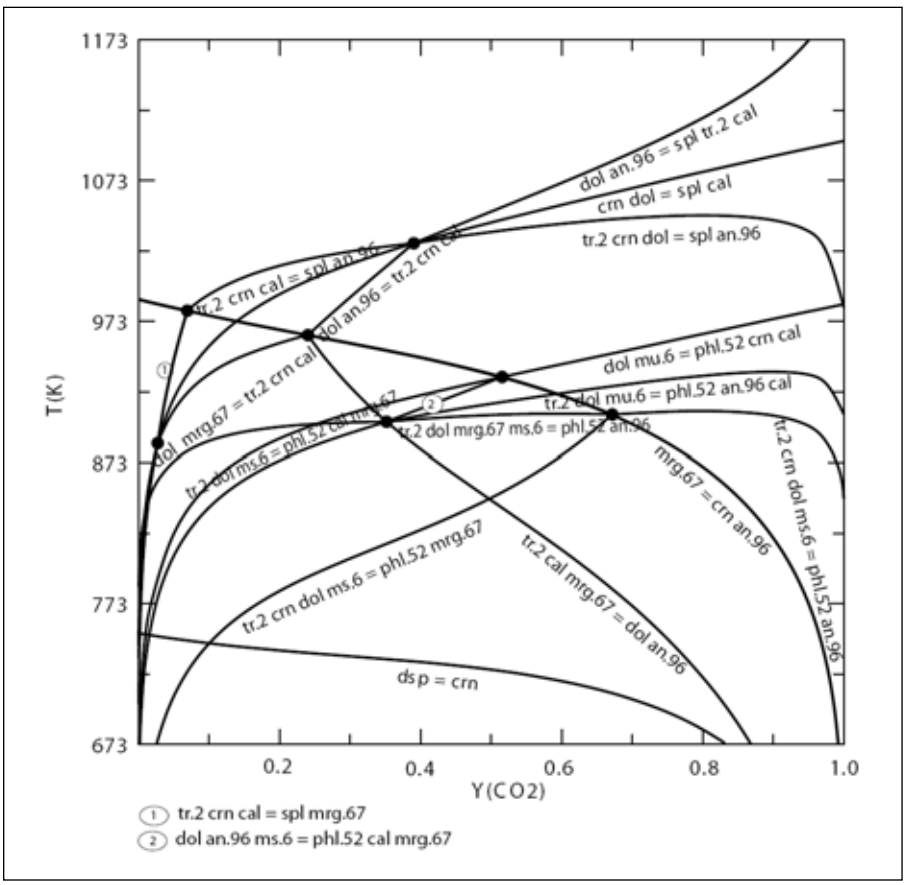

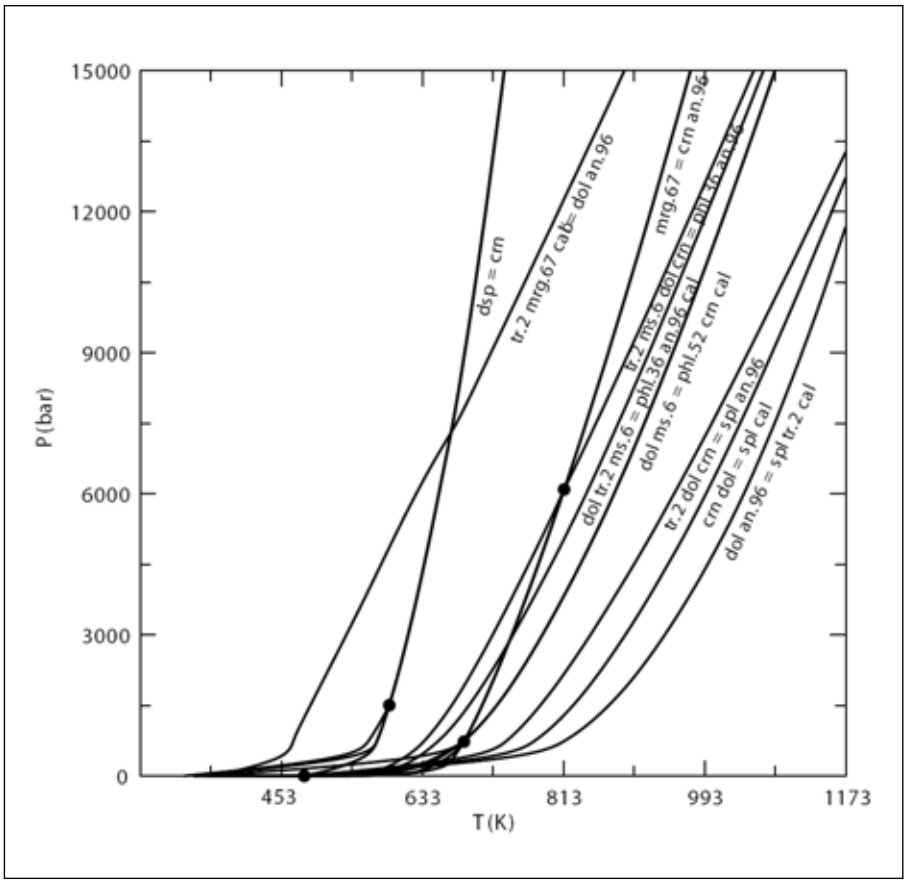

Fig. 4.24: Phase diagrams for sample WB6 calculated based on activity corrected thermodynamic mineral data as well general conditions to be set at P=9kbar and X_{CO2} =0.8 respectively.

WB1

The chemical system for sample WB1 is defined by CaO-MgO-Al_2O_3-SiO_2-H_2O-CO_2 (CMASH+CO_2).

Thermodynamic calculations were carried out using an activity of spinel of 0.47 and scapolite of 0.06. The activity for An was calculated by AX2 and is 0.94 whereas for the amphibole endmember tremolite has an activity of 0.29.

In terms of reaction pattern spinel inclusion in corundum as well as the co-existence of corundum and dolomite combined with the almost complete absence of amphibole as seen in Fig. 4.14 gives evidence that reaction (1) was most probably responsible for the formation of spinel during a prograde metamorphic path. The presence of corundum and dolomite however indicates that reaction (1) was crossed during the retrograde path after peak metamorphism established. The symplectite which is visible in both Fig. 4.14 and Fig. 4.15 consists of fine grained corundum, scapolite, and amphibole as seen in Fig. 4.15. This assemblage can be explained by reaction (9).

amphibole + scapolite + corundum = anorthite + spinel (9)

Similar to sample WB6 a drastic change in fluid composition is believed to be the reason for this disequilibrium reaction texture rather than changes in temperature or pressure. Finally, a fine reaction rim observed in Fig. 4.15 between pargasite and dolomite consists of scapolite was difficult to be interpret but most likely is describing reaction (10).

amphibole + dolomite + corundum = scapolite + spinel (10)

Regarding the limiting conditions for M1 the sequence of metamorphic textures indicate that reaction (1) took place before reaction (9). This implies however that M1 has to be situated toward the right side of the intersection of reaction (1) and (9) in the T-X_{CO2} phase diagram. Minimum conditions are therefore given by this intersection at X_{CO2} 0.87 and 740°C. Also in terms of pressure a statement can be made. Due to the sequence of reaction patterns M1 must be located above the intersection of reaction (1) and (9) which is at 720°C and 8.5kbar in the calculated P-T phase diagram. The maximum condition for M2 is defined by reaction (9). Reaction (1) was crossed during the retrograde path as well as reaction (10) most probably. Reaction (3) was not reached however due to the absence of margarite in sample WB1. As scapolite forming reactions several possibilities are indicated in the calculated phase diagrams. However reaction (11) is most likely to be the scapolite forming reaction.

calcite + anorthite = scapolite (11)

For the formation of a 1st corundum generation reactions (3) and (5) took place most likely. Additionally in sample WB1 reaction (12) would also be a possibility.

dolomite + anorthite = amphibole + scapolite + corundum (12)

This indicates that during the prograde path there are several options for corundum to be formed again. On the retrograde path corundum can be formed by crossing reaction (9) as well as reaction (1). Because reaction (9) is responsible for the symplectite it is assumed that this reaction is not the cause for gem quality ruby to be formed in this deposit. On the retrograde path there is also reaction (10) possibly involved in ruby formation. Conclusively there are several options for ruby to form after peak metamorphic conditions M1 were reached (Fig. 4.25).

4.4.2 Mahenge Mts

4.4.2.1 Kitwaro Mine

TZG03

Thermodynamic phase diagram calculations for sample TZG03 were made in the CaO-MgO-Al_2O_3-SiO_2-H_2O-CO_2 (CMASH+CO_2) system.

For thermodynamic phase diagram calculations the activity of minerals was calculated by AX2. The activity of An is 0.96. Measured sapphirine composition indicates an ionic ratio of Si : Al of 1.5 : 9 and not 2 : 8. Therefore the sapphirine modification

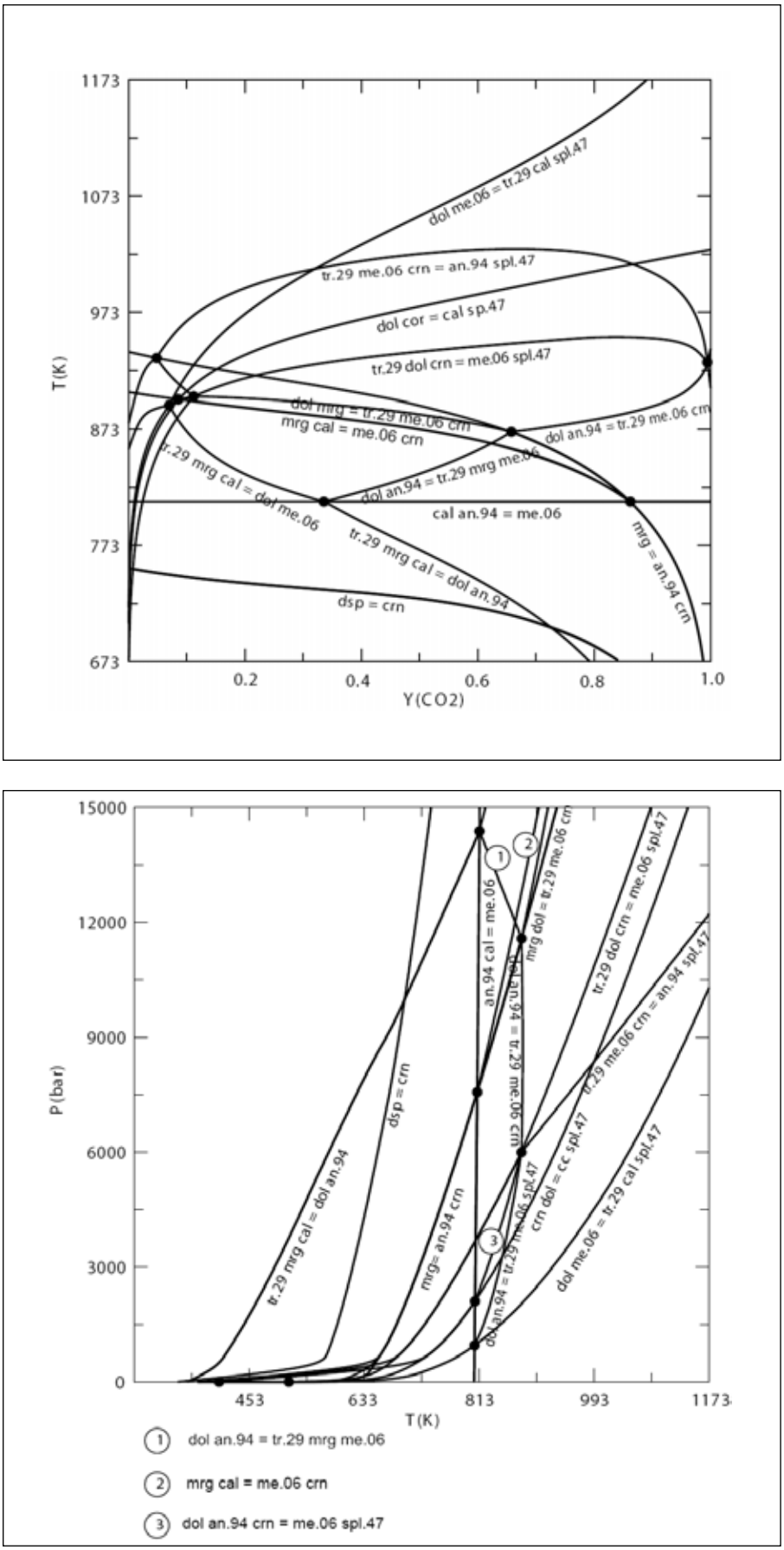

Fig. 4.25: Phase diagrams for sample WB1 calculated based on activity corrected thermodynamic mineral data as well general conditions to be set at P=9kbar and X_{CO2} =0.8 respectively.

Sa351 (AX2) which is equivalent to Spr7 (PerpleX) was chosen for further calculations. Activity calculations of sapphirine yielded 0.36. An tremolite activity of 0.05 was calculated for amphibole.

In the investigated sample TZG03 sapphirine exists as large crystals (Fig. 4.16). This implies that the sapphirine forming reactions (13) and (14) were overstept on a prograde metamorphic path.

amphibole + dolomite + corundum = sapphirine + anorthite (12)

dolomite + corundum + anorthite = sapphirine + calcite (13)

The absence of spinel in sample TZG03 is evidence that reaction (1) was not overstept. In Fig. 4.17 a symplectitic overgrowth consisting of fine corundum and dolomite crystals next to well preserved sapphirine and calcite crystals can be observed. This assemblage indicates that conditions changed rapidly from a prograde metamorphic setting to a retrograde path when reaction (13) was crossed suddenly. Only little changes in temperature and/or fluid composition are enough to enable this reaction. In Fig. 4.18 the presence of pargasite, dolomite, and corundum indicate reaction (12) to be crossed on a retrograde path as well. It can be assumed that reaction (3) was not reached since margarite is absent in this specimen.

Possible reactions for the formation of a 1st generation corundum phase are reaction (5) and (3) during the prograde metamorphic path. The formation of a 2nd generation corundum phase was possible by crossing reactions (12 & 13).

Minimum conditions for M1 to take place are described by reaction (13). As metamorphic textures indicate M1 conditions are on the right hand side from the intersecting point with reaction (12) which marks the point of minimum conditions at 760°C and a X_{CO2} of 0.67. The maximum condition for M1 is indicated by reaction (1) which was not overstept. By taking metamorphic textures into account again the P-T phase diagram indicates conditions for M1 to be between 650 and 860°C (Fig. 4.26).

4.4.2.2 Ipangko Mine

TZH08

For sample TZH08 the thermodynamic phase diagram calculations were carried out in the CaO-MgO-Al_2O_3-SiO_2-H_2O-CO_2 (CMASH+CO_2) system.

Sapphirine was also found in sample TZH08. The calculated activity for sapphirine (Spr7, sa351) was 0.49. The result of activity calculations for phlogopite indicated an activity of 0.49. The activity for anorthite is 0.97.

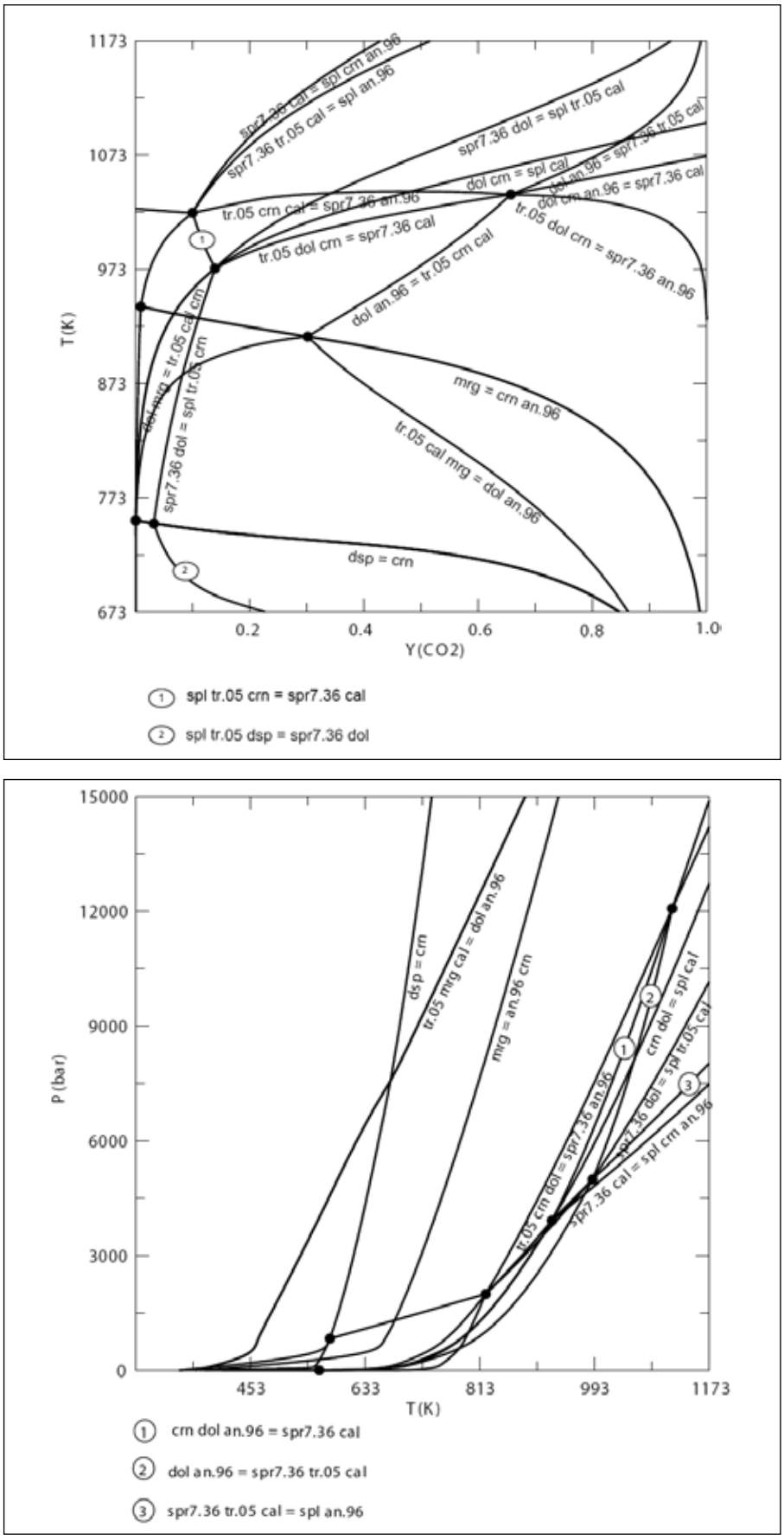

Fig. 4.26: Phase diagrams for sample TZG03 calculated based on activity corrected thermodynamic mineral data as well general conditions to be set at P=9kbar and X_{CO2} =0.8 respectively.

Within this thinsection three typical mineral associations were identified: 1) anorthite and corundum are stable next to each other (Fig. 4.20). 2) sapphirine is found to be present as large crystals as seen in Fig. 4.19. These textures indicate that reaction (13) was overstepped during the prograde path (M1). 3) symplectite associations are present in sample TZH08 as observed in Fig. 4.20 also. The symplectite consists of fine crystals of corundum and phlogopite and represents the retrograde part of reaction (13). In sample TZH08 there is no spinel thus reaction (1) was not reached. Conclusively, this indicates the observed mineral assemblages were formed very close between M1 and M2 and only subtle changes in temperature and fluid composition occurred to be responsible for the observed symplectite to form.

As a minimum condition for M1 the reaction (13) can be proposed. Further did M1 not cross conditions described by reaction (1) which is therefore the upper limit for M1. Mrg was not encountered in sample TZH08 either which indicates the intersection of reaction (3) with reaction (13) to be the minimum condition for M1. Taken the T-X_{CO2} phase diagram into account this defines a minimum of 660°C and X_{CO2} of 0.08. This very low X_{CO2} value however has to be regarded as a minimum condition only and that in reality the conditions may be towards a CO_2 rich fluid composition more likely. Evidence for such an assumption can be found in the P-T phase diagram which was calculated for TZH08. Due to observed metamorphic textures and the fact that spinel is absent in sample TZH08 it can be assumed that the intersection point of reaction (1) with reaction (13) was not undercut. This defines minimum conditions for M1 at 705°C and 5.4kbar however. Going back to the T-X_{CO2} phase diagram this would imply a X_{CO2} value of 0.17 at least which was taken as the minimum X_{CO2} value in the following. Unfortunately, the observed mineral assemblage did not allow restricting the thermodynamic conditions any further.

As a corundum forming reactions reaction (5) and (3) are most likely for a 1st corundum generation whereas reaction (13) was responsible for corundum to form in symplectite. It can be assumed however that M1 metamorphism was responsible for gem quality corundum to form in this locality (Fig. 4.27).

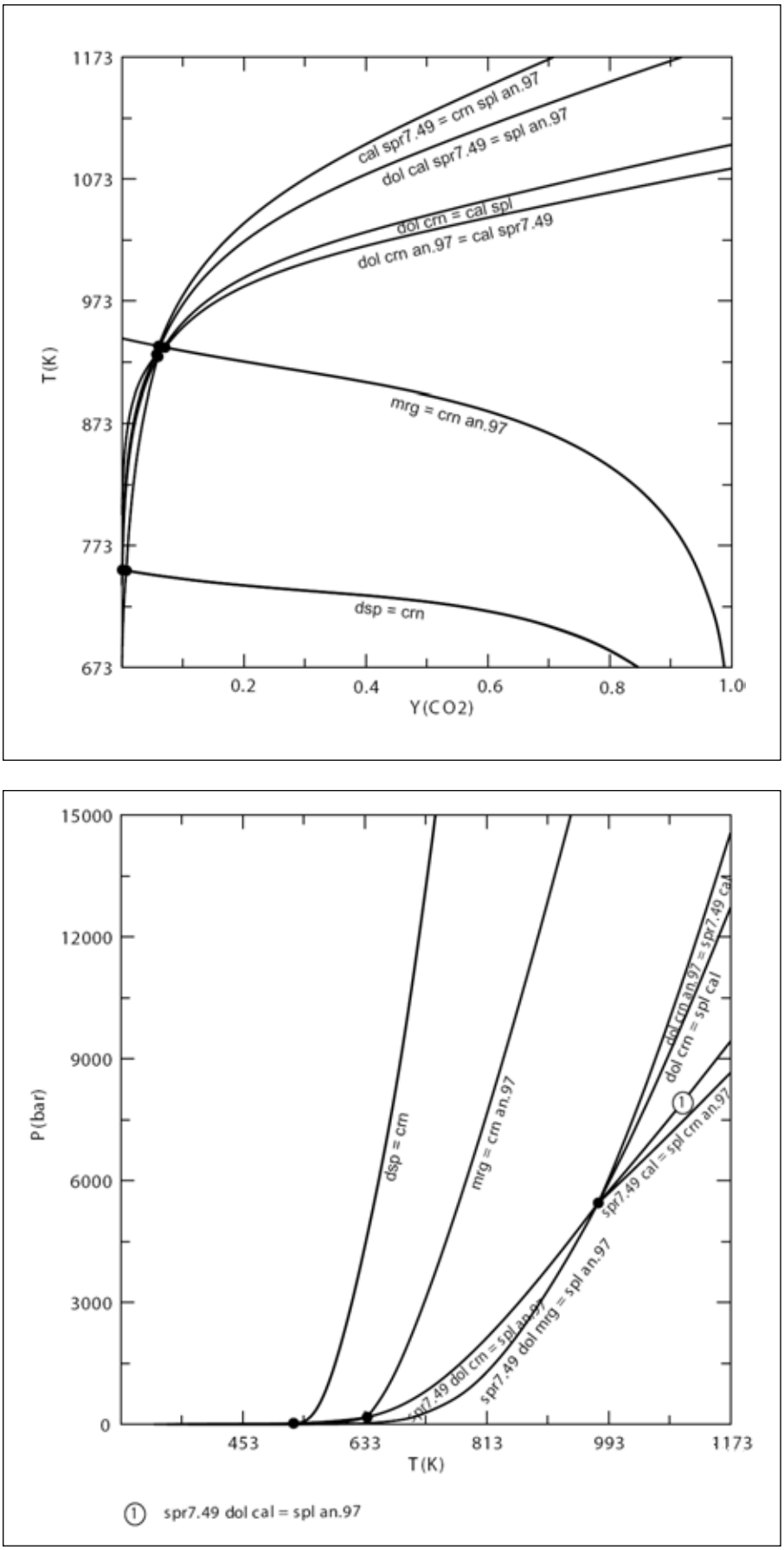

Fig. 4.27: Phase diagrams for sample TZH08 calculated based on activity corrected thermodynamic mineral data as well general conditions to be set at P=9kbar and X_{CO2} =0.8 respectively.

4.5 Discussion

4.5.1 Whole Rock Chemistry

It was discovered that the ruby mineralisations in the Uluguru Mts are confined to calcite-marbles where as the ruby mines in the Mahenge Mts are found in dolomite-marbles. This indicates excess content of Mg for the ruby deposit in the Mahenge Mts compared to the Uluguru Mts. This again is in agreement with the different mineral assemblages found in the two deposits. In the Mahenge Mts for example the Mg-rich phase sapphirine is encountered while Ca-rich scapolite is found in the Uluguru Mts only.

There are several elements, such as the oxides Na_2O, K_2O and FeO/ Fe_2O_3, which were found to behave similar in both localities for example. The observed increase in these elements is believed to be related to the influx by an external source. A close relationship with fluids which travelled through the investigated marbles is most likely. Whether the increased values of Al_2O_3 and SiO_2 derive from compositional differences within the host rock itself or if an increase is related to fluid-rock interactions which took place after sedimentation can not be determined conclusively. Al however is known to be difficult to mobilise and therefore an in situ concentration in Al-rich layers together with SiO_2 is more likely. Such a situation could be found for example where clay minerals are sedimented together with carbonate minerals. A similar case is observed for TiO_2. Normally, the unmineralised host rocks are lower in TiO_2 content compared to their mineralised counterparts. As mentioned above TiO_2 could also be concentrated in marbles when deposition of detritic material was higher. TiO_2 could have been deposited as heavy minerals such as ilmenite for example. Due to the high density of such minerals a more proximal position of the carbonate platform would be implicated therefore. Also the content in P_2O_5 is seen to be a residue of compositional variations due to sedimentary differences and not the result of fluid-rock interaction. As a possible source for P_2O_5, organic matter is most likely. The increased value for SO_3 at Visakazi II Mine may also be related to organic matter. Although, SO_3 could have been brought in to the investigated marbles by fluids later on as well.

Finally, in this context it would be interesting to discuss the content of Cr within the examined rocks. Cr as the main chromophore for rubies is an essential element to be present for the formation of gem quality rubies. Cr_2O_3 is usually the trace-element with the highest content in rubies and reaches contents of more than 1wt%. An appropriate source for Cr_2O_3 has to be found therefore. Unfortunately, Cr_2O_3 was not included in the whole rock analysis and no whole rock data is available therefore. Although Muhongo & Errera (1993) indicate a fluid related influx of Cr, it can not be determined conclusively based on the data available whether the source for Cr_2O_3 is indeed related to fluids or a sedimentary origin is more likely.

Conclusively, it can be said that in order to be able to explain the elevated contents of certain oxides such as Na_2O, K_2O and FeO/ Fe_2O_3 a fluid-rock interaction with at least one fluid was likely to have happened for the investigated marble-hosted ruby deposits in the Morogoro Region, Tanzania.

4.5.2 Petrography and Mineral Chemistry

In Tab. 4.8 a compilation of all mineral assemblages encountered during this study is displayed.

First, it has to be mentioned that there are two corundum generations present in the marble-hosted deposits of the Morogoro Region, Tanzania. A 1st generation which was formed during a prograde metamorphic path and a 2nd generation after peak metamorphic conditions were reached on the retrograde limb of the metamorphic path.

Regarding the two deposits, the most striking difference was the absence of spinel for mineral assemblages in the Mahenge Mts. In the contrary there was no sapphirine found in the Uluguru Mts. White mica however was found in the Uluguru Mts only. The presence of scapolite was typical for Visakazi Mine which was further the only difference in mineral assemblage compared to Mwalazi Mine. On the other hand there was titanite detected in Ipangko Mine only where as sulphides seem to be absent in Kitwaro Mine. Tourmaline finally was found in all localities except in Ipangko (Tab. 4.19).

Mineral Paragenesis by Locality :

Mwalazi	crn	spl	cal	dol	am	spr	scp	phl	pg	mrg	an	chl	ap	rt	tur	ttn	py/po/ccp
TZM04	x	x	x	x	x			x				x	x	x			(x)
TZM06	x			x				x			x	x	(x)	x			(x)
TZM07	x	x		x	x			x				x	x		x		
TZM08	x	(x)		x				x	x	(x)	x	x	x	x	x		(x)
Total	**x**	**x**	**x**	**x**	**x**			**x**	**x**	**(x)**	**x**	**x**	**x**	**x**	**x**		**(x)**

Visakazi	crn	spl	cal	dol	am	spr	scp	phl	pg	mrg	an	chl	ap	rt	tur	ttn	py/po/ccp
WB1	x	x	x	x	x		x	x			x	x	x	(x)			
WB6	x	x		x	x		x	x		x	x	x	x	(x)	x		(x)
WB10	(x)			(x)	(x)			(x)	x	x	(x)	(x)	(x)	(x)			(x)
Total	**x**	**x**	**x**	**x**	**x**		**x**	**x**	**x**	**x**	**x**	**x**	**x**	**(x)**	**x**		**(x)**

Kitwaro	crn	spl	cal	dol	am	spr	scp	phl	pg	mrg	an	chl	ap	rt	tur	ttn	py/po/ccp
TZG03	x		x	x	x	x		x			x	(x)	x	x	x		
TZM07-5	x		x		x			x			x	(x)	x	x	x		
TZM07-7	x			x	x			x				(x)	x	x			
Total	**x**		**x**	**x**	**x**	**x**		**x**			**x**	**x**	**x**	**x**	**x**		

Ipangko	crn	spl	cal	dol	am	spr	scp	phl	pg	mrg	an	chl	ap	rt	tur	ttn	py/po/ccp
TZH08	x		x			x		x			x		x				(x)
WB5	x							x			x	(x)	x	(x)		x	(x)
WB7	x		x					x			x	(x)	x	x		x	(x)
Total	**x**		**x**			**x**		**x**			**x**	**x**	**x**	**x**		**x**	**x**

x: examined by EPMA or SEM coupled WD-XRF
(x): observed but not examined

Tab. 4.19: Mineral assemblage compilation by localities as observed in this study.

According to metamorphic mineral assemblages and textures a chart of time-resolved mineral paragenesis was created (Fig. 4.9). This chart allows to recognise which minerals occurred together during the three metamorphic events which are described for the Eastern Granulites. Because the degree of re-crystallisation was always high metamorphism could not be linked to deformation based on petrography.

From the paragenesis shown in Tab. 4.20 it can be concluded by the presence of phlogopite that K_2O entered the investigated systems in an early stage already. As mentioned in chapter 4.5.1 fluids are assumed to be responsible for the influx of K_2O and other elements. Further evidence for such an assumption is provided by the high F-content measured in Phl from both deposits. This again implies that a fluid was introduced to the ruby bearing marbles either pre- or syn-M1 already.

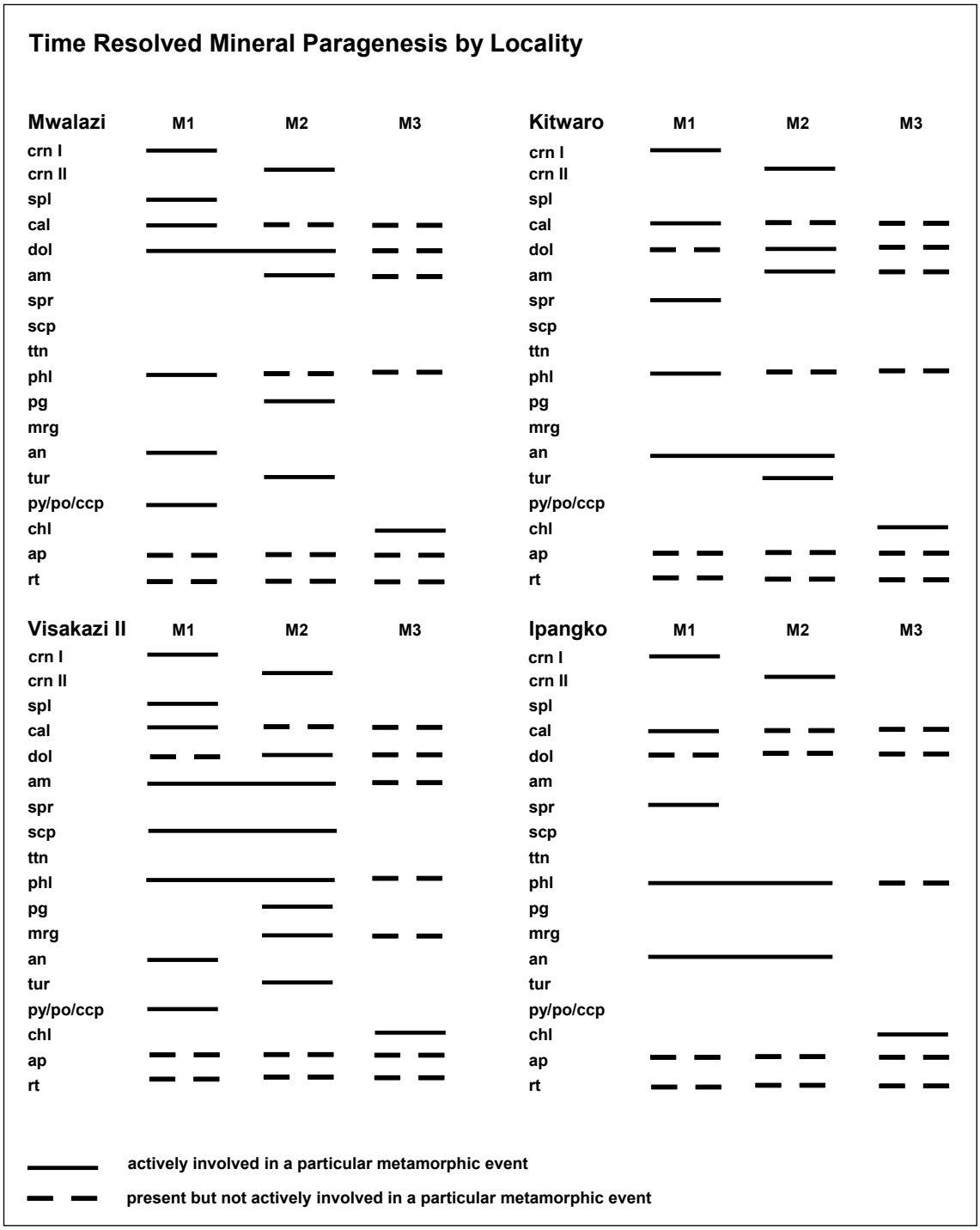

Tab. 4.20: Time-resolved mineral paragenesis as observed in petrographic sample investigated from 4 different ruby mines within the Uluguru and Mahenge Mts, Morogoro Region, Tanzania.

As indicated tourmaline was found in both deposits as well. Gneisses and metapellites contained in the basement of the Eastern Granulites seem to be a reasonable possibility for a B source. The presence of tourmaline normally is linked to pegmatites. With pegmatites there are also fluids introduced to the host rock. During this study it was found that tourmaline occurs during M2 only. This however indicates that fluid related processes must have occurred during both metamorphic events, M1 and M2. Further, it can be recognised that tourmaline was always present with 2nd generation of corundum which provides further evidence that 2nd generation corundum was formed indeed by a fluid-controlled process. The involvement of two intrusion episodes is also in agreement with what is published in literature. Fritz et al. (2005) for example recognise two pegmatite generations to be present in the Uluguru and Mahenge Mts.

Similar situations where fluids along with tourmaline formation are involved in ruby forming processes are encountered in marbles from Jegdalek/ Afghanistan, Nangimali/ Kashmir, and Luc Yen/ Vietnam (Garnier et al., 2008).

The mineral assemblage encountered in the Mahenge Mts including sapphirine seems to be rather exclusive. Up to present, there is only one more marble-hosted ruby deposit known which shows a similar paragenesis including sapphirine. This deposit is located in the Hunza Valley in Pakistan (Garnier et al., 2008).

4.5.3 Thermodynamic Calculations

Thermodynamic phase diagram calculations revealed that in the Uluguru and the Mahenge Mts two different reactions set the limit for M1 during peak metamorphism. In the Uluguru Mts reaction (1) : dolomite + corundum = calcite + spinel was recognised as the limiting reaction (Fig. 4.28) where as in the Mahange Mts reaction (13) : dolomite + corundum + anorthite = sapphirine + calcite is marking the minimum condition for M1. These two reactions have a similar trend where as reaction (13) is present at slightly lower temperatures. In a T-X_{CO2} space, the two reactions are apart by about 20°C the most. It can be concluded therefore that for comparable X_{CO2} values, similar temperature conditions were present in both deposits.

Further, it was recognised that the reactions observed in the Mahenge and the Uluguru Mts describe a anticlockwise metamorphic path which indicates isobaric cooling after peak metamorphism as suggested by Appel et al. (1998), Fritz et al. (2005 & 2009) and Tenczer et al. (2011). Möller et al. (2000) as well as Hauzenberger et al. (2005) further showed a slow cooling history to be present in the Eastern Granulites. Together with what was observed in petrographic investigations carried out in this study a rapid change of pressure or temperature can therefore be excluded as a reason for the symplectites to occur during M2 metamorphism in the Uluguru and Mahenge Mts. A third possibility, a rapid change in fluid composition, seem therefore more likely to be the case.

Finally, minimum conditions for peak metamorphism M1 were investigated. To further concentrate the essence of information obtained from thermodynamic calculations

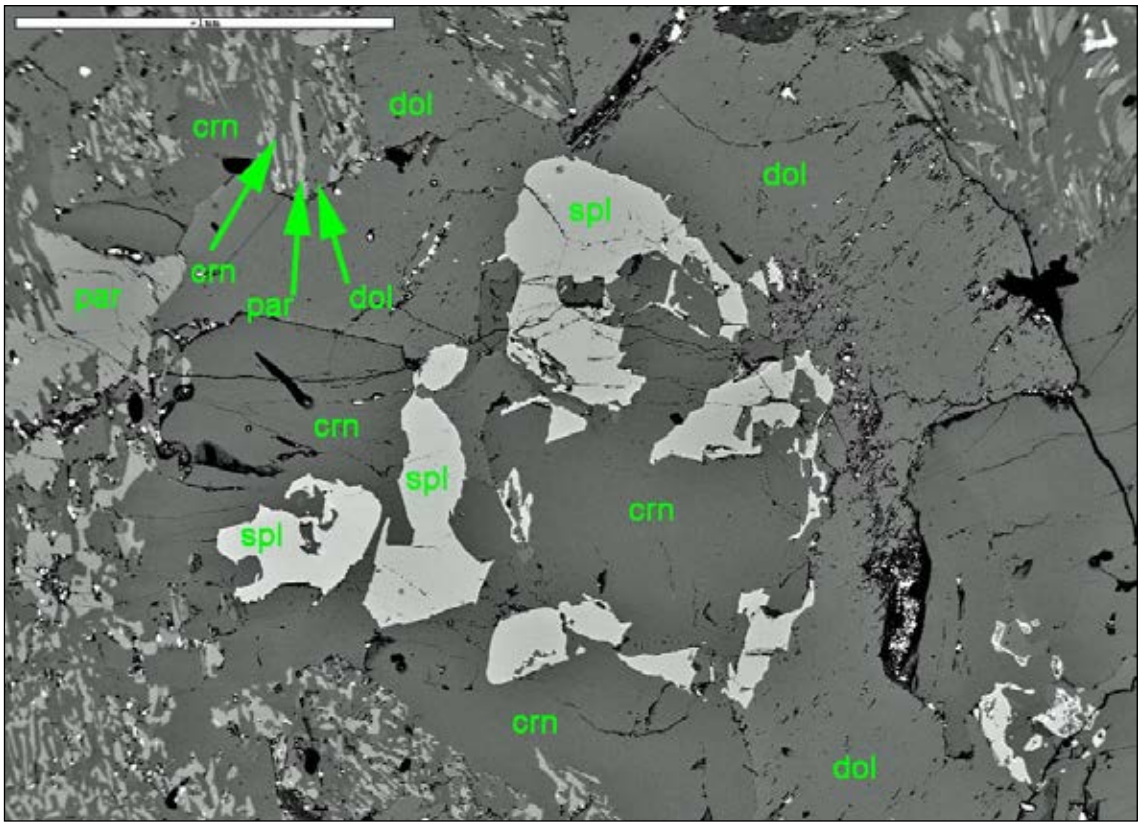

Fig. 4.28: In this BSE image from sample TZM07 the reaction dolomite + corundum = calcite + spinel can be seen in the center of the picture. This reaction is recognised to define the minimum condition for M1 metamorphism in the Uluguru Mts. A symplectite to the upper left corner further indicates a rapid change in fluid composition which forced these minerals to grow instantly exposing a texture describing a state of disequilibrium.

the individual conditions of the mines were combined to minimum conditions for the two deposits, the Uluguru and the Mahenge Mts (Tab. 4.21). The values indicated are still minimum values and in the case of pressure and X_{CO2} can be even higher in reality for the case of the Mahenge Mts. The minimum conditions found for both deposit however clearly describe conditions for a metamorphism to have taken place at Granulite facies conditions.

	T [°C]	P [kbar]	X_{CO2}
Uluguru Mts			
Mwalazi Mine	650	-	0.24
Visakazi II Mine	740	8.5	0.87
Conclusion	**740**	**8.5**	**0.87**
Mahenge Mts			
Kitwaro Mine	760	3.9	0.67
Ipangko Mine	705	5.4	0.17
Conclusion	**760**	**5.4**	**0.67**

Tab. 4.21: Results of minimum thermodynamic conditions for M1 indicate that peak metamorphism in the Uluguru and the Mahenge Mts took place at Granulite facies.

CHAPTER V

GEMMOLOGY

5.1 Traditional Gem Testing

Because the physical and optical properties had been tested for rubies from the Morogoro Region by Hänni & Schmetzer (1991) already, only a small group of samples from the Uluguru and the Mahenge Mts were examined to confirm their gemmological parameters. In contrary, pleochroism and reaction to UV light was tested for all rubies which were examined either by FTIR and/ or UV-vis.

5.1.1 Description of the Rough

Since the crystal morphology was described in detail by Hänni & Schmetzer (1991) already it was decided not to undertake further crystallographic examinations on rubies from the Mororogoro Region during this study. Regarding the habit of rough the following statements still would like to be made however.

There were three main types distinguishable similar to what was mentioned by Hänni & Schmetzer (1991) already. There were flattened to tabular crystals, pseudo-cubic, and corroded specimens with irregular terminations observed. Among these three habits the corroded form with irregular terminations was found to be the most common. The more euhedral habits are rarer but more frequent in crystals of better quality. As crystallographic examinations by Hänni & Schmetzer (1991) revealed the basal plane c (0001) and the positive rhombohedron r (10-11) are the main crystal faces exhibited by rubies deriving from the Morogoro Region. Rubies in which the rhombohedral faces r and r' were dominant tend to form pseudo-cubic crystals. In all samples examined by Hänni & Schmetzer (1991) two of the eight corners of each individual crystal "cube" were cut by triangular faces representing the basal planes c leading to a habit resembling the one of spinel octahedra. The fact that in corundum the angles between rhombohedral faces r and r' is 93.9° and not 109.5° as recorded for spinel may be used as a tool to differentiate the two minerals in rough were other methods of separation are difficult to apply. Finally, it was further reported that six subordinated prism faces a (11-20) were observed in a few samples. In contrast to samples from Mogok, Myanmar (Burma) but in rare cases only the examined rubies exhibited hexagonal dipyramids n (22-43) (Fig. 5.1).

The rough produced in the Morogoro Region usually reaches the local market as broken pieces of roughly 1 to a few carats in size. Most of these samples are heavily fractured and show intersecting traces of twinning on their surfaces affecting the gemstones transparency and overall appearance. Therefore most of the samples produced today are of cabochon grade only and may have to be improved by either heat treatment applying a flux or had to undergo the process of glass-filling in order to reduce the effect of the ruptures reaching a gem's surface.

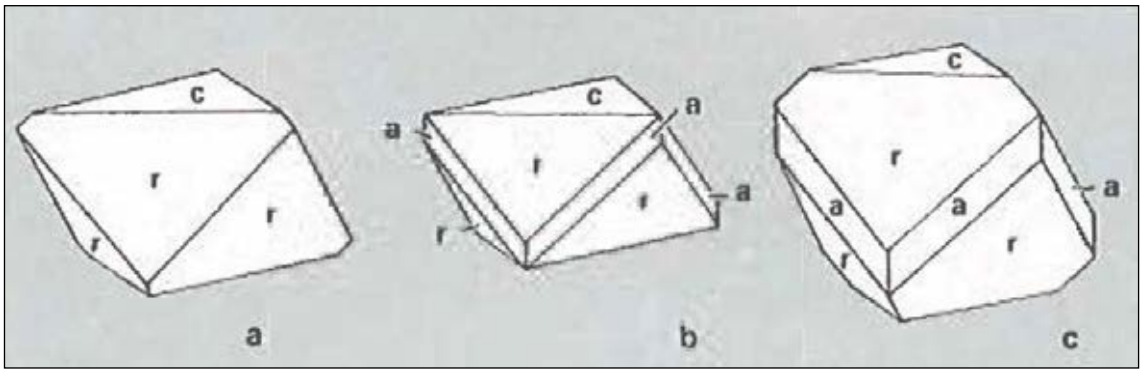

Fig. 5.1: Crystal faces observed in Morogoro Region rubies resembling frequently the octahedral habit of spinel. Subtle differences in face angles allow a differentiation of the two minerals based on their habitus however (after Hänni & Schmetzer, 1991).

5.1.2 Visual Appearance

The colour in Morogoro Region rubies range from pale pink (very light, slightly greyish) to intense red and purplish red (medium dark, strong). Most of the rubies coming from either the Uluguru Mts or the Mahenge Mts are of medium saturation however and possess a tint of purple as a modifier resulting in a raspberry like colour. Colour zoning was visible by the unaided eye in a small number of samples only.

As mentioned before, most of the rough is heavily cracked and/or contains fissures reaching the surface. In accordance to Hänni & Schmetzer (1991) diaphaneity can be described as translucent to transparent depending on the number of inclusions and cracks a stone in particular contains.

It was further observed that the mines in the planes below Mahenge town tend to produce somewhat finer material in terms of transparency than what is found elsewhere in the Mahenge Mts. In the Uluguru Mts the production from the mines Visakazi II and Msonge are of the best quality form the region in terms of colour saturation and clarity.

5.1.3 Physical Properties

The examination by a hand held dichroscope revealed pleochroism in rubies from the Morogoro Region to be similar to what is observed in rubies from other marble-hosted deposits as well. Mostly the pleochroism is moderate in intensity displaying an orangy red colour parallel to the c-axis and a purplish red colour perpendicular to the c-axis.

When illuminated by a strong fiber-optic light a hazy blueish sheen was observed in about a quarter of the rubies originating from the Uluguru Mts. The observed phenomenon is related to a scattering effect of white light on very fine dispersed inclusions (pers. comm. Michael Krzemnicki). Rubies from the Mahenge Mts however showed this phenomenon in rare cases only. The described blueish sheen is also known to be found in rubies from other marble-hosted such as Jegdalek/ Afghanistan, Murgab/ Tajikistan, and Luc Yen/ Vietnam.

Exposed to long-wave ultraviolet radiation (365nm) a medium to strong orangy red fluorescence was usually observed whereas the reaction to short-wave ultraviolet (254nm) radiation was a somewhat weak to faint red fluorescence only.

Viewed with a spectroscope rubies from the Morogoro region showed always a doublet of two sharp lines located at the red end of the spectrum at 692 and 694nm respectively. Another pair of sharp lines were observed frequently at 475 and 476nm. Finally, a broad band between 500 and 600nm however weakly visible only, had been observed in several cases.

The physical properties were examined by standard gemmological methods on a selected group of samples from both the Uluguru (n=11) and the Mahenge Mts (n=8) only. The values shown in Tab. 5.1 are generally in good accordance to what is described for corundum by Webster (1994). In average the specific gravity (SG) was found to be in the range of 3.97 +0.10/-0.06g/cm^3 for both localities. Due to a usually large variation in SG, the values calculated for the tested samples may not be taken as a general reference value for rubies originating from the Morogoro Region. In fact, if the stones were clean their SG ranged between 3.97 and 4.01g/cm^3 which is consistent with what was mentioned by Hänni & Schmetzer (1991) previously.

The refractive indices (RI) in contrary are much more in the range which is commonly observed in rubies. Here values of 1.771-1.763 for Uluguru-rubies as well as 1.770-

"Uluguru Mts."

Reference Number	Mine Locality	SG	RI		Bi-refrigence
RUTZM-11-7C	Mwarazi	4.07	1.770	1.762	0.008
RUTZM-11-10C	Mwarazi	4.04	1.770	1.762	0.008
MA3-2C	Mwarazi	3.96	1.770	1.761	0.009
RUTZM-50-2C	Msonge	3.95	1.770	1.761	0.009
RUTZM-50-3C	Msonge	3.94	1.771	1.763	0.008
RUTZM-50-4C	Msonge	3.91	1.770	1.762	0.008
RUTZM-53-6C	Visakazi II	3.91	1.770	1.762	0.008
RUTZM-53-9C	Visakazi II	3.93	1.770	1.760	0.010
RUTZM-53-13C	Visakazi II	3.97	1.770	1.762	0.008
RUTZM-54-1D	Morogoro Region HT	4.01	1.778	1.770	0.008
RUTZM-54-5D	Morogoro Region HT	4.01	1.774	1.767	0.007
average		3.97	1.771	1.763	0.008

"Mahenge"

Reference Number	Mine Locality	SG	RI		Bi-refrigence
M3-2C	Mayote	3.94	1.770	1.761	0.009
RUTZH-05-11C	Mayote	3.97	1.770	1.760	0.010
RUTZH-06-5C	Mayote	3.95	1.770	1.763	0.007
M4-8C	Lukande	4.02	1.770	1.761	0.009
RUTZH-10-2C	Lukande	3.98	1.770	1.763	0.007
RUTZH-11-5C	Lukande	3.94	1.770	1.765	0.005
M1-4C	Epangko	4.01	1.770	1.763	0.007
RUTZH-22-4C	Epangko	3.92	1.770	1.763	0.007
average		3.97	1.770	1.762	0.008

Tab. 5.1: Physical properties as tested for a limited number of samples from the Morogoro Region, Tanzania. Interesting are the variations in SG for samples with numerous inclusions.

1.762 for Mahenge-rubies are recorded in average. The resulting bi-refringence values is 0.008 for both localities respectively.

5.1.4 Microscopic Characteristics

By applying gemmological microscopy to all of the 80 samples examined in this study several growth features and inclusions had been observed in rubies from the Morogoro Region, Tanzania. First of all pronounced twinning along rhombohedral faces is prominent and observed frequently in rubies form the Morogoro Region. The twinning planes often occur in two sets and intersect at a typical angle of almost 90°. Along the trace of these intersecting slip-planes hollow tubes formed which are frequently filled with a translucent, poly-crystalline substances identified as diaspore, boehmite or gibbsite by Fourier Transform IR-Spectrometry (FTIR) (see chapter 5.2.2). Such tubes are observed frequently in rubies from the Uluguru Mts and occasionally in rubies from the Mahenge Mts respectively (Fig. 5.2).

As a specialty compared to the rubies from the Mahenge Mts it was observed that rubies from the Uluguru Mts occasionally showed fine but deeply red coloured rims along repeated twinning planes. Further, there are angular, hexagonal looking growth structures visible, accompanied by diffuse to distinct colour zoning. In rubies from the Mahenge Mts in the contrary "swirl"-like growth features, as known typically in rubies from Mogok Myanmar (Burma), could occasionally be observed where intergrowing growth structures formed a complex pattern (Fig.5.3 & Fig.5.5). In contrast to other rubies coming from marble-hosted deposits (except Mogok, Myanmar (Burma)) none of the Morogoro Region rubies showed blue colour zones.

Healed fissures were observed with elongated, thin, and bent voids producing a particular pattern along the fissure's contact plane known as "fingerprints". When the

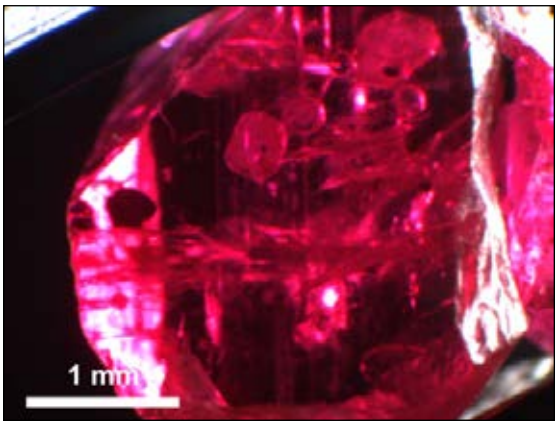

Fig. 5.2: Sample RUTZM-53/12C from Visakazi II Mine, Uluguru Mts shows large, rounded, colourless apatite crystals together with angular shaped, turbid, whitish carbonate crystals. The long and parallel tubes penetrating the sample vertically were identified to be filled by boehmite. Zircon is present as small rounded colourless crystals with equatorial tension fissures. Finally, graphite was observed as black flakes. Magnification 25x.

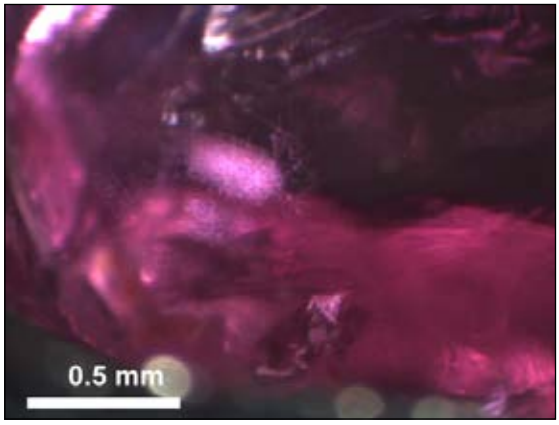

Fig. 5.3: In Sample M4/ 9C from Lukande, Mahenge Mts a nest of rutile silk is visible. Just above a few fine, singular needles accompanied by iridescent particles are able to be distinguished. To the bottom right, complex growth structures form a pattern known as swirls. Magnification 50x

healing process of fissures was almost perfect, the contact planes were decorated with small pseudo-octahedral negative crystals instead (Hughes, 1997). Few fissures also showed a frosted looking surface covered by Aluminium-Hydroxides such as diaspore, boehmite or gibbsite indicated by FTIR (see chapter 5.2.2).

Beside in healed fissures negative crystals occurred rarely in rubies from the Uluguru and were observed occasionally in rubies from the Mahenge Mts only. Negative crystals were either empty or filled with one or two phases. As Hänni & Schmetzer (1991) indicated before, it was sometimes difficult to verify by microscopy only whether a pseudo-octahedral looking feature was indeed a negative crystal or in fact a spinel inclusion. In contrast to Hänni & Schmetzer (1991) the examined pseudo-octahedral features in this study turned out to be voids in most cases however (Fig. 5.4).

Rutile was come across occasionally as transparent orangy brown to translucent or opaque brown to almost black grains or rods (Fig.5.4). Rutile was further present as "silk", a dense combination of minute reflective rutile needles and dust-like particles, also. "Silk" was observed frequently in whitish, turbid clouds or angular bands in both Uluguru as well as Mahenge rubies (Fig.5.3). Also flake-like inclusions as known from Jegdalek/ Afghanistan, Luc Yen/ Vietnam or Mong Hsu/ Myanmar (Burma) had been seen. Stringers as mentioned also in rubies from Mong Hsu or Chumar and Ruyil/ Nepal completed the inclusion scene. Anntenae-like, cross-hatch, or brush-stroke like inclusions as they are reported for rubies from Chumar and Ruyil, Mong Hsu or Jegdalek respectively were absent in rubies from the Morogoro Region however.

Short, colourless prisms of apatite were observed as an additional and very frequent inclusion (Fig.5.5). Similar short apatite columns are also known to be found

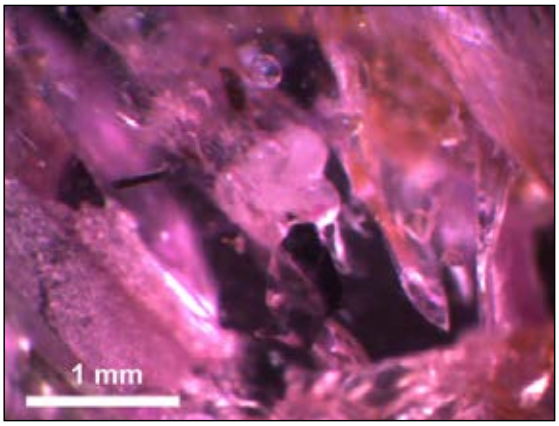

Fig. 5.4: In the middle of this microphotograph of sample RUTZM-53/ 8C from Visakazi II Mine, Uluguru Mts a conglomerate of rounded, turbid, whitish carbonate and rounded, colourless apatite inclusions is visible. Below an opaque, black graphite flakes is recognisable whereas above a colourless, angular inclusion turned out to be a neg. crystal containing an undefined liquid and CO_2-rich gas phase. To the right a small rounded crystal with tension fissures was identified to be zircon. Finally, there is also an opaque, black rod of massive rutile to be seen next to the graphite inclusion in this sample. Magnification 25x.

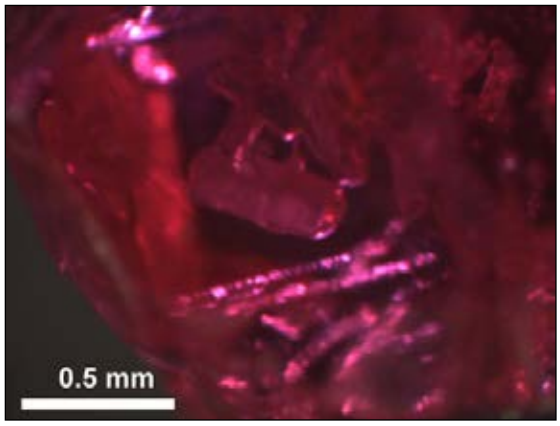

Fig. 5.5: Well crystallised apatite inclusions as euhedral short columns are found in sample RUTZH-11/ 2C from Lukande, Mahenge. Swirls towards the left resembling a growth feature typically known for rubies from Mogok, Myanmar (Burma) indicate the presence of complex growth patterns. Magnification 50x.

in rubies deriving from Myanmar (Burma), Vietnam or Afghanistan. Mostly apatite is encountered as rounded, colourless or somewhat turbid inclusions however (Fig.5.3, Fig.5.5, Fig.5.7). A next inclusion occurring almost at the same frequency is present as transparent, colourless or translucent, turbid, white crystals sometimes occurring in rounded to ondulous shapes and other times as angular, rhombohedric prims. These inclusions were identified as to be either the carbonate phase calcite or dolomite (Fig.5.2, Fig.5.4, Fig.5.6). The differentiation whether an inclusion was either calcite or dolomite was not possible by microscopy only and therefore based on Raman-Spectrometry (see chapter 5.2.1). Opaque dark graphite-flakes with sometimes pseudo-hexagonal shapes and almost metallic luster were seen frequently in rubies from the Uluguru Mts however rarely in rubies from the Mahenge Mts (Fig.5.2, Fig.5.4, Fig.5.6). Where graphite occurred as small flakes they formed turbid dark looking clouds. Zircon was not as abundant but still viewed frequently in all Morogoro Region rubies as transparent, colourless, rounded crystals. Zircon occured either as isolated crystals or when small in size often as swarms. Further, zircon inclusions exhibited frequently disk-like equatorial tension fissures also know as "Saturn" inclusions (Fig.5.2, Fig.5.4). Occasionally in rubies from the Uluguru Mts but rarely in rubies from the Mahenge Mts the sodium-rich amphibole pargasite as well as the iron-sulfide pyrite was seen. Pargasite formed as transparent, colourless, small acicular, sometimes ondulous crystals (Fig. 5.8). Pargasite is reported to be present in rubies also from Mogok/ Myanmar (Burma), Hunza/ Pakistan, and Jegdalek/ Afghanistan only. Pyrite on the other hand occurred sometimes as small, irregular crystals and other times as nicely crystallised cubes but always opaque with a metallic luster and brassy colour (Fig.5.6). It is to be notified that in literature pyrite is not mentioned to occur in rubies from Nepal.

The rest of the identified mineral inclusions were rarely seen only but with high diagnostic value in terms of origin determination by inclusions.

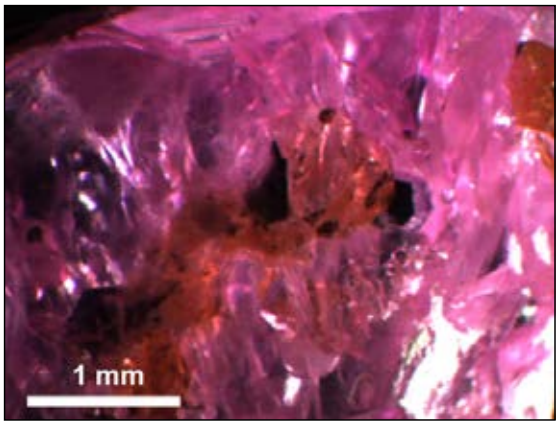

Fig. 5.6: Yellow tourmaline of uvite composition was found with opaque, black graphite flakes and pseudo-hexagonal phlogopite platelets. An opaque, rounded, brassy coloured grain of pyrite is seen above the tourmaline in this microphotograph. Finally, small, colourless spheres of apatite and larger turbid whitish crystals of a carbonate phase complete the inclusion scene of sample RUTZM-53/ 8C, Viasakazi Mine, Uluguru Mts. Magnification 25x.

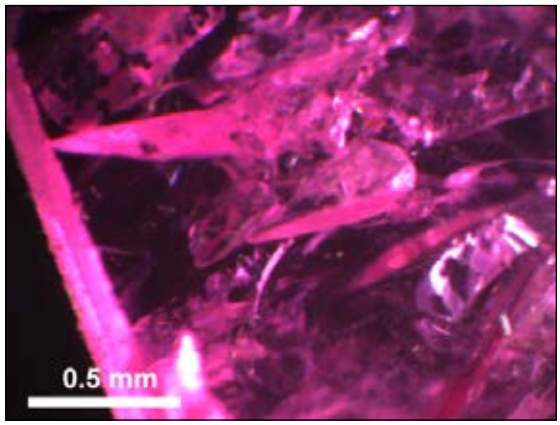

Fig. 5.7: In this microphotoprahy wedge-shaped crystals can be seen in the center. Unforunately, it wasn't possible to clearly determine whether these crystals are dolomite or magnesite inclusions due to similar Raman reference spectra. Most other features seen in this picture are related to fissures and fractures penetrating sample RUTZM-53/ 11C, Visakazi II Mine, Uluguru Mts. Magnification 50x.

The transparent, colourless wedge-shaped inclusions found in rubies from both the Uluguru and Mahenge Mts were not possible to be identified exactly whether they are dolomite or magnesite inclusions. This uncertainty derives from almost identical Raman reference spectra of the two minerals in question. In case they were indeed magnesite crystals this would be the first time this mineral is reported as an inclusion in rubies (Fig.5.7, see Appendix B.1). Unfortunately, there were no such inclusions exposed directly to the surface of a sample and therefore could not be examined any further.

Spinel in the contrary was identified clearly and observed as in rare cases as colourless octahedral inclusions in Uluguru rubies. Brown, transparent to translucent pseudo-hexagonal platelets were identified as phlogopite in rubies from the Uluguru Mts (Fig.5.9). Margarite, another mica mineral phase and absent in rubies from Mogok Myanmar (Mogok) was noted in Uluguru Mts rubies in rare occasions. A last rare mineral inclusion observed in rubies form the Uluguru Mts was yellow tourmaline of uvite to dravite composition (Fig.5.6, see chapter 4, Appendix B.1). Beside the Morogoro Region, tourmaline are further known to be present as inclusions in ruby specimens from Chumar & Ruyil, Nepal and Hunza, Pakistan only.

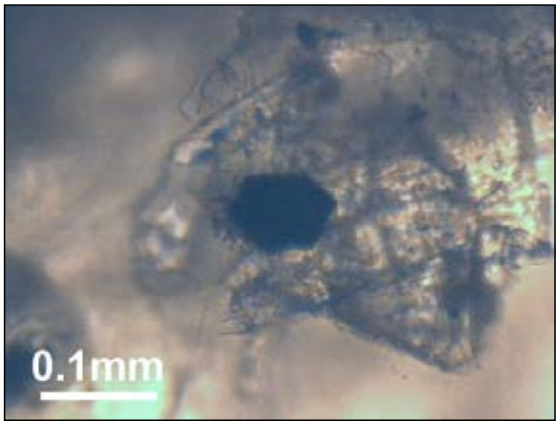

Fig. 5.8: In sample RUTZH05/ 4C there is an acicular inclusion observed which was identified to be pargasite amphibole (red arrow). The colourless inclusion underneath was found to be calcite. Magnification 200x.

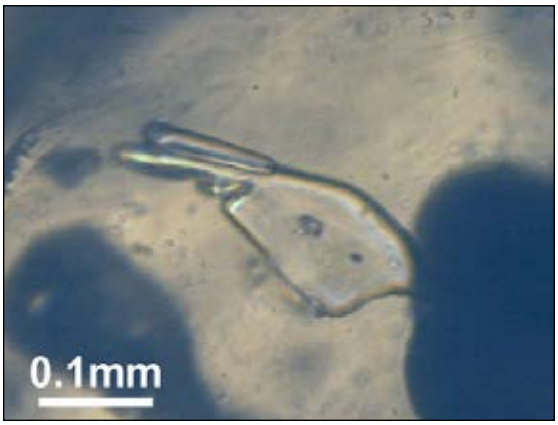

Fig. 5.9: Sample RUTZM-53/ 11C from Visakazi II Mine, Uluguru Mts contained a nicely formed pseudo-hexagonal phlogopite platelet. Magnification 200x.

In rubies from the Mahenge Mts on the other hand there were two more mineral phases identified. Colourless anorthite feldspar as small undulous inclusions, and titanite as slightly brownish crystals (see Appendix B.1). Regarding their potential for origin determination between rubies from other marble-hosted deposits it is to be mentioned that anorthite is reported to be present in rubies form Mong Hsu, Chumar & Ruyil, as well from Murgab/ Tajikistan but being absent in rubies from Jegdalek/ Afghanistan. Titanite finally, is known in rubies from Mogok, Luc Yen, Jegdalek, and Murgab as mentioned in literature. Garnet as described by Hänni & Schmetzer (1991) had not been seen in the samples examined however. Also fluorite which is diagnostic for rubies from Mong Hsu had never been encountered in rubies from the Morogoro Region.

After all and as mentioned above, the majority of the samples were heavily fractured. Often these fractures were filled with an orangy looking staining substance of iron-rich composition such as known for goethite or limonite.

5.1.4.1 Distinctive Inclusion Features

The observations made by microscopy during this study gave reason to further investigate inclusion features to evaluate whether specific combinations may have distinctive characteristics to be used in origin determination. Consequently, an in depth literature research on inclusion features recorded in marble-hosted rubies was carried out during this study as well. The results are summarised below in Tab. 5.2.

5.2 Advanced Gemmological Examinations

The advanced testing methods applied in the framework of this study are mainly spectrometric techniques. These techniques offer a versatile range of possibilities to test gemstones without destructive sampling. Therefore, various spectrometric techniques established as standard advanced gemmological testing methods in the field of gemmology and are widely applied in gemlabs around the world.

5.2.1 Raman Spectrometry

As mentioned above a Renishaw, InVia, Raman unit was employed to identify mineral inclusions found in rubies during this research project. Once the Raman Shift spectra were collected they were match-searched by a built-in reference database to confirm the inclusions' identity. Since the observed mineral phases had been discussed in the previous chapter it is neglected to go into further details here again. Selected Raman Spectra can be found in Appendix B.1 however.

5.2.2 Fourier Transformed Infrared Spectrometry (FTIR)

Already in the late 1970's FTIR entered the arsenal of analytical methods applied in gemmology. FTIR was used for various purposes ever since (Suhner 1979, Fritsch & Stockton 1987). Diamond type determination, indirect determination of heat treatments in corundum, separation of natural from synthetic quartz, as well as identification of filling materials in emeralds are a few of the large variety of FTIR applications known in gemmology today.

In the previous gemmological work by Hänni & Schmetzer (1991) it was left undone however to examine ruby samples from the Morogoro Region by FTIR. Therefore, this situation was taken as an opportunity to carry out a major FTIR investigation during

this study :

locality		hazy blueish sheen	blue colour zones	swirl structures	neg. xtls primary	silk	apatite	graphite	zircon	pargasite amphibole	spinel
Uluguru Mts (n=37)	Tanzania	x	-	-	(x)	xx	xx	xx	x	x	(x)
Mahenge Mts (n=43)	Tanzania	(x)	-	x	x	xx	xx	(x)	x	(x)	-

literature :

locality		hazy blueish sheen	blue colour zones	swirls structures	neg. xtls primary	silk	apatite	graphite	zircon	pargasite amphibole	spinel
Uluguru & Mahenge	Tanzania			+	+	+	+	+	+		+
Luc Yen	Vietnam	+	+	+	+	+	+	+	+		+
Yuan Jiang	China	+		+		+	+		+		
Mong Hsu	Burma		++				+				+
Mogok	Burma			++	+	++	+	+	+	+	+
Chumar & Ruyil	Nepal	+	+	+	+	+	+	+	!		
Nagimali	Pakistan		(+)		(+)	+	+				
Hunza	Pakistan			+	+	!	+	+		+	+
Jegdalek	Afghanistan	+	++	+	(+)	+	+	++	+	+	+
Murgab	Tajikistan	+	++		++	+		+	+		

- : not found by the author in the samples examined in this study
(x) : rarely observed in the samples examined in this study, <10%
x : occasionally observed in the samples examined in this study, >10%
xx : frequently observed in the samples examined in this study, >50%
xxx : commonly observed in the samples examined in this study, >75%

: not mentioned in literature
(+) : mentioned in literature as to be rarely observed
+ : mentioned in literature but no further specification regarding the frequency
++ : mentioned in the literature as to be observed frequently
! : mentioned in literature as to be absent

Tab. 5.2:
Compared to previous publications it was possible to identify nine additional inclusion phases and one colour feature for rubies from the Morogoro Region, Tanzania during this study. According to the presented compilation of inclusion features found in rubies from marble-hosted deposits origin characteristic mineral inclusion assemblages are possible to be defined.

Further, the following common mineral inclusions had been observed but not included into the list. They are however generally found in rubies of all the investigated marble-hosted deposits: boehmite/diaspore, calcite/dolomite, kaolinite as well as massive rutile crystals.

this study :

locality	phlogopite	margarite	chlorite	gibbsite	tourmaline	anorthite	titanite	pyrite	zoisite	garnet	fluorite	references
Uluguru Mts (n=37)	(x)	(x)	(x)	(x)	(x)	-	-	x	-	-	-	this study
Mahenge Mts (n=43)	-	-	-	(x)	-	(x)	(x)	(x)	-	-	-	this study

literature :

locality	phlogopite	margarite	chlorite	gibbsite	tourmaline	anorthite	titanite	pyrite	zoisite	garnet	fluorite	references
Uluguru & Mahenge										+		1, 3, 11
Luc Yen	+	+		+	+		+	+				5, 6, 7, 9, 10, 13, 14, 15
Yuan Jiang												2
Mong Hsu	+		+			+			+		+	9, 10, 13, 17, 18, 19, 20
Mogok	+	!		(x)	(x)		+	+		+		6, 9, 10, 11, 13, 19
Chumar & Ruyil	++	+			+	+		!	+			4, 9, 10, 12, 22
Nagimali								++				9, 10, 16
Hunza	+	+	(+)					+				6, 8, 9, 10, 13
Jegdalek	+	+			!	!	+	+		+		4, 9, 10, 13, 16
Murgab						+	+					16, 21

references :

1) Balmer et al. (2009)
2) Balmer et al. (2010)
3) Bank & Henn (1989)
4) Bowersox et al. (2000)
5) Garnier et al. (2002)
6) Garnier et al. (2008)
7) Giuliani et al. (2003)
8) Gübelin (1982)
9) Gübelin & Koivula (1997)
10) Gübelin & Koivula (2008)
11) Hänni & Schmetzer (1991)
12) Harding & Scarratt (1986)
13) Hughes (1997)
14) Kane et al. (1991)
15) Long et al. (2004)
16) Pardieu et al. (2009)
17) Peretti et al. (1995)
18) Peretti et al. (1996)
19) Schlüssel (2002)
20) Smith (1995)
21) Smith (1998)
22) Smith et al. (1997)

this study instead. It was the aim to close this gap in describing the marble-hosted rubies from the Uluguru and Mahenge Mts by FTIR as an advanced gemmological testing method as well as to further explore the analytical potential of this widely available technique in the world of gemmology.

5.2.2.1 FTIR Fingerprinting

FTIR fingerprinting, the approach to compare FTIR signatures of known reference minerals with a sample spectrum in order to identify superimposed spectrum features derived from mineral inclusion phases, is not yet carried out systematically in gemmology. Only a few Aluminium- and Iron-Hydroxide phases such as diaspore, boehmite and goethite along with the minerals chlorite and kaolinite are considered routinely in corundum today. Due to a large overlap in the occurrence of these mineral phases in corundum from various deposits the detection of such mineral inclusions had no implication for origin determination purposes so far. Therefore, attempts to further investigate the potential of FTIR fingerprinting as an application for origin determination had not yet been undertaken in gemmology.

5.2.2.2 Obstacles in Terms of FTIR Fingerprinting Applied on Corundum in Gemmology

One reason for the failure of FTIR fingerprinting to establish as a useful method for origin determination in the past may be found in the databases which are available. FTIR databases focus typically on a spectrum range where FTIR fingerprinting is

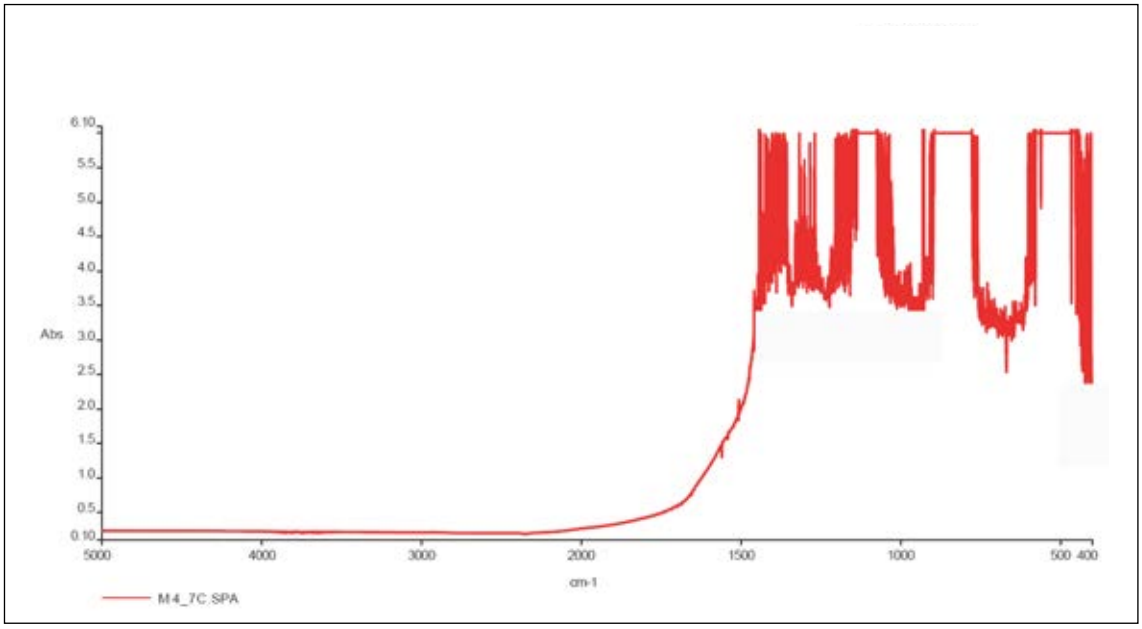

Fig. 5.10: An nearly undisturbed corundum spectrum was recorded on a ruby single crystal from the Lukande Mine, Mahenge Mts (sample M4_7C). This full range FTIR spectrum between 400 to 5000cm^{-1} reveals elevated absorption behaviour of corundum in the range below 1500cm^{-1}. This makes it impossible to use standard databases data for FTIR fingerprinting on corundum samples. A specific database which focuses on the range above 1500cm^{-1} has to be created therefore.

applied in inorganic chemistry or material sciences, in the range between 400 and 2000cm^{-1}. This range however is blocked in the case of corundum by a strong absorption of corundum itself (<400-1500cm^{-1}) and therefore not applicable for FTIR fingerprinting (Fig. 5.10). To be able to indentify superimposed signals of inclusions or sub-microscopic impurities in corundum, reference data of mineral samples in this very specific spectral range is crucial however.

The open source internet based RRUFF project data base (available online from : http://rruff.info) would contain such a collection for examples where a large number of FTIR spectra of various reference minerals are compiled. Unfortunately for the case of gemmology, the spectra are often collected in attenuated total reflectance mode (ATR) which shows high noise to signal ratios and low sensitivity in the spectral range above 1500cm^{-1}. Further, the reference spectra contained in the RRUFF database do not cover the range above 4000 cm^{-1} (Fig. 5.11). Due to the lack of suitable reference spectra data, features in the range above 1500cm^{-1} and especially beyond the water stretching vibration range (>3700cm^{-1}) hadn't been taken into account much in gemmology up to present.

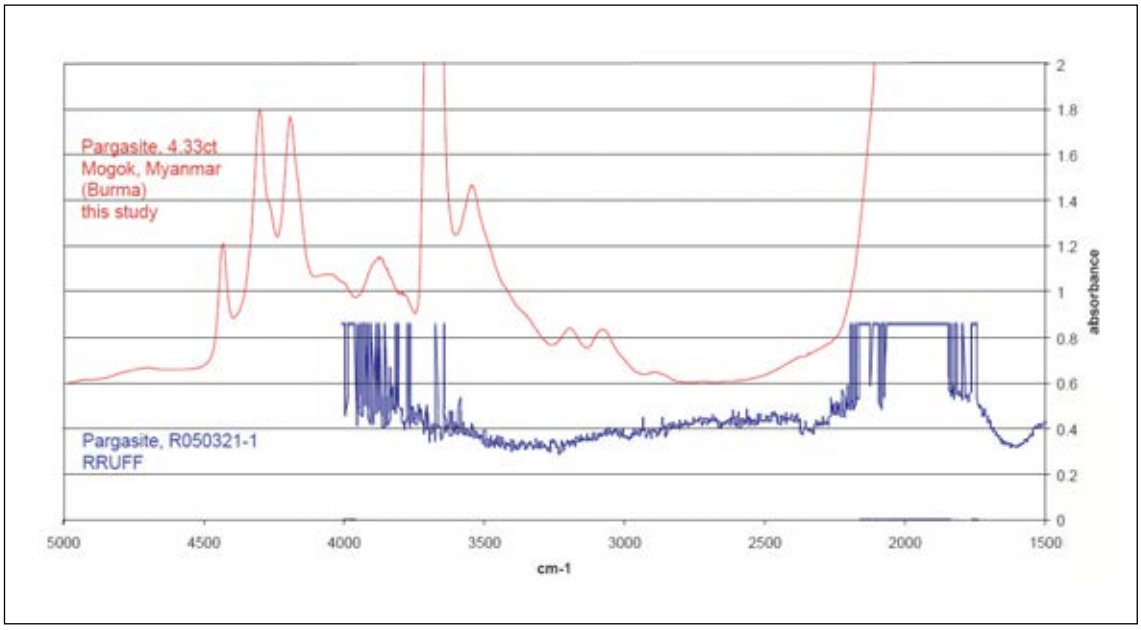

Fig. 5.11: Differences in two pargasite amphibole reference spectra in terms of sensitivity and spectral range becomes obvious in the displayed spectral range. The spectrum from sample R05032-1 is available from the online RRUFF project data base and was collected from a mineral fragment in ATR mode whereas the reference spectrum collected in this study was obtained from a mineral sample weighing 4.33ct by applying a beam condenser unit.

An other reason why FTIR fingerprinting did not establish in gemmology as an analytical method is the fact that the vibronic centers in the examined range above 1500 cm^{-1} are mostly overtones of fundamental vibrations and not fundamental vibrations itself. Overtones are found at positions which correspond to a multitude of the initial wavenumbers of a given fundamental vibration. These overtones are per se lower in intensity than the fundamental vibrations (pers.comm. E. Libowitzky, University of Vienna). Superimposed on a corundum spectrum and in some cases even interfering with atmospheric artefacts such as water vapour contained in air, an overtone signal can easily be missed.

To tackle this unsatisfying situation it was tried to close this gap by collecting a first set of FTIR reference spectra matching the specific requirements in gemmology. Subsequently, FTIR spectra beyond 1500cm^{-1} were collected from macroscopic single crystals where available or KBr reference samples from powdered sample materials where necessary (e.g. gibbsite). A selection of these FTIR reference spectra is attached in Appendix B.2.

5.2.2.3 Reference Material

The examined macroscopic reference mineral samples included the amphibole varieties actinolite and pargasite, the carbonate mineral dolomite, tourmaline, scapolite and the Alumium-Hyroxide diaspore. Whereas the KBr reference samples included the mineral phases calcite and magnesite, the mica phases chlorite, and phlogopite, as well as the Aluminum-Hydroxide gibbsite.

5.2.2.4 Sample Material

Subsequent to the reference spectra collection an FTIR investigation for potential FTIR fingerprinting was carried out on rough, untreated ruby samples. Out of the 80 loose samples which were introduced in chapter 1 there were rubies from the Uluguru Mts (n=27), the Mahenge Mts (n=33) both from the Morogoro Region, Tanzania as well as other marble-hosted ruby deposits such as Mogok, Burma (n=8), Murgab , Tajikistan (n=5), Luc Yen, Vietnam (n=7) and Yuan Jiang, Yunnan Province, China (n=7) measured.

Sample preparation was carried out as explained in chapter 1.

5.2.2.5 Common Mineral Inclusion Phases

Comparing the collected spectra with the data published by Beran & Rossman (2006) it can be stated that most of the examined samples contained either diaspore or boehmite as an Aluminum-Hydroxide phase. This was further confirmed by gemmolgical microscopy as polycrystalline substances in hollow tubes along intersecting twinning planes or frosted looking coatings along surface reaching fissures were observed. According to the collected reference data as well as the published FTIR signatures by Farmer (1974) and Balan et al. (2001) it was further possible to detect calcite and/or dolomite as well as kaolinite in many of the tested samples.

5.2.2.6 The Detection of Chlorite and Gibbsite by FTIR Fingerprinting

Beside these more common FTIR features there were also additional observations made. Traditionally in gemmology the peaks in the range from 3300-3700cm^{-1} had been related to chlorite group minerals. During the FTIR investigation in this study

however it was recognised that these peaks might have been misinterpreted occasionally.

The reason for calling a long standing interpretation into question is another phase which shows peaks in the same spectral range. In the examined water stretching vibration range from 3100-3700cm^{-1} gibbsite [Al(OH$_3$)], an Aluminium-Hydroxide, shows specific peaks at 3375/3395, 3470-3450, 3525, and 3620cm^{-1} (Tab.5.3). On the other hand, a chlorite KBr pellet sample investigated in the framework of this study as well as the spectra of chlorite group minerals published in the RRUFF project database lack the distinctive peak in the range of 3525cm^{-1} (Fig. 5.12). This particular peak however had been included as being part of the chlorite group peak series by various researchers in the past (e.g. Schwarz et al., 2008).

The second prominent peak of gibbsite at 3620cm^{-1} however may interfere with a peak related to kaolinite. Unfortunately, kaolinite shows a typical absorption in this range as well. A second characteristic absorption peak of kaolinite at 3695cm^{-1} (Bell et al., 1991, Balan et al., 2001) is missing in the FTIR signature of gibbsite however which makes these two mineral phases still distinguishable.

Chlorite			**Gibbsite**		
3420-3430	bp	RRUFF; Schwarz et al., 2006; this study	3375/3395	sp	Balan et al.. 2006a, Balan et al. 2006b, Kloprogge et al. 2002
3560-3575	bp	RRUFF; Schwarz et al., 2006; this study	3470-3450	bp	Balan et al.. 2006a, Balan et al. 2006b, Kloprogge et al. 2002
3675-3685	sp	RRUFF, this study	**3525**	sp	Balan et al.. 2006a, Balan et al. 2006b, Kloprogge et al. 2002
			3620	sp	Balan et al.. 2006a, Balan et al. 2006b, Kloprogge et al. 2002

Tab. 5.3: Peak list of chlorite and gibbsite in the range between 3000-4000cm^{-1}. Peaks in bold fonts are prominent features whereas peaks in regular fonts are subordinated features, sp stands for sharp peak where as bp represents broad peaks.

Taking gibbsite into consideration it was observed that several spectra of the analysed corundum samples in this study showed a good match with the mineral phase in question (Fig. 5.12).

In fact, gibbsite had been detected as a mineral phase forming inclusions in corundum before. Nordstrandite, a triclinic polymorph of gibbsite, was described in rubies coming from Vietnam by various authors already (first mentioned by Kane et al., 1991). The link to features found in FTIR spectra however were never made until today.

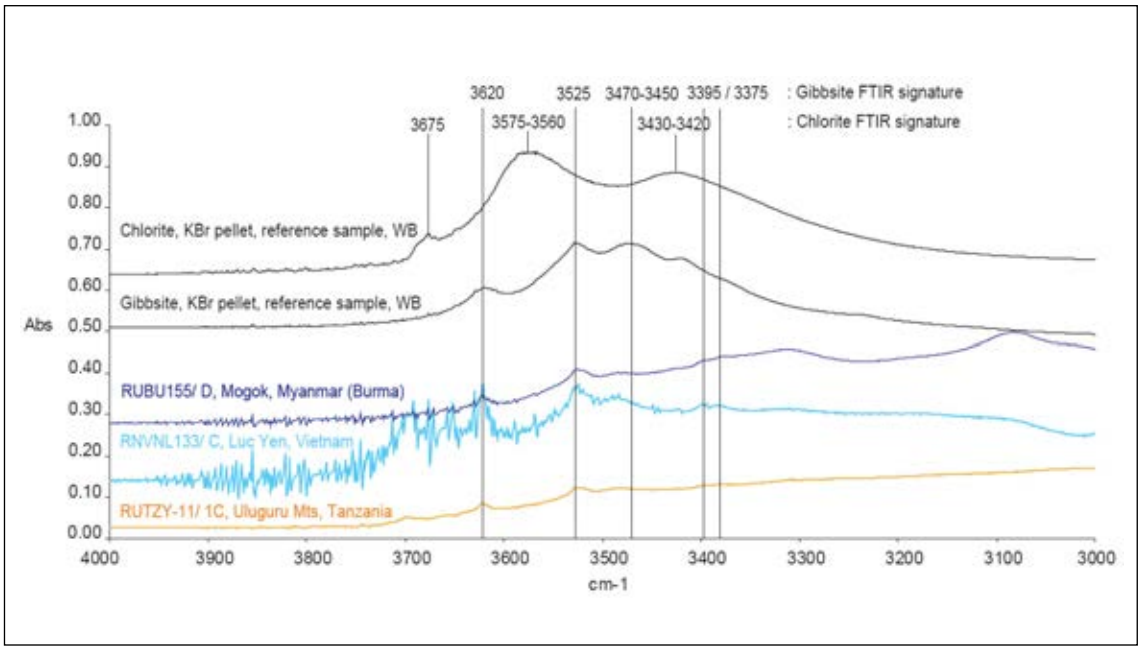

Fig. 5.12: The comparison of a chlorite and gibbsite FTIR spectra, obtained from two KBr pellets, reveals clear differences in the main features of the FTIR signatures of these two minerals. Consequently, a possibility to distinguish the presence of chlorite from gibbsite inclusions in ruby by FTIR occurs therefore.

In the same diagram there are three sample spectra shown were superimposed signal of gibbsite in single crystal ruby samples was recorded. Although the signal was not intensive it was still possible to clearly determine the presence of gibbsite in all of the three samples. The peaks not labelled in the spectra are caused by additional inclusions of kaolinite in sample RUTZY-11/ 1C or boehmite and calcite in RUBU155/ C respectively. To improve the clarity of the diagram, it was neglected to label the according peaks however.

5.2.2.7 The Detection of Tourmaline and Amphibole as Inclusion Phases in Marble-Hosted Rubies by FTIR Fingerprinting

Furthermore, it was also possible to detect two additional mineral phases by FTIR fingerprinting which have never been described in corundum by FTIR spectrometry in gemmology before. In both sample groups from the Uluguru Mts as well as the Mahenge Mts tourmaline and amphibole had been detected in several samples (Fig. 5.13 & Fig. 5.14). Surprisingly, even in one sample from Mogok, Myanmar (Burma) a weak tourmaline signature was detected as well. Surprisingly because this is the first time when tourmaline is described as a mineral inclusion phase in rubies from Mogok.

The diagnostic value of these mineral phases newly detected by FTIR in terms of origin determination for marble-hosted rubies is displayed above in Tab. 5.2.

5.2.3 Ultraviolet-visible-near Infrared Photospectrometry (UV-vis)

UV-vis spectrophotometry is another well-established analytical method which by now had been applied in gemmology for more than 30 years already. Especially in coloured gemstones, UV-vis spectrophotometry was a helpful method to investigate the effect and interactions of chromophores which are responsible for the colour of a given gemstone.

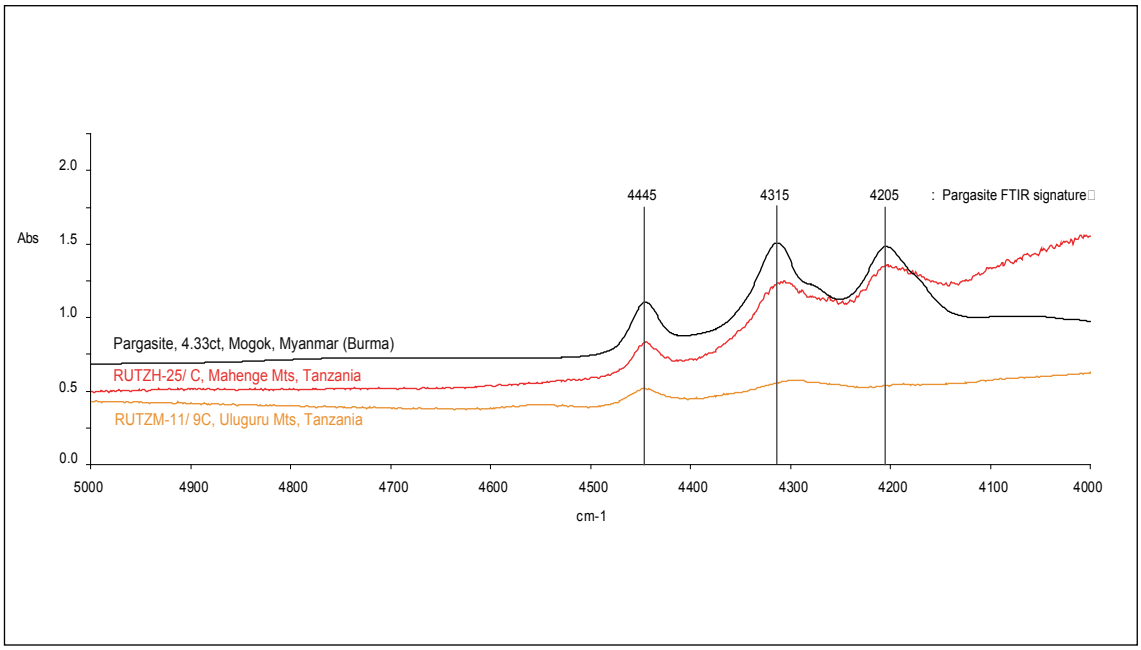

Fig. 5.13: The comparison of a FTIR spectrum of a transparent 4.33ct pargasite amphibole reference sample from Mogok, Myanmar (Burma) with the weak but still detectable superimposed signatures found in a rubies from the Uluguru Mts (RUTZM-11/ 9C) and the Mahenge Mts (RUTZH-25/ C) allowed the positive identification of amphibole as a mineral inclusion in the examined ruby samples.

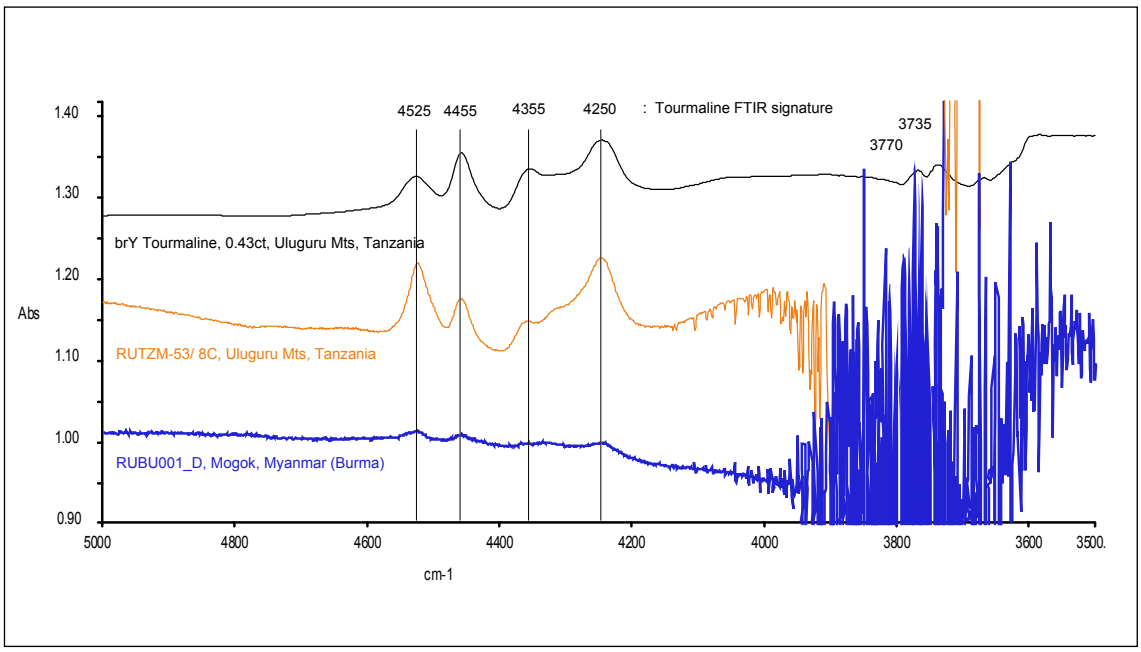

Fig. 5.14: FTIR reference spectrum of a brownish yellow dravite tourmaline from the Uluguru Mts, Tanzania was compared with ruby spectra collected in this study. The comparison revealed the presence of tourmaline as an inclusion phase. Sample RUTZM-53/ 8C derives from a marble-hosted ruby deposit in the Uluguru Mts Tanzania where as sample RUBU001/ D comes from Mogok Myanmar (Burma).

In the course of this study it was found however that there is a bigger potential for this method to be used as a tool in origin determination in gemmology. As it was observed ruby spectra showed variations in absorption patterns in respect to their origin especially in the UV-range (Fig. 5.15). These observations offered the opportunity to

take UV-vis spectra investigation beyond the usual description of chromophores and examine the potential of UV-vis as a tool for origin determination in further detail.

Already Bosshart (1982) was aware of the differences in UV-vis spectra and established a procedure to distinguish natural from synthetic rubies by UV-vis spectrum analysis. In this study this trace was followed and tried to adapt the procedure introduced by Bosshart (1982) for origin determination purposes on marble-hosted rubies.

5.2.3.1 Sample Material

For this part of the presented research 41 UV-vis spectra had been consulted. This included 10 Mogok ruby spectra from the original work of Bosshart (1982) as well as 31 new spectra which had been collected from ruby samples in this study. These new spectra were taken from 16 samples from the Uluguru and Mahenge Mts in the Morogoro Region, Tanzania, 10 samples from Luc Yen, Vietnam as well as from 5 additional samples from Mogok, Myanmar (Burma).

5.2.3.2 Description of UV-vis Spectra Obtained from Rubies from the Morogoro Region

The spectra collected by UV-vis showed two characteristic absorptions bands in the range of 400 and 550nm respectively. Additionally, there were several sharp peaks recorded which showed variations in their intensity due to polarisation. These peaks were found at 692/ 694nm, 659/ 668nm, 475/ 477nm, and 468nm respectively.

Finally, there was in rubies from both deposits, the Uluguru Mts as well as the Mahenge Mts, a shoulder at ~315nm observed occasionally (Fig. 5.15).

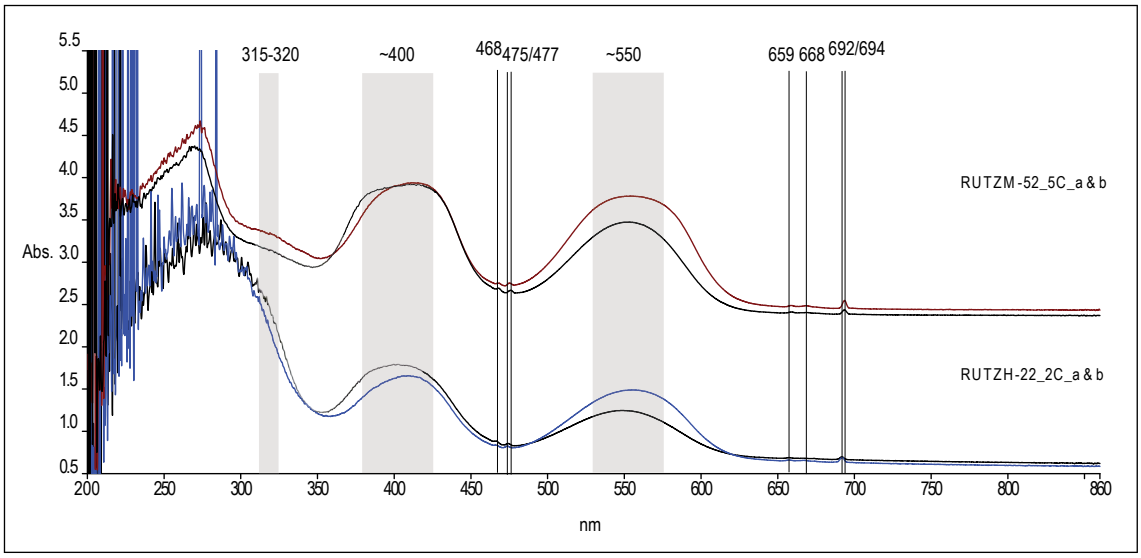

Fig. 5.15: Spectrum features found in rubies from the Morogoro Region (RUTZM-52_5C : Mwalazi Mine Uluguru Mts , RUTZH-22_2C : Ipangko Mine Mahenge Mts) are characterised by two main bands and several sharp absorption peaks. A shoulder around 315nm occurs occasionally only. Differences between the two displayed spectra are visible in the UV range especially.

After the more traditional description of chomophore related spectrum features the procedure of Bosshart (1982) was considered more in detail.

5.2.3.3 UV-vis Ruby Spectrum Analysis by Bosshart (1982)

Bosshart (1982) observed that in rubies, both of natural or synthetic origin, a distinct variation in the shape and depth of the absorption minimum in the UV range can be found. His approach was to numerically describe the shape and position of this absorption minimum by a horizontal profile laid at 0.5 absorbance units above the absolute absorption minimum and by λ and W representing the centre position and the width of the profile respectively (Fig. 5.16). The data set consisting of the absolute minimum position λ_0 and the profile coefficient (λ / W) were found to vary within wide limits and thus to offer means of separation for natural and synthetic rubies. According to the sample's orientation, the two examined parameters were then plotted in separate Cartesian coordinate systems where the values for the absorption minimum λ_0 were represented on the abscissa and the coefficient λ/W on the ordinate (Fig. 5.17).

In retrospective and taking into account that the technical possibilities were limited at the time of publication the procedure introduced by Bosshart (1982) showed three limitations.

First, the proposed method of recording oriented spectra appeared not to be entirely sufficient in terms of polarisation effects. The fact that the measured absorption is dependent on the path length the analysing ray is taking through a sample wasn't taken into account either. Finally, a given spectrum could not be characterized by the suggested procedure occasionally when the 0.5 absorbance units which were set to be the level where the width W of the absorption minimum λ was measured, exceeded the top of the Cr absorption band at 410nm and no intersection with the spectrum could be established. This problematic was encountered especially in the case of less saturated rubies or pink sapphires.

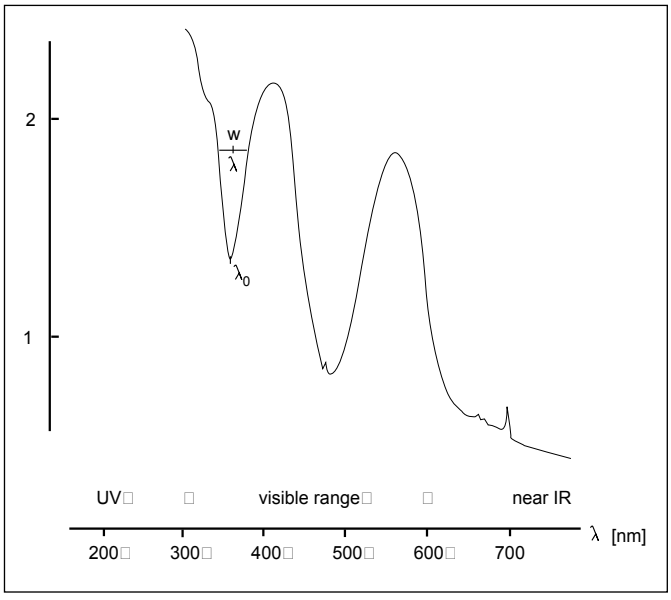

Fig. 5.16: Parameters introduced by Bosshart (1982) in order to numerically describe ruby UV-vis spectra.

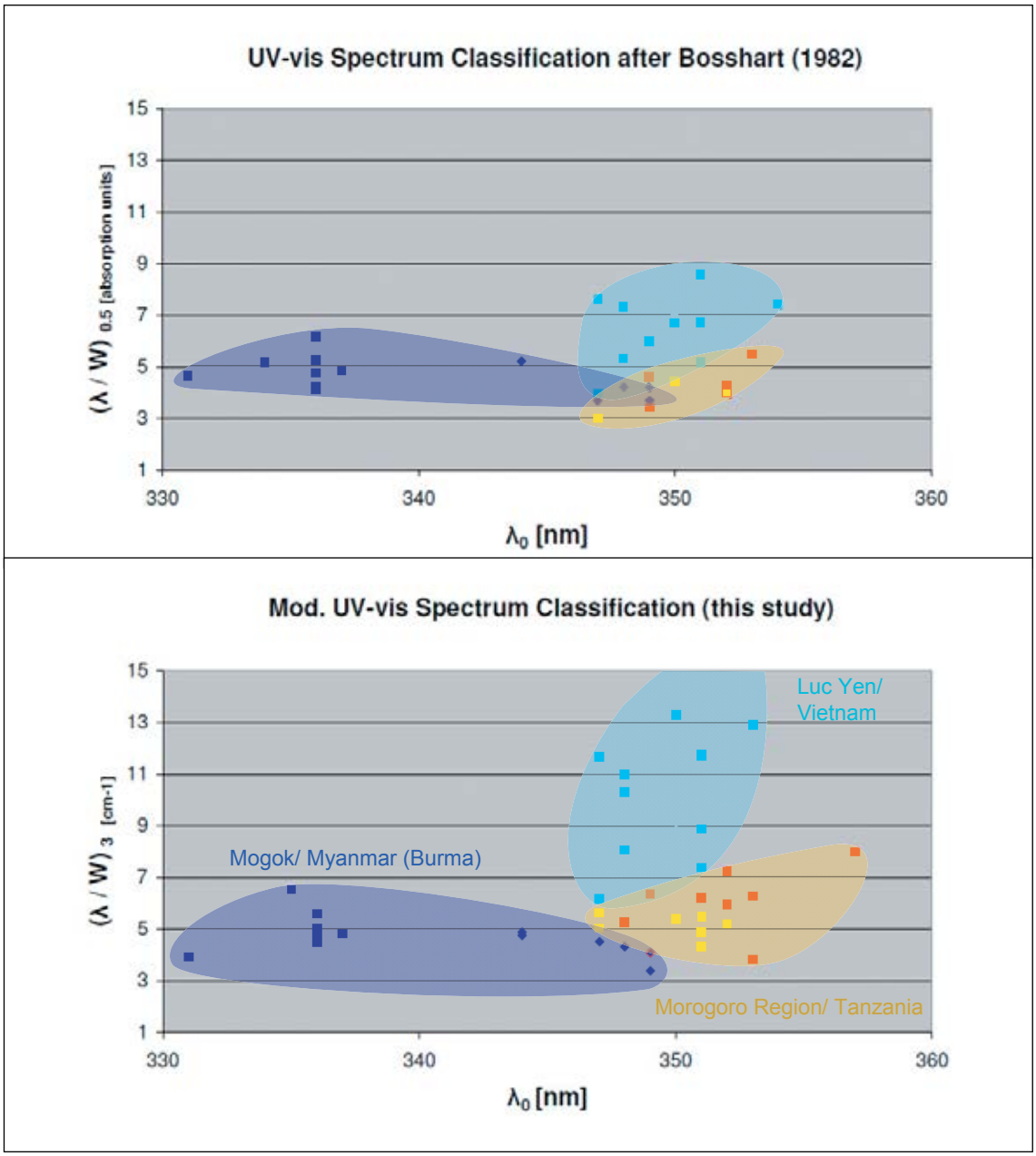

Fig. 5.17: Comparison of a λ_0 versus (λ/W) plot after Bosshart (1982) and the modified approach presented in this study. Rubies from Mogok Myanmar (Burma) are plotted in blue, Luc Yen Vietnam in turquiose and the Morogoro Region in red (Mahenge Mts) and yellow (Uluguru Mts) respectively. The modified approach results in a reduction of the populations overlap in the area between 345 and 350nm which allows a clear separation of ruby o-ray spectra collected from samples of the three investigated localities.

Subsequently, it was the goal of this study to modify the approach introduced by Bosshart (1982) in a way that the detected limitations could be eliminated. Further, it was investigated whether there is a potential to widen the focus of UV-vis spectrum analysis from determining authenticity towards a new procedure to allow origin determination on rubies instead.

5.2.3.4 Modified Procedure

Continuing by analysing the procedure introduced by Bosshart (1982), it was soon confirmed that polarisation plays a key role in adequately interpreting a given UV-vis spectrum. Artefacts related to polarisation effects are common because extraordinary beam (e-ray) spectra are mostly not pure e-ray spectra but a mixture of ordinary (o-ray) and e-ray characteristics. This phenomenon is related to the fact that sample positioning of cut samples is often difficult. The table of cut stones are rarely oriented perfectly perpendicular or parallel to the c-axis which would be necessary in order to obtain undisturbed o- and e-ray spectra. The simplest solution to overcome this problem was to just consider o-ray spectra for this study only. o-rey spectra are not disturbed by polarisation effects in whatever direction the UV-vis spectrum may had been taken.

The second effect which was investigated to be eliminated was the fact that the measured absorption is dependent on the path length of the beam travelling through a sample (Lambert-Beer law). Plots in absorption coefficient do take this fact into account. Accordingly, the collected spectra had to be processed after the following formula in order to convert the collected spectra from absorbance to absorption coefficient or absorptivity.

$\alpha = \ln 10 * (A / t)$: modified after Lambert-Beer law

α : absorption coefficient [cm^{-1}], A : absorbance, t : optical path length [cm]

As an initial step in this data processing procedure the optical path t has to be evaluated. For samples examined in this study, this was an easy task to be measured. Most stones were present as slabs after two parallel windows had been polished onto the rough samples. In this case the optical path corresponded to the sample's thickness. For cut stones however the procedure is not as simple and the orientation of the optical axis compared to the gemstone's table has to be defined first. If the axis is perpendicular to the table facet or the girdle, the ray path measurement can be carried out in the same direction accordingly. If the optical axis is in an oblique position to the table however an approximation procedure has to be carried out. It is suggested to measure the sample's thickness or length of ray path by the distance between a star facet on the crown of a given gemstone and the corresponding pavilion facet on the opposite surface.

After a UV-vis spectrum is recorded it has to be divided by the measured path length t and multiplied by the logarithmus naturalis of 10 according to the equation mentioned above. Data processing as described can be done by any spectrum calculation software such as Spectrum by Perkin Elmer for example.

The resulting spectra in absorptivity can be understood as being optically normalised. Consequently, this allows direct comparison of the spectra obtained from samples of any thickness. The effect of different path lengths could therefore be ruled out.

Finally, the last obstacle was taken by simply adjusting the profile height from 0.5 absorption units in absorbance to 3cm^{-1} in absorptivity. This corresponds in most cases to a lower value than formerly suggested by Bosshart (1982) but still allowing the detection of presence or absence of the shoulder at ~315nm. Trials with even smaller profile heights failed in this regard. This shoulder however is a major characteristic of the investigated absorption minimum in the UV range and therefore cannot be neglected.

5.2.3.5 Comparison of the suggested modified approach with the approach introduced by Bosshart (1982)

Following a spectrum processing procedure as described above, certain changes in the characteristics of a λ_0 versus (λ/W) plot can be recognized. First of all, there are more data points contained in the plot of the modified approach due to the reduced profile height (Fig. 5.18). Further, it can be seen that the overlap of rubies from Mogok Myanmar (Burma) and from the Mororgoro Region is nearly entirely eliminated in the plot of the modified approach presented in this study. Clusters of the three investigated localities can now clearly be separated. In the diagram after the modified approach rubies from Mogok plot at low to intermediate (λ/W) levels between 3.4 and 6.5 and spread laterally from 330 to 350nm. Accordingly, the cluster shape is horizontally elongated. Rubies from Vietnam on the other hand were found to plot at very high (λ/W) levels from 7.3 to 14.3 with a small lateral variation of less than 10nm and centred around 350nm. This population plots more in a vertically elongated pattern. The rubies from the Morogoro Region finally take an intermediate position in the λ_0 versus (λ/W) plot with a tendency towards higher absorption minimum levels from 347 to 357nm. Thus, the cluster has more a triangular-like shape.

During the UV-vis spectra investigation it was further possible to identify two separate clusters within the Mogok population. The two clusters represent two types of spectra which were observed to be present in this population. The cluster on the right is characterized by spectra containing a shoulder at 315nm where as the cluster on the left lacks such a spectrum feature. Additionally, it was observed that the tested Vietnamese rubies never showed a shoulder at 315nm whereas rubies from the Morogoro Region, Tanzania seem to represent a population with both spectra types. Distinct differences in the λ_0 versus (λ/W) plot however can not be found for the two types of spectra in the Morogoro Region population.

5.3 Discussion

5.3.1 Traditional Gem Testing

Already in the field there were differences in the quality of rough encountered especially for the gem material coming from the mine of Lukande in the plains to the east of the Mahenge Mts. A possible explanation may be the deposit itself. At Lukande rubies are found in placers and not in primary deposits as elsewhere in the Mahenge Mts. By a natural selection process rubies of better quality got concentrated in these placers similar to what is known for diamond placers in West Africa for example. Specimens which are fractured or heavily included are usually less resistant to transportation damage. Therefore, specimens of lower quality get destroyed often on the way of transportation and are more likely to be removed from the detritus prior to sedimentation in a placer deposit.

Later, during the investigation of physical properties of rubies from the Morogoro Region an unusually large variation in SG for corundum samples was recorded. These fluctuations in SG are interpreted as artefacts caused by numerous inclusions of mineral phases with drastically different SG compared to corundum. In case these inclusions consisted of calcite (with an SG of 2.71 g/cm^3) a volumetric fraction of 7 vol% would be sufficient enough to lower the SG of the tested ruby to the lowest levels which were registered in this study.

An in depth investigation on inclusion features confirmed that certain combinations imply strong characteristics for specific origins. Based on the inclusion feature compilation introduced in Tab. 5.2 it was possible to define a set of distinctive inclusion features thereafter (Tab. 5.4).

Especially, the combination of features such as the presence or absence of a hazy blueish glow when illuminated with a strong fiberoptic torch, blue colour zones, as well as "swirl"-type growth structures, and the presence of absence of "silk" were found to be highly distinctive in terms of origin determination for rubies. This first group of inclusion features has also the advantage to be checked easily by standard gem microscopy and detected with a high reproducibility in rubies from marble-hosted deposits. Consequently, the four indicated features allow a first rough classification already. In the case of Luc Yen/ Vietnam, Chumar & Ruyil/ Nepal, and Jegdalek/ Afghanistan an overlap in characteristics is recorded however. Therefore, an additional set of inclusion features can be considered including the following inclusion phases: graphite, pargasite amphibole, spinel, tourmaline, gibbsite, pyrite, garnet, and fluorite. Also in case of uncertainty it is suggested to consider the recorded frequencies of inclusions mentioned in Tab. 5.4.

Inclusion features which hadn't been included in the list of distinctive inclusion features were either found not being distinctive enough as they are ubiquitous inclusion features such as negative crystals, apatite, and zircon or there was not enough evidence in terms of reproducibility. The latter was the case for anorthite, titanite, zoisite, margarite, and chlorite. Phlogopite was excluded from the list of distinctive

mineral inclusions because judged on the mineral paragenesis reported for marble-hosted ruby deposits (Garnier et al., 2008) phlogopite was not found frequently but in most deposits. Phlogopite is therefore not considered a distinctive mineral inclusion.

Based on the eleven inclusion features mentioned in Tab. 5.4 a separation of the eleven marble-hosted ruby deposits be means of inclusion features is possible.

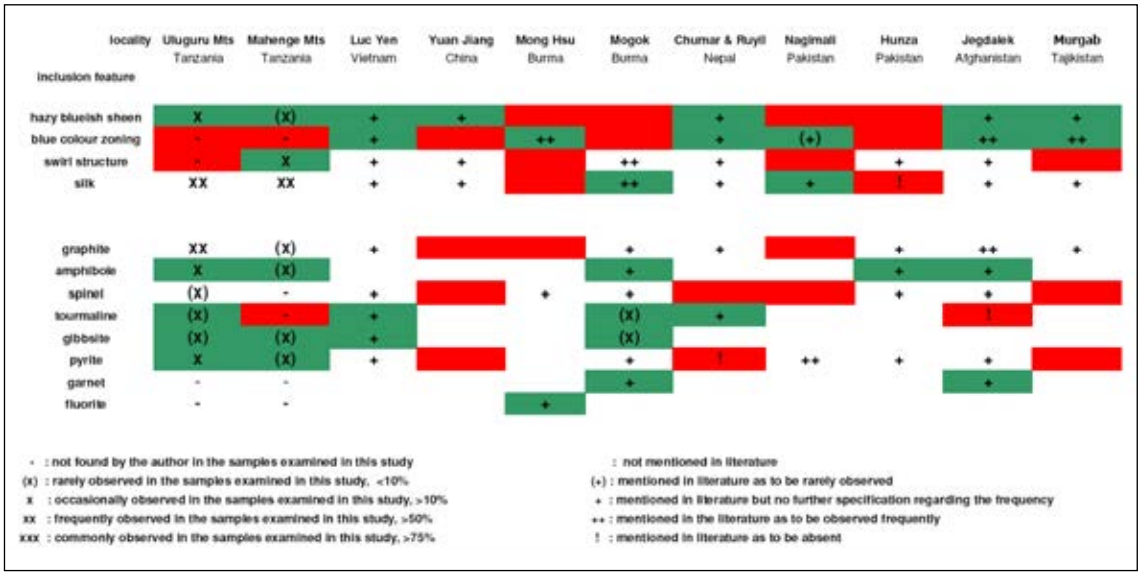

Tab. 5.4: The combination of inclusion features being present (green) or absent (red) in a given ruby give indication of its geographic provenance. This table was modified after Tab. 5.2.

5.3.2 Advanced Gem Testing

5.3.2.1 FTIR Fingerprinting

The careful examination of ruby FTIR spectra in comparison with a specifically designed reference data collection revealed FTIR fingerprinting to be an additional tool to detect the presence of mineral inclusions and sub-microscopic impurities in gemmology. As it was recognised during this research a powerful reference data collection which is characterised by spectra of the most significant minerals known as inclusions and sub-microscopic impurities together with high resolution in the specific spectrum range above 1500cm^{-1} are key to an accurate spectrum interpretation by FTIR fingerprinting for corundum samples. Only if these pre-conditions are fulfilled and combined with the skills of an experienced operator the full information available in an FTIR spectrum can be extracted.

The detection of gibbsite, amphibole, and tourmaline in marble-hosted rubies during this study highlighted three examples of mineral phases which have not yet been detected by FTIR in gemmology yet.

It was further possible to point out that an overlapping FTIR signature of chlorite-group minerals and the Aluminium-Hydroxide phase gibbsite in the range of 3300-3700cm^{-1} may have lead to a potential misinterpretation in the past. To rule out such a possibility in the future gibbsite, besides chlorite, has to be considered as a potential mineral phase in the mentioned spectrum range as well.

Gibbsite is further regarded to represent a weathering product of boehmite which itself is a well-known inclusion phase for corundum from various deposits. As indicated by Deer et al. (1996) gibbsite is further the most OH-saturated of the three Aluminum-Hydroxide phases diaspore, boehmite and gibbsite and stable at low temperatures only. Gibbsite [$Al(OH_3)$] looses structural water and changes gradually to boehmite [α-Al(OOH)] when heated. If there is even more heat applied boehmite transforms to diaspore and finally above 450°C (P=1bar) corundum [α-Al_2O_3] is formed (Deer et al., 1996). If this process is reversed the mentioned mineral phases occur in reverse order with decreasing temperatures accordingly. It is therefore not surprising that boehmite in combination with gibbsite was found in several cases among the examined samples. On the contrary, gibbsite was never found to be present in combination with diaspore during this study however. This in return is consistent and confirming the hypothesis gibbsite to be a break-down product of boehmite.

As thermostability investigations by Kloprogge et al. (2002) indicate, the detection of gibbsite as an inclusion phase by FTIR can be used even further as an analytical application in gemmology. Since gibbsite is found to be instable above temperatures of about 350°C its presence can be used as an indication of "no heat" which means that there was no heat treatment applied to a ruby displaying a gibbsite signature

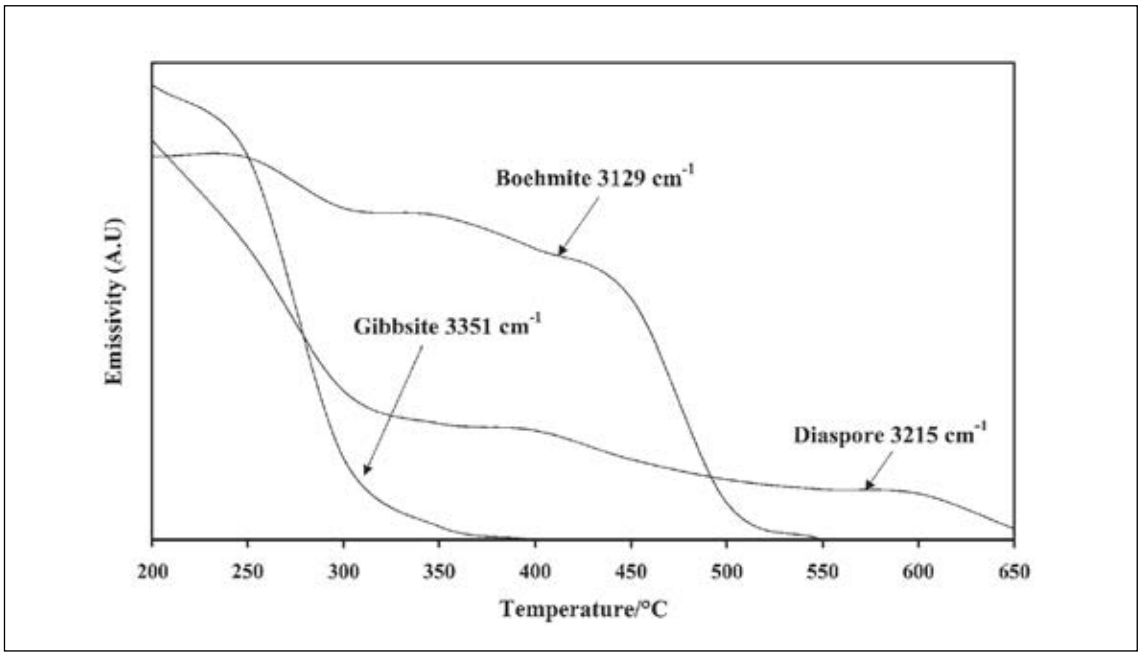

Fig. 5.18: Thermostability investigations of Aluminium-Hydroxide phases by Kloprogge et al. (2002) revealed that gibbsite is stable up to a temperature of about 350°C only. The presence of gibbsite in corundum FTIR spectra can therefore be used as an indication of "no heat".

in its FTIR spectrum. At least, a temperature of 350°C was not exceeded. Gibbsite is therefore even more sensitive in terms of detection of thermal treatments than boehmite or diaspore which frequently had been considered in gemmology up to present (Fig. 5.18).

Regarding pargasite amphibole, it was described in the chapter 4 as a major component of the ruby mineralisation mineral paragenesis found in the two investigated deposits in the Morogoro Region. Consistently, amphibole was detected to be present as mineral inclusions in both localities in the Morogoro Region.

Tourmaline on the other hand was observed as an accessory mineral in the Uluguru Mts only. During advanced gem testing on rubies from other marble-hosted deposits tourmaline was further recognised as an inclusion mineral in rubies from Mogok, Myanmar (Burma) as well. This observation introduces tourmaline as a new mineral phase identified as an inclusion in Mogok rubies. Evidence for the presence of tourmaline inclusions in Mogok rubies however was found by FTIR so far only. This leads to the conclusion that the detected inclusions are present as sub-microscopic particles in fact and had therefore been missed by standard microscopic investigations until present.

The detection of pargasite amphibole as well as tourmaline as mineral inclusion phases in the Morogoro rubies by FTIR were confirmed by Raman spectrometry in the following (Appendix B.1).

5.3.2.2 UV-vis spectrum analysis

From the UV-vis spectra collected in this study it can be concluded that spectra from both the Uluguru as well as the Mahenge Mts were dominated by the strong signature of Cr^{3+} in general. Cr^{3+} is the main chromophore and therefore responsible for the intense red colour found in rubies. Cr^{3+} shows sharp peaks typically at 692/694nm, 659/668nm (Smith et al., 1997), 475/477nm and 468nm. Broad absorption bands also related to Cr^{3+} are found at about 550 and 400nm respectively (Schmetzer et al., 1983). Theses were common features observed in the spectra collected form Morogoro Region rubies. A shoulder in the range between 300 and 320nm and related to Fe^{3+} (Bosshart, 1982) was observed occasionally only (Fig. 5.16).

Through comparative UV-vis spectra analysis of ruby spectra, Bosshart (1982) was able to show that there are differences in the shape of UV-vis spectra mainly in the range of the UV absorption minima. Following a modified procedure introduced in this study it was possible to demonstrate that besides the initial application, the separation of natural from synthetic rubies, there is also a strong potential for ruby UV-vis spectra analysis to be used as a new tool for origin determination of marble-hosted rubies in general. In particular, the rubies from the two marble-hosted deposits in the Morogoro Region, Tanzania could not been separated on the basis of UV-vis spectra analysis however.

5.3.3 New Procedures for Origin Determination on Rubies from Marble-Hosted Deposits

The combination of Raman spectrometry and FTIR fingerprinting together with standard gem microscopy allowed a clear identification of inclusion features such as growth structures, colour zoning and fluorescence phenomena as well as mineral inclusions and sub-microscopic particles present in a given gem stone.

In the course of this study it was further possible to successfully introduce FTIR fingerprinting as a new tool for origin determination purposes. By applying the chart of distinctive inclusion features presented above (Tab. 5.4) a determination of origin is made possible.

Further, it was shown that by modifying the approach of UV-vis spectrum analysis by Bosshart (1982) it is possible to differentiate UV-vis spectrum characteristics found in samples from the Morogoro Region/ Tanzania, Luc Yen/ Vietnam, and Mogok/ Myanmar (Burma). This was mainly achieved by converting the collected ruby spectra from absorbance into absorptivity which separated the population clusters in λ_0 versus (λ/W) plots more clearly. Rubies from other deposit types may reveal even different spectrum characteristics and are likely to plot in additional populations (see Bosshart (1982)). This however had not been covered in this study.

CHAPTER VI

TRACE-ELEMENT ANALYSIS

In gemmology, Energy Dispersive X-Ray Fluorescence Spectrometry (ED-XRF) was the state-of-the-art method to investigate various gem materials for their trace element composition since the mid-80's. From origin determination to the separation between natural and synthetic gemstones, detection of lead-glass fissure fillings, and the distinction of fresh and sea water pearls, ED-XRF has many applications in gemmology (Stern & Hänni, 1982, Muhlmeister et al., 1998).

Although ED-XRF was established as the standard method for trace-element analysis in gemmology, certain limitations were still recognised. Especially, the calibration process where matrix-matched standards are required as well as the weak performance in the range of light elements were negative aspects to be dealt with.

Then Jackson et al. (1992) introduced Laser-Ablation-Inductively-Coupled-Plasma-Mass-Spectrometry (LA-ICP-MS) for micro-analysis of geological materials as a new analytical method to earth sciences. The possibility to simultaneously detect a vast range of isotopes and concentrations, combined with low limits of detection (LOD), high spatial resolution, as well as simple sample preparation were soon recognised as key strengths of this new method. The main criterion for LA-ICP-MS to be accepted as a trace-element analysis technique in gemmology was the 'quasi non-destructive' sampling mode of this newly introduced method (Guillong & Günther, 2001). When yellowish-orange Be-diffusion treated sapphires reached the global gem market in 2002 the time was right to draw the attention of gemmologists around the world to LA-ICP-MS (Hänni & Pettke, 2002, Emmet et al., 2003). In the following, several gem laboratories invested in purchasing such a piece of equipment, which started a new era of advanced gemmological testing. With LA-ICP-MS one of the latest but also highly sophisticated methods in solid-state analytics joined the arsenal of gem testing techniques applied in gemmology.

As mentioned above ED-XRF is not capable of detecting light elements such as Li, Be, B, Na, and Mg satisfyingly. To examine the potential of light trace-elements and possibly to refine the origin determination procedures applied by specialised gem laboratories today, LA-ICP-MS was chosen to be the main trace-element analytical technique applied in this study.

In order to obtain a comparison in, and to illustrate the differences between, these two techniques, a small group of samples from the Morogoro Region, Tanzania, was tested by both methods.

The procedures, results, and conclusions of these investigations are presented in the following.

6.1 Performance Comparison between ED-XRF and LA-ICP-MS

The following comparison is based on the instruments introduced above. It has to be stressed here that the results of this comparison are not applicable directly to other ED-XRF and LA-ICP-MS instrument setups, because there are so many different analytical setups available, each having its characteristic performance. A separate investigation would have to be carried out each time such a system wanted to be compared. The procedure described in the following would be adaptable however.

ED-XRF and LA-ICP-MS are fundamentally different analytical methods. First of all there are different parameters quantified. With ED-XRF there is a frequency dependent X-ray intensity measured which is characteristic for certain elements. Contents of such elements can be calculated thereafter based on matrix-matched standards of known composition. This method strongly depends on the sample's matrix which influences the penetration depth and therefore the intensity of the sample's response to X-ray irradiation. The X-ray penetration depth of an ED-XRF unit is of the order of 1µm only. ED-XRF can therefore be considered to be a surface analysis method. Importantly, ED-XRF is a non-destructive testing method.

In LA-IPC-MS on the other hand, time-dependent intensities of mass to charge ratios are measured which again correspond to the content of certain isotopes in a sample. The signal intensity of a given isotope, however, depends not only on the content but also on the ablation rate of a sample. In other words if more sample material is ablated per second the measured intensity will be higher (at constant element concentration). The ablation rate is therefore a material specific parameter and has to be correlated between sample and standard. Consequently, an internal standard is used to compensate for the matrix dependent ablation rate of a given material. Moreover, this also accounts for changes in beam size between the analysis of standards and samples. Provided that the LA-ICP-MS setup is optimized for robust plasma conditions (e.g., Pettke, 2006) the requirement for matrix-matched calibration protocols are strongly relaxed. Therefore, calibrations in LA-ICP-MS can be based on widely available and well-determined international standard materials such as the NIST glass standards SRM 610 or SRM 612 (e.g., Jochum et al., 2011) matrix-matched calibration protocols are not required. With ED-XRF, on the other hand, standardization can be a serious challenge when corundum samples with various trace-element compositions have to be collected and their trace-element compositions determined first.

This peculiar feature of LA-ICP-MS was not fully appreciated by the gemmological community when LA-ICP-MS was first introduced to gemmology. Gemmologist with a mainly analytical background influenced by the concept of ED-XRF were first trying to create matrix-matched standards. A short publication by Wang et al. (2006) reported that even the Gemological Institute of America (GIA), the World's Foremost Authority in Gemology™, promoted the introduction of Czochralski created synthetic corundum to be used as standard material. Such procedures have now been abandoned. Regarding the mode of sampling, LA-ICP-MS is not a surface related method but measures a sample volume which is ablated from the sample. Consequently,

LA-ICP-MS is a destructive analytical method; however, the crater size formed from a spot analysis can be tuned to a depth between 2 and 50 µm depth, depending on the analytical routine employed. Such minute pits are left on the sample surface as a toll for high quality data.

In order to performing meaningful methods comparison measurements, as well as general considerations had to be made first. Of these, the dimension of sampling is considered first.

The X-ray beam of an ED-XRF is usually in the range of 100-1000µm in diameter (300µm in this study) and considerably larger compared to the narrow laser beam of a LA-ICP-MS (120µm, in this study). This results in an increased spatial resolution of LA-ICP-MS compared to ED-XRF. Occasional variations in composition due to zonations of an examined crystal are thus expected to have a stronger influence on the result of a single spot LA-ICP-MS analysis than on a comparable measurement by ED-XRF. Especially, if a zonation is wider than half the diameter of the applied pit size aliasing effects influences the results and a zonation would become detectable (Nyquist-Shannon sampling theorem). To obtain comparable data sets and minimise aliasing effects, four LA-ICP-MS spot measurements were made for each sample which were averaged to single values subsequently. This procedure allowed decreasing the spatial resolution of LA-ICP-MS data to comparable levels with ED-XRF. Moreover, for uncertainties on the average values exceeding those typical for repetitive analysis of a compositionally homogeneous sample (1 - 2 % 1 standard deviation), chemical within-crystal variations (i.e., zonations) are indicated.

As mentioned above ED-XRF has a smaller range of elements being detectable compared to LA-ICP-MS. Elements to be tested in this comparison had to be chosen accordingly. To follow a simple approach the five elements which traditionally had been tested by ED-XRF for corundum origin determinations were therefore selected (Ti, V, Cr, Fe, Ga). To obtain direct comparability the ED-XRF data had to be converted from wt% into ppm. This conversion was carried out by a spread sheet where the wt% oxide values were multiplied with the mol fraction of the element accordingly. The obtained results are shown in Tab. 6.1.

Subsequent to the data conversion, five element specific diagrams were created (Fig. 6.2). In the diagrams for Ti, V, Cr, Fe, and Ga error bars were included. From diagrams displayed in Fig. 6.2 it is obvious that the error for LA-ICP-MS measurements is much smaller than corresponding measurements taken by ED-XRF. This reflects the high analytical precision of LA-ICP-MS which is expressed by small standard deviation values.

Discussing the individual plots briefly, it can be observed that for Ti data measured by ED-XRF are higher than those determined by LA-ICP-MS. The 1:1 diagonal line represents the ideal case where samples measured either with ED-XRF or LA-ICP-MS return identical results.

	Ti	Ti	Stdev	Stdev	LoD	LoD	V	V	Stdev	Stdev	LoD	LoD
	LA-ICP-MS	ED-XRF	LA-ICP-MS	ED-XRF	LA-ICP-MS	ED-XRF	LA-ICP-MS	ED-XRF	LA-ICP-MS	ED-XRF	LA-ICP-MS	ED-XRF
Uluguru	ppm	ppm	ppm	ppm	ppm	ppm	ppm	ppm	ppm	ppm	ppm	ppm
MA3/ 2C	142.19	159	1.44	bdl	0.18	30	36.636	120	0.174	bdl	0.016	21
RUTZM-11/ 7C	118.57	214	1.41	bdl	0.17	30	63.046	220	0.252	68	0.016	21
RUTZM-50/ 2C	151.45	386	1.90	60	0.21	30	44.359	97	0.253	bdl	0.020	21
RUTZM-50/ 3C	137.18	222	1.73	bdl	0.26	30	67.679	186	0.294	bdl	0.020	21
RUTZM-50/ 4C	144.22	225	1.88	bdl	0.24	30	30.804	137	0.213	bdl	0.025	21
RUTZM-53/ 6C	116.70	156	1.74	bdl	0.23	30	23.905	78	0.193	68	0.025	21
RUTZM-53/ 9C	117.30	174	1.66	bdl	0.21	30	24.312	72	0.184	bdl	0.023	21
RUTZM-53/ 13C	115.23	145	1.66	bdl	0.32	30	32.903	108	0.216	bdl	0.023	21
Mahenge												
M3/ 2C	129.73	166	1.44	bdl	0.18	30	25.858	99	0.174	bdl	0.016	21
RUTZH-05/ 11C	133.12	377	1.46	60	0.19	30	11.697	0	0.103	bdl	0.015	21
RUTZH-10/ 2C	51.13	90	1.00	bdl	0.18	30	139.837	440	0.393	68	0.018	21
RUTZH-25/ C	111.61	264	1.43	bdl	0.17	30	31.865	133	0.186	bdl	0.021	21
M1/ 4C	102.98	182	1.01	bdl	0.16	30	69.189	155	0.194	bdl	0.009	21
RUTZH-22/ 4C	72.86	94	1.17	bdl	0.15	30	22.709	110	0.158	bdl	0.013	21

	Cr	Cr	Stdev	Stdev	LoD	LoD	Fe	Fe	Stdev	Stdev	LoD	LoD
	LA-ICP-MS	ED-XRF	LA-ICP-MS	ED-XRF	LA-ICP-MS	ED-XRF	LA-ICP-MS	ED-XRF	LA-ICP-MS	ED-XRF	LA-ICP-MS	ED-XRF
Uluguru	ppm	ppm	ppm	ppm	ppm	ppm	ppm	ppm	ppm	ppm	ppm	ppm
MA3/ 2C	2145.54	2587	4.50	68	0.80	14	1041.75	1052	5.84	70	1.64	7.8
RUTZM-11/ 7C	2556.76	3882	5.18	137	0.78	14	540.83	702	4.40	bdl	1.50	7.8
RUTZM-50/ 2C	1369.90	2076	4.55	68	1.02	14	414.83	579	4.62	bdl	2.32	7.8
RUTZM-50/ 3C	1824.16	2919	4.94	68	0.98	14	493.17	504	4.26	bdl	2.14	7.8
RUTZM-50/ 4C	860.36	1309	3.62	68	1.01	14	1327.58	1651	8.24	70	2.34	7.8
RUTZM-53/ 6C	3191.65	4702	7.23	137	1.05	14	35.39	122	1.61	bdl	2.47	7.8
RUTZM-53/ 9C	535.81	774	2.82	bdl	0.96	14	70.24	138	2.02	bdl	2.44	7.8
RUTZM-53/ 13C	3346.55	5023	7.02	137	0.98	14	83.81	143	2.14	bdl	2.20	7.8
Mahenge												
M3/ 2C	190.08	255	4.50	bdl	1.08	14	258.65	309	5.84	bdl	1.76	7.8
RUTZH-05/ 11C	867.24	1401	3.11	68	0.81	14	187.39	420	2.65	bdl	1.51	7.8
RUTZH-10/ 2C	3935.56	4980	7.21	137	0.92	14	192.73	409	2.98	bdl	1.72	7.8
RUTZH-25/ C	2683.00	3766	5.45	137	0.91	14	104.85	191	2.08	bdl	1.85	7.8
M1/ 4C	3291.23	3836	4.56	137	0.59	14	1776.61	1931	6.03	70	0.97	7.8
RUTZH-22/ 4C	3729.97	4313	7.06	137	0.81	14	242.73	287	3.35	bdl	1.49	7.8

	Ga	Ga	Stdev	Stdev	LoD	LoD
	LA-ICP-MS	ED-XRF	LA-ICP-MS	ED-XRF	LA-ICP-MS	ED-XRF
Uluguru	ppm	ppm	ppm	ppm	ppm	ppm
MA3/ 2C	61.477	45	0.262	bdl	0.017	7.4
RUTZM-11/ 7C	22.577	18	0.169	bdl	0.014	7.4
RUTZM-50/ 2C	56.395	63	0.320	bdl	0.022	7.4
RUTZM-50/ 3C	28.432	19	0.212	bdl	0.023	7.4
RUTZM-50/ 4C	56.876	68	0.324	bdl	0.023	7.4
RUTZM-53/ 6C	94.198	74	0.427	bdl	0.017	7.4
RUTZM-53/ 9C	79.929	43	0.372	bdl	0.025	7.4
RUTZM-53/ 13C	55.155	42	0.309	bdl	0.019	7.4
Mahenge						
M3/ 2C	29.700	22	0.262	bdl	0.018	7.4
RUTZH-05/ 11C	45.255	61	0.236	bdl	0.018	7.4
RUTZH-10/ 2C	90.019	61	0.363	bdl	0.019	7.4
RUTZH-25/ C	49.430	31	0.259	bdl	0.019	7.4
M1/ 4C	40.919	44	0.174	bdl	0.011	7.4
RUTZH-22/ 4C	30.601	19	0.212	bdl	0.014	7.4

Tab. 6.1: The data compiled in the table above allows a direct comparison of the performance of LA-ICP-MS versus ED-XRF. The indicated LODs of ED-XRF are taken from Guillong & Günther (2001) representing values which are typical for ED-XRF units employed in gemmological laboratories.

V shows considerably higher values for ED-XRF compared to data obtained from LA-ICP-MS. As error-bars imply there is a fairly large error reported for ED-XRF for this element, especially prominent for lower content values where the two data sets differ the most. Regressing the points would yield a positive V value for ED-XRF at zero V for LA-ICP-MS.

The data for Ga are slightly lower for ED-XRF measurements than for their LA-ICP-MS counterparts. Already Guillong et al. (2001) reported a similar behaviour but provided no conclusive explanation either. An interference during the calibration process with $(^{138}Ba)^{++}$ as Guillong et al. (2001) speculated can be excluded for the case of this study because Ga was measured on the isotope ^{71}Ga.

Cr plots in an elongated population parallel but closer to the bisecting line than V for example. This indicates a good correlation for the measurements of this particular element between both methods. The values are yet slightly increased for ED-XRF measurements. In comparison to Ti the elongated pattern of Cr indicates a somewhat larger variation in the content of this particular element.

For Fe finally the measurements show a good correlation for the two methods as well. The populations of both investigated localities plot almost on the bisecting diagonal. The variation in Fe is large and even bigger than what was encountered for Cr.

The comparison between the two methods allowed further the calculation of calibration curves, to convert a measurement done by one technique into what would be obtained by the other technique. As it was explained above, the correlation between the two methods showed linear behaviours for the examined elements. As a first approach it is therefore suggested to carry out a linear regression to create corresponding calibration curves. Such a procedure was carried out for Cr as an example. The resulting curve and corresponding linear function are included in Fig. 6.3.

Trace element concentrations vary by up to two orders of magnitude (e.g., Fe); hence, the agreement found between ED-XRF and LA-ICP-MS for Ga, Fe and Cr are well better than the natural variability the data document. For Ti, a limited natural variability is observed; hence, the discrepancy between ED-XRF and LA-ICP-MS is significant and should be considered for source fingerprinting. The non-zero intercept for the ED-XRF measurements of V suggests that there may be an interference problem. Therefore, V values as determined here by ED-XRF should be taken with much caution.

Regarding the two populations which had been tested during this comparison there were no locality specific patterns observed in general. All samples plotted in a similar way and followed the same correlation trend for all measurements.

Further, a calibration curve was calculated for Cr by linear regression. The corresponding linear equation allows the estimation of LA-ICP-MS values for a given measurements acquired by ED-XRF.

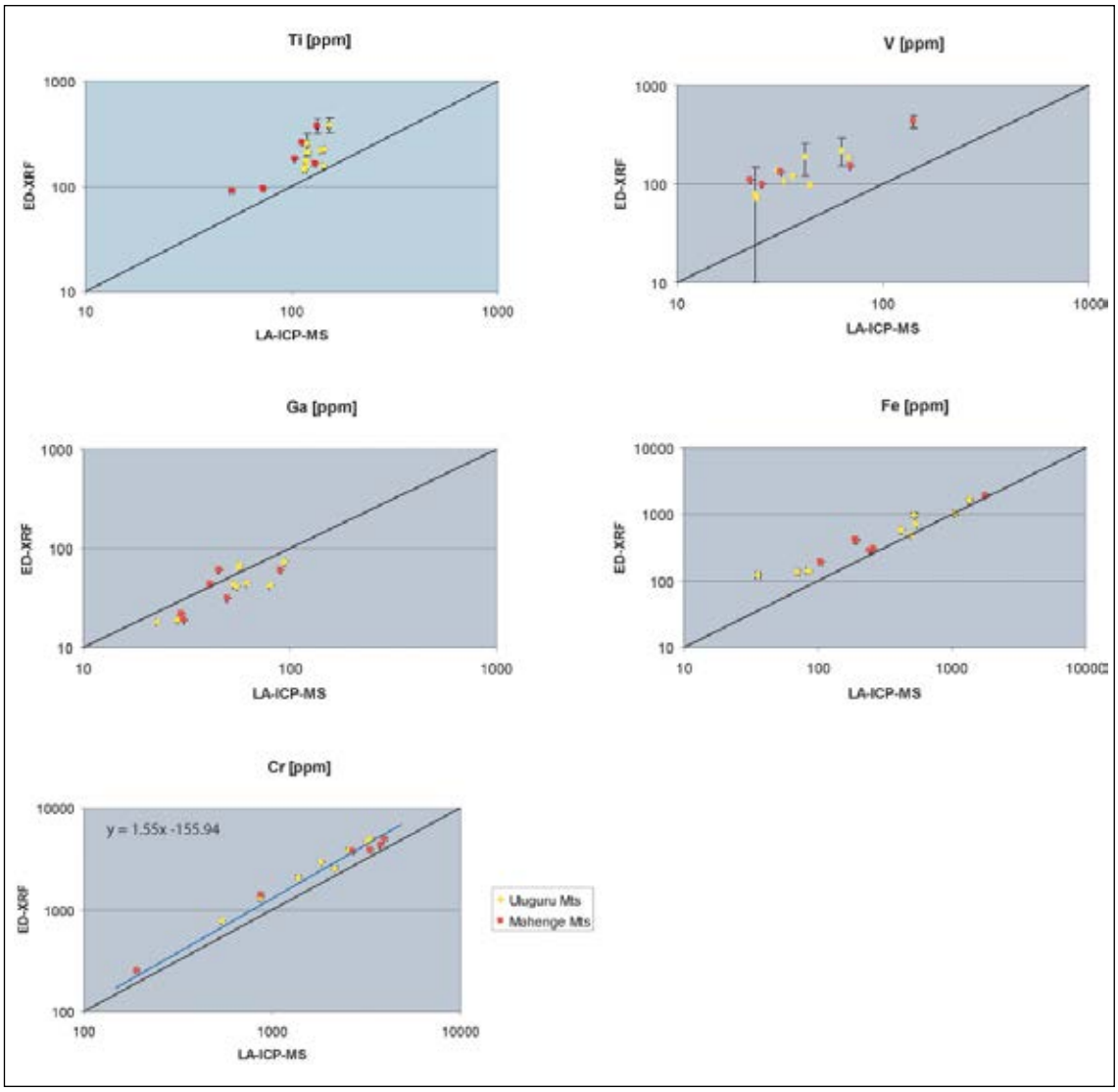

Fig. 6.1: In the displayed plots, results obtained from ED-XRF and LA-ICP-MS trace-element analysis on rubies from the Morogoro Region, Tanzania are presented. The plots demonstrate the degree of correlation for the two methods under the given conditions mentioned in chapter 1.

6.2 Sample Material

This study focuses on rubies from metamorphic deposits in general and marble-hosted ruby deposits in particular. Therefore, rubies from the marble-hosted deposits of the Morogoro Region, Tanzania (Uluguru Mts, n=45, Mahenge Mts, n=58), Shan State, Myanmar (Burma) (Mogok, n=9, Namyaseik n=3), Luc Yen, Vietnam (An Phu, n=7), Murgab, Tajikistan (Snijnie, n=5), and Yunnan, China (Yuan Jiang, n=8) were investigated. Rubies from Mangari, Kenya (John Saul Mine, n=3) were also examined, as an example of a non-marble hosted metamorphic type. An indication whether there may be clear differences between these genetic types can possibly be obtained, acknowledging that three samples only is a statistically non-representative sample number. The rubies from John Saul Mine are found in the contact aureole between a graphitic gneiss and an ultramafic intrusion. The ruby formation is seen as related to a desilication process (Mercier et al., 1999). Overall there was a total of 138 samples were tested by LA-ICP-MS.

ED-XRF was also deployed as a second trace element analytical technique. During this investigation the same 14 samples from the Morogoro Region, Tanzania (Uluguru Mts (n=8) and Mahenge Mts (n=5)) were used on which standard gemmological testing was carried out as described in chapter 5.

The samples were present either as thick sections still in rock matrix to allow examinations by petrological methods, as rough stones with two parallel polished facets or as cut gemstones for gemmological testing (Appendix A.1).

Sample preparation was carried out as described in chapter 1.

6.2.1 Sample Positioning

Once the samples are cleaned they can be positioned into the laser ablation chamber. To properly position the samples, they are mounted on small pieces of Blu-Tack ®. The sticky, soft, plastilline-like substance allows re-adjusting the position of a sample in order to obtain a flat surface perpendicular to the laser beam.

In principle, a turbulent flow pattern of the carrier gas in the sample chamber is tried to be achieved. In an ideal case this would allow the carrier gas to pick up the aerosol produced during the ablation process most efficiently. Therefore, the sample positioning has to be carried out carefully.

The laser ablation cell employed in this study is custom-made, with a turbulent gas flow throughout the cell. Therefore, irregular surfaces as imposed by a series of stones in the cell have no negative effect on LA-ICP-MS analytical performance. From experience it works best if samples are aligned in rows parallel to the flow direction of the aerosol carrier He. An ascending positioning from the entry towards the exit opening of the sample chamber supports this requirement. Also if samples are very different in size, it has to be tried to still follow this concept. In this case, smaller samples will be positioned close to inlet where as the bigger ones find their place towards the outlet. It should be ensured, however, that the surfaces of the samples in the last row (close to the outlet) are not higher than the opening itself. Samples cannot be placed in the corners of the laser ablation cell either, because the flow pattern is not favourable in these areas, resulting in much prolonged chamber washout times after analysis. As a guideline, areas near the in- and outlet which are more than about 45° to the left and right from the longitudinal axis should be avoided. In the case that faceted and rough samples are analysed together in the same run, the rough samples should preferably be placed towards the entrance of the sample chamber. Laser ablation should then start near the ablation chamber exit, so that aerosol particles that may be lost in the ablation chamber may not be remobilized during later analyses and thus cross-contaminate later measurements. Following this strategy, one works its way gradually through the samples towards the inlet and therefore against the carrier gas current. Finally, to guarantee the same conditions for samples and standards (i.e., calibration materials), the standards are mounted together with the samples into the ablation cell.

6.3 LA-ICP-MS Instrument Starting Procedure

In order to obtain stable analytical conditions at maximized detection power a series of parameters has to be optimized and monitored during the starting procedure daily. These are fundamental measures to create data sets which can be compared with each other if generated during several sessions and over a longer period of time.

After sample loading, the laser ablation chamber has to be flushed with pure He for about a minute. This procedure ensures proper wash out of contaminating air adsorbed onto the sample material and the chamber walls that may cause problems of plasma stability. The ICP-MS is then started, and once a stable plasma is achieved, the ablation chamber is connected and the ablation chamber He flow is slowly increased to ca. 1.0 l/min, and the H_2 is added as well (see Tab. 1.1). Then, the ICP-MS should be on for at least 1.5hours. During this time, the ablation chamber and aerosol transport system is properly flushed, and the ICP-MS is thermally equilibrated. This reduces the importance of polyatomic interferences and instrumental drift during later analysis. The instrument would then be ready for daily optimization.

Daily optimization includes (i) maximizing the signal to background intensity ratios for the elements of interest, (ii) adjusting the Th oxide production rate to below 0.5 % (i.e., $^{232}Th/^{248}ThO > 200$) and establishing robust plasma conditions by adjusting U and Th beams to equal intensities during ablation of SRM 610 (i.e., U/Th intensity ratio of 1). The latter are referred to robust plasma conditions where elemental fractionation is minimized; details and explanations are provided by Pettke (2006). Analytical conditions are achieved by dynamically varying the Ar gas flows, the RF-power, and by optimization of ion extraction lens settings in the ICP-MS unit. Finally, it is advised to keep record of the instrument parameters in a logbook in order to monitor the instruments performance over time.

6.4 Element Menu

The sequence and conditions of the elements recorded during analysis are to be defined in the element menu. As a next step appropriate isotopes have to be selected to create an element menu which meets the requirements of the research targets. There are a few thoughts which have to be considered in order to minimise such a selection.

A lean element menu not only simplifies the data processing due to a reduced data set but potentially decreases the LOD during the LA-ICP-MS data acquisition. Since the deployed LA-ICP-MS in this study was a single collector unit, only one isotope can be measured at the time. Therefore, several isotopes are measured in sequence or sweeps. A typical dwell time (acquisition time) is 10msec. This means in case 50 elements are measured for 10msec per sweep and taking into account the time for the collector to adjust form one isotope to the next (i.e., detector settling time; 3 msec for this instrument in dual detector mode), one sweep takes 650msec to be completed. In order to reduce the LODs for certain elements selectively, the dwell

time can be increased from the typical 10 msec to, say, 30 msec, thus further extending the sweep time. Therefore, typical sweep times of element menus employed in this study were of the order of 700 msec. If an element menu is reduced to just 20 elements, however, the sweep time is decreased to 260 msec; hence, more sweeps can be recorded per second and this improves the representative recording of the analytical signal. These considerations illustrate that the element menu has to be set up according to the specific requirements of a given analytical investigation.

To optimize the selection of the smallest set of distinctive elements useful for source tracing, these elements have to be identified first. It was therefore another goal of this study to investigate which set of elements will fulfil the requirement to describe the trace-element composition of rubies from marble-hosted deposits adequately.

As an initial step literature data were consulted first. Guillong et al. (2001) were among the first researchers who applied LA-ICP-MS to gem quality corundum and, therefore, their element selection was examined carefully. In the year 2001, it was not possible to exceed a selection of 40 elements due to software limitations in data reduction and processing. Ten years later, subsequent software improvements allow now 50 elements (using Lamtrace; Jackson et al., 2008) or more (using e.g. Sills; Guillong et al., 2008) to be tested simultaneously. Although accepting the fact that sweep time will be increased it was decided to include most of the elements analysed by Guillong et al. (2001). Additionally, Ca, P, As, and the Rare Earth Elements (REE) Nd, Sm, Eu, Gd were included in the isotope sequence to be investigated in this study. Only ^{133}Cs was excluded from the previous element menu which was not significantly detected by Guillong et al. (2001). The reason why Ca and P were included was their use as a monitor for the identification of elements associated with accidental (submicroscopic) carbonate and apatite inclusions in rubies from marble-hosted deposits during gemmological examinations (see chapter 5). It was therefore interesting to verify whether there are elevated values found in the matrix of marble-hosted rubies. The REE finally, were also included to possibly better determine the presence and type of submicroscopic inclusions, because REE are commonly absent from corundum matrix.

Once the elements to be tested were selected, the appropriate isotopes had to be picked, in order to minimizing the danger of interferences. As explained earlier, mass to charge ratios and not isotopes themselves are measured with LA-ICP-MS. In the evaluation process mainly polyatomic or isobaric interferences have to be considered. Polyatomic interferences originate from spontaneous interactions between the sample material (^{27}Al, in corundum) and the carrier gas (in the set up applied, He, H_2 and Ar), and/or entrained air (O_2 and N_2, or their isotopes respectively). Another source for potential interferences derives from doubly charged ions.

For Ge both cases cause a potential interference. ^{70}Ge interferes with doubly charged $^{140}Ce^{++}$ whereas ^{72}Ge may interfere with $^{36}Ar^{36}Ar$ bi-atomic compounds. In this case ^{73}Ge was chosen to be measured. Although ^{73}Ge has an interference with $^{40}Ar^{33}S$ such a bi-atomic compound is very unlikely to be encountered due to the almost pure Al_2O_3 matrix of the tested corundum. A similar case was encountered with ^{44}Ca where a

polyatomic interference with $^{28}Si^{16}O$ and doubly charged $^{88}Sr^{++}$ has to be considered normally. Since in corundum Si and Sr can be neglected, ^{44}Ca was still selected to be measured in the routine of this study. However, $(^{27}Al^{16}O)^{+}$ interferes on $^{43}Ca^{+}$; hence, ^{44}Ca was recorded instead. Further, and as a positive side effect, the LOD for Ca could potentially be reduced due to the higher abundance of ^{44}Ca compared to ^{42}Ca which usually is selected for Ca measurements in common silicate materials. In ^{31}P the bi-atomic compounds $(^{15}N^{16}O)^{+}$, $(^{14}N^{17}O)^{+}$, and $(^{14}N^{16}OH)^{+}$ have to be taken into account. This interference derives from entrained air causing a frequently encountered effect; hence, P determinations are reliable only when well above the respective LODs, at ca. 3 ppm or higher. Taking these complications into account isotopes were selected accordingly. The finalised element menu is shown in Tab. 1.1.

Further element menu reductions which are suggested for trace-element investigations on marble-hosted rubies are discussed in the results in chapter 6.7.

6.5 Sampling Mode

In principle, there are two modes in which LA-ICP-MS measurements can be carried out, spot and raster mode. In spot mode there are microscopic pits drilled into the sample's surface whereas in raster mode grooves in the form of thin lines are cut into the sample's surface. In both modes the diameters of either the pit or groove lines are adjusted by selecting the appropriate aperture. In gemmology both modes are used nowadays. Several differences between the two modes can be found, however (Tab. 6.2). All LA-ICP-MS measurements were carried out in spot mode during this study.

spot mode:	**raster mode:**
▪ "high" spatial resolution : less resistant in terms of zonation effects	▪ "low" spatial resolution : more resistant in terms of zonation effects
▪ information is collected from a single spot, data obtained from several spots can be averaged to receive area information however	▪ information is collected from an area only
▪ if positioned carefully spots are not visible to the unaided eye, diameters are commonly between 40 and 60µm for routine lab analysis	▪ rasters are visible to the unaided eye, raster sizes are typically in the range of about 200-300µm in length and about 100µm in width, rasters can be used as a hallmark however
▪ higher degree of freedom : the measurement can be controlled better, precise pit positioning	▪ lower degree of freedom : the positioning needs more space and can not be adjusted if using a hallmark
▪ spot depth profiling in view plane possible	▪ depth profiling in cross-section possible
▪ manual pit positioning by adjusting the sample table's position by the microscope's nonius	▪ requires an automated sample rotary table system

Tab. 6.2: Comparison of sampling modes.

Although a minute volume of, in the case of gem stones, precious sample material has to be ablated, the damage caused by LA-ICP-MS can be neglected. Even with a pit size of 120µm in diameter and a maximal depth of 120µm the ablated sample material would still be in the range of a few µg, or less than 0.000001ct, only. A loss in this range can not be detected by a standard carat balance, however. Pit sizes applied in routine gemmological lab analysis usually are between 40 to 60µm, which is about the thickness of a human hair. If a pit is positioned in the corner of a facet or along the girdle the beauty of a cut gem stone is not harmed either and visible by using a hand lens only. In case a pit is still absolutely intolerable it could be easily removed by minor repolishing.

It has to be considered however that the pit size influences the LOD directly. The more sample material per second is ablated the more CPS are generated per unit element concentration and the lower the LOD will be. In this study sample damage was not an issue because almost all samples belong to the author. To achieve low LOD it was therefore possible to maximise the pit size to 120µm (Fig. 6.2) and to produce long (up to ca. 60s) signals ensuring statistically significant recording of all the elements determined in the menu.

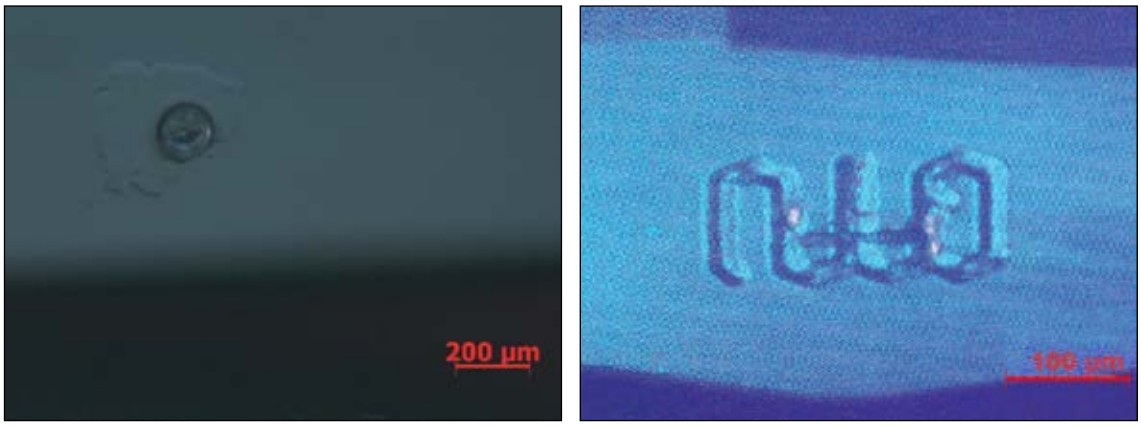

Fig. 6.2: On the left, a microphotograph is shown taken from a sample analysed during this study with a pit 120µm in diameter. To the right, an emblem engraved into the girdle of a gemstone can be seen (Abduriyim & Kitawaki, 2006b). The hallmark was ablated in raster mode while a LA-ICP-MS analysis was carried out. The width of the raster line is 16µm where as the depth is indicated to be between 4-7µm. The used hallmark measures 230µm in length and 80µm in width.

6.6 Ablation Procedure

The ablation process is the initial and crucial part of a LA-ICP-MS measurement. As mentioned above, sample material gets ablated during the ablation process, picked up by the carrier gas, and transported to the ICP-MS unit as an aerosol. To allow ideal conditions for the ablation to take place several parameters have to be taken into account.

First of all the wavelength of the laser has to be considered. To allow an efficient absorption of the energy provided by the laser, the laser's wavelength has to be in the range where the sample material absorbs light preferably up to 100%. This ab-

sorbance behaviour depends on the optical characteristic of a given mineral however. Most minerals show very high absorption below 200nm (see also chapter 5). The deployed ArF Eximer laser with a characteristic, monochromatic wavelength of 193nm is thus perfectly suitable. Normally, the cheaper quintupled Nd:YAG solid source lasers with a wavelength of 213nm are employed in gem labs today. For routine lab analysis this seems to be appropriate.

In recent times also the carrier gas mixture experienced major developments. Changing from pure Ar to Ar-He, He and finally a He-H_2 carrier gas mixture it was possible to achieve drastic improvements in LOD due to gains in element sensitivities (Günther & Heinrich, 1999, Guillong & Heinrich, 2007). Notably the use of H_2 admixed to the aerosol carrier gas considerably increases the detection power of Elan instruments as employed here. Since there is H_2 gas involved a special gas storage container had to be installed and safety precautions had to be followed. This normally exceeds the possibilities of a gem lab. Therefore, the use of He as the standard carrier gas in gemmology is most recommended.

To allow a steady production of sample aerosol the pulse rate of the laser has to be chosen accordingly. Here it is important to make sure the pulse rate is higher than the sampling rate. Otherwise the pulsed character of the ablation generated aerosol will be detected in form of a saw tooth shaped intensity signal. In this study, the sampling rate was in accordance to a sweep time of 0.698sec, 1.43Hz. On the other hand, the pulse rate of the laser was fixed at 10Hz. The condition that the pulse rate has to be higher than the sampling rate was therefore fulfilled easily.

Due to the number of samples which are measured in a LA-ICP-MS campaign the data acquisition is usually divided into several blocks. In order to correct for instruments drift bracketing standardization is employed, i.e., the first as well as the last two measurements of a block are made on the standard material. During this study either the NIST standards SRM 610 or SRM 612 were used as external standards.

Since different materials have different ablation rates there is an internal standard needed to compensate for the difference in ablation rate compared to the external standard. This way, the element sensitivities as determined on the external standard material are converted to those relevant for sample analysis, based on which the element concentrations for the sample analysis can be calculated. As internal standard major components of the sample matrix are chosen usually. In the case of corundum, Al was set to be the internal standard. Subsequently, the Al_2O_3 content of the investigated rubies was chosen to be 99wt%. Because ^{27}Al is a 100% abundance isotope, the intensities of Al at 120 µm beam size would reach near, or could even exceed, detector saturation levels. Therefore, the intensity of the $^{27}Al+$ beam was selectively reduced with the help of bandpass filtering (Pettke, 2008).

The next point to be considered was the positioning of the ablation itself. To receive the most reliable information about the matrix composition, areas with no visible inclusions, fractures or other (near-)surface features were chosen as a target area. In this regard, the microscope attached CCD camera, the best visualization optics

available on the market, allows careful surface examination. The CCD camera further allows online supervision of the sampling process during the ablation. In combination with monitoring the signal behaviour the reaching of inclusions or fissures can be detected and reported in the logbook.

Also the number and pattern of ablation pits has to be considered. Four shots were taken for each sample in this study, sample size permitting. Additionally, an L-shaped ablation pattern was chosen to allow clear re-location of signals to the corresponding pits. Following this procedure, the first three shots were taken in a straight line where as the last shot was set aside to allow unambiguous back-tracking of single shots in a LA-ICP-MS profile also in the future. In case measurements had to be taken on the girdle of a cut gemstone it is recommended to proceed always in the same direction in respect to the gems table facet. Otherwise it will not be possible to orient a profile unambiguously after analysis.

Finally, each ablation was started with a 50sec. background signal acquisition to properly determine background signal levels. Long background signals help to keep the LOD at a minimum as well, because the variability of the measurements around the background mean are an important parameter in the LOD calculation (e.g., Longerich et al., 1996). The ablation itself should not be deeper than the diameter of the pit to exclude depth-dependent element fractionation problems. Due to narrow line width this topic has a bigger impact in raster mode normally. Taking into account that the width of the ablated groove can be of a few µm only, depth limits can reached easily and need to be compensated with a fast raster transport speed.

In the case of this study, pit sizes of 120µm were applied. Sample signals were recorded for 50 to 60sec., which corresponds to a pit depth of 50 to 60µm only at the set ablation rates of ca. 0.06 µm per pulse (see below). Consequently, depth-related element fractionation problems could be avoided.

6.6.1 Strategies to Avoid Surface Contamination

A second field of improvements for the application of LA-ICP-MS to gemstones was found in the ablation procedure. Influenced from the application of ED-XRF where surface contamination is not an issue to be considered, gemmologist normally did not take into account surface contamination issues when LA-ICP-MS first was introduced to gemmology. As it is seen in a figure published by Abduriyim & Kitawaki (2006a) no measures were taken to avoid potential misinterpretation of contaminated signals due to surface contamination (see Fig. 6.3). Because the LODs with LA-ICP-MS are in several cases orders of magnitude lower than what can be achieved by ED-XRF (Guillong et al., 2001, Tab. 6.1) even minute amounts of any not sample derived material can contaminate and even dominate an analysis by LA-ICP-MS. Therefore, special care is indicated.
In order to evaluate whether such a phenomenon is present or not the signal behaviour of an ablation in the initial stage had to be examined. The second step was to select appropriate markers to monitor such a contamination.

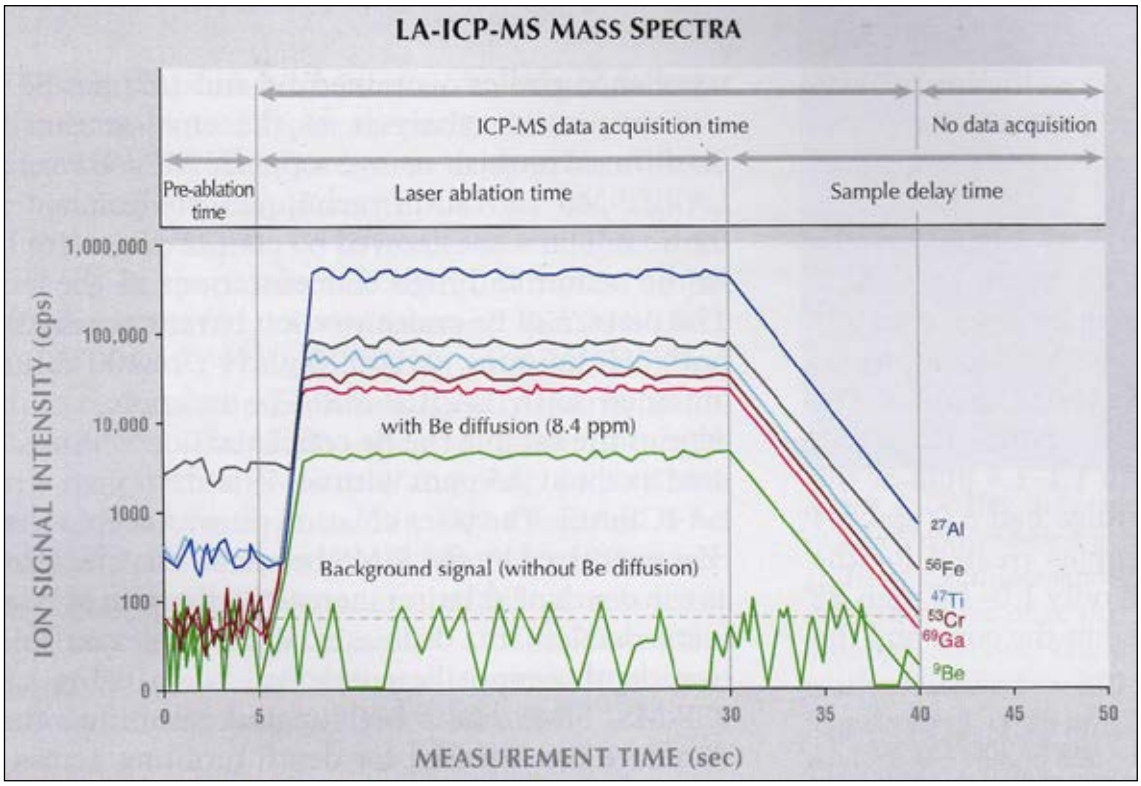

Fig. 6.3: The displayed figure published in Abduriyim & Kitawaki (2006a) indicates that there were no precautions taken in order to avoid surface contamination during the ablation process. Consequently, potentially contaminated surface material was included in the analysis.

As the counts per second (CPS) versus time plot indicates (Fig. 6.4) several isotopes showed higher contents during the first few seconds of an ablation process. The most obvious isotopes were Na, Pb, Zn, and Cu. A possible explanation for these elevated values could be that Zn and Cu derives from a brass metal cutting wheel employed during the polishing process. Na and Pb are commonly known to have elevated signals due to surface contaminations and are often used to identify surface contaminations (finger prints, dirt, staining etc.). In the case of cut or polished gemstones Pb can also derive from lead dopes which may be used to keep the gemstone in position while cutting. Na and Pb were therefore chosen to monitor the signal in the initial stage of an ablation process for this study. Al on the other hand was added to the elements being monitored to represent the sample matrix of the uncontaminated corundum.

As a selected CPS versus time plot shows, increased values of Na and Pb were recorded at the beginning of an ablation (Fig. 6.5). The CPS for the two elements reached constant values at a lower level after a few seconds only. This indicates the presence of a surface layer which shows a different composition than what is recorded later during the ablation in the subjacent homogenous uncontaminated sample matrix. This surface layer is responsible for the recorded surface contamination. Whether the contamination is present in the form of a solid layer or particles disseminated in sample matrix is not known for this case, however.

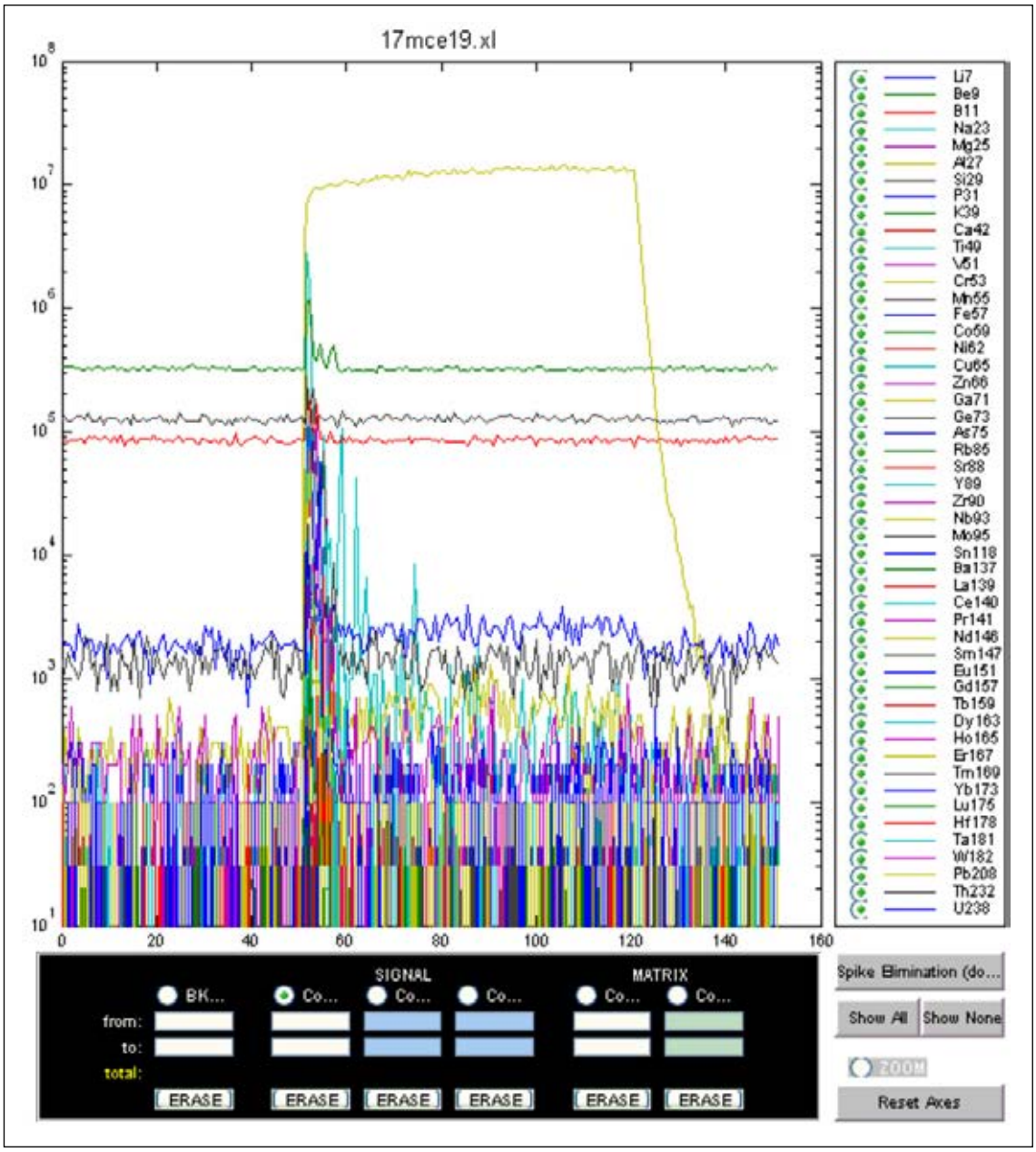

Fig. 6.4: Elevated signals at the beginning of an ablation illustrate the presence of surface contamination.

The suggested approach to solve this problem is to apply a pre-ablation to the target area of the ablation in both spot and raster mode. Especially in raster mode it is necessary to follow such a procedure since it is not possible to bypass this problem by setting the integration limits in the data reduction software accordingly. In raster mode, contaminated sample material is constantly ablated and thus added to the signal if there is no pre-ablation carried out first.

The next question was how deep such a pre-ablation must be to efficiently remove the contaminated surface layer subsequently to the suggested cleaning procedure (see chapter 1). Such layers are commonly very thin and of the order of a few µm only, commonly even less. To evaluate the thickness the wash-out behaviour was examined first. When the ablation comes to a halt a sudden drop of all measured elements is recorded (see Fig. 6.4). The reason for this observation is the sudden stop

in the supply of ablated sample material. Particles still on their way from the surface of the sample to the ICP-MS unit are then washed out gradually until the values reach back ground levels again. The time span from when the ablation stops until the recorded isotopes values reach back ground levels again is considered to define the wash-out behaviour of a given system. The wash-out behaviour is mainly dependent on the gas flow, the sample cell's design, as well as the tube system connecting the sample cell with the ICP-MS unit.

In Fig. 6.5 this time span is indicated by a blue bar in the CPS versus time plot at the end of the ablation. Compared with the time span Na values need to reach a steady

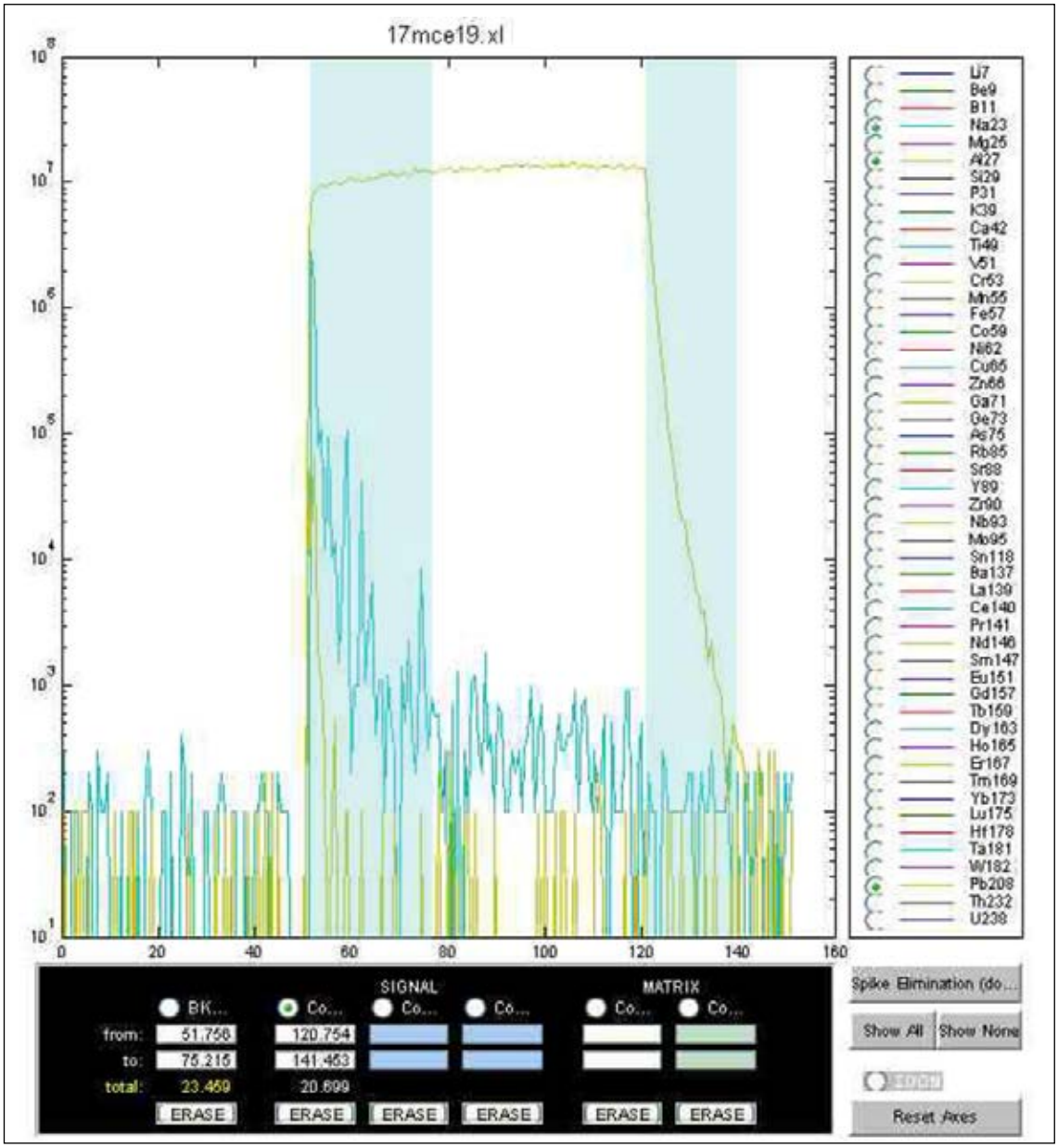

Fig. 6.5: The estimation of the thickness of an unknown surface contamination is done by comparing the wash-out pattern at the end of an ablation with the CPS decline pattern at the beginning of an ablation. If it takes longer for the CPS of contamination markers to come down to steady-state values than for the sample cell to wash-out (as e.g., monitored by the decay of the Al signal after stopping laser ablation) it is assumed that the additional time is caused by an ablated surface contamination.

state at the beginning of the ablation, it is visible that more time is needed. The difference in time is caused by the particle supply of a contaminated surface layer. In the example shown in Fig. 6.5 this time difference was estimated to be 2.79sec.

After it was possible to define the time which was needed to remove the contaminated surface layer, it was still not known how deep the pre-ablation must be to remove this layer. To evaluate the ablation depth, the ablation rate had to be estimated first. The ablation rate defines what sample layer thickness is removed per laser pulse. Multiplied by the ablation time and knowing the ablation rate, the ablation depth is obtained as a result.

The approach in order to estimate the ablation rate was to compare the time of ablation with the depth of the corresponding pit caused by the examined ablation. For this purpose the ablation has to be carried out without a pre-ablation. The depth itself was measured optically with the nonius of a microscope. Subsequently, the calculated ratio, depth versus time, corresponds to the approximate ablation rate in µm/sec. Such estimation was carried out on 5 samples at various laser fluence values, since the ablation rate also depends on this parameter. For the ca. 22 - 24 J/cm2 laser fluence employed here, an ablation rate of ca. 0.06 µm per pulse was obtained, translating into ca. 0.6 µm ablation rate per second when employing 10 Hz laser pulse rate. Note that this ablation rate is not directly applicable to other LA-ICP-MS systems because laser wavelengths and pulse widths may differ for different laser systems; hence, the ablation rate is best determined by experiment for a given LA-ICP-MS setup.

Applied to the time which is needed to remove the contamination it can be concluded that the surface layer must be of a thickness of the order of about 3µm in the example illustrated in Fig. 6.5. This again indicates that with the given instrument parameters the pre-ablation should be of a duration of about 5sec to be on the safe side. Then, to exclude cross-contamination, the sample ablation should be started only after the CPS of the matrix marker, Al in the case of corundum, reached background levels again (Fig. 6.6).

If pre-ablations are applied in raster mode the groove diameter may has to be reconsidered. This case occurs when the total depth of the ablated groove is deeper than the width of the groove itself. In this case, the guideline not to drill deeper than the width of the pit or raster to certainly avoid elemental fractionation would no longer be met and the width would have to be adjusted, i.e., increased. As indicated by Abduriyim & Kitwawaki (2006b) the hallmark applied has a line thickness of 16µm where as the depth is in the range of 4-7µm. Even with applying a pre-ablation of 5µm depth the maximal tolerable depth of 16µm wouldn’t be reached. In this particular example no adjustment is necessary.

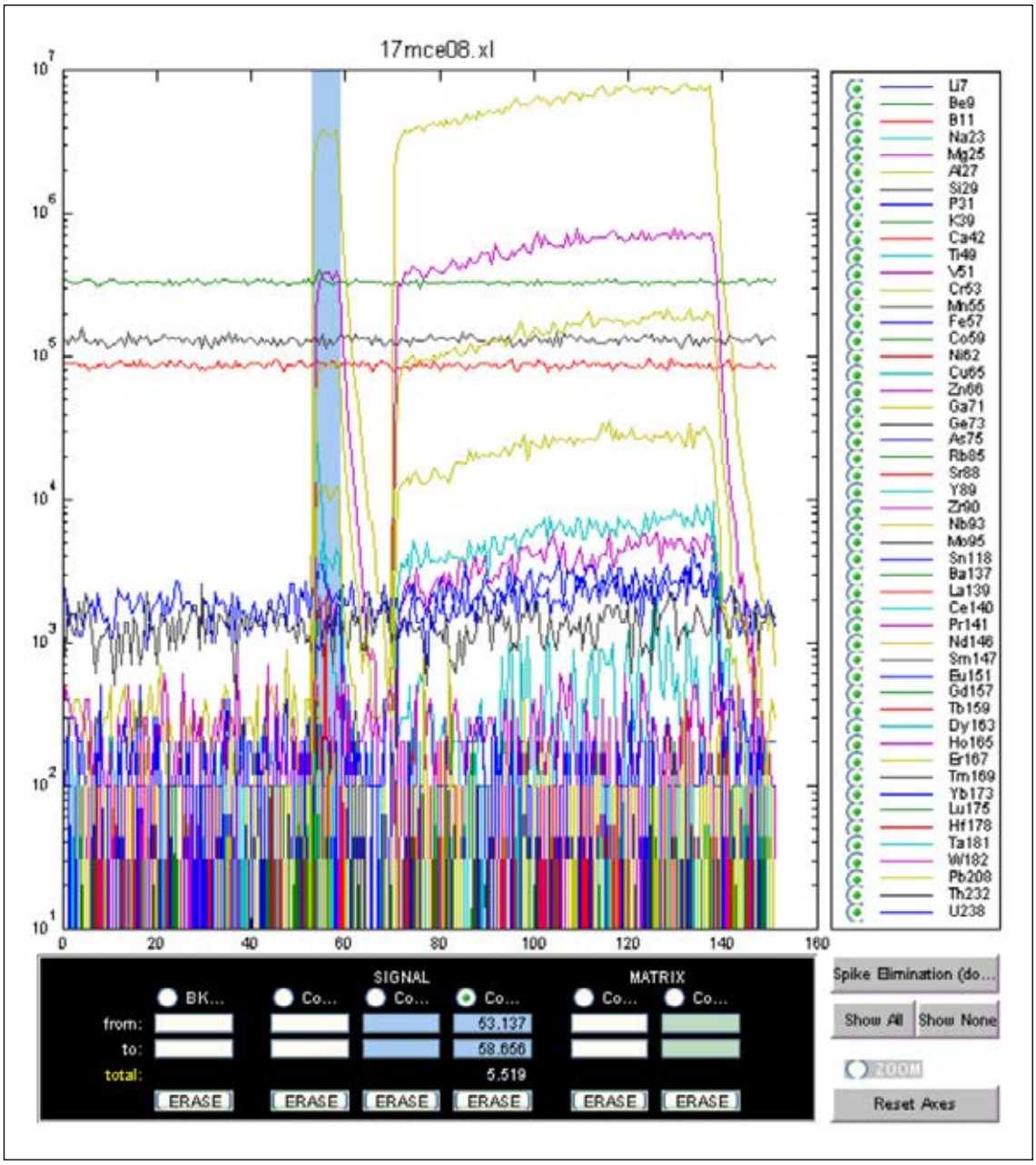

Fig. 6.6: The CPS versus time plot of a LA-ICP-MS shot with applied pre-ablation demonstrates the efficiency of the suggested approach in order to remove surface contamination. The levels of all measured isotopes instantly reach constant levels during sample ablation subsequent to a pre-ablation procedure.

6.7 Results

457 single analyses by LA-ICP-MS on 138 samples from 6 different localities have been acquired for this trace-element analysis campaign. Here, only a reduced table of selected elements is displayed (Tab. 6.3). The values displayed are reported as averages for each sample. For detailed information single shot values including standard deviation (stdev) and LOD values are attached in Appendix B.5. Further explanations and interpretations concerning the data collected during this study are given in the following.

Sample	File	N	Mine	Li7	1Stdev	Be9	1Stdev	B11	1Stdev	Na23	1Stdev	Mg25	1Stdev	Al27	1Stdev	Si29	1Stdev	P31	1Stdev	Ca44	1Stdev
Uluguru Mts, TAN				µg/g	µg/g	µg/g	µg/g	µg/g	µg/g	µg/g	µg/g	µg/g	µg/g	wt%	µg/g	µg/g	µg/g	µg/g	µg/g	µg/g	µg/g
MA3/ 2C	21jja07-10.xl	4	Mwarazi	0.73	0.08	bdl	bdl	1.51	0.20	1.84	0.06	120.9	1.8	99	213	253	17	13.8	0.4	bdl	bdl
MA3/ 3C	15jja03-06.xl	4	Mwarazi	0.54	0.07	bdl	bdl	0.78	0.13	0.18	0.02	78.4	1.2	99	200	221	10	13.7	0.3	bdl	bdl
RUTZM-04/ 2B_1	23jja03-08.xl	6	Mwarazi	0.87	0.11	bdl	bdl	1.43	0.24	0.26	0.04	119.3	2.2	99	276	230	21	7.3	0.5	bdl	bdl
RUTZM-04/ 2B_2	23jja09-11.xl	4	Mwarazi	0.85	0.11	bdl	bdl	0.96	0.22	0.29	0.04	138.5	2.3	99	271	258	21	6.8	0.5	bdl	bdl
RUTZM-04/ 2B_3	23jja12.xl	1	Mwarazi	0.72	0.11	bdl	bdl	1.58	0.24	bdl	bdl	115.3	2.2	99	283	155	23	6.2	0.5	bdl	bdl
RUTZM-04/ 2B_4	23jja13-15.xl	3	Mwarazi	0.77	0.11	bdl	bdl	1.11	0.24	0.20	0.04	112.7	2.2	99	281	235	23	6.8	0.5	bdl	bdl
RUTZM-04/ 2B_5	23jja16-17.xl	2	Mwarazi	bdl	bdl	bdl	bdl	1.30	0.30	0.54	0.07	121.4	2.8	99	353	200	35	7.4	0.8	130	8
RUTZM-08/ 2B_1	24jjb03-06.xl	4	Mwarazi	0.90	0.12	0.14	0.11	0.84	0.17	40.34	0.35	91.7	2.1	99	298	172	22	4.9	0.5	61	5
RUTZM-08/ 2B_2	24jjb07-09.xl	3	Mwarazi	0.65	0.10	bdl	bdl	0.80	0.18	0.44	0.04	114.7	2.3	99	299	161	23	4.4	0.5	bdl	bdl
RUTZM-08/ 2B_3	24jjb10-12.xl	3	Mwarazi	0.74	0.11	bdl	bdl	0.66	0.17	1.94	0.08	123.5	2.4	99	301	146	21	4.3	0.5	bdl	bdl
RUTZM-08/ 2B_5	24jjb14.xl	1	Mwarazi	0.94	0.14	bdl	bdl	0.86	0.20	40.04	0.44	101.1	2.4	99	340	771	25	3.6	0.5	28	5
RUTZM-08/ 2B_6	24jjb15.xl	1	Mwarazi	0.94	0.13	bdl	bdl	1.00	0.20	21.97	0.31	109.1	2.4	99	322	226	23	3.7	0.5	bdl	bdl
RUTZM-08/ 2B_7	24jjb17.xl	1	Mwarazi	0.81	0.11	0.10	0.09	0.97	0.17	61.46	0.45	139.1	2.3	99	282	209	20	4.7	0.4	22	4
RUTZM-11/ 3C	16mcd15-18.xl	4	Mwarazi	0.07	0.02	bdl	bdl	bdl	bdl	2.69	0.07	78.8	1.3	99	212	281	30	2.3	0.4	408	77
RUTZM-11/ 4C	16mcd11-14.xl	4	Mwarazi	0.11	0.05	bdl	bdl	0.42	0.13	38.98	0.26	71.8	1.5	99	251	288	34	2.4	0.5	bdl	bdl
RUTZM-11/ 5C	16mcd03-06.xl	4	Mwarazi	bdl	bdl	bdl	bdl	0.20	0.07	8.63	0.07	63.5	1.0	99	173	185	20	2.0	0.2	bdl	bdl
RUTZM-11/ 6C	16mce03-07.xl	5	Mwarazi	0.01	0.02	bdl	bdl	0.31	0.10	2.67	0.05	59.3	0.9	99	177	189	19	1.8	0.2	bdl	bdl
RUTZM-11/ 7C	16mcd07-10.xl	4	Mwarazi	bdl	bdl	bdl	bdl	0.22	0.08	1.21	0.04	72.2	1.0	99	173	184	19	1.8	0.2	bdl	bdl
RUTZM-12/ 1C	16mce16-19.xl	4	Mwarazi	0.14	0.06	bdl	bdl	0.40	0.17	3.35	0.08	52.1	1.0	99	209	231	25	2.3	0.4	160	41
RUTZM-12/ 2C	16mcd19-22.xl	4	Mwarazi	0.06	0.03	bdl	bdl	1.15	0.12	15.27	0.12	84.8	1.2	99	184	156	20	1.8	0.3	345	81
RUTZM-51/ C	16mcc15-18.xl	4	Mwarazi	bdl	bdl	bdl	bdl	0.33	0.08	4.02	0.07	78.5	1.2	99	196	262	27	2.6	0.3	bdl	bdl
RUTZM-50/ 1C	16mcb07-10.xl	4	Msonge	bdl	bdl	bdl	bdl	0.28	0.09	0.82	0.03	57.8	1.0	99	192	150	20	2.5	0.3	bdl	bdl
RUTZM-50/2C	16mca12-16.xl	5	Msonge	0.16	0.04	bdl	bdl	0.51	0.14	4.93	0.09	99.5	1.4	99	198	286	22	2.7	0.4	bdl	bdl
RUTZM-50/ 3C	16mcb03-06.xl	4	Msonge	0.18	0.03	bdl	bdl	0.26	0.06	0.73	0.04	81.2	1.2	99	192	196	18	2.6	0.3	225	35
RUTZM-50/4C	16mca07-11.xl	5	Msonge	0.10	0.03	bdl	bdl	0.31	0.11	2.90	0.07	89.6	1.4	99	197	248	26	2.9	0.3	bdl	bdl
RUTZM-50/5C	16mca03-06.xl	4	Msonge	0.11	0.04	0.28	0.14	0.58	0.17	10.76	0.17	95.6	1.7	99	232	235	38	3.8	0.5	bdl	bdl
RUTZM-22/ 1B_1	15mca03-08.xl	6	Visakazi II	bdl	bdl	bdl	bdl	0.43	0.16	0.91	0.06	89.4	1.8	99	270	bdl	bdl	3.6	0.5	bdl	bdl
RUTZM-22/ 1B_2	15mca09-13.xl	5	Visakazi II	bdl	bdl	bdl	bdl	0.72	0.20	0.82	0.06	87.5	1.9	99	283	bdl	bdl	2.5	0.6	bdl	bdl
RUTZM-22/ 1B_3	15mca14-15,18.xl	3	Visakazi II	bdl	bdl	bdl	bdl	bdl	bdl	0.21	0.08	53.2	2.8	99	417	bdl	bdl	1.7	0.6	bdl	bdl
RUTZM-22/ 1B_4	15mca19-22.xl	4	Visakazi II	bdl	bdl	bdl	bdl	0.49	0.17	1.49	0.06	85.7	1.8	99	272	bdl	bdl	3.2	0.6	bdl	bdl
RUTZM-25/ 1B_2	15mcc04.xl	1	Visakazi II	bdl	bdl	bdl	bdl	bdl	bdl	bdl	bdl	54.1	1.3	99	240	bdl	bdl	3.8	0.6	bdl	bdl
RUTZM-25/ 1B_3	15mcc07-09.xl	3	Visakazi II	bdl	bdl	bdl	bdl	bdl	bdl	0.13	0.03	82.5	1.5	99	220	bdl	bdl	2.5	0.4	bdl	bdl
RUTZM-25/ 1B_4	15mcc10.xl	1	Visakazi II	bdl	bdl	bdl	bdl	bdl	bdl	0.08	0.02	81.1	1.3	99	201	bdl	bdl	2.3	0.4	bdl	bdl
RUTZM-31/ 1B	16mcf03-06.xl	4	Visakazi II	0.10	0.04	bdl	bdl	0.49	0.17	0.11	0.03	74.4	1.4	99	236	bdl	bdl	1.7	0.4	bdl	bdl
RUTZM-53/ 1C	16mcc07-10.xl	4	Visakazi II	bdl	bdl	bdl	bdl	0.39	0.12	0.40	0.04	84.3	1.4	99	209	303	26	2.2	0.4	bdl	bdl
RUTZM-53/ 2C	16mcc11-14.xl	4	Visakazi II	0.09	0.05	bdl	bdl	0.49	0.18	2.34	0.07	65.6	1.4	99	233	194	25	2.6	0.4	bdl	bdl
RUTZM-53/ 3C	16mcc03-06.xl	4	Visakazi II	0.08	0.04	bdl	bdl	0.99	0.19	5.07	0.10	79.4	1.5	99	226	255	35	2.5	0.4	bdl	bdl
RUTZM-53/ 6C	16mcb11-14.xl	4	Visakazi II	0.07	0.04	bdl	bdl	bdl	bdl	0.09	0.02	74.1	1.3	99	212	145	21	2.6	0.4	bdl	bdl
RUTZM-53/ 9C	16mcb15-18.xl	4	Visakazi II	bdl	bdl	bdl	bdl	bdl	bdl	0.12	0.03	73.8	1.2	99	202	203	22	1.9	0.4	bdl	bdl
RUTZM-53/13C	16mca17-20.xl	4	Visakazi II	bdl	bdl	bdl	bdl	0.32	0.08	0.17	0.02	69.9	1.2	99	197	229	26	2.4	0.4	bdl	bdl
RUTZY-11/ 1C	21jjd11-14.xl	4	local market	0.84	0.11	0.07	0.06	1.02	0.20	0.19	0.03	100.0	1.8	99	252	300	17	9.6	0.4	bdl	bdl
RUTZY-11/ 2C	16jje15-18.xl	4	local market	0.64	0.10	bdl	bdl	0.92	0.20	1.90	0.08	65.9	1.5	99	281	355	22	14.1	0.5	195	6
RUTZY-11/ 4C	21jja03-06.xl	4	local market	0.84	0.11	bdl	bdl	1.14	0.25	0.92	0.06	99.6	2.0	99	254	361	24	16.4	0.6	bdl	bdl
RUTZM-13/ 2C	16jjf03-06.xl	4	local market	0.67	0.09	bdl	bdl	0.77	0.16	1.93	0.07	94.5	1.6	99	244	213	15	12.2	0.4	bdl	bdl
RUTZM-13/ 4C	21jja11-14.xl	4	local market	0.62	0.07	0.04	0.04	1.06	0.17	2.09	0.06	114.6	1.7	99	203	209	15	12.3	0.4	23	3

Sample	File	N	Mine	Li7	1Stdev	Be9	1Stdev	B11	1Stdev	Na23	1Stdev	Mg25	1Stdev	Al27	1Stdev	Si29	1Stdev	P31	1Stdev	Ca44	1Stdev
Mahenge Mts, TAN				µg/g	µg/g	µg/g	µg/g	µg/g	µg/g	µg/g	µg/g	µg/g	µg/g	wt%	µg/g	µg/g	µg/g	µg/g	µg/g	µg/g	µg/g
M3/ 1C	16jjb03-06.xl	4	Mayote	0.65	0.08	0.10	0.07	0.70	0.14	3.12	0.07	70.0	1.3	99	235	250	12	11.3	0.3	15	3
M3/ 2C	16jje07-10.xl	4	Mayote	0.83	0.10	bdl	bdl	1.18	0.20	2.90	0.09	100.4	1.8	99	257	218	18	14.9	0.4	102	4
RUTZH-05/ 3C	16jjb07-10.xl	4	Mayote	0.55	0.07	bdl	bdl	0.64	0.11	0.64	0.03	71.8	1.2	99	212	254	11	10.2	0.3	10	2
RUTZH-05/ 4C	21jjb03-06.xl	4	Mayote	0.74	0.10	bdl	bdl	1.20	0.20	2.37	0.07	129.3	2.0	99	241	256	20	13.7	0.5	bdl	bdl
RUTZH-05/ 9C	21jjc03-06.xl	4	Mayote	0.74	0.09	bdl	bdl	1.11	0.19	1.77	0.05	128.7	2.0	99	229	250	14	11.9	0.4	40	3
RUTZH-05/ 11C	21jjd07-10.xl	4	Mayote	0.80	0.10	bdl	bdl	0.99	0.18	0.15	0.03	107.2	1.8	99	237	179	15	9.5	0.4	78	3
RUTZH-05/ 12C	17mce20-23.xl	4	Mayote	bdl	bdl	bdl	bdl	0.19	0.07	0.37	0.03	88.4	1.2	99	186	161	18	2.2	0.3	bdl	bdl
RUTZH-05/ 13C	17mce11-14.xl	4	Mayote	bdl	bdl	bdl	bdl	0.25	0.08	0.12	0.02	51.3	0.8	99	164	128	16	2.1	0.2	bdl	bdl
RUTZH-06/ 03C	17mce03-06.xl	4	Mayote	0.03	0.02	bdl	bdl	0.18	0.07	0.34	0.03	56.4	0.9	99	174	194	20	1.8	0.2	bdl	bdl
M4/ 3C	16jjb15-18.xl	4	Lukande	0.62	0.08	bdl	bdl	0.65	0.12	0.42	0.02	73.7	1.3	99	224	160	11	9.4	0.3	25	2
M4/ 5C	16jja15-18.xl	4	Lukande	0.76	0.10	bdl	bdl	1.00	0.21	0.31	0.03	44.2	1.2	99	269	206	17	12.7	0.4	bdl	bdl
RUTZH-10/ 2C	21jje03-06.xl	4	Lukande	0.94	0.12	bdl	bdl	1.12	0.21	5.56	0.11	41.4	1.2	99	262	239	17	10.1	0.5	bdl	bdl
RUTZH-10/ 4C	17mcd14-17.xl	4	Lukande	bdl	bdl	bdl	bdl	0.30	0.07	0.98	0.04	44.7	0.9	99	190	212	26	2.1	0.3	bdl	bdl
RUTZH-11/ 1C	16jjd11-14.xl	4	Lukande	0.67	0.09	0.26	0.10	0.63	0.15	2.89	0.08	34.6	1.0	99	246	327	16	8.7	0.4	bdl	bdl
RUTZH-11/ 3C	16jjd03-06.xl	4	Lukande	0.60	0.09	bdl	bdl	0.49	0.16	0.17	0.16	86.9	1.6	99	269	262	17	8.1	0.4	bdl	4
RUTZH-11/ 2C	16jjd07-10.xl	4	Lukande	0.59	0.07	bdl	bdl	0.76	0.11	11.02	0.02	72.6	1.4	99	214	226	11	10.4	0.3	25	bdl
RUTZH-11/ 14C	17mcd18-22.xl	5	Lukande	0.15	0.04	bdl	bdl	0.23	0.06	1.94	0.05	55.2	0.9	99	182	203	18	2.8	0.3	bdl	bdl
RUTZH-18/ 5B_1	23jjc03.xl	1	Kitwaro	0.62	0.11	0.16	0.14	0.97	0.20	0.18	0.03	75.0	1.9	99	305	208	24	4.7	0.5	bdl	bdl
RUTZH-18/ 5B_2	23jjc04.xl	1	Kitwaro	0.59	0.11	bdl	bdl	1.14	0.24	0.14	0.03	68.3	1.8	99	309	bdl	bdl	5.5	0.6	bdl	bdl
RUTZH-18/ 5B_3	23jjc05.xl	1	Kitwaro	bdl	bdl	bdl	bdl	0.97	0.29	1.89	0.12	96.3	2.7	99	376	178	38	3.4	0.8	bdl	bdl
RUTZH-18/ 5B_4	23jjc07.xl	1	Kitwaro	0.45	0.14	bdl	bdl	0.92	0.27	bdl	bdl	100.8	3.3	99	467	bdl	bdl	4.8	0.7	bdl	bdl
RUTZH-18/ 5B_5	23jjc08.xl	1	Kitwaro	0.75	0.11	bdl	bdl	1.26	0.21	9.87	0.19	103.3	2.1	99	288	672	23	5.4	0.5	310	6
RUTZH-18/ 5B_6	23jjc09.xl	1	Kitwaro	bdl	bdl	bdl	bdl	0.71	0.21	bdl	bdl	74.2	2.1	99	347	135	35	5.5	0.7	bdl	bdl
RUTZH-18/ 5B_7	23jjc10.xl	1	Kitwaro	bdl	bdl	bdl	bdl	0.62	0.26	bdl	bdl	77.4	2.3	99	369	bdl	bdl	4.0	0.8	bdl	bdl
RUTZH-18/ 5B_8	23jjc11.xl	1	Kitwaro	bdl	bdl	bdl	bdl	1.26	0.29	1.13	0.09	157.1	3.4	99	380	bdl	bdl	5.3	0.7	bdl	bdl
RUTZH-18/ 7B_1	24jja03-04.xl	2	Kitwaro	bdl	bdl	bdl	bdl	1.12	0.29	0.10	0.04	69.8	2.0	99	339	bdl	bdl	5.3	0.7	bdl	bdl
RUTZH-18/ 7B_2	24jja05.xl	1	Kitwaro	bdl	bdl	bdl	bdl	0.75	0.32	bdl	bdl	81.2	3.2	99	503	bdl	bdl	18.1	1.1	bdl	bdl
RUTZH-18/ 7B_3	24jja06.xl	1	Kitwaro	bdl	bdl	bdl	bdl	bdl	bdl	bdl	bdl	58.9	2.8	99	504	bdl	bdl	13.3	1.1	bdl	bdl
RUTZH-18/ 7B_4	24jja07.xl	1	Kitwaro	0.80	0.12	bdl	bdl	0.82	0.20	bdl	bdl	120.6	2.4	99	304	229	23	5.2	0.6	bdl	bdl
RUTZH-18/ 7B_5	24jja08-09.xl	2	Kitwaro	0.74	0.11	bdl	bdl	0.84	0.19	0.28	0.04	71.4	1.7	99	289	122	22	5.5	0.5	16	5
RUTZH-18/ 7B_6	24jja10.xl	1	Kitwaro	0.80	0.12	0.12	0.11	0.68	0.20	bdl	bdl	96.1	2.2	99	313	93	22	5.2	0.5	bdl	bdl
RUTZH-18/ 7B_8	24jja12.xl	1	Kitwaro	bdl	bdl	bdl	bdl	bdl	bdl	0.61	0.14	84.1	4.9	99	758	bdl	bdl	5.5	1.5	bdl	bdl
RUTZH-18/ 7B_9	24jja13.xl	1	Kitwaro	bdl	bdl	bdl	bdl	0.63	0.29	0.24	0.05	97.6	2.5	99	360	bdl	bdl	4.4	0.8	bdl	bdl
RUTZH-18/ 7B_10	24jja14.xl	1	Kitwaro	bdl	bdl	bdl	bdl	bdl	bdl	0.22	0.04	69.8	2.1	99	351	bdl	bdl	6.3	0.7	bdl	bdl
RUTZH-23/ C	17mcc17-20.xl	4	Kitwaro	0.05	0.02	bdl	bdl	0.41	0.12	5.86	0.08	39.6	0.8	99	184	505	24	2.9	0.3	416	54
RUTZH-25/ C	17mcd11-13.xl	3	Kitwaro	0.08	0.04	bdl	bdl	bdl	bdl	11.38	0.13	82.3	1.2	99	185	184	19	3.6	0.3	bdl	bdl
RUTZH-27/ 2C	17mcc07-11.xl	4	Kitwaro	bdl	bdl	bdl	bdl	0.26	0.09	3.67	0.07	69.0	1.1	99	187	181	24	12.3	0.4	255	54
M1/ 3C	15jjd07-10.xl	4	Ipangko	0.67	0.08	bdl	bdl	0.59	0.12	3.36	0.08	86.3	1.4	99	224	269	11	10.9	0.3	bdl	bdl

Sample	File	N	Mine	Li7	1Stdev	Be9	1Stdev	B11	1Stdev	Na23	1Stdev	Mg25	1Stdev	Al27	1Stdev	Si29	1Stdev	P31	1Stdev	Ca44	1Stdev
Mahenge Mts, TAN				µg/g	µg/g	µg/g	µg/g	µg/g	µg/g	µg/g	µg/g	µg/g	µg/g	wt%	µg/g	µg/g	µg/g	µg/g	µg/g	µg/g	µg/g
M1/ 4C	16jja03-06.xl	4	Ipangko	0.50	0.06	bdl	bdl	0.79	0.12	5.57	0.08	82.8	1.2	99	192	251	10	12.5	0.3	bdl	bdl
M1/ 5C	16jjb11-14.xl	4	Ipangko	0.59	0.08	0.07	0.07	0.88	0.17	6.10	0.12	67.6	1.4	99	263	271	17	11.7	0.4	bdl	bdl
RUTZH-19/ 2B_1	23jjb03.xl	1	Ipangko	0.71	0.10	bdl	bdl	0.62	0.18	bdl	bdl	53.3	1.5	99	278	104	22	6.3	0.5	bdl	bdl
RUTZH-19/ 2B_2	23jjb04.xl	1	Ipangko	bdl	bdl	bdl	bdl	bdl	bdl	0.39	0.05	78.8	2.1	99	334	125	30	5.8	0.7	bdl	bdl
RUTZH-19/ 2B_3	23jjb05.xl	1	Ipangko	0.77	0.12	bdl	bdl	bdl	bdl	bdl	bdl	87.7	1.9	99	290	bdl	bdl	6.0	0.5	bdl	bdl
RUTZH-19/ 2B_4	23jjb06.xl	1	Ipangko	0.83	0.12	bdl	bdl	0.64	0.17	0.08	0.03	81.7	1.9	99	301	159	22	5.9	0.5	bdl	bdl
RUTZH-19/ 2B_5	23jjb07.xl	1	Ipangko	0.62	0.11	bdl	bdl	0.62	0.19	bdl	bdl	106.4	2.2	99	295	199	24	6.2	0.5	bdl	bdl
RUTZH-19/ 2B_6	23jjb09-10.xl	2	Ipangko	0.72	0.11	bdl	bdl	0.93	0.19	bdl	bdl	177.4	2.7	99	286	137	23	5.9	0.5	bdl	bdl
RUTZH-19/ 2B_7	23jjb11.xl	1	Ipangko	0.50	0.10	bdl	bdl	bdl	bdl	bdl	bdl	233.9	3.4	99	316	179	26	6.3	0.6	bdl	bdl
RUTZH-19/ 2B_8	23jjb12-13.xl	2	Ipangko	0.57	0.11	0.14	0.12	0.85	0.27	0.36	0.06	178.2	3.2	99	344	177	30	5.5	0.6	bdl	bdl
RUTZH-19/ 2B_9	23jjb14.xl	1	Ipangko	bdl	bdl	bdl	bdl	0.99	0.26	0.15	0.05	82.2	2.4	99	370	bdl	bdl	5.1	0.8	bdl	bdl
RUTZH-19/ 2B_10	23jjb15.xl	1	Ipangko	0.32	0.08	bdl	bdl	0.62	0.21	2.64	0.12	85.3	2.2	99	335	217	27	5.4	0.6	bdl	bdl
RUTZH-19/ 2B_11	23jjb16.xl	1	Ipangko	0.59	0.10	bdl	bdl	bdl	bdl	0.12	0.04	78.1	1.8	99	299	137	24	5.1	0.5	bdl	bdl
RUTZH-20/ 1B_1	15mcb03-06.xl	4	Ipangko	0.10	0.05	bdl	bdl	0.43	0.16	0.30	0.04	60.5	1.5	99	265	bdl	bdl	2.5	0.5	bdl	bdl
RUTZH-20/ 1B_2	15mcb07-12.xl	6	Ipangko	0.08	0.04	bdl	bdl	0.39	0.13	0.16	0.03	66.6	1.5	99	248	bdl	bdl	2.6	0.5	bdl	bdl
RUTZH-20/ 1B_3	15mcb13-17.xl	5	Ipangko	bdl	bdl	0.22	0.12	0.33	0.12	0.11	0.02	165.4	2.0	99	218	bdl	bdl	2.3	0.4	bdl	bdl
RUTZH-22/ 2C	21jjc07-10.xl	4	Ipangko	0.64	0.08	bdl	bdl	1.01	0.16	0.23	0.03	81.8	1.5	99	215	304	13	9.5	0.3	bdl	bdl
RUTZH-22/ 3C	21jjd03-06.xl	4	Ipangko	0.92	0.11	bdl	bdl	1.05	0.24	0.86	0.06	366.8	3.2	99	278	355	20	11.1	0.5	bdl	bdl
RUTZH-22/ 4C	16jjc11-12,14,f11-12	5	Ipangko	0.78	0.11	bdl	bdl	0.85	0.19	2.10	0.10	57.2	1.4	99	254	296	17	11.3	0.4	41	5
RUTZH-22/ 6C	17mcd03-06.xl	4	Ipangko	bdl	bdl	bdl	bdl	0.27	0.11	0.56	0.04	37.8	0.9	99	211	159	25	2.4	0.3	bdl	bdl

Sample	File	N	Mine	Li7	1Stdev	Be9	1Stdev	B11	1Stdev	Na23	1Stdev	Mg25	1Stdev	Al27	1Stdev	Si29	1Stdev	P31	1Stdev	Ca44	1Stdev
Mangari, KEN				µg/g	µg/g	µg/g	µg/g	µg/g	µg/g	µg/g	µg/g	µg/g	µg/g	wt%	µg/g	µg/g	µg/g	µg/g	µg/g	µg/g	µg/g
RUKEM-22/ 1C	15jjb11-14.xl	4	John Saul	0.80	0.09	bdl	bdl	0.76	0.16	0.16	0.02	147.5	2.0	99	243	264	14	12.3	0.4	bdl	bdl
RUKEM-22/ 2C	15jjb15-18.xl	4	John Saul	0.76	0.10	0.17	0.11	2.00	0.21	1.53	0.05	158.6	2.2	99	255	241	15	11.1	0.4	bdl	bdl
RUKEM-22/ 3C	21jje07-10.xl	4	John Saul	0.92	0.11	0.11	0.09	0.93	0.19	1.00	0.05	228.0	2.8	99	258	227	16	9.3	0.4	156	5

Sample	File	N	Mine	Li7	1Stdev	Be9	1Stdev	B11	1Stdev	Na23	1Stdev	Mg25	1Stdev	Al27	1Stdev	Si29	1Stdev	P31	1Stdev	Ca44	1Stdev
Shan State, MYA				µg/g	µg/g	µg/g	µg/g	µg/g	µg/g	µg/g	µg/g	µg/g	µg/g	wt%	µg/g	µg/g	µg/g	µg/g	µg/g	µg/g	µg/g
BUMGIT01/ C	24Ora03-06.xl	4	Namyaseik	0.78	0.10	0.06	0.06	1.01	0.21	0.40	0.04	42.9	1.1	99	257	587	37	5.7	0.4	bdl	bdl
BUMGIT02 /C	24Ora07-10.xl	4	Namyaseik	0.84	0.11	bdl	bdl	1.24	0.26	0.14	0.03	24.7	0.9	99	270	638	41	4.9	0.4	524	95
BUMGIT03/ C	24Ora11-14.xl	4	Namyaseik	0.74	0.10	0.07	0.06	1.10	0.23	0.32	0.03	32.9	1.0	99	260	766	39	5.1	0.4	613	88
BUMGIT04/ C	24Ora15-18.xl	4	Mogok	0.80	0.11	0.08	0.06	1.12	0.24	0.09	0.02	51.5	1.3	99	276	443	40	4.4	0.4	bdl	bdl
BUMGIT05/ C	24Orb03-06.xl	4	Mogok	0.77	0.11	bdl		0.94	0.24	0.24	0.04	107.2	1.9	99	281	836	39	4.8	0.4	792	89
BUMGIT06/ C	24Orb07-10.xl	4	Mogok	0.74	0.09	0.06	0.05	1.10	0.20	0.10	0.02	102.1	1.7	99	249	515	35	4.1	0.4	551	77
BUMGIT07/ C	24Orb11-14.xl	4	Mogok	0.77	0.11	bdl	bdl	0.99	0.24	0.99	0.05	96.4	1.9	99	288	563	44	4.9	0.4	518	99
RUBU001/ D	17mcb07-10.xl	4	Mogok	0.07	0.03	bdl	bdl	0.26	0.07	0.15	0.02	38.2	0.7	99	154	258	19	2.3	0.2	200	40
RUBU003/ D	17mca07-10.xl	4	Mogok	0.05	0.02	bdl	bdl	0.24	0.07	0.10	0.02	40.7	0.7	99	146	235	16	3.0	0.2	bdl	bdl
RUBU004/ D	17mcb11-14.xl	4	Mogok	bdl	bdl	bdl	bdl	0.17	0.07	0.90	0.03	18.6	0.5	99	159	176	19	2.8	0.2	bdl	bdl
RNBU048/ D	17mcb03-06.xl	4	Mogok	bdl	bdl	bdl	bdl	0.27	0.07	1.34	0.04	20.9	0.5	99	158	266	18	2.5	0.2	216	40
RUBUM02/ C	17mce07-10.xl	4	Mogok	bdl	bdl	0.13	0.07	0.24	0.08	0.88	0.05	75.2	1.2	99	205	150	20	2.4	0.3	bdl	bdl

Sample	File	N	Mine	Li7	1Stdev	Be9	1Stdev	B11	1Stdev	Na23	1Stdev	Mg25	1Stdev	Al27	1Stdev	Si29	1Stdev	P31	1Stdev	Ca44	1Stdev
Yunnan, CHN				µg/g	µg/g	µg/g	µg/g	µg/g	µg/g	µg/g	µg/g	µg/g	µg/g	wt%	µg/g	µg/g	µg/g	µg/g	µg/g	µg/g	µg/g
RNYN19/ C	24Org07-10.xl	4	Yuan Jiang	0.53	0.06	0.04	0.03	0.43	0.10	1.01	0.03	25	0.7	99	199	487	23	4.7	0.2	474	55
RNYN23/ C	24Orf07-10.xl	4	Yuan Jiang	0.42	0.05	0.05	0.03	0.38	0.09	5.39	0.07	57	1.0	99	195	800	21	3.9	0.2	1005	50
RNYN30/ C	24Org03-06.xl	4	Yuan Jiang	0.49	0.06	bdl	bdl	0.27	0.08	0.85	0.03	36	0.8	99	190	443	21	4.8	0.2	603	51
RNYN31/ C	24Orf03-06.xl	4	Yuan Jiang	0.48	0.06	bdl	bdl	0.41	0.09	1.52	0.03	34.7	0.8	99	195	291	21	5.2	0.2	357	48
RNYN50/ C	24Ore11-14.xl	4	Yuan Jiang	0.62	0.07	0.06	0.04	0.40	0.12	0.73	0.03	37.8	0.9	99	216	bdl	bdl	5.3	0.3	bdl	bdl
RNYN51/ C	24Ore07-10.xl	4	Yuan Jiang	0.47	0.06	0.05	0.04	0.46	0.11	6.68	0.08	61.4	1.0	99	192	448	23	4.9	0.2	364	55
RNYNXX/ C	24Org11-14.xl	4	Yuan Jiang	0.55	0.07	0.05	0.03	0.59	0.10	7.02	0.06	34.3	0.8	99	208	467	22	4.5	0.2	415	54
RNYNZZ/ C	24Orf11-14.xl	4	Yuan Jiang	0.51	0.06	0.08	0.05	0.49	0.10	4.37	0.07	37.5	0.8	99	214	bdl	bdl	4.5	0.2	bdl	bdl

Sample	File	N	Mine	Li7	1Stdev	Be9	1Stdev	B11	1Stdev	Na23	1Stdev	Mg25	1Stdev	Al27	1Stdev	Si29	1Stdev	P31	1Stdev	Ca44	1Stdev
Luc Yen, VIE				µg/g	µg/g	µg/g	µg/g	µg/g	µg/g	µg/g	µg/g	µg/g	µg/g	wt%	µg/g	µg/g	µg/g	µg/g	µg/g	µg/g	µg/g
RNVNL038/ C	24Orc07-10.xl	4	An Phu	0.46	0.05	0.05	0.03	0.52	0.11	bdl	bdl	12.1	0.4	99	185	1091	20	6.4	0.2	1509	45
RNVNL039/ C	24Ord11-14.xl	4	An Phu	0.47	0.06	0.11	0.05	0.46	0.11	0.47	0.02	39.6	0.8	99	191	381	23	4.8	0.2	565	50
RNVNL042/ C	24Orc11-14.xl	4	An Phu	0.50	0.06	0.04	0.04	0.60	0.12	0.09	0.01	64.5	1.1	99	197	511	24	5.8	0.2	701	50
RNVNL043/ C	24Ord07,10.xl	2	An Phu	0.45	0.05	0.10	0.04	0.46	0.10	0.87	0.03	87.2	1.1	99	175	876	18	5.2	0.2	1155	42
RNVNL046/ D	24Orc03-06.xl	4	An Phu	0.41	0.05	bdl	bdl	0.49	0.11	0.77	0.03	34.8	0.7	99	184	647	19	7.1	0.2	906	45
RNVNL133/ D	24Ore03-06.xl	4	An Phu	0.42	0.05	0.04	0.03	0.46	0.09	1.77	0.04	45.2	0.8	99	179	523	19	5.8	0.2	620	44
RNVNLY01/ C	24Ord15-18.xl	4	An Phu	0.73	0.09	bdl	bdl	0.65	0.14	0.21	0.02	41.9	1.0	99	235	274	29	5.8	0.3	bdl	bdl

Sample	File	N	Mine	Li7	1Stdev	Be9	1Stdev	B11	1Stdev	Na23	1Stdev	Mg25	1Stdev	Al27	1Stdev	Si29	1Stdev	P31	1Stdev	Ca44	1Stdev
Murgab, TJK				µg/g	µg/g	µg/g	µg/g	µg/g	µg/g	µg/g	µg/g	µg/g	µg/g	wt%	µg/g	µg/g	µg/g	µg/g	µg/g	µg/g	µg/g
RUTJ001/ C	17mcc03-06.xl	4	Snijnie	0.07	0.03	0.15	0.06	0.17	0.07	0.14	0.02	17.2	0.5	99	168	175	18	2.5	0.3	bdl	bdl
RUTJ002/ D	17mca11-14.xl	4	Snijnie	bdl	bdl	bdl	bdl	0.35	0.08	bdl	bdl	11.3	0.4	99	152	217	18	2.6	0.2	bdl	bdl
RUTJ003/ D	17mcd07-10.xl	4	Snijnie	0.08	0.04	0.11	0.09	0.24	0.10	0.51	0.03	24.0	0.6	99	186	212	24	2.3	0.3	bdl	bdl
RUTJ004/ D	17mca03-06.xl	4	Snijnie	0.05	0.02	bdl	bdl	0.34	0.08	0.08	0.02	11.7	0.4	99	153	273	18	3.0	0.2	bdl	bdl
RUTJ005/ D	17mca15-18.xl	4	Snijnie	bdl	bdl	0.07	0.06	0.27	0.07	0.10	0.02	18.2	0.5	99	158	188	19	2.4	0.2	bdl	bdl

Sample name suffix indicate the state of the sample (A: thin section, B: thick section, C: polished window on a rough sample, D: cut stone)

Sample	File	N	Mine	Ti49	1Stdev	V51	1Stdev	Cr53	1Stdev	Fe57	1Stdev	Zn66	1Stdev	Ga71	1Stdev	Ge73	1Stdev	As75	1Stdev
Uluguru Mts, TAN				µg/g	µg/g	µg/g	µg/g	µg/g	µg/g	µg/g	µg/g	µg/g	µg/g	µg/g	µg/g	µg/g	µg/g	µg/g	µg/g
MA3/ 2C	21jja07-10.xl	4	Mwarazi	142.2	1.4	36.6	0.2	2146	4	1041.7	5.8	2.36	0.10	61.48	0.26	0.096	0.027	0.230	0.019
MA3/ 3C	15jja03-06.xl	4	Mwarazi	103.6	1.1	18.9	0.1	1637	3	859.8	4.6	0.52	0.05	53.24	0.21	0.150	0.036	0.351	0.019
RUTZM-04/ 2B_1	23jja03-08.xl	6	Mwarazi	148.2	1.8	43.8	0.2	6292	9	685.4	5.5	0.53	0.08	39.70	0.25	0.132	0.055	0.377	0.026
RUTZM-04/ 2B_2	23jja09-11.xl	4	Mwarazi	163.2	1.8	49.8	0.2	7783	10	714.6	5.6	0.60	0.07	40.68	0.25	0.118	0.042	0.116	0.018
RUTZM-04/ 2B_3	23jja12.xl	1	Mwarazi	161.1	1.9	45.0	0.2	6686	10	638.5	5.5	0.36	0.07	37.72	0.25	bdl	bdl	0.169	0.020
RUTZM-04/ 2B_4	23jja13-15.xl	3	Mwarazi	156.0	1.9	47.9	0.2	7170	10	645.4	5.6	0.39	0.07	39.44	0.25	bdl	bdl	0.146	0.019
RUTZM-04/ 2B_5	23jja16-17.xl	2	Mwarazi	122.1	2.1	37.3	0.3	7607	13	612.8	6.8	0.42	0.10	43.50	0.33	bdl	bdl	0.103	0.022
RUTZM-08/ 2B_1	24jjb03-06.xl	4	Mwarazi	114.9	1.7	43.3	0.2	3377	7	515.2	5.2	0.39	0.07	22.50	0.20	0.198	0.059	0.218	0.022
RUTZM-08/ 2B_2	24jjb07-09.xl	3	Mwarazi	148.6	1.9	51.5	0.3	3789	8	526.1	5.3	0.65	0.08	26.88	0.21	bdl	bdl	0.178	0.020
RUTZM-08/ 2B_3	24jjb10-12.xl	3	Mwarazi	161.2	2.0	45.0	0.2	3085	7	504.6	5.2	0.31	0.06	19.44	0.19	bdl	bdl	0.170	0.020
RUTZM-08/ 2B_5	24jjb14.xl	1	Mwarazi	125.2	2.0	46.7	0.3	3263	8	537.2	6.1	0.33	0.07	22.09	0.23	bdl	bdl	0.216	0.024
RUTZM-08/ 2B_6	24jjb15.xl	1	Mwarazi	142.4	2.0	53.1	0.3	2412	7	518.2	5.7	0.43	0.07	21.46	0.21	bdl	bdl	0.157	0.021
RUTZM-08/ 2B_7	24jjb17.xl	1	Mwarazi	180.8	1.9	59.8	0.3	2089	5	514.8	5.0	0.33	0.06	16.18	0.16	bdl	bdl	0.166	0.019
RUTZM-11/ 3C	16mcd15-18.xl	4	Mwarazi	118.4	1.7	83.6	0.4	3482	7	381.6	4.5	1.57	0.14	43.56	0.28	0.214	0.074	0.085	0.027
RUTZM-11/ 4C	16mcd11-14.xl	4	Mwarazi	100.6	1.9	58.9	0.4	3146	8	547.1	6.4	5.30	0.24	35.46	0.30	bdl	bdl	0.098	0.029

Sample	File	N	Mine	Ti49	1Stdev	V51	1Stdev	Cr53	1Stdev	Fe57	1Stdev	Zn66	1Stdev	Ga71	1Stdev	Ge73	1Stdev	As75	1Stdev
Uluguru Mts, TAN				µg/g	µg/g	µg/g	µg/g	µg/g	µg/g	µg/g	µg/g	µg/g	µg/g	µg/g	µg/g	µg/g	µg/g	µg/g	µg/g
RUTZM-11/ 5C	16mcd03-06.xl	4	Mwarazi	86.9	1.2	70.4	0.3	3312	6	549.1	4.5	1.34	0.10	40.12	0.23	bdl	bdl	0.127	0.024
RUTZM-11/ 6C	16mce03-07.xl	5	Mwarazi	94.0	1.3	60.6	0.2	3151	6	540.3	4.4	1.00	0.09	27.64	0.19	0.177	0.053	0.070	0.019
RUTZM-11/ 7C	16mcd07-10.xl	4	Mwarazi	118.6	1.4	63.0	0.3	2557	5	540.8	4.4	0.49	0.08	22.58	0.17	0.201	0.049	0.086	0.018
RUTZM-12/ 1C	16mce16-19.xl	4	Mwarazi	85.1	1.4	221.3	0.6	2910	7	531.3	5.2	1.95	0.14	69.27	0.35	0.088	0.038	0.053	0.017
RUTZM-12/ 2C	16mcd19-22.xl	4	Mwarazi	126.1	1.5	23.1	0.2	1774	5	150.2	2.5	4.80	0.15	55.33	0.28	0.263	0.094	0.077	0.020
RUTZM-51/ C	16mcc15-18.xl	4	Mwarazi	127.8	1.7	80.7	0.3	3681	7	154.1	2.8	2.03	0.14	49.35	0.28	0.250	0.067	0.097	0.024
RUTZM-50/ 1C	16mcb07-10.xl	4	Msonge	94.9	1.4	49.3	0.3	1797	5	191.3	2.9	bdl	bdl	34.29	0.23	0.159	0.066	0.076	0.025
RUTZM-50/2C	16mca12-16.xl	5	Msonge	151.4	1.9	44.4	0.3	1370	5	414.8	4.6	1.54	0.15	56.40	0.32	0.273	0.096	0.105	0.027
RUTZM-50/ 3C	16mcb03-06.xl	4	Msonge	137.2	1.7	67.7	0.3	1824	5	493.2	4.3	1.63	0.10	28.43	0.21	bdl	bdl	0.067	0.022
RUTZM-50/4C	16mca07-11.xl	5	Msonge	144.2	1.9	30.8	0.2	860	4	1327.6	8.2	0.28	0.08	56.88	0.32	bdl	bdl	0.116	0.029
RUTZM-50/5C	16mca03-06.xl	4	Msonge	154.8	2.3	49.1	0.3	1842	6	167.5	3.6	0.64	0.15	64.34	0.41	bdl	bdl	0.214	0.050
RUTZM-22/ 1B_1	15mca03-08.xl	6	Visakazi II	141.2	2.4	38.0	0.3	5155	11	117.9	3.4	0.55	0.20	50.49	0.39	bdl	bdl	0.180	0.044
RUTZM-22/ 1B_2	15mca09-13.xl	5	Visakazi II	129.6	2.4	38.0	0.3	5025	12	118.2	3.6	bdl	bdl	58.90	0.45	bdl	bdl	0.123	0.038
RUTZM-22/ 1B_3	15mca14-15,18.xl	3	Visakazi II	94.8	4.1	22.1	0.5	2958	17	66.0	5.1	bdl	bdl	33.69	0.65	bdl	bdl	0.099	0.058
RUTZM-22/ 1B_4	15mca19-22.xl	4	Visakazi II	124.2	2.3	36.8	0.3	4855	11	108.7	3.4	0.58	0.22	56.56	0.43	bdl	bdl	0.145	0.036
RUTZM-25/ 1B_2	15mcc04.xl	1	Visakazi II	90.7	1.8	133.2	0.5	655	4	70.0	2.6	bdl	bdl	34.18	0.31	bdl	bdl	bdl	bdl
RUTZM-25/ 1B_3	15mcc07-09.xl	3	Visakazi II	143.7	2.0	104.7	0.4	1761	6	77.9	2.4	0.53	0.14	99.60	0.47	bdl	bdl	bdl	bdl
RUTZM-25/ 1B_4	15mcc10.xl	1	Visakazi II	80.6	1.4	104.2	0.4	1820	5	79.6	2.2	bdl	bdl	103.61	0.44	bdl	bdl	bdl	bdl
RUTZM-31/ 1B	16mcf03-06.xl	4	Visakazi II	126.6	2.0	71.7	0.4	3461	8	460.8	5.6	0.58	0.13	24.37	0.24	bdl	bdl	0.195	0.041
RUTZM-53/ 1C	16mcc07-10.xl	4	Visakazi II	129.2	1.8	56.2	0.3	6266	10	79.2	2.2	0.33	0.08	84.02	0.40	0.188	0.050	0.084	0.029
RUTZM-53/ 2C	16mcc11-14.xl	4	Visakazi II	96.7	1.7	53.1	0.3	5419	10	92.0	2.6	1.07	0.17	80.36	0.44	0.217	0.060	0.119	0.029
RUTZM-53/ 3C	16mcc03-06.xl	4	Visakazi II	131.6	2.0	51.2	0.3	7447	12	87.6	2.5	0.87	0.14	86.85	0.44	0.233	0.098	0.132	0.041
RUTZM-53/ 6C	16mcb11-14.xl	4	Visakazi II	116.7	1.7	23.9	0.2	3192	7	35.4	1.6	0.24	0.08	94.20	0.43	bdl	bdl	0.072	0.023
RUTZM-53/ 9C	16mcb15-18.xl	4	Visakazi II	117.3	1.7	24.3	0.2	536	3	70.2	2.0	0.23	0.07	79.93	0.37	0.127	0.045	0.077	0.021
RUTZM-53/13C	16mca17-20.xl	4	Visakazi II	115.2	1.7	32.9	0.2	3347	7	83.8	2.1	0.34	0.07	55.15	0.31	bdl	bdl	0.083	0.021
RUTZY-11/ 1C	21jjd11-14.xl	4	local market	130.5	1.5	78.4	0.3	6067	9	489.1	4.5	0.45	0.06	37.54	0.23	0.139	0.053	0.136	0.017
RUTZY-11/ 2C	16jje15-18.xl	4	local market	92.0	1.4	46.2	0.2	8155	11	198.4	3.2	9.13	0.21	37.12	0.25	bdl	bdl	0.114	0.019
RUTZY-11/ 4C	21jja03-06.xl	4	local market	121.1	1.6	53.0	0.2	8126	10	457.1	4.7	2.40	0.13	37.86	0.25	bdl	bdl	0.478	0.032
RUTZM-13/ 2C	16jjf03-06.xl	4	local market	120.7	1.4	18.5	0.1	779	3	54.9	1.5	1.38	0.08	48.90	0.25	bdl	bdl	0.134	0.015
RUTZM-13/ 4C	21jja11-14.xl	4	local market	156.7	1.4	42.0	0.2	2249	4	38.9	1.2	1.60	0.07	44.14	0.21	bdl	bdl	0.259	0.017

Sample	File	N	Mine	Ti49	1Stdev	V51	1Stdev	Cr53	1Stdev	Fe57	1Stdev	Zn66	1Stdev	Ga71	1Stdev	Ge73	1Stdev	As75	1Stdev
Mahenge Mts, TAN				µg/g	µg/g	µg/g	µg/g	µg/g	µg/g	µg/g	µg/g	µg/g	µg/g	µg/g	µg/g	µg/g	µg/g	µg/g	µg/g
M3/ 1C	16jjb03-06.xl	4	Mayote	84.2	1.1	11.5	0.1	318	2	167.6	2.3	0.33	0.05	35.63	0.19	0.091	0.034	0.152	0.015
M3/ 2C	16jje07-10.xl	4	Mayote	129.7	1.6	25.9	0.2	190	2	258.7	3.4	4.81	0.14	29.70	0.21	0.165	0.049	0.254	0.022
RUTZH-05/ 3C	16jjb07-10.xl	4	Mayote	94.1	1.0	54.7	0.2	4016	5	746.3	4.3	0.36	0.04	62.42	0.23	bdl	bdl	0.104	0.012
RUTZH-05/ 4C	21jjb03-06.xl	4	Mayote	179.8	1.8	30.1	0.2	634	3	124.8	2.3	0.54	0.07	40.03	0.23	0.077	0.028	0.128	0.018
RUTZH-05/ 9C	21jjc03-06.xl	4	Mayote	167.0	1.6	159.3	0.4	3542	6	220.3	2.7	1.08	0.07	153.96	0.42	0.470	0.066	0.274	0.019
RUTZH-05/ 11C	21jjd07-10.xl	4	Mayote	133.1	1.5	11.7	0.1	867	3	187.4	2.7	0.36	0.05	45.25	0.24	0.082	0.032	0.124	0.015
RUTZH-05/ 12C	17mce20-23.xl	4	Mayote	175.5	1.8	21.3	0.2	530	3	159.8	2.5	0.27	0.07	47.51	0.25	0.105	0.040	0.059	0.017
RUTZH-05/ 13C	17mce11-14.xl	4	Mayote	59.8	0.9	13.3	0.1	567	2	84.4	1.6	0.23	0.07	156.45	0.40	0.195	0.053	bdl	bdl
RUTZH-06/ 03C	17mce03-06.xl	4	Mayote	86.4	1.2	26.1	0.2	1790	4	277.7	3.1	0.41	0.08	184.39	0.46	bdl	bdl	0.072	0.015
M4/ 3C	16jjb15-18.xl	4	Lukande	108.0	1.2	18.1	0.1	212	1	621.7	4.2	0.25	0.04	30.83	0.17	0.080	0.030	0.121	0.013
M4/ 5C	16jja15-18.xl	4	Lukande	54.9	1.0	15.8	0.1	283	2	173.7	2.7	0.30	0.07	30.95	0.21	0.098	0.035	0.400	0.026
RUTZH-10/ 2C	21jje03-06.xl	4	Lukande	51.1	1.0	139.8	0.4	3936	7	192.7	3.0	1.08	0.08	90.02	0.36	0.133	0.041	0.110	0.016
RUTZH-10/ 4C	17mcd14-17.xl	4	Lukande	132.3	1.4	107.8	0.3	1964	5	217.7	3.0	0.29	0.07	85.89	0.35	0.241	0.060	0.042	0.013
RUTZH-11/ 1C	16jjd11-14.xl	4	Lukande	47.0	0.9	73.1	0.3	7202	9	4385.9	12.4	0.45	0.06	84.79	0.32	0.121	0.035	0.085	0.014
RUTZH-11/ 3C	16jjd03-06.xl	4	Lukande	115.2	1.7	65.1	0.2	4875	4	885.0	4.9	0.42	0.07	34.59	0.29	bdl	bdl	0.135	0.016
RUTZH-11/ 2C	16jjd07-10.xl	4	Lukande	140.2	1.2	52.3	0.2	1613	6	552.5	4.9	0.49	0.05	58.73	0.18	0.157	bdl	0.102	0.012
RUTZH-11/ 14C	17mcd18-22.xl	5	Lukande	98.1	1.3	50.7	0.2	2364	5	319.3	3.5	0.40	0.07	28.61	0.19	0.191	0.050	0.053	0.014
RUTZH-18/ 5B_1	23jjc03.xl	1	Kitwaro	95.2	1.6	20.1	0.2	3441	8	296.4	4.1	bdl	bdl	33.33	0.25	bdl	bdl	0.164	0.022
RUTZH-18/ 5B_2	23jjc04.xl	1	Kitwaro	89.6	1.5	20.2	0.2	2867	7	296.8	4.1	0.32	0.07	33.91	0.26	0.224	0.072	0.164	0.022
RUTZH-18/ 5B_3	23jjc05.xl	1	Kitwaro	180.0	2.7	26.5	0.2	6742	13	289.8	5.0	0.41	0.10	79.22	0.48	bdl	bdl	0.107	0.025
RUTZH-18/ 5B_4	23jjc07.xl	1	Kitwaro	124.7	2.7	21.8	0.3	3510	12	288.5	6.1	bdl	bdl	33.81	0.39	bdl	bdl	0.186	0.032
RUTZH-18/ 5B_5	23jjc08.xl	1	Kitwaro	89.3	1.4	18.4	0.2	3597	7	275.8	3.7	bdl	bdl	31.15	0.23	bdl	bdl	0.115	0.018
RUTZH-18/ 5B_6	23jjc09.xl	1	Kitwaro	78.6	1.6	18.8	0.2	3184	8	282.7	4.6	bdl	bdl	30.17	0.27	bdl	bdl	bdl	bdl
RUTZH-18/ 5B_7	23jjc10.xl	1	Kitwaro	104.6	2.0	20.1	0.2	3289	9	299.1	5.0	bdl	bdl	33.84	0.31	bdl	bdl	0.092	0.025
RUTZH-18/ 5B_8	23jjc11.xl	1	Kitwaro	186.4	2.7	65.8	0.4	5434	12	349.3	5.5	0.27	0.09	40.30	0.34	bdl	bdl	0.092	0.024
RUTZH-18/ 7B_1	24jja03-04.xl	2	Kitwaro	93.0	1.7	28.6	0.2	1787	6	339.6	4.9	bdl	bdl	22.98	0.23	bdl	bdl	0.166	0.026
RUTZH-18/ 7B_2	24jja05.xl	1	Kitwaro	209.9	3.8	14.2	0.2	2545	11	270.2	6.5	bdl	bdl	78.83	0.63	bdl	bdl	0.217	0.037
RUTZH-18/ 7B_3	24jja06.xl	1	Kitwaro	141.5	3.1	38.6	0.4	4679	15	320.7	7.1	bdl	bdl	95.67	0.70	bdl	bdl	0.191	0.039
RUTZH-18/ 7B_4	24jja07.xl	1	Kitwaro	298.7	2.7	22.3	0.2	2426	6	303.7	4.1	bdl	bdl	66.54	0.35	bdl	bdl	0.236	0.023
RUTZH-18/ 7B_5	24jja08-09.xl	2	Kitwaro	143.6	1.8	18.9	0.2	3109	7	287.4	3.8	0.18	0.06	86.21	0.38	bdl	bdl	0.149	0.020
RUTZH-18/ 7B_6	24jja10.xl	1	Kitwaro	180.7	2.2	19.9	0.2	4426	9	296.6	4.2	bdl	bdl	59.35	0.34	bdl	bdl	0.099	0.019
RUTZH-18/ 7B_8	24jja12.xl	1	Kitwaro	115.5	4.2	27.2	0.5	5623	24	255.0	9.5	bdl	bdl	45.09	0.71	bdl	bdl	bdl	bdl
RUTZH-18/ 7B_9	24jja13.xl	1	Kitwaro	112.4	2.0	27.5	0.2	1409	6	359.1	5.4	bdl	bdl	22.15	0.24	bdl	bdl	0.112	0.026
RUTZH-18/ 7B_10	24jja14.xl	1	Kitwaro	82.7	1.7	30.6	0.2	2654	8	329.7	5.0	0.35	0.09	38.50	0.30	bdl	bdl	0.145	0.026
RUTZH-23/ C	17mcc17-20.xl	4	Kitwaro	57.0	1.0	70.1	0.3	7997	9	400.8	4.0	1.90	0.12	71.29	0.31	0.210	0.062	0.050	0.016
RUTZH-25/ C	17mcd11-13.xl	3	Kitwaro	111.6	1.4	31.9	0.2	2683	5	104.9	2.1	5.11	0.16	49.43	0.26	0.140	0.043	0.044	0.013
RUTZH-27/ 2C	17mcc07-11.xl	4	Kitwaro	106.7	1.4	14.1	0.1	2503	5	158.4	2.6	1.08	0.11	19.62	0.17	bdl	bdl	0.104	0.022
M1/ 3C	15jjd07-10.xl	4	Ipangko	96.5	1.1	35.0	0.2	4257	6	606.3	4.3	0.39	0.05	49.52	0.22	0.111	0.034	0.195	0.016
M1/ 4C	16jja03-06.xl	4	Ipangko	103.0	1.0	69.2	0.2	3291	5	1776.6	6.0	0.45	0.05	40.92	0.17	0.130	0.032	0.283	0.016
M1/ 5C	16jjb11-14.xl	4	Ipangko	87.2	1.2	59.5	0.2	2810	6	1464.5	7.6	0.23	0.06	49.32	0.26	bdl	bdl	0.160	0.018
RUTZH-19/ 2B_1	23jjb03.xl	1	Ipangko	78.2	1.3	52.8	0.3	2469	6	1056.8	7.0	0.22	0.06	39.12	0.25	bdl	bdl	0.466	0.028
RUTZH-19/ 2B_2	23jjb04.xl	1	Ipangko	134.0	2.0	58.4	0.3	2421	7	1241.5	9.1	0.19	0.08	40.66	0.31	bdl	bdl	0.171	0.025
RUTZH-19/ 2B_3	23jjb05.xl	1	Ipangko	101.3	1.5	51.2	0.3	2861	7	1130.9	7.6	0.20	0.06	43.35	0.27	bdl	bdl	0.250	0.023
RUTZH-19/ 2B_4	23jjb06.xl	1	Ipangko	124.5	1.8	57.3	0.3	2459	6	1228.7	8.2	0.34	0.07	39.72	0.27	bdl	bdl	0.198	0.022
RUTZH-19/ 2B_5	23jjb07.xl	1	Ipangko	170.9	2.0	55.3	0.3	2921	7	1487.4	8.8	0.37	0.07	47.37	0.29	bdl	bdl	0.147	0.021
RUTZH-19/ 2B_6	23jjb09-10.xl	2	Ipangko	481.3	3.3	69.7	0.3	3363	7	965.5	6.9	0.34	0.07	107.42	0.42	bdl	bdl	0.136	0.019
RUTZH-19/ 2B_7	23jjb11.xl	1	Ipangko	358.2	3.2	137.9	0.5	4837	9	1351.5	9.0	0.27	0.07	135.99	0.52	bdl	bdl	0.235	0.025
RUTZH-19/ 2B_8	23jjb12-13.xl	2	Ipangko	379.8	3.5	105.9	0.4	3797	9	1492.6	10.4	0.36	0.10	89.74	0.46	0.422	0.111	0.150	0.023
RUTZH-19/ 2B_9	23jjb14.xl	1	Ipangko	117.3	2.1	80.0	0.4	2141	7	1028.5	9.3	bdl	bdl	44.61	0.35	bdl	bdl	0.102	0.024
RUTZH-19/ 2B_10	23jjb15.xl	1	Ipangko	62.0	1.4	90.5	0.4	5822	11	781.1	7.3	0.76	0.10	108.72	0.50	bdl	bdl	0.248	0.026
RUTZH-19/ 2B_11	23jjb16.xl	1	Ipangko	144.7	1.9	52.8	0.3	2835	7	1164.2	8.0	bdl	bdl	43.42	0.28	0.195	0.066	0.146	0.021
RUTZH-20/ 1B_1	15mcb03-06.xl	4	Ipangko	163.1	2.6	50.8	0.4	1670	7	1022.7	9.5	bdl	bdl	46.04	0.39	bdl	bdl	0.177	0.060
RUTZH-20/ 1B_2	15mcb07-12.xl	6	Ipangko	222.5	2.9	59.8	0.4	2182	7	1367.4	10.5	bdl	bdl	45.62	0.36	0.322	0.103	0.103	0.038

Sample	File	N	Mine	Ti49	1Stdev	V51	1Stdev	Cr53	1Stdev	Fe57	1Stdev	Zn66	1Stdev	Ga71	1Stdev	Ge73	1Stdev	As75	1Stdev
Mahenge Mts, TAN				µg/g	µg/g	µg/g	µg/g	µg/g	µg/g	µg/g	µg/g	µg/g	µg/g	µg/g	µg/g	µg/g	µg/g	µg/g	µg/g
RUTZH-20/ 1B_3	15mcb13-17.xl	5	Ipangko	704.4	4.3	100.0	0.4	3224	8	1649.0	10.1	bdl	bdl	75.24	0.40	bdl	bdl	0.080	0.025
RUTZH-22/ 2C	21jjc07-10.xl	4	Ipangko	105.4	1.2	58.1	0.2	7120	8	363.8	3.3	0.92	0.06	22.32	0.15	bdl	bdl	0.194	0.016
RUTZH-22/ 3C	21jjd03-06.xl	4	Ipangko	118.1	1.6	57.1	0.3	1821	5	601.5	5.5	0.50	0.07	65.61	0.33	0.154	0.041	0.191	0.021
RUTZH-22/ 4C	16jjc11-12,14,f11-12	5	Ipangko	72.9	1.2	22.7	0.2	3730	7	242.7	3.3	1.47	0.11	30.60	0.21	bdl	bdl	0.096	0.015
RUTZH-22/ 6C	17mcd03-06.xl	4	Ipangko	67.1	1.3	32.3	0.2	1058	4	1289.3	8.0	0.31	0.07	157.27	0.53	bdl	bdl	0.068	0.016

Sample	File	N	Mine	Ti49	1Stdev	V51	1Stdev	Cr53	1Stdev	Fe57	1Stdev	Zn66	1Stdev	Ga71	1Stdev	Ge73	1Stdev	As75	1Stdev
Mangari, KEN				µg/g	µg/g	µg/g	µg/g	µg/g	µg/g	µg/g	µg/g	µg/g	µg/g	µg/g	µg/g	µg/g	µg/g	µg/g	µg/g
RUKEM-22/ 1C	15jjb11-14.xl	4	John Saul	217.7	1.9	30.9	0.2	3375	6	8.0	0.7	0.44	0.06	219.65	0.51	0.262	0.054	0.267	0.021
RUKEM-22/ 2C	15jjb15-18.xl	4	John Saul	201.1	1.9	20.2	0.1	3186	6	8.0	0.8	0.41	0.06	175.83	0.48	0.161	0.048	0.181	0.019
RUKEM-22/ 3C	21jje07-10.xl	4	John Saul	511.9	3.1	37.7	0.2	2753	6	22.2	1.1	1.63	0.08	273.56	0.62	0.330	0.066	0.089	0.014

Sample	File	N	Mine	Ti49	1Stdev	V51	1Stdev	Cr53	1Stdev	Fe57	1Stdev	Zn66	1Stdev	Ga71	1Stdev	Ge73	1Stdev	As75	1Stdev
Shan State, MYA				µg/g	µg/g	µg/g	µg/g	µg/g	µg/g	µg/g	µg/g	µg/g	µg/g	µg/g	µg/g	µg/g	µg/g	µg/g	µg/g
BUMGIT01/ C	24Ora03-06.xl	4	Namyaseik	120.3	1.6	331.7	0.6	2868	6	63.6	2.0	0.84	0.08	72.64	0.33	bdl	bdl	0.210	0.028
BUMGIT02 /C	24Ora07-10.xl	4	Namyaseik	35.6	0.9	185.4	0.5	2251	5	67.5	2.3	0.45	0.07	86.66	0.38	bdl	bdl	0.280	0.033
BUMGIT03/ C	24Ora11-14.xl	4	Namyaseik	49.2	1.0	504.9	0.8	3364	7	283.2	3.6	0.57	0.07	174.80	0.52	0.198	0.068	0.117	0.027
BUMGIT04/ C	24Ora15-18.xl	4	Mogok	72.1	1.3	586.4	0.9	2146	6	34.6	2.0	0.44	0.07	24.66	0.18	bdl	bdl	0.137	0.028
BUMGIT05/ C	24Orb03-06.xl	4	Mogok	154.3	2.0	530.2	0.9	2748	7	160.9	3.0	0.38	0.06	145.00	0.50	bdl	bdl	0.111	0.027
BUMGIT06/ C	24Orb07-10.xl	4	Mogok	152.0	1.7	372.6	0.6	1983	5	120.8	2.4	0.26	0.05	111.80	0.39	bdl	bdl	0.064	0.020
BUMGIT07/ C	24Orb11-14.xl	4	Mogok	130.9	1.8	339.4	0.7	1996	6	80.8	2.5	0.31	0.06	37.11	0.26	bdl	bdl	0.107	0.028
RUBU001/ D	17mcb07-10.xl	4	Mogok	64.2	0.9	683.6	0.7	4523	6	166.3	2.2	0.42	0.07	126.87	0.35	bdl	bdl	0.063	0.015
RUBU003/ D	17mca07-10.xl	4	Mogok	69.4	0.9	323.2	0.5	1995	4	61.2	1.3	1.16	0.08	15.23	0.12	bdl	bdl	0.054	0.015
RUBU004/ D	17mcb11-14.xl	4	Mogok	30.6	0.6	136.2	0.3	2636	5	24.8	1.0	0.63	0.08	60.10	0.25	bdl	bdl	0.070	0.014
RNBU048/ D	17mcb03-06.xl	4	Mogok	51.7	0.8	216.6	0.4	4268	6	76.6	1.6	0.63	0.08	73.92	0.28	bdl	bdl	0.079	0.017
RUBUM02/ C	17mce07-10.xl	4	Mogok	124.0	1.6	666.7	0.9	1867	5	142.7	2.7	0.30	0.08	47.80	0.28	bdl	bdl	0.069	0.017

Sample	File	N	Mine	Ti49	1Stdev	V51	1Stdev	Cr53	1Stdev	Fe57	1Stdev	Zn66	1Stdev	Ga71	1Stdev	Ge73	1Stdev	As75	1Stdev
Yunnan, CHN				µg/g	µg/g	µg/g	µg/g	µg/g	µg/g	µg/g	µg/g	µg/g	µg/g	µg/g	µg/g	µg/g	µg/g	µg/g	µg/g
RNYN19/ C	24Org07-10.xl	4	Yuan Jiang	97.7	1.1	133.5	0.3	4899	6	35.9	1.2	6.62	0.12	50.93	0.21	bdl	bdl	0.047	0.012
RNYN23/ C	24Orf07-10.xl	4	Yuan Jiang	335.5	2.0	173.7	0.3	8097	8	43.6	1.2	0.76	0.05	77.60	0.25	0.208	0.042	0.063	0.012
RNYN30/ C	24Org03-06.xl	4	Yuan Jiang	63.5	0.8	77.7	0.2	4271	5	28.7	1.0	0.27	0.04	49.46	0.19	bdl	bdl	0.071	0.012
RNYN31/ C	24Orf03-06.xl	4	Yuan Jiang	54.7	0.8	54.5	0.2	1968	4	29.9	1.1	0.40	0.04	33.57	0.17	bdl	bdl	0.048	0.013
RNYN50/ C	24Ore11-14.xl	4	Yuan Jiang	50.5	0.9	36.3	0.2	2842	5	152.7	2.2	0.55	0.05	33.54	0.18	bdl	bdl	0.189	0.016
RNYN51/ C	24Ore07-10.xl	4	Yuan Jiang	126.9	1.2	68.9	0.2	5366	6	78.7	1.5	1.11	0.06	41.74	0.18	0.144	0.034	0.062	0.014
RNYNXX/ C	24Org11-14.xl	4	Yuan Jiang	55.1	0.8	100.9	0.3	7502	8	16.0	1.0	0.65	0.05	58.91	0.23	bdl	bdl	0.062	0.012
RNYNZZ/ C	24Orf11-14.xl	4	Yuan Jiang	57.8	0.9	37.1	0.2	4992	6	71.8	1.6	0.99	0.06	38.81	0.19	bdl	bdl	0.065	0.013

Sample	File	N	Mine	Ti49	1Stdev	V51	1Stdev	Cr53	1Stdev	Fe57	1Stdev	Zn66	1Stdev	Ga71	1Stdev	Ge73	1Stdev	As75	1Stdev
Luc Yen, VIE				µg/g	µg/g	µg/g	µg/g	µg/g	µg/g	µg/g	µg/g	µg/g	µg/g	µg/g	µg/g	µg/g	µg/g	µg/g	µg/g
RNVNL038/ C	24Orc07-10.xl	4	An Phu	81.6	0.9	23.0	0.1	5586	6	258.2	2.4	2.15	0.08	36.81	0.17	0.153	0.036	0.056	0.014
RNVNL039/ C	24Ord11-14.xl	4	An Phu	132.2	1.2	27.8	0.1	5786	6	19.6	1.0	9.69	0.12	12.33	0.10	bdl	bdl	bdl	bdl
RNVNL042/ C	24Orc11-14.xl	4	An Phu	177.8	1.4	144.3	0.3	5837	7	65.1	1.5	0.59	0.05	18.53	0.13	bdl	bdl	0.042	0.015
RNVNL043/ C	24Ord07,10.xl	2	An Phu	347.4	1.8	319.1	0.4	4724	5	63.3	1.2	1.19	0.06	41.35	0.17	0.117	0.032	0.054	0.012
RNVNL046/ D	24Orc03-06.xl	4	An Phu	43.0	0.7	10.4	0.1	4014	5	117.1	1.7	2.56	0.08	48.28	0.19	bdl	bdl	0.095	0.015
RNVNL133/ D	24Ore03-06.xl	4	An Phu	90.6	0.9	14.9	0.1	8630	7	32.0	0.9	2.16	0.07	29.64	0.14	bdl	bdl	0.125	0.014
RNVNLY01/ C	24Ord15-18.xl	4	An Phu	236.1	2.0	102.8	0.3	4821	7	156.6	2.5	0.91	0.07	104.38	0.36	0.212	0.062	0.060	0.013

Sample	File	N	Mine	Ti49	1Stdev	V51	1Stdev	Cr53	1Stdev	Fe57	1Stdev	Zn66	1Stdev	Ga71	1Stdev	Ge73	1Stdev	As75	1Stdev
Murgab, TJK				µg/g	µg/g	µg/g	µg/g	µg/g	µg/g	µg/g	µg/g	µg/g	µg/g	µg/g	µg/g	µg/g	µg/g	µg/g	µg/g
RUTJ001/ C	17mcc03-06.xl	4	Snijnie	225.4	1.9	123.6	0.3	1694	4	152.0	2.3	1.20	0.10	84.42	0.32	0.409	0.074	0.100	0.020
RUTJ002/ D	17mca11-14.xl	4	Snijnie	77.6	1.0	134.5	0.3	2705	5	65.1	1.4	1.21	0.09	104.79	0.32	0.533	0.071	0.069	0.015
RUTJ003/ D	17mcd07-10.xl	4	Snijnie	464.9	2.9	78.6	0.3	1916	5	42.9	1.4	0.97	0.10	81.09	0.33	0.470	0.081	0.052	0.016
RUTJ004/ D	17mca03-06.xl	4	Snijnie	154.8	1.4	60.7	0.2	2176	4	30.7	1.1	1.28	0.09	68.96	0.27	0.507	0.081	0.111	0.022
RUTJ005/ D	17mca15-18.xl	4	Snijnie	280.9	2.0	131.2	0.3	1457	4	154.5	2.2	1.20	0.09	87.92	0.30	0.474	0.069	0.104	0.016

Sample	File	N	Mine	Zr90	1Stdev	Nb93	1Stdev	Sn118	1Stdev	Ce140	1Stdev	Pb208	1Stdev	Th232	1Stdev	U238	1Stdev
Uluguru Mts, TAN				µg/g	µg/g	µg/g	µg/g	µg/g	µg/g	µg/g	µg/g	µg/g	µg/g	µg/g	µg/g	µg/g	µg/g
MA3/ 2C	21jja07-10.xl	4	Mwarazi	0.007	0.002	0.008	0.002	0.09	0.02	0.005	0.002	0.31	0.02	bdl	bdl	0.001	0.001
MA3/ 3C	15jja03-06.xl	4	Mwarazi	0.006	0.002	0.004	0.001	0.07	0.02	bdl	bdl	0.31	0.02	bdl	bdl	bdl	bdl
RUTZM-04/ 2B_1	23jja03-08.xl	6	Mwarazi	0.014	0.005	0.019	0.004	0.11	0.03	bdl	bdl	0.34	0.02	bdl	bdl	0.006	0.002
RUTZM-04/ 2B_2	23jja09-11.xl	4	Mwarazi	0.015	0.005	0.027	0.004	0.13	0.03	bdl	bdl	0.32	0.02	bdl	bdl	bdl	bdl
RUTZM-04/ 2B_3	23jja12.xl	1	Mwarazi	0.017	0.006	0.021	0.004	0.09	0.03	bdl	bdl	0.20	0.02	0.008	0.002	bdl	bdl
RUTZM-04/ 2B_4	23jja13-15.xl	3	Mwarazi	0.037	0.007	0.026	0.005	0.11	0.03	0.004	0.002	0.14	0.01	0.016	0.003	0.013	0.003
RUTZM-04/ 2B_5	23jja16-17.xl	2	Mwarazi	0.025	0.008	0.028	0.006	bdl	bdl	bdl	bdl	0.13	0.02	0.005	0.002	bdl	bdl
RUTZM-08/ 2B_1	24jjb03-06.xl	4	Mwarazi	0.011	0.004	0.019	0.004	0.09	0.02	0.074	0.006	0.48	0.03	0.004	0.002	0.062	0.006
RUTZM-08/ 2B_2	24jjb07-09.xl	3	Mwarazi	0.095	0.010	0.013	0.004	0.08	0.03	0.007	0.002	0.09	0.01	0.008	0.002	0.011	0.003
RUTZM-08/ 2B_3	24jjb10-12.xl	3	Mwarazi	0.015	0.005	0.024	0.004	0.11	0.03	bdl	bdl	0.14	0.01	bdl	bdl	0.009	0.002
RUTZM-08/ 2B_5	24jjb14.xl	1	Mwarazi	0.015	0.006	0.036	0.006	0.13	0.03	0.019	0.004	0.18	0.02	0.008	0.003	0.052	0.006
RUTZM-08/ 2B_6	24jjb15.xl	1	Mwarazi	0.007	0.004	0.022	0.005	0.14	0.03	0.012	0.003	0.19	0.02	bdl	bdl	0.045	0.006
RUTZM-08/ 2B_7	24jjb17.xl	1	Mwarazi	bdl	bdl	0.032	0.005	0.22	0.03	0.132	0.008	0.25	0.02	0.004	0.002	0.026	0.004
RUTZM-11/ 3C	16mcd15-18.xl	4	Mwarazi	bdl	bdl	0.016	0.005	0.09	0.03	0.020	0.005	0.04	0.01	bdl	bdl	0.014	0.004
RUTZM-11/ 4C	16mcd11-14.xl	4	Mwarazi	0.021	0.010	0.022	0.006	0.15	0.06	0.030	0.007	0.14	0.02	bdl	bdl	0.011	0.004
RUTZM-11/ 5C	16mcd03-06.xl	4	Mwarazi	0.011	0.004	0.012	0.003	0.15	0.02	0.005	0.002	0.02	0.01	bdl	bdl	0.003	0.001
RUTZM-11/ 6C	16mce03-07.xl	5	Mwarazi	0.054	0.011	0.007	0.003	bdl	bdl	0.006	0.003	0.03	0.01	bdl	bdl	0.002	0.001
RUTZM-11/ 7C	16mcd07-10.xl	4	Mwarazi	0.015	0.005	0.008	0.002	0.06	0.02	bdl	bdl	0.03	0.01	bdl	bdl	0.005	0.002
RUTZM-12/ 1C	16mce16-19.xl	4	Mwarazi	0.236	0.027	0.019	0.005	0.09	0.03	0.017	0.005	0.05	0.01	0.031	0.007	0.037	0.006
RUTZM-12/ 2C	16mcd19-22.xl	4	Mwarazi	0.012	0.004	0.008	0.003	0.09	0.02	0.011	0.003	0.03	0.01	0.015	0.005	0.008	0.002
RUTZM-51/ C	16mcc15-18.xl	4	Mwarazi	0.013	0.004	0.013	0.004	0.14	0.03	0.010	0.004	0.08	0.01	bdl	bdl	0.008	0.003
RUTZM-50/ 1C	16mcb07-10.xl	4	Msonge	bdl	bdl	0.011	0.004	0.09	0.03	0.007	0.003	0.02	0.01	0.005	0.002	bdl	bdl
RUTZM-50/2C	16mca12-16.xl	5	Msonge	0.051	0.010	0.010	0.004	0.11	0.03	0.017	0.004	0.06	0.01	0.192	0.012	0.009	0.003
RUTZM-50/ 3C	16mcb03-06.xl	4	Msonge	0.017	0.005	0.010	0.004	0.15	0.03	0.010	0.004	0.05	0.01	bdl	bdl	bdl	bdl
RUTZM-50/4C	16mca07-11.xl	5	Msonge	0.017	0.008	0.007	0.003	0.12	0.03	bdl	bdl	0.08	0.01	bdl	bdl	0.005	0.002
RUTZM-50/5C	16mca03-06.xl	4	Msonge	0.144	0.018	0.038	0.008	0.20	0.05	0.049	0.008	0.10	0.02	0.008	0.003	0.017	0.005
RUTZM-22/ 1B_1	15mca03-08.xl	6	Visakazi II	0.021	0.009	0.027	0.008	bdl	bdl	0.009	0.005	0.05	0.02	bdl	bdl	bdl	bdl

Sample	File	N	Mine	Zr90	1Stdev	Nb93	1Stdev	Sn118	1Stdev	Ce140	1Stdev	Pb208	1Stdev	Th232	1Stdev	U238	1Stdev
Uluguru Mts, TAN				µg/g	µg/g	µg/g	µg/g	µg/g	µg/g	µg/g	µg/g	µg/g	µg/g	µg/g	µg/g	µg/g	µg/g
RUTZM-22/ 1B_2	15mca09-13.xl	5	Visakazi II	0.047	0.012	0.022	0.008	0.17	0.06	0.026	0.008	bdl	bdl	bdl	bdl	bdl	bdl
RUTZM-22/ 1B_3	15mca14-15,18.xl	3	Visakazi II	bdl	bdl	bdl	bdl	bdl	bdl	bdl	bdl	bdl	bdl	bdl	bdl	bdl	bdl
RUTZM-22/ 1B_4	15mca19-22.xl	4	Visakazi II	bdl	bdl	0.018	0.007	bdl	bdl	bdl	bdl	0.04	0.02	0.007	0.004	bdl	bdl
RUTZM-25/ 1B_2	15mcc04.xl	1	Visakazi II	bdl	bdl	bdl	bdl	bdl	bdl	bdl	bdl	bdl	bdl	bdl	bdl	bdl	bdl
RUTZM-25/ 1B_3	15mcc07-09.xl	3	Visakazi II	0.019	0.008	bdl	bdl	0.14	0.04	bdl	bdl	bdl	bdl	bdl	bdl	bdl	bdl
RUTZM-25/ 1B_4	15mcc10.xl	1	Visakazi II	bdl	bdl	bdl	bdl	bdl	bdl	bdl	bdl	bdl	bdl	bdl	bdl	0.004	bdl
RUTZM-31/ 1B	16mcf03-06.xl	4	Visakazi II	bdl	bdl	0.012	0.006	bdl	bdl	0.007	0.004	0.03	0.01	bdl	bdl	bdl	bdl
RUTZM-53/ 1C	16mcc07-10.xl	4	Visakazi II	0.016	0.007	0.016	0.005	0.14	0.04	0.008	0.003	0.03	0.01	bdl	bdl	0.009	0.004
RUTZM-53/ 2C	16mcc11-14.xl	4	Visakazi II	0.017	0.006	0.018	0.005	0.08	0.03	0.009	0.004	0.05	0.01	bdl	bdl	bdl	bdl
RUTZM-53/ 3C	16mcc03-06.xl	4	Visakazi II	0.023	0.008	0.024	0.007	0.14	0.04	bdl	bdl	2.37	0.07	bdl	bdl	bdl	bdl
RUTZM-53/ 6C	16mcb11-14.xl	4	Visakazi II	bdl	bdl	0.008	0.003	0.08	0.03	bdl	bdl	0.02	0.01	bdl	bdl	bdl	bdl
RUTZM-53/ 9C	16mcb15-18.xl	4	Visakazi II	0.007	0.003	0.005	0.003	0.06	0.02	bdl	bdl	0.03	0.01	bdl	bdl	bdl	bdl
RUTZM-53/13C	16mca17-20.xl	4	Visakazi II	0.017	0.005	0.009	0.004	0.08	0.02	bdl	bdl	0.02	0.01	bdl	bdl	bdl	bdl
RUTZY-11/ 1C	21jjd11-14.xl	4	local market	0.008	0.003	0.014	0.003	0.13	0.02	bdl	bdl	0.26	0.02	bdl	bdl	bdl	bdl
RUTZY-11/ 2C	16jje15-18.xl	4	local market	0.019	0.006	0.022	0.004	0.11	0.03	0.008	0.003	0.13	0.02	0.006	0.002	bdl	bdl
RUTZY-11/ 4C	21jja03-06.xl	4	local market	0.022	0.005	0.022	0.004	0.12	0.03	bdl	bdl	0.71	0.03	bdl	bdl	bdl	bdl
RUTZM-13/ 2C	16jjf03-06.xl	4	local market	0.012	0.004	0.005	0.002	0.09	0.02	0.003	0.001	0.23	0.02	0.005	0.002	0.005	0.002
RUTZM-13/ 4C	21jja11-14.xl	4	local market	0.020	0.004	0.008	0.002	0.09	0.02	0.005	0.001	0.26	0.01	0.018	0.002	0.017	0.002

Sample	File	N	Mine	Zr90	1Stdev	Nb93	1Stdev	Sn118	1Stdev	Ce140	1Stdev	Pb208	1Stdev	Th232	1Stdev	U238	1Stdev
Mahenge Mts, TAN				µg/g	µg/g	µg/g	µg/g	µg/g	µg/g	µg/g	µg/g	µg/g	µg/g	µg/g	µg/g	µg/g	µg/g
M3/ 1C	16jjb03-06.xl	4	Mayote	bdl	bdl	0.008	0.002	0.09	0.02	0.004	0.001	0.60	0.02	bdl	bdl	0.012	0.002
M3/ 2C	16jje07-10.xl	4	Mayote	0.005	0.003	0.004	0.002	0.12	0.03	0.003	0.002	0.27	0.02	bdl	bdl	bdl	bdl
RUTZH-05/ 3C	16jjb07-10.xl	4	Mayote	0.011	0.003	0.013	0.002	0.10	0.02	0.002	0.001	0.28	0.01	0.002	0.001	0.004	0.001
RUTZH-05/ 4C	21jjb03-06.xl	4	Mayote	0.008	0.004	0.005	0.002	0.11	0.02	bdl	bdl	0.38	0.02	bdl	bdl	0.006	0.002
RUTZH-05/ 9C	21jjc03-06.xl	4	Mayote	0.018	0.004	0.011	0.002	0.14	0.02	0.004	0.001	0.26	0.02	bdl	bdl	0.005	0.002
RUTZH-05/ 11C	21jjd07-10.xl	4	Mayote	0.011	0.004	0.005	0.002	0.08	0.02	bdl	bdl	0.19	0.01	bdl	bdl	0.002	0.001
RUTZH-05/ 12C	17mce20-23.xl	4	Mayote	0.099	0.011	bdl	bdl	0.07	0.02	bdl	bdl	0.03	0.01	0.005	0.003	0.010	0.003
RUTZH-05/ 13C	17mce11-14.xl	4	Mayote	0.008	0.003	0.005	0.002	0.07	0.02	0.010	0.003	0.02	0.01	bdl	bdl	bdl	bdl
RUTZH-06/ 03C	17mce03-06.xl	4	Mayote	0.007	0.003	0.010	0.003	0.07	0.02	0.007	0.003	0.02	0.01	bdl	bdl	bdl	bdl
M4/ 3C	16jjb15-18.xl	4	Lukande	0.005	0.002	0.003	0.001	0.10	0.02	0.003	0.001	0.33	0.02	bdl	bdl	0.006	0.002
M4/ 5C	16jja15-18.xl	4	Lukande	bdl	bdl	bdl	bdl	0.10	0.03	0.319	0.008	0.97	0.03	bdl	bdl	0.009	0.002
RUTZH-10/ 2C	21jje03-06.xl	4	Lukande	0.013	0.004	0.012	0.003	0.12	0.02	0.005	0.002	0.46	0.02	bdl	bdl	bdl	bdl
RUTZH-10/ 4C	17mcd14-17.xl	4	Lukande	0.167	0.011	0.017	0.004	0.10	0.02	0.008	0.003	0.03	0.01	0.005	0.002	0.009	0.003
RUTZH-11/ 1C	16jjd11-14.xl	4	Lukande	0.015	0.004	0.021	0.003	0.09	0.02	0.002	0.001	0.13	0.01	0.003	0.001	0.011	0.002
RUTZH-11/ 3C	16jjd03-06.xl	4	Lukande	0.012	0.005	0.011	0.003	0.09	0.03	bdl	0.002	0.22	0.02	bdl	bdl	0.005	0.002
RUTZH-11/ 2C	16jjd07-10.xl	4	Lukande	0.013	0.003	0.011	0.002	0.13	0.02	0.005	bdl	0.26	0.01	bdl	bdl	0.007	0.002
RUTZH-11/ 14C	17mcd18-22.xl	5	Lukande	0.017	0.005	0.018	0.004	0.08	0.02	0.008	0.003	0.03	0.01	bdl	bdl	0.010	0.003
RUTZH-18/ 5B_1	23jjc03.xl	1	Kitwaro	bdl	bdl	0.008	0.003	0.09	0.03	bdl	bdl	0.13	0.02	bdl	bdl	0.005	0.002
RUTZH-18/ 5B_2	23jjc04.xl	1	Kitwaro	0.022	0.006	bdl	bdl	bdl	bdl	0.014	0.003	0.18	0.02	0.057	0.006	0.023	0.004
RUTZH-18/ 5B_3	23jjc05.xl	1	Kitwaro	bdl	bdl	0.012	0.004	bdl	bdl	0.010	0.004	0.07	0.02	bdl	bdl	bdl	bdl
RUTZH-18/ 5B_4	23jjc07.xl	1	Kitwaro	bdl	bdl	0.008	0.004	0.12	0.04	bdl	bdl	0.34	0.03	bdl	bdl	bdl	bdl
RUTZH-18/ 5B_5	23jjc08.xl	1	Kitwaro	0.011	0.005	0.011	0.003	bdl	bdl	0.030	0.004	0.18	0.02	bdl	bdl	0.005	0.002
RUTZH-18/ 5B_6	23jjc09.xl	1	Kitwaro	bdl	bdl	bdl	bdl	bdl	bdl	bdl	bdl	0.22	0.02	bdl	bdl	bdl	bdl
RUTZH-18/ 5B_7	23jjc10.xl	1	Kitwaro	0.010	0.005	0.013	0.005	0.12	0.04	bdl	bdl	0.15	0.02	bdl	bdl	bdl	bdl
RUTZH-18/ 5B_8	23jjc11.xl	1	Kitwaro	0.015	0.007	bdl	bdl	0.18	0.04	0.049	0.007	0.20	0.02	0.019	0.005	0.032	0.006
RUTZH-18/ 7B_1	24jja03-04.xl	2	Kitwaro	0.014	0.005	bdl	bdl	0.11	0.04	bdl	bdl	0.11	0.02	0.039	0.006	0.010	0.003
RUTZH-18/ 7B_2	24jja05.xl	1	Kitwaro	bdl	bdl	0.014	0.006	0.17	0.06	bdl	bdl	0.11	0.02	bdl	bdl	bdl	bdl
RUTZH-18/ 7B_3	24jja06.xl	1	Kitwaro	bdl	bdl	0.027	0.008	0.20	0.06	bdl	bdl	0.09	0.02	bdl	bdl	bdl	bdl
RUTZH-18/ 7B_4	24jja07.xl	1	Kitwaro	0.013	0.005	0.010	0.003	0.15	0.03	0.015	0.003	0.21	0.02	0.011	0.003	bdl	bdl
RUTZH-18/ 7B_5	24jja08-09.xl	2	Kitwaro	bdl	bdl	0.012	0.003	0.09	0.03	bdl	bdl		0.01		0.002	bdl	bdl
RUTZH-18/ 7B_6	24jja10.xl	1	Kitwaro	bdl	bdl	0.017	0.004	bdl	bdl	0.003	0.002	0.13	0.02	bdl	bdl	bdl	bdl
RUTZH-18/ 7B_8	24jja12.xl	1	Kitwaro	bdl	bdl	bdl	bdl	bdl	bdl	bdl	bdl	bdl	bdl	bdl	bdl	bdl	bdl
RUTZH-18/ 7B_9	24jja13.xl	1	Kitwaro	0.017	0.007	bdl	bdl	bdl	bdl	bdl	bdl	0.11	0.02	bdl	bdl	0.008	0.003
RUTZH-18/ 7B_10	24jja14.xl	1	Kitwaro	0.046	0.011	0.010	0.004	bdl	bdl	bdl	bdl	0.04	0.01	0.013	0.004	0.064	0.007
RUTZH-23/ C	17mcc17-20.xl	4	Kitwaro	0.019	0.006	0.026	0.005	0.08	0.02	0.005	0.002	0.04	0.01	bdl	bdl	bdl	bdl
RUTZH-25/ C	17mcd11-13.xl	3	Kitwaro	0.023	0.006	0.015	0.004	0.07	0.02	bdl	bdl	0.04	0.01	bdl	bdl	0.006	0.003
RUTZH-27/ 2C	17mcc07-11.xl	4	Kitwaro	0.011	0.004	0.015	0.004	0.09	0.03	0.011	0.003	0.03	0.01	bdl	bdl	0.008	0.002
M1/ 3C	15jjd07-10.xl	4	Ipangko	0.025	0.004	0.011	0.002	0.08	0.02	0.009	0.002	0.43	0.02	bdl	bdl	bdl	bdl
M1/ 4C	16jja03-06.xl	4	Ipangko	0.010	0.002	0.012	0.002	0.08	0.02	0.005	0.001	0.79	0.02	0.002	0.001	0.005	0.001
M1/ 5C	16jjb11-14.xl	4	Ipangko	0.010	0.003	0.010	0.003	0.10	0.02	bdl	bdl	0.25	0.02	0.002	0.001	0.009	0.003
RUTZH-19/ 2B_1	23jjb03.xl	1	Ipangko	0.010	0.004	bdl	bdl	bdl	bdl	bdl	bdl	0.27	0.02	bdl	bdl	bdl	bdl
RUTZH-19/ 2B_2	23jjb04.xl	1	Ipangko	bdl	bdl	bdl	bdl	0.09	0.03	bdl	bdl	0.13	0.02	bdl	bdl	bdl	bdl
RUTZH-19/ 2B_3	23jjb05.xl	1	Ipangko	bdl	bdl	bdl	bdl	bdl	bdl	bdl	bdl	0.27	0.02	bdl	bdl	bdl	bdl
RUTZH-19/ 2B_4	23jjb06.xl	1	Ipangko	bdl	bdl	0.004	0.002	bdl	bdl	bdl	bdl	0.23	0.02	bdl	bdl	bdl	bdl
RUTZH-19/ 2B_5	23jjb07.xl	1	Ipangko	0.020	0.006	0.006	0.002	0.09	0.03	bdl	bdl	0.46	0.03	bdl	bdl	bdl	bdl
RUTZH-19/ 2B_6	23jjb09-10.xl	2	Ipangko	0.013	0.004	0.011	0.004	0.12	0.03	bdl	bdl	0.11	0.01	0.003	0.001	0.005	0.002
RUTZH-19/ 2B_7	23jjb11.xl	1	Ipangko	0.029	0.008	0.051	0.007	0.17	0.03	bdl	bdl	0.43	0.03	bdl	bdl	bdl	bdl
RUTZH-19/ 2B_8	23jjb12-13.xl	2	Ipangko	0.057	0.010	0.032	0.006	0.13	0.04	0.004	0.002	0.24	0.02	0.009	0.003	0.024	0.004
RUTZH-19/ 2B_9	23jjb14.xl	1	Ipangko	bdl	bdl	bdl	bdl	bdl	bdl	bdl	bdl	0.14	0.02	bdl	bdl	0.008	0.003
RUTZH-19/ 2B_10	23jjb15.xl	1	Ipangko	bdl	bdl	0.025	0.005	0.09	0.03	0.014	0.004	0.36	0.03	0.018	0.004	0.019	0.004
RUTZH-19/ 2B_11	23jjb16.xl	1	Ipangko	bdl	bdl	0.008	0.003	bdl	bdl	bdl	bdl	0.14	0.01	bdl	bdl	bdl	bdl
RUTZH-20/ 1B_1	15mcb03-06.xl	4	Ipangko	bdl	bdl	0.015	0.007	bdl	bdl	0.017	0.007	bdl	bdl	bdl	bdl	bdl	bdl
RUTZH-20/ 1B_2	15mcb07-12.xl	6	Ipangko	0.025	0.011	0.019	0.007	0.22	0.06	bdl	bdl	bdl	bdl	0.009	0.004	0.011	0.005
RUTZH-20/ 1B_3	15mcb13-17.xl	5	Ipangko	0.067	0.012	0.032	0.007	0.27	0.05	0.017	0.005	bdl	bdl	0.015	0.004	0.068	0.008
RUTZH-22/ 2C	21jjc07-10.xl	4	Ipangko	0.013	0.003	0.016	0.003	0.13	0.02	0.003	0.001	0.21	0.01	bdl	bdl	bdl	bdl
RUTZH-22/ 3C	21jjd03-06.xl	4	Ipangko	0.008	0.003	0.009	0.003	0.12	0.03	0.008	0.002	0.23	0.02	0.013	0.003	0.007	0.002
RUTZH-22/ 4C	16jjc11-12,14,f11-1	5	Ipangko	0.010	0.005	0.011	0.003	0.12	0.02	0.007	0.005	0.18	0.02	0.003	0.003	0.004	0.003
RUTZH-22/ 6C	17mcd03-06.xl	4	Ipangko	0.014	0.005	0.015	0.005	0.10	0.03	bdl	bdl	0.03	0.01	bdl	bdl	0.006	0.003

Sample	File	N	Mine	Zr90	1Stdev	Nb93	1Stdev	Sn118	1Stdev	Ce140	1Stdev	Pb208	1Stdev	Th232	1Stdev	U238	1Stdev
Mangari, KEN				µg/g	µg/g	µg/g	µg/g	µg/g	µg/g	µg/g	µg/g	µg/g	µg/g	µg/g	µg/g	µg/g	µg/g
RUKEM-22/ 1C	15jjb11-14.xl	4	John Saul	0.013	0.004	0.009	0.003	0.10	0.02	bdl	bdl	0.53	0.02	bdl	bdl	bdl	bdl
RUKEM-22/ 2C	15jjb15-18.xl	4	John Saul	0.010	0.004	0.061	0.005	0.08	0.02	bdl	bdl	8.93	0.06	bdl	bdl	bdl	bdl
RUKEM-22/ 3C	21jje07-10.xl	4	John Saul	0.037	0.006	0.053	0.006	0.13	0.02	0.404	0.010	0.33	0.02	0.611	0.012	0.049	0.004

Sample	File	N	Mine	Zr90	1Stdev	Nb93	1Stdev	Sn118	1Stdev	Ce140	1Stdev	Pb208	1Stdev	Th232	1Stdev	U238	1Stdev
Shan State, MYA				µg/g	µg/g	µg/g	µg/g	µg/g	µg/g	µg/g	µg/g	µg/g	µg/g	µg/g	µg/g	µg/g	µg/g
BUMGIT01/ C	24Ora03-06.xl	4	Namyaseik	0.192	0.015	0.066	0.008	1.01	0.09	0.006	0.003	0.20	0.02	bdl	bdl	0.033	0.005
BUMGIT02 /C	24Ora07-10.xl	4	Namyaseik	0.022	0.006	0.017	0.005	0.77	0.09	bdl	bdl	0.09	0.01	bdl	bdl	bdl	bdl
BUMGIT03/ C	24Ora11-14.xl	4	Namyaseik	0.021	0.006	0.024	0.005	0.70	0.08	bdl	bdl	0.06	0.01	bdl	bdl	bdl	bdl
BUMGIT04/ C	24Ora15-18.xl	4	Mogok	0.024	0.007	0.024	0.005	0.79	0.08	bdl	bdl	0.15	0.02	bdl	bdl	0.009	0.003
BUMGIT05/ C	24Orb03-06.xl	4	Mogok	0.023	0.008	0.021	0.005	0.62	0.08	bdl	bdl	0.06	0.01	bdl	bdl	bdl	bdl
BUMGIT06/ C	24Orb07-10.xl	4	Mogok	0.020	0.006	0.015	0.004	0.62	0.07	bdl	bdl	0.07	0.01	bdl	bdl	bdl	bdl
BUMGIT07/ C	24Orb11-14.xl	4	Mogok	0.018	0.006	0.018	0.006	0.67	0.08	bdl	bdl	0.08	0.01	bdl	bdl	bdl	bdl
RUBU001/ D	17mcb07-10.xl	4	Mogok	0.012	0.004	0.018	0.004	0.06	0.02	0.005	0.002	0.06	0.01	bdl	bdl	0.007	0.002
RUBU003/ D	17mca07-10.xl	4	Mogok	0.022	0.005	0.011	0.003	0.09	0.02	0.004	0.002	0.08	0.01	0.002	0.001	0.003	0.001
RUBU004/ D	17mcb11-14.xl	4	Mogok	bdl	bdl	0.008	0.003	0.09	0.02	0.005	0.002	0.07	0.01	bdl	bdl	0.003	0.001
RNBU048/ D	17mcb03-06.xl	4	Mogok	0.010	0.004	0.014	0.003	0.07	0.02	bdl	bdl	0.08	0.01	bdl	bdl	bdl	bdl
RUBUM02/ C	17mce07-10.xl	4	Mogok	bdl	bdl	bdl	bdl	0.09	0.02	0.006	0.003	0.06	0.01	bdl	bdl	0.011	0.004

Sample	File	N	Mine	Zr90	1Stdev	Nb93	1Stdev	Sn118	1Stdev	Ce140	1Stdev	Pb208	1Stdev	Th232	1Stdev	U238	1Stdev
Yunnan, CHN				µg/g	µg/g	µg/g	µg/g	µg/g	µg/g	µg/g	µg/g	µg/g	µg/g	µg/g	µg/g	µg/g	µg/g
RNYN19/ C	24Org07-10.xl	4	Yuan Jiang	0.041	0.006	0.048	0.005	0.19	0.03	0.004	0.002	0.11	0.01	0.003	0.001	0.012	0.002
RNYN23/ C	24Orf07-10.xl	4	Yuan Jiang	0.054	0.007	0.143	0.008	0.17	0.02	0.003	0.002	0.19	0.01	0.011	0.002	0.007	0.002
RNYN30/ C	24Org03-06.xl	4	Yuan Jiang	0.032	0.005	0.037	0.004	0.14	0.02	bdl	bdl	0.15	0.01	bdl	bdl	0.004	0.002
RNYN31/ C	24Orf03-06.xl	4	Yuan Jiang	0.014	0.004	0.019	0.003	0.15	0.02	0.004	0.001	0.25	0.01	bdl	bdl	0.006	0.002
RNYN50/ C	24Ore11-14.xl	4	Yuan Jiang	0.015	0.005	0.026	0.004	0.22	0.03	bdl	bdl	0.11	0.01	bdl	bdl	0.004	0.002
RNYN51/ C	24Ore07-10.xl	4	Yuan Jiang	0.034	0.006	0.051	0.005	0.18	0.03	0.005	0.002	0.41	0.02	bdl	bdl	0.009	0.002
RNYNXX/ C	24Org11-14.xl	4	Yuan Jiang	0.049	0.007	0.076	0.007	0.19	0.02	0.007	0.002	0.06	0.01	bdl	bdl	0.003	0.001
RNYNZZ/ C	24Orf11-14.xl	4	Yuan Jiang	0.036	0.006	0.044	0.005	0.17	0.03	0.006	0.002	0.21	0.01	bdl	bdl	0.007	0.002

Sample	File	N	Mine	Zr90	1Stdev	Nb93	1Stdev	Sn118	1Stdev	Ce140	1Stdev	Pb208	1Stdev	Th232	1Stdev	U238	1Stdev
Luc Yen, VIE				µg/g	µg/g	µg/g	µg/g	µg/g	µg/g	µg/g	µg/g	µg/g	µg/g	µg/g	µg/g	µg/g	µg/g
RNVNL038/ C	24Orc07-10.xl	4	An Phu	0.035	0.005	0.051	0.005	0.35	0.03	bdl	bdl	0.22	0.01	bdl	bdl	bdl	bdl
RNVNL039/ C	24Ord11-14.xl	4	An Phu	0.038	0.006	0.048	0.005	0.27	0.03	bdl	bdl	0.11	0.01	bdl	bdl	bdl	bdl
RNVNL042/ C	24Orc11-14.xl	4	An Phu	0.033	0.005	0.048	0.005	0.20	0.03	bdl	bdl	0.08	0.01	bdl	bdl	bdl	bdl
RNVNL043/ C	24Ord07,10.xl	2	An Phu	0.026	0.005	0.052	0.005	0.36	0.03	0.002	0.001	0.22	0.01	bdl	bdl	0.006	0.002
RNVNL046/ D	24Orc03-06.xl	4	An Phu	0.027	0.005	0.033	0.004	0.60	0.04	bdl	bdl	0.21	0.01	bdl	bdl	0.008	0.002
RNVNL133/ D	24Ore03-06.xl	4	An Phu	0.058	0.006	0.108	0.007	15.48	0.09	0.007	0.002	2.18	0.03	0.032	0.004	0.005	0.001
RNVNLY01/ C	24Ord15-18.xl	4	An Phu	0.037	0.007	0.035	0.005	0.79	0.05	bdl	bdl	0.11	0.01	bdl	bdl	bdl	bdl

Sample	File	N	Mine	Zr90	1Stdev	Nb93	1Stdev	Sn118	1Stdev	Ce140	1Stdev	Pb208	1Stdev	Th232	1Stdev	U238	1Stdev
Murgab, TJK				µg/g	µg/g	µg/g	µg/g	µg/g	µg/g	µg/g	µg/g	µg/g	µg/g	µg/g	µg/g	µg/g	µg/g
RUTJ001/ C	17mcc03-06.xl	4	Snijnie	0.007	0.003	0.009	0.003	0.14	0.02	bdl	bdl	0.02	0.01	bdl	bdl	bdl	bdl
RUTJ002/ D	17mca11-14.xl	4	Snijnie	0.006	0.003	0.009	0.003	0.09	0.02	bdl	bdl	0.07	0.01	bdl	bdl	bdl	bdl
RUTJ003/ D	17mcd07-10.xl	4	Snijnie	0.021	0.005	0.022	0.005	0.28	0.03	0.008	0.004	0.03	0.01	0.010	0.003	0.004	0.002
RUTJ004/ D	17mca03-06.xl	4	Snijnie	bdl	bdl	0.012	0.003	0.13	0.03	bdl	bdl	0.11	0.01	0.021	0.003	0.004	0.001
RUTJ005/ D	17mca15-18.xl	4	Snijnie	0.009	0.004	0.006	0.002	0.18	0.02	bdl	bdl	0.06	0.01	bdl	bdl	bdl	bdl

Tab. 6.3: The presented data compilation is a selection of LA-ICP-MS data which was acquired during this study. The measurements were taken under the conditions and parameters indicated in chapter 1. The values represent averaged composition values by sample. The number of shots which were analysed for a particular sample are indicated in the column N. Beside the averaged composition values the external reproducibility of the sample measurements are reported as the one standard deviation values (1 stdev). Due to rare detection and thus low reproducibility the elements K, Mn, Co, Ni Cu, Rb, Sr, Y, Mo, Ba, La, Pr, Nd, Sm, Eu, Gd, Tb, Dy, Ho, Er, Tm, Yb, Lu, Ta, and W were excluded from the summary table, but data are reported in the Appendix B.5.

6.7.1 Data Processing

For the initial data processing which included the conversion of data files recorded by the ICP-MS unit into element concentrations, a MATLAB software package called SILLS (Guillong et al., 2008) was applied. This freeware program allowed an easy to use data compilation, manual setting of integration limits for background and signal as well as automated spike removal (outlier identification based on Grubb's test). The graphic display of spectra as well as the easy to use procedures are the most striking advantages compared to previous software such as LAMTRACE for example.

As mentioned above the Al_2O_3 content of rubies is at least 99 wt% and this value was used for internal standardization during data reduction.

For further data processing and to generate various plots an 'R'-based software package was used. The open source software called Geochemical Data Toolkit (GCDKit)

Version 2.3 (2008) written by V.Janousek, C.M. Farrow, and V. Erban was specifically designed for statistical calculations of geological datasets. The program allows the creation of scatter plot matrices, principal component analysis as well as to plot binary and ternary diagrams of large datasets.

6.7.2 Reduction of Element Menu

From the extensive data set acquired in this study, the minimal set of elements necessary to sufficiently describe the trace-element composition of rubies from marble-hosted deposits was determined, in order to facilitate data interpretation. Moreover, only elements which can be measured with a high reproducibility in samples from marble-hosted deposits qualify to be used in such a minimal set of elements employed for source fingerprinting.

Following these pre-conditions it was decided to select all the elements which showed a reproducibility of 90% in at least one of the investigated deposits based on data collected by multiple single shot measurements. 18 out of the 50 tested elements conform to this criterion (Tab. 6.4). Although all of the excluded elements were significantly detected in several cases, they still did not attain this defined level of external reproducibility. Among these elements were Be, K, Ca, Mn, Co, Ni, Cu, Sr, Mo, Ba, Hf, Ta, W, Th, U, and all the tested REEs. Here, the elements Be, Ca, Cu, and REEs would like to be discussed in further detail.

As mentioned earlier Be diffusion-treated corundum reached the international gem market in 2002. It was soon argued that also natural, unheated corundum had elevated Be contents. The content of Be in untreated rubies was therefore a major topic in recent years in gemmology. As a result of this study, it can be stated that the Be content of all tested marble-hosted ruby samples were below 0.4 ppm, mostly much lower (i.e., below LOD).

Surprisingly, Ca did not qualify either. Surprisingly because the investigated rubies derived mainly from marble-hosted deposits where Ca is abundant. Although in 85 of the 457 measurements small amounts of Ca were significantly detected, the number did not reach the required level of reproducibility in none of the deposits either. Apparently, Ca is therefore contained in (sub-)microscopic carbonate inclusions but not in the lattice of the surrounding corundum itself.

Also Cu did not reach the level of reproducibility although the LOD was low, of the order of 0.05 ppm only. This also demonstrates that the polyatomic interference production of $(^{38}Ar^{27}Al)^{+}$ on ^{65}Cu was not significant at the analytical conditions employed.

The disqualification of all the REEs on the other hand was a bit less surprising. This is because REE inclusions such as xenotime or monazite are typically found in sapphires from basalt hosted deposits. Nevertheless, it was one of the targets of this trace-element analysis to investigate the existence of such inclusions in marble-hosted rubies.

Only Ce with 135 significantly detected readings is to be mentioned. The amounts however were extremely low, usually near the LOD, and in the range of 0.01 ppm or lower. As a result, REEs reached in none of the deposits a reproducibility of 90%.

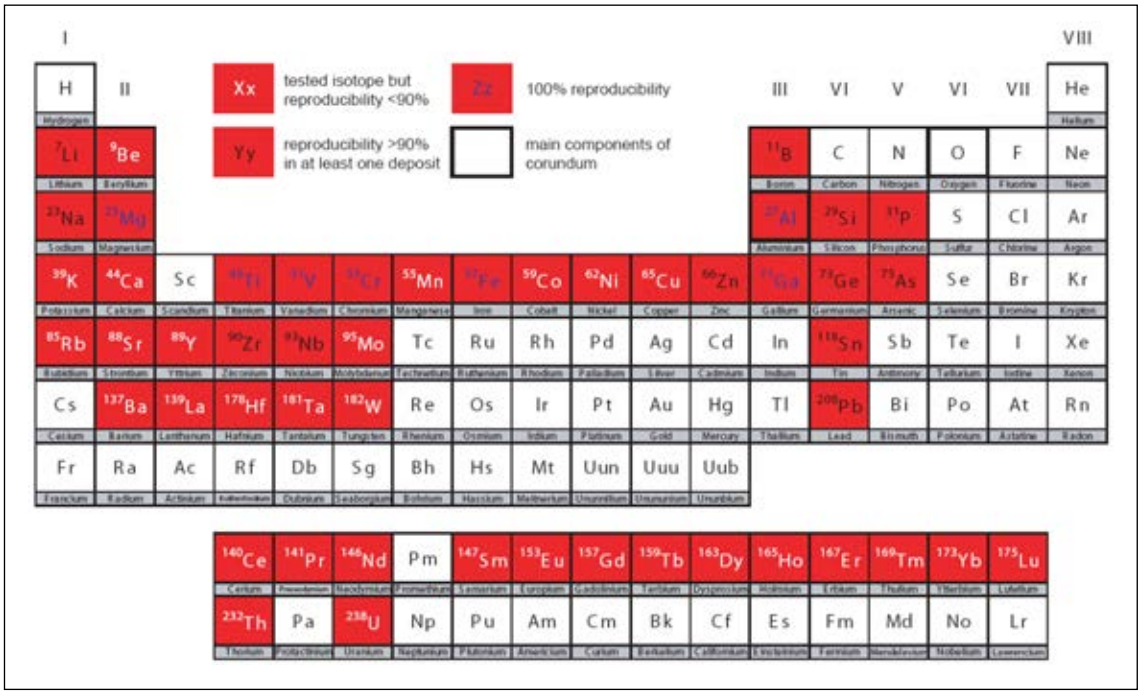

Tab. 6.4: Overview of elements which were tested during this study. Reproducibilities are indicated by a colour code. To duplicate the requirements for analysis made by gemmological laboratories this evaluation was made on the basis of single shot measurements.

From the remaining 18 elements further reductions were made. Although Na, P, Si, and Pb were detected and found to fulfil the requirements mentioned above, they were still decided to be excluded from further data processing. This decision was taken based on two reasons.

First, Na and Pb are related to contaminations as described in chapter 6.6.1 It was observed that in several cases tiny cracks not seen on the surface were then reached during the ablation process. Along with these cracks minute fluid inclusions and dirt were ablated. Elevated Na contents were found as a consequence. Therefore, Na was excluded from further data analysis. A similar case was encountered for Pb which was therefore also excluded.

For Si and P however polyatomic interferences were responsible to get removed from the list of elements to be investigated in further detail. ^{29}Si has a potential interference with $^{27}AlH_2$ where as ^{31}P has known interferences with $^{15}N^{16}O$, $^{14}N^{17}O$, and $^{14}N^{16}OH$ that may not be properly accounted for by simple background subtraction. Moreover, notably for Si, the significant values were always close to the LODs for a given analysis. To avoid misinterpretation of data these two elements were also eliminated.

14 elements were thus finally selected for further analysis. The outcome of these investigations is presented in the following paragraph.

6.7.3 Trace-Element Characterisation of Marble-Hosted Rubies – The Definition of Distinctive Plots for Origin Determination Purposes

As a first attempt a locality specific table of reproducibility was generated for all 14 elements which were selected for further data analysis (Tab. 6.5). This table was based on the reproducibility compilation which is attached in Appendix B.5. As it is shown in Tab. 6.5 a rough indication of a sample origin can be assumed by the detection of a certain element or element combination. A major separation of deposits was made on the basis of whether Li and B were reproducibly detected. These light elements, especially B, are often linked to pegmatites and may therefore reveal important information about geological provenance. Subdivisions were then made based on the detection and reproducibility of elements which were even more locality-specific. Ge for example was registered to be found reproducibly in Snijnie Mine, Murgab, Tajikistan and John Saul Mine, Mangari, Kenya only.

Type	Mogok	Visakazi	Snijnie	Lukande	Luc Yen	Namyaseik	John Saul
Mines	Mogok Mwarazi Mayote	Visakazi II Msonge Kitwaro Ipangko	Snijnie	Lukande	Luc Yen Yuan Jiang	Namyaseik	John Saul
Elementes							
Li					x	x	x
B					x	x	x
Mg	x	x	x	x	x	x	x
Ti	x	x	x	x	x	x	x
V	x	x	x	x	x	x	x
Cr	x	x	x	x	x	x	x
Fe	x	x	x	x	x	x	x
Zn	x	-	x	-	x	x	x
Ga	x	x	x	x	x	x	x
Ge			x				x
As				x		x	x
Zr					x	x	-
Nb				-	x	x	x
Sn	-	-	x	x	x	x	-

Tab. 6.5: A first classification based on the reproducibility and detection of 14 elements which were selected for further data analysis. Seven deposit types based on their element fingerprint were distinguished. Each deposit type includes the deposit it was named after as well as others if indicated in the header accordingly. The combined detection and, or absence of, highlighted elements discriminates rubies from the investigated marble-hosted ruby deposits as a function of their locality.

The following considerations will be based on data averaged by sample, to minimize the effect of possible outliers. Error bars will not be plotted in the following diagrams, because these are commonly hidden behind the symbol size used in the plots (see chapter 6.1). For further information, the entire data set including standard deviation values and LOD for each shot is attached in the Appendix B.5.

As a first attempt the data set was subject to discrimination diagrams traditionally employed in corundum origin determination. It can be observed that these diagrams possess a strong potential for deposit identification. As shown in Fig 6.7 a major

overlap does not allow the differentiation between deposits of the same kind, however. Also the ternary plots suggested by Guillong et al. (2001) do not allow a conclusive distinction based on trace-element analysis (Fig. 6.8). This may be mainly because the distinctive plots suggested by Guillong et al. (2001) were designed for origin determination on sapphires and not for rubies.

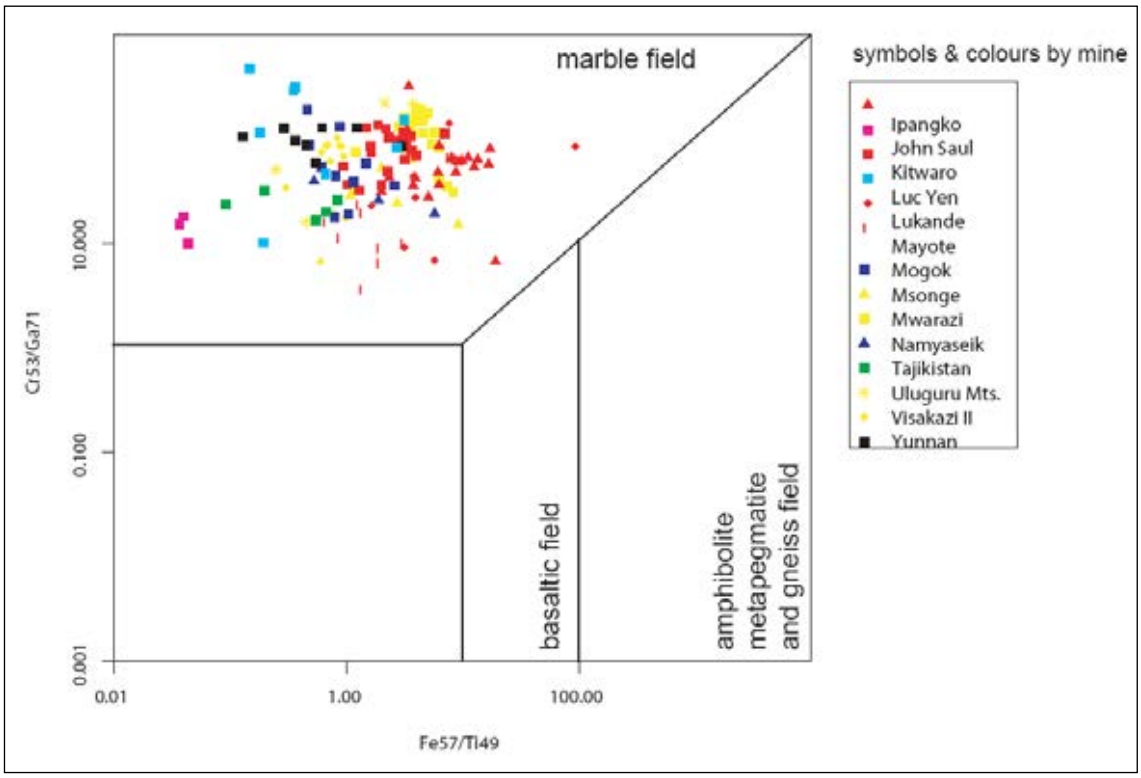

Fig. 6.7: The displayed diagram of the element ratios Fe/Ti versus Cr/Ga was first introduced by Sutherland et al. (1998 & 2003). The plot allows a basic corundum deposit classification according to their geological provenance. While the data obtained in this study all plot into the marble field as they should, the diagram does not allow the separation between different marble-hosted deposits.

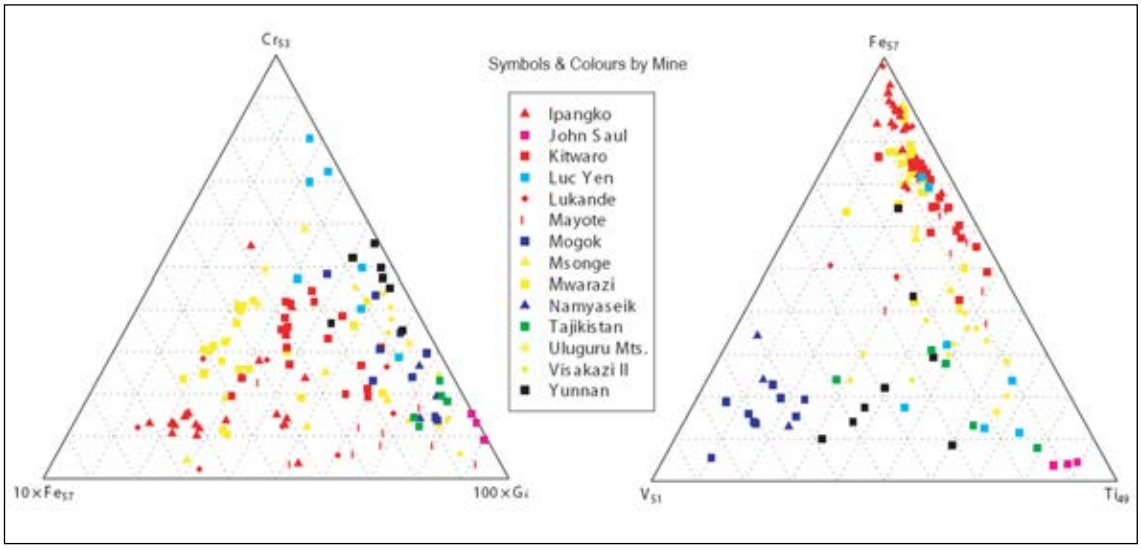

Fig. 6.8: The plots suggested by Guillong et al. (2001) showed major overlaps for the ruby deposits investigated during this study. Nevertheless, the plot V-Fe-Ti may possess a certain potential to differentiate rubies from Mogok against other marble-hosted rubies. Especially for rubies from Vietnam, Tajikistan, Yunnan, and the Morogoro Region, Tanzania however the overlap is still significant and clear differentiation is thus not possible.

The next approach was to create a scatter plot matrix where all possible binary element combinations were displayed in one diagram (Fig. 6.9). This diagram allowed instant comparison of various element combinations next to each other.

As an immediate result it was possible to recognise the correlation between B and Li (R=0.69). Due to the fact that Li was detected more often within the tested populations it was decided therefore to focus on Li for further investigations. The elements Zn, As, and Zr do not provide enough potential in order to distinguish rubies from different deposits. Aside from outliers, there were often not enough data points available to create significant diagrams including Zn, As, or Zr. Due to the outliers the standard deviation of these elements often exceeded the calculated average, thus adding a high degree of uncertainty on the average data for these elements (see Appendix B.5). Therefore, these three elements were no longer evaluated.

Ge on the other hand is a very distinctive element since it was measured reproducibly in rubies from Tajikistan and John Saul Mine in Kenya only. This element is if present an excellent source indicator for either the Luc Yen / Yuan Jiang or the John Saul Mine.

After this final evaluation, a set of 10 elements remained. These were considered finally to be the minimal number of elements to be tested in order to distinctively describe the examined system including the 6 investigated ruby deposits. The 10 elements are: Li, Mg, Ti, V, Cr, Fe, Ga, Ge, Nb, and Sn.

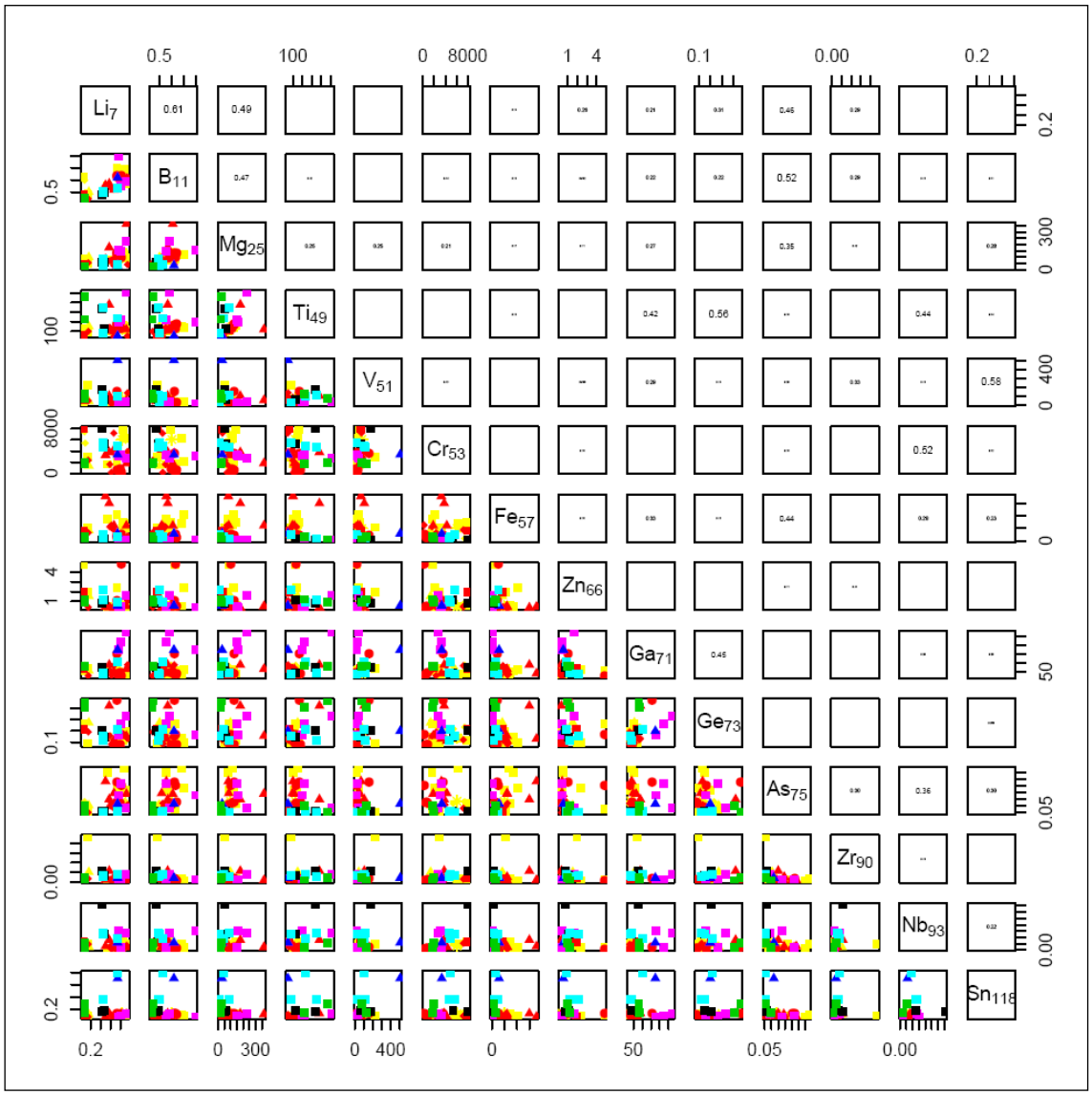

Fig. 6.9: The displayed scatter plot matrix shows all possible 91 combinations between the remaining 14 elements which were selected for further investigations. Each simplified plot represents one of these combinations. In order to read the matrix one follows the column in which a particular diagram is located. At the end of this column the corresponding element of the abscissa is indicated. The element which is displayed on the ordinate is mentioned at the end of the corresponding row of a particular diagram. Further, on the upper half from the bisecting diagonal the correlation factor is indicated in the appropriate field. It also has to be pointed out that outliers are displayed more prominently than they occur in the actual binary plots.

The challenge however still remains whether there are enough diagnostic combinations among the finalised group of elements which allow a distinctive description by trace-element composition of the examined ruby deposits. 15 relationships were necessary to be covered for a complete definition of the investigated system including 6 ruby deposits (Fig. 6.10).

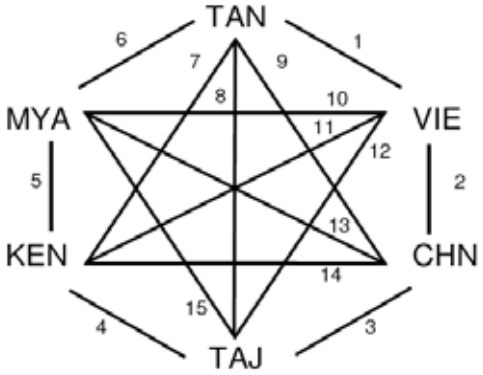

Fig. 6.10: A simple diagram demonstrates the 15 relationships which exist among the 6 ruby deposits examined in this study. Origin determination by trace-element analysis is possible only if for each of the 15 relationships a distinctive element combination can be found.

After various permutations and examination of their binary plots, 15 criteria, 14 element ratios and the plot after Sutherland et al. (1998 & 2003), turned out to fulfil the task of describing the system completely. The element ratios are the following: Li/Sn, V/Fe, Nb/Sn, Mg/Ge, Cr/Mg, Ga/V, Mg/V, Mg/Ti, Mg/Fe, Ti/Ga, Fe/Ti, Fe/Sn, Ga/Sn, and Fe/Sn. The most distinctive binary plot in terms of origin determination turns out to be the element combination Li versus Sn. In this plot (Fig. 6.11) 10 out of the 15 relationships displayed in Fig. 6.11 are covered in just one diagram. Note that rubies from Myanmar (Burma) plot in two separate clusters in this element abundance diagram.

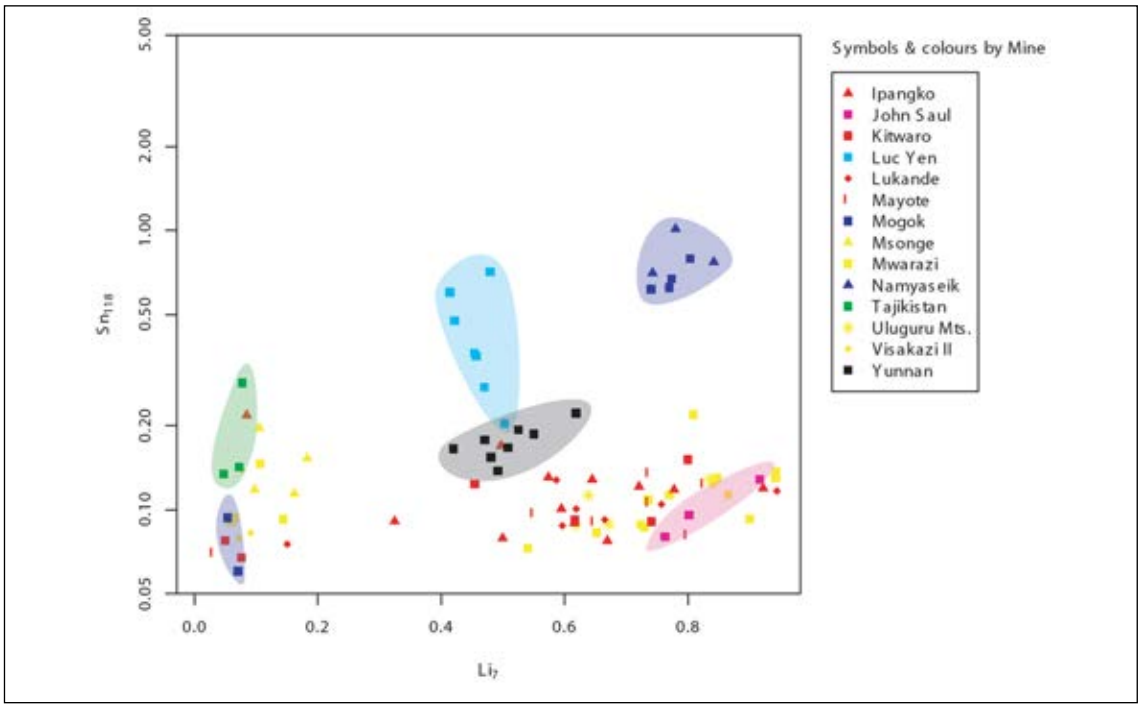

Fig. 6.11: The most distinctive binary element combination was Li-Sn where not less than 10 out of the 15 relationships of the examined system were distinguishable. Clusters are coloured after the following colour code: Morogoro Region/ TAN (yellow : Uluguru Mts, red: Mahenge Mts), John Saul Mine/ KEN (pink), Murgab /TJK (green), Mogok & Namyaseik / MYA (dark blue), Yunnan /CHN (black) and Luc Yen / VIE (light blue).

To condensate the set of element combinations even further, ternary plots of element abundance ratios were calculated next. This final step in data analysis carried out in this research revealed 4 ternary plots to be sufficient to describe the system distinctively (Fig 6.12). With these four plots all 15 relationships were covered. Due to minor overlaps the distinction between rubies from Vietnam and Yunnan, Vietnam and the Morogoro Region, as well as rubies the Morogoro Region and Yunnan turned out to be least reliable, however.

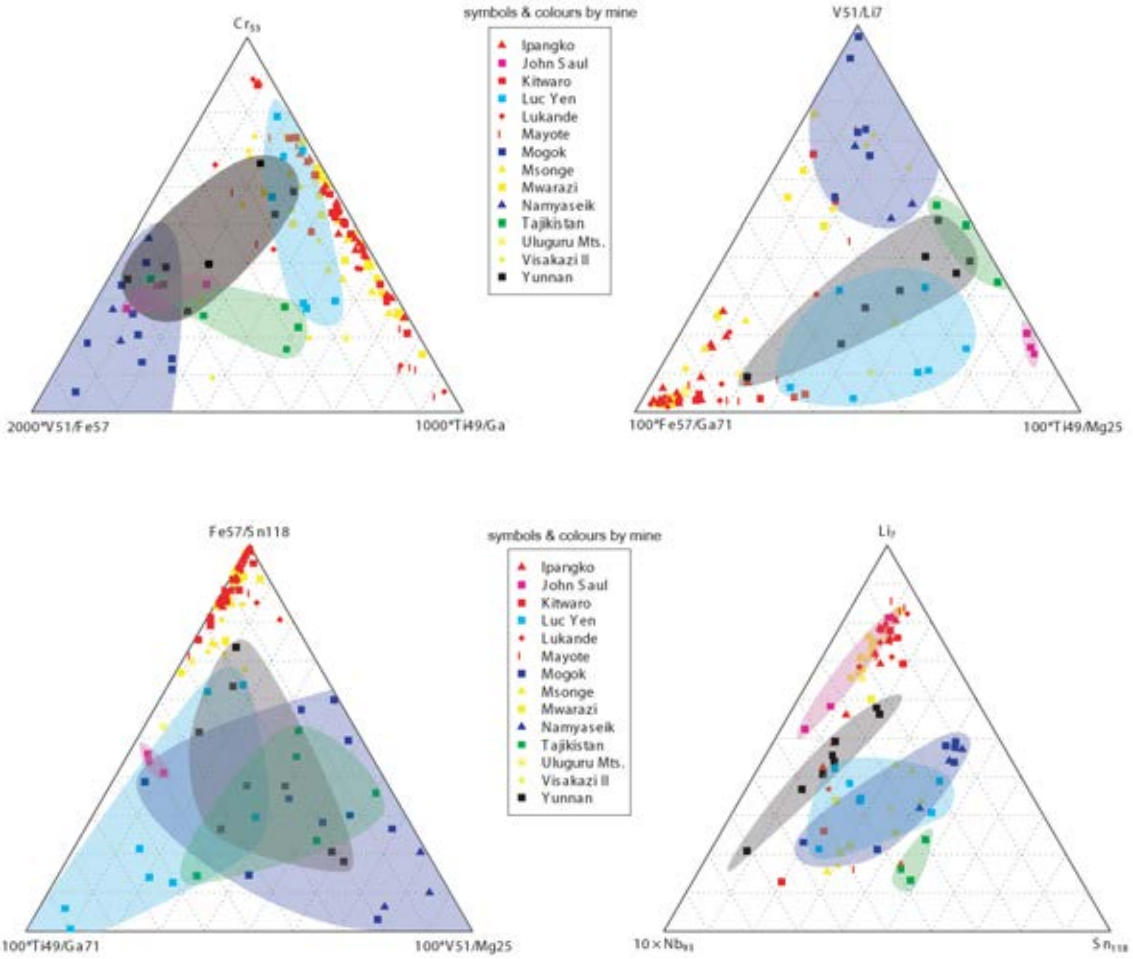

Fig. 6.12: The four displayed ternary plots allow a full description by trace-element analysis of the following ruby origins: Morogoro Region/ TAN (yellow : Uluguru Mts, red: Mahenge Mts), John Saul Mine/ KEN (pink), Murgab /TJK (green), Mogok & Namyaseik / MYA (dark blue), Yunnan /CHN (black) and Luc Yen / VIE (light blue). The areas of 5 out of the 6 populations were put in colour in order to improve the clarity of the diagrams.

6.7.4 Principal Component Analysis

In the framework of this study it was also tried to explore the potential of further statistical data analysis. As previously suggested by Guillong et al. (2001) Principal Component Analysis (PSA) was applied to the data set generated during this study. PCA was available as a built in function from the open source software package GDCKit.

PCA is one of many multivariate data analysis techniques where data is statistically tested in a multi-dimensional data space. Multivariate data analysis is applied usually when a data set with more than 3 variables has to be statistically examined. As an output of PCA a 2-dimensional diagram is generated where the examined data set is displayed as a projection in the direction of the two variables with the highest variance. PCA is therefore very sensitive to outliers and variables with a high reproducibility should be incorporated only. This is because a data point is plotted only if there exists a value for all the tested variables.

In the case of this study the 6 elements with near-100% reproducibility (Mg, Ti, V, Cr, Fe, Ga) as well as Zn, the element with the next highest reproducibility rate (356 out of 457 single shot measurements, which correlates to a reproducibility of 78%), were tested. The presented PCA result in Fig. 6.13 shows the main trace-element characteristics of each deposit clearly. Rubies form Mogok & Namyaseik, Myanmar (Burma) are dominated by high V values where as rubies from John Saul Mine, Kenya typically possesses high values for Ga. Rubies from the Morogoro Region are characterised by high values in Fe and Mg compared to other marble-hosted deposits. High Cr contents are typical for rubies from Yunnan, China. The deposits in Luc Yen, Vietnam and Murgab, Tajikistan take an intermediate position in terms of trace-element composition. Again, as indicated in the previous chapter, it can be seen that rubies from Luc Yen, Vietnam and Yunnan, China overlap the most with the clusters of Morogoro Region rubies. These results confirm that PCA is a powerful tool in origin determination. 12 out of the 15 relationships (3 with minor overlaps, however) among the 6 investigated deposits are distinct in this plot.

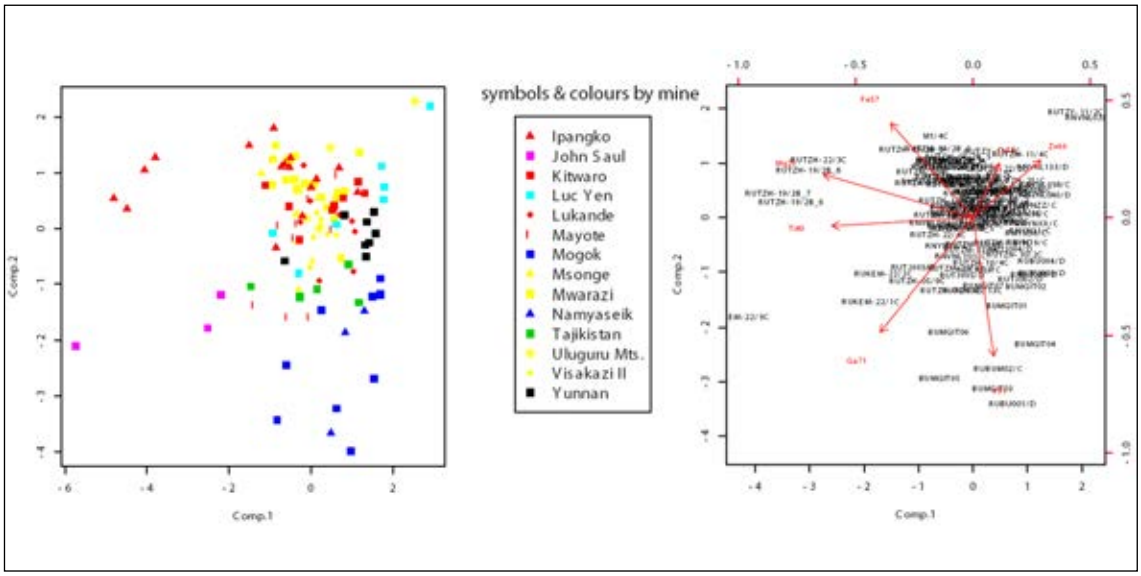

Fig. 6.13: The diagram shown above is a two-dimensional projection of a multi-dimensional data space generated by PCA. The clusters shown in the diagram of the left allow the recognition of the main trace-element characteristics of rubies from the tested deposits. In the diagram on the right, a projection of the axis according to the variables examined by PCA is displayed. The combination of the two diagrams permits the interpretation of different clusters in terms of their trace-element characteristics.

6.7.5 Trace-Element Characterisation of Rubies from Morogoro Region, Tanzania

Above it was demonstrated that a separation of the 6 investigated deposits is possible on the basis of trace-element analysis. However, the rubies from the Uluguru and Mahenge Mts, respectively, cannot reliably be distinguished, the overlap of the two deposits in the Morogoro Region, Tanzania, is simply too prominent. From the scatter plot matrix introduced previously, only the element combination Fe/Cr reveals some trends among the two populations the Uluguru and Mahenge Mts, Tanzania (Fig. 6.14).

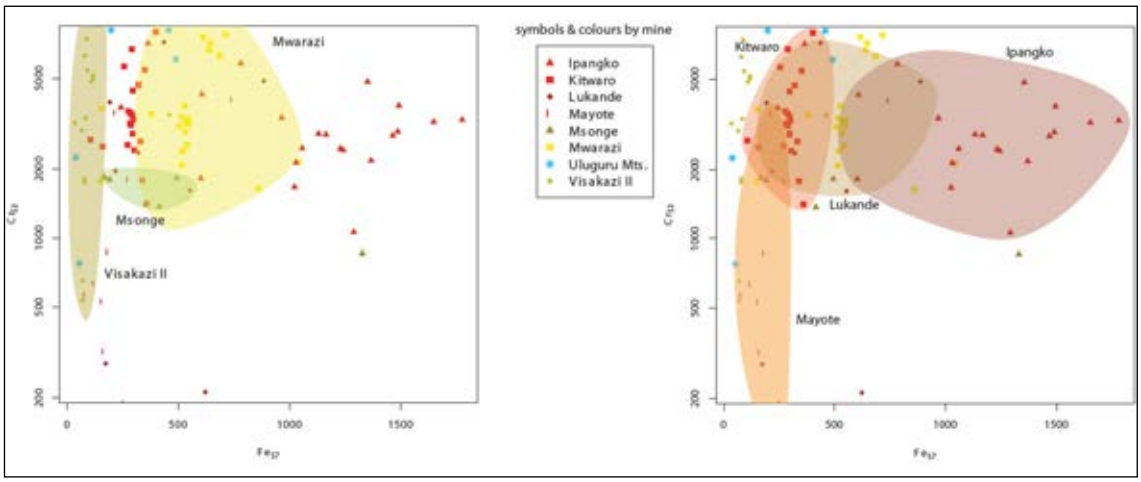

Fig. 6.14: Although no clear separation can be made based on trace-element analysis, certain trends can still be recognised for rubies deriving from deposits in the Morogoro Region, Tanzania. To enhance the clarity of diagrams, the various clusters of the different mines were put in colour for the Uluguru Mts (left diagram) and the Mahenge Mts (right diagram). The rubies labelled Uluguru Mts were purchased at the local market of Mkuyuni in the Uluguru Mts and turned out to be a mixed lot including rubies from Mwalazi as well as Visakzi II Mine.

Generally, it can be said that rubies from the Uluguru Mts tend to have lower contents of Fe than rubies from the Mahenge Mts. In particular, the deposits from the Uluguru Mts have populations clustering below 150ppm for Visakazi II Mine and between 500 to 750 ppm for Mwalazi Mine. There is no trend recognized for rubies from Msonge Mine. However, this may well be due to the small number of samples from this mine.

7 samples were purchased at Mkuyuni Market, Uluguru Mts, Tanzania, without exact origin declaration. The local dealer who sold the parcel indicated the Uluguru Mts as their origin, however. Based on the data obtained here, the following statements can be made. According to their grouping in the Fe/Cr binary plot the samples most probably derived from two mines, Mwalazi and Visakazi II. This is a reasonable outcome since the two mines were the most active in the Uluguru Mts at the time of visit. Note that it is common to find mixed lots with rubies from several mines even on local markets. This however stresses the importance of sample collection at the mine itself in order to obtain sample material with the highest possible level of confidence in terms of origin.

For rubies from the Mahenge Mts, the following observations can be reported. With the exception of Mayote Mine, rubies from the Mahenge Mts were found to be high

in Cr which typically exceeded contents of 1000 ppm. As it was reported in chapter 5 rubies from the Mayote Mine tend to be more pink than red in colour. This observation goes well along with the decreased Cr values found in these rubies. On the other hand rubies from Kitwaro clustered at low Fe contents between 100 to 400 ppm. Rubies from Ipangko again showed a much wider range in Fe contents, mainly above 750 ppm. The plot for rubies from Lukande, finally, produces a significant overlay with all deposits from the Mahenge Mts. This resembles the alluvial deposit type of Lukande Mine which obviously contains rubies from several mines.

6.8 Discussion

A major objective of this research project was the examination of marble-hosted ruby samples by LA-ICP-MS. To start with, a performance comparison was carried out to demonstrate the strength of LA-ICP-MS compared to ED-XRF. The increased sensitivity with low LOD, high accuracy combined with a broad range of detectable elements, as well as the simple sample preparation and application of standard materials for calibration were recognised as key advantages of LA-ICP-MS.

On the other side the ‘quasi non-destructive’ sampling mode has to be counted as a disadvantage of LA-ICP-MS. The microscopic sample damage however is affecting neither a gemstone’s weight nor its beauty significantly and could therefore be neglected. Additionally, due to the high spatial resolution of LA-ICP-MS aliasing effects may occur if a gemstone is zoned. To take this phenomenon into account a procedure of recording several measurements per stone and calculate averaged data for further use is suggested. On the contrary, the high spatial resolution allows depth profiling investigations which are not possible with ED-XRF.

This combination where advantages outnumber disadvantages sets LA-ICP-MS ahead of ED-XRF in terms of analytical performance. The analytical strengths are also the reason for the ever growing acceptance of LA-ICP-MS as a new analytical method for trace-element analysis in gemmology.

The much appreciated high-quality data generated by LA-ICP-MS do also come with a price though. The highly sophisticated character of this analytical technique requires not only a skilled operator with a sound base in analytics but also an adequate budget to cover for the high initial costs as well as the high maintenance cost while running the system. The high running costs are mainly due to the consumption of expensive carrier gases. Therefore, ED-XRF will probably remain the standard technique for trace-element analysis for many gem laboratories, accepting the limitations of this method also illustrated here. Collaborations with research facilities in order to get access to carry out trace-element analysis by LA-ICP-MS may offer a feasible approach for gemmological laboratories with limited lack of expertise and/or funding.

Among the anticipated outcome of this study was the definition of gemmology-specific procedures for LA-ICP-MS analysis and data interpretation.

It could be shown in the framework of this study, as also published by Balmer et al. (2008), that a combined approach of an acid-washing procedure followed by ultrasonic cleaning allows gemmologists to clean the surfaces also of rough unpolished surfaces efficiently. For polished samples, cleaning the sample's surface by a paper tissue drenched in ethanol was found to be sufficient instead.

Also in terms of sample positioning in the ablation chamber, several recommendations can be made. In general, it is suggested to place rough and/or smaller samples close to the inlet of the sample chamber where as polished and/ or bigger samples should be placed towards the outlet. Thanks to the turbulent ablation chamber carrier gas flow employed in this study, stones of different sizes and uneven surfaces can be analyzed well. To minimise cross-contamination it is further advised to carry out ablations by proceeding in the direction of the inlet, against the carrier gas flow.

With the application of surface cleaning shots or cleaning rasters prior to the actual ablation the data quality can be further improved. Remaining surface contamination can be removed and clean signals deriving from the ablation of sample material only can be achieved. It has to be made sure however that the depth of such a pre-ablation exceeds the depth where surface contamination can be detected. As it was possible to demonstrate in this study, surface contaminations on clean surfaces following the sample preparation mentioned above are typically in the range of a few µm only or less. Pre-ablations reaching a depth of 5µm are sufficient to remove the undesired contaminated surface layer and are therefore suggested as a routine procedure. Since the chosen instrument parameters of a given system also affect the ablation rate, it has to be evaluated for each LA-ICP-MS set up individually how much ablation time this corresponds to.

Standardised ablation patterns finally help to avoid confusion in terms of correlation and re-location of data with their corresponding ablation pits generated by single shot measurements. A simple way to do so is to take 4 spot measurements per sample in an L-shaped arrangement, allowing for unambiguous identification of each analytical measurement even after off-line data processing.

Recommendations for subsequent data processing are also made. The search for the smallest set of elements necessary to describe the investigated system distinctively resulted in a drastic reduction of the number of element finally used. Not only light elements which were in the focus of this investigation but also elements which became detectable on a reproducible basis due to lower LODs were finally found to be diagnostic and therefore useful for origin determination. Consequently, a set of 10 elements including Li, Mg, Ti, V, Cr, Fe, Ga, Ge, Nb, and Sn is recommended to be tested for further trace-element analysis on marble-hosted rubies, out of the 50 elements recorded in this study.

In contrast to Li and Mg, the outcome of this research project indicates that REE do not possess any distinctive potential for origin determination purposes. The content of REE is in most cases to low to be considered routinely. REE are therefore suggested

to no longer be included in the element menu of trace-element analysis on marble-hosted rubies.

It can further be stated that for marble-hosted ruby samples examined in this study Be levels never exceeded values of 0.4 ppm. Although there is untreated corundum from other deposit types with potentially higher contents of Be, it can be said that if marble-hosted rubies show Be contents above 0.4ppm combined with signs of heat-treatment, a Be diffusion-treatment is strongly indicated.

During the process of in-depth data analysis it was also recognised that certain element combinations possess a distinctive character in terms of origin determination. The binary plot between Li and Sn as well as the four ternary plots introduced in chapter 6.7.3 turned out to be the most powerful diagrams in this regard. Principal Component Analysis (PCA) further confirmed a strong potential for origin determination data analysis in gemmology. Consequently, most of the examined relationships between the six investigated deposits were distinguishable in one plot generated by PCA. To pinpoint a specific deposit, combination of the suggested plots and diagrams was most efficient in terms of origin determination. In contrast, the more traditional plots introduced by Guillong et al. (2001) and Sutherland et al. (1998, 2003) were found not to be origin-specific for ruby origin determination purposes. The plot by Sutherland et al. (1998, 2003) possesses a potential for a rough classification in terms of geologic provenance, however, clearly indicating whether a given ruby may be marble-hosted or not. Refined analysis could then be carried out along the lines documented above.

The most challenging task in this study in terms of trace-element analysis, however, was to investigate whether it will be possible to separate rubies from similar geological environments, in this case marble-hosted deposits. The analytical target of this study stands therefore in contrast to the early work of Guillong et al. (2001) where the focus laid on sapphires from geologically different deposit types.

Rubies from Mogok & Namyaseik, Myanmar (Burma) were found to be characterised by a high content of V compared to the other marble-hosted ruby deposits. Rubies from Murgab, Tajikistan on the other hand were typically distinguished by the content of Ge. Otherwise distinctive ternary plots as well as PCA indicate that rubies from the Morogoro Region, Tanzania, share characteristics in trace-element composition with rubies from Yuan Jiang, Yunnan, China as well as Luc Yen, Vietnam. Rubies from the Morogoro Region, however, show higher values for Fe than other marble-hosted deposits. In contrast, Rubies from John Saul Mine, were found to behave much different compared to all the other tested deposits. Rubies from John Saul Mine are characterised by elevated Ga contents compared to marble-hosted ruby deposits which resembles a mafic signature. This observation can be explained by the difference in geologic provenance. Mercier et al. (1999) showed that the John Saul Mine is located at the contact between a graphitic-gneiss and an ultramafic intrusion; hence, the rubies formed in a very different geological setting.

Aside from minor differences rubies from the Uluguru and Mahange Mts, Morogoro Region, Tanzania are geochemically identical and not distinguishable from each other on the basis of trace-element analysis. Because of the major overlaps in chemical signatures of rubies from individual mines in the Morogoro Region, Tanzania, only certain trends within the examined populations based on trace-element analysis can be observed. Most interesting was the cluster of rubies from Lukande Mine, Mahenge Mts, Tanzania, where rubies from various deposits were recognised. This observation is consistent with the alluvial deposit style of this particular mine. Finally, a sample lot of rubies of unknown origin which was bought at the local market in Mkuyuni, Uluguru Mts, Tanzania. Their trace element analysis indicates that stones originate from the two most active mines in the area Mwalazi and Visakazi II Mine. This demonstrates that it is best to obtain stones directly from the mine for chemical characterization and possible use of these data in origin determination. If done so, a reference data base could be collected, allowing to measure stones of unknown provenance for origin determination, employing procedures described here. This work documents that origin determination of marble-hosted rubies based on their trace-element composition is well feasible.

CHAPTER VII

CONCLUSIONS

7.1 Confusion about the Origin of Morogoro Rubies Resolved

Earlier gemmological publications addressed the rubies originating from the Morogoro Region as coming from one deposit only. Maps published by the GTS and the actual situation encountered in the field did not correspond in terms of mine names mentioned by Hänni & Schmetzer (1991) however. Based on this contradicting information it already became evident in the field that there must be two deposits at least being responsible for the rubies found in the Morogoro Region, Tanzania. The answer was finally found by identifying both, the Uluguru and Mahenge Mts, as to be the source area for marble-hosted rubies from the Morogoro Region, Tanzania.

Hänni & Schmetzer (1991) already mentioned that there was an early ruby production from the Morogoro Region recognised which didn't match with the rubies produced later on in this region. This stands in contradiction to what is found nowadays. In fact, the marble-hosted rubies of the Morogoro Region are very similar in both gemmological as well as trace-element characteristics. Based on literature a possible explanation for the observed discrepancy could be the ruby deposit near Ngong'horo in the south of the Uluguru Mts. Altherr et al.(1982) reported this deposit to be in connection with an anatexite instead of marbles. During the fieldwork of this study Nong'horo was re-discovered and found to be located near the former mining area of Visakazi Mine (see Appendix A.3). This deposit was confirmed in the field to be in connection with the migmatised basement and therefore located geologically in a different environment than the marble-hosted ruby deposits. This different geological setting was then also well reflected in the characteristics of the rubies deriving from this particular deposit as described by Hänni & Schmetzer (1991). It finally has to be noted that the publication by Altherr et al. (1982) was not mentioned by Hänni & Schmetzer (1991) and a connection to an earlier and somewhat different production in the Uluguru Mts deriving form the Nong'horo Ruby Mine was not made at that time.

7.2 Advanced Gemmological Testing and Trace-Element Analysis of Morogoro Rubies

By carrying out FTIR measurements in this study it was possible to close an analytical gap for the rubies of the Morogoro Region which was not yet covered by previous research. Extensive FTIR analysis combined with newly created reference data for the purpose of FTIR fingerprinting in the range above 1500cm^{-1} made it possible to positively identify inclusion phases in ruby such as tourmaline and amphibole. It was further indicated that in order to avoid misinterpretation besides chlorite, gibbsite has to be considered as a potential mineral phase in the range between 3100-3700cm^{-1} as well. Due to highly sensitive thermostability the presence of gibbsite furthermore provides additional information on the heat treatment status of rubies tested by FTIR.

Additionally, an enhanced UV-vis spectrum analysis procedure where locality specific shapes of UV minima are numerically described was introduced as a useful tool in terms of origin determination. In the following rubies from Luc Yen/ Vietnam, Mogok/ Myanmar (Burma) as well as the Morogoro Region/ Tanzania could be identified based on their UV-vis spectrum characteristics.

The distinguished locality specific clusters in Fig. 5.17, however, could not be linked to variations in Fe/Cr ratios as assumed previously. As shown in Fig. 6.14 there is a major overlap for this trace-element combination and therefore the expected relationship can not be confirmed. At this stage it isn't possible to further verify the reason of the distinct optical behaviour as recorded in UV-vis spectrum analysis (chapter 5.2.3).

Nevertheless, the made observations imply to keep a close look on UV-vis spectra features beyond the range which was considered in gemmology traditionally.

Further during this study, the power of trace-element analysis by LA-ICP-MS in terms of origin determination could be demonstrated. Consequently, the ambitious task to separate rubies from similar geological environments, in this case marble-hosted deposits, based on their trace-element composition was proven feasible. By a combination of 10 selected elements (Li, Mg, Ti, V, Cr, Fe, Ga, Ge, Nb, Sn) it was possible to differentiate the 6 investigated ruby deposits from each other. As rubies from John Saul indicate a separation between rubies from different geological environments should be possible even more clearly. To prove this assumption by including a significant number of samples from other deposit types, however, was beyond the scope of this study.

In the course of LA-ICP-MS trace-element analysis, rubies from the Morogoro Region were characterised by the means of trace-element analysis and found to be especially high in Fe-content in comparison with rubies from other marble-hosted ruby deposits such as from Myanmar (Burma) for example.

7.3 Applications for Origin Determination

Indisputable, trace-element analysis by LA-ICP-MS is the state-of-the-art in origin determination in gemmology today. Nevertheless, LA-ICP-MS is still not a one step solution to determine a gemstone's geographic provenance. In the contrary and as a general rule, origin determination should never be based on one indication only but be confirmed by a combination of consistent evidence, supporting one common origin in the best case. The combination of at least two criteria obtained from independent analytical methods puts an origin call on a solid base which provides a satisfying level of confidence for both the end consumer and the laboratory issuing an origin report.

Origin determination in gemmology is based on 3 fields of analytic investigations: inclusion feature identification, UV-vis spectrometry, and trace-element analysis (Fig. 7.1).

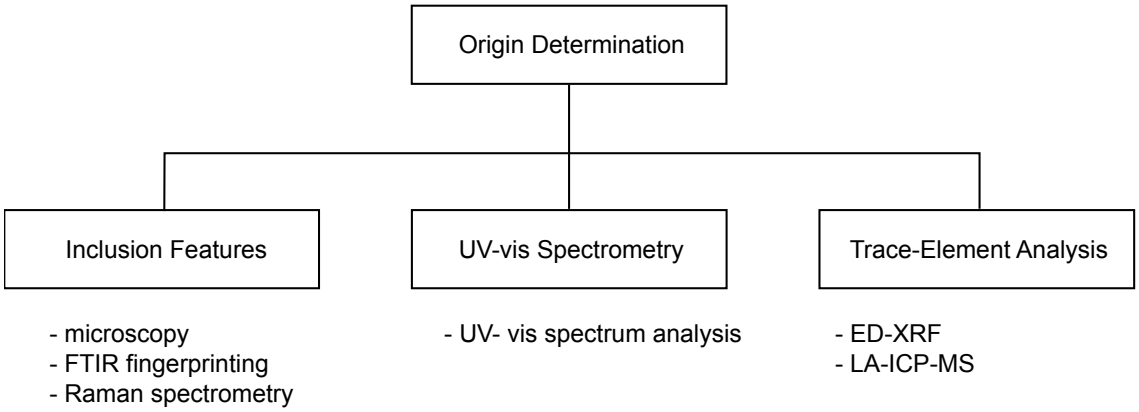

Fig. 7.1: The three fields of analytic investigations which are considered for origin determination in gemmology are inclusions feature, spectrometry, and trace-element analysis.

From an analytical point of view it is suggested to perform spectrometric investigations first and trace-element analysis only if further confirmation is required. This mainly because trace-element analysis are costly and time consuming. This stresses the importance of spectrum analysis and their related procedures.

As mentioned before, new achievements could be made in all three fields of analytic investigations during this study. FTIR fingerprinting was introduced as a new tool to be applied for mineral inclusion phase identification. By a compilation chart indicating locality specific inclusion assemblages origin distinctive inclusion feature combinations were defined. Further, in UV-vis spectrometry a numerical procedure was introduced which allows origin determination by UV-vis spectrum analysis. Regarding trace-element analysis there were new criteria for origin determination based on LA-ICP-MS defined. In particular, distinctive binary, ternary, and PCA plots were indicated as well as refined sampling and measurement procedures were proposed.

Especially, the presented procedures involving microscopy, UV-vis spectrum analysis, and FTIR fingerprinting may help smaller labs with a limited equipment arsenal to still perform origin determination to a certain level when combined with the skills of an experienced gemmologist. These analytics are further less sophisticated and need less maintenance than trace-element analytics. They also exist in portable versions for off-premise testing. This combination of characteristics makes spectrometric investigation still a versatile, efficient and cost-saving approach for origin determination.

Finally, it was experienced to be very difficult to identify whether a Morogoro ruby originates either from the Uluguru or the Mahenge Mts. Despite subtle differences in mineral inclusion composition as well as trace-element composition it is suggested to neglect the differentiation but address the rubies from these two deposits as Morogoro rubies. A differentiation between Morogoro rubies and rubies from other marble-host deposits is well feasible, however, as UV-vis spectrum analysis, inclusion feature identification and trace-element analysis indicate.

7.4 Genetic Model

From what was observed in samples from the Uluguru and Mahenge Mts both deposits underwent the same geologic history as indicated by similar P-T-t paths. This conclusion is not only confirmed by similar metamorphic conditions describing a metamorphic grade of granulite facies but also similar chemical fingerprint of the investigated Morogoro rubies. As a consequence and mentioned in the previous chapter, the separation based on trace-element analysis was not possible for the rubies deriving from the Uluguru and Mahenge Mts respectively.

The initial sedimentation of the host rock was probably in close proximity to the hinterland as possible sedimentation of organic matter as well as heavy minerals indicate. A lagoon or lacustrine sediment basin on the passive continent margin of former East Gondwana seems to be a reasonable possibility (Fritz et al., 2005, Garnier et al., 2008). As comparable units in Mozambique further indicate, sedimentation took place during Neoproterozoic times most probably (Bingen et al., 2011). On a deposit scale, subtle differences in the composition of host-rock marbles between the Uluguru and Mahenge Mts were observed however. In the Uluguru Mts ruby mines are found within calcite-marbles whereas ruby mines in the Mahenge Mts are found to be related to dolomite-marbles. This results also in different mineral paragenesis of the two deposits. Petrographically, the mineral assemblage found in the Uluguru Mts is characterized by phlogopite-amphibole-carbonate-corundum-plagioclase-spinel-white mica +/- scapolite, tourmaline, chlorite whereas the combination of phlogopite-carbonate-corundum-plagioclase-sapphirine +/- amphibole, sphene, tourmaline, chlorite describes the mineral assemblage present in samples from the Mahenge Mts.

Compared to host rock compositions with a total FeO/Fe_2O_3 content <0.3wt%, Na_2O content <0.1wt%, and K_2O content <0.1wt% for all investigated deposits, a significant rise in these oxides can be observed towards the mineralised zones. The record of elevated contents for these particular elements in mineralised zones gives reason for the interpretation that fluids may be responsible for the influx from an external source. Further evidence was found also in metamorphic textures where symplectites document a rapid change in thermodynamic conditions. Due to the geological development of the Eastern Granulites where isobaric cooling (Fritz et al., 2005 & 2009) and long cooling history (Appel et al., 1998; Moeller et al., 2000; Hauzenberger et al., 2005; Tenczer et al., 2011) are documented, drastic changes of pressure and temperature are ruled out and leaves variations of fluid composition as a possibility for the formation symplectites only. In connection with these symplectites there is also the formation of a 2nd ruby generation recognised. This however emphasises the genetic relationship between the occurrence of ruby and the structural controlled fluid infiltration in both the Uluguru and Mahenge Mts. Finally, there is also tourmaline found to be associated with the 2nd generation ruby formation which provides even further evidence for a fluid related corundum formation. Regarding time, the fluids are interpreted to be introduced to the marbles of the Eastern Granulite cover sequence when migmatisation took place within the basement. This might be the case shortly after peak metamorphic conditions during M1 were reached caused by the

continent-continent collision related to the East African Orogeny (Fritz et al., 2005 & 2009).

The ruby formation in the Morogoro Region is visualised by time lapse snap shots of the geological development of the Morogoro Region as follows (Fig. 7.2):

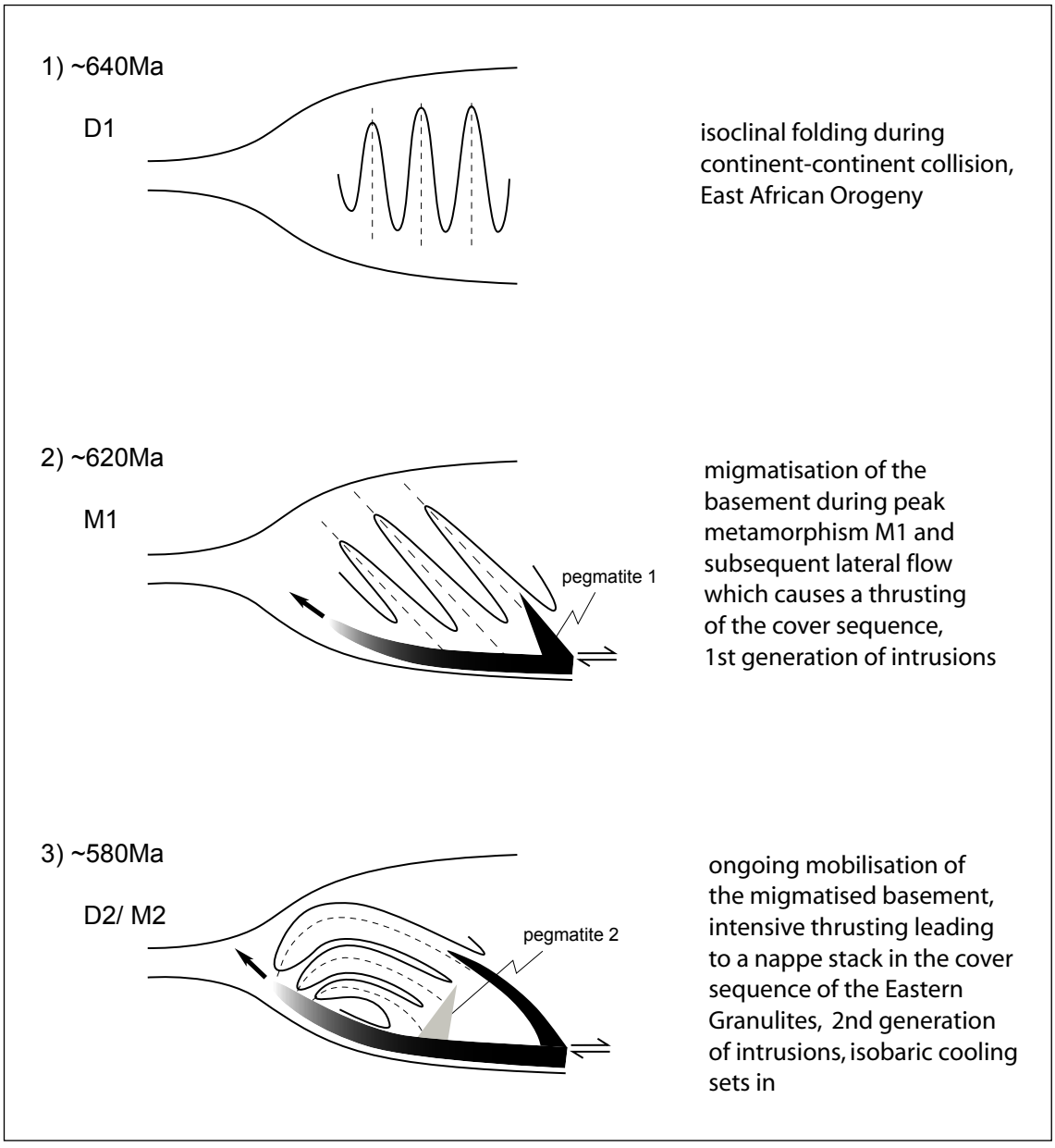

Fig. 7.2: Time lapse snap shots visualise the geologic development of Eastern Granulite cover sequence and therefore the marbles hosting ruby mineraliations in the Morogoro Region, Tanzania. The ruby formation was found to be related to fluid infiltration triggered by the migmatisation of the Eastern Granulite basement. This event is directly related to the East African Orogeny and restricted to time limits between ~620 and ~580Ma.

1) Continent-continent collision tectonics establish ~640Ma (Tenczer et al., 2006 : 650-640Ma, Fritz et al., 2005 : ~640Ma) during the East African Orogeny which is characterised by crustal thickening. Contemporaneously, isoclinal folds develop dur-

ing D1. Because the ruby formation is confined to mineralised boudins in D1 fold hinges, 1st generation ruby formation must have taken place after D1 structures developed.

2) Peak metamorphic conditions at M1 (~750°, 8-9kbar) are reached shortly after D1 when the basement starts to be migmatised due to the gravitational overload. At the same time a first generation of concordant intrusions of mafic signature penetrate the overlaying cover sequence (~620Ma, Fritz et al., 2009). As a consequence, fluids infiltrate the marbles of the Eastern Granulite cover sequence which are in close position to the décollement. Further, a 1st generation ruby formation was observed to take place at peak metamorphic conditions (M1).

Additional evidence for a close proximity to the décollement and a migmatised basement as well as the involvement of fluids is given by the nowadays exploited ruby mineralisation of Ngong'horo in the south of the Uluguru Mts which is linked to anatexites (Altherr et al., 1982).

3) During D2 thrusting is experienced in the Eastern Granulite cover sequence when lateral flow of the now migmatised basement sets in. As a result the already folded cover sequence is thrusted onto the basement and a nappe stack starts to form. During this time a second generation of pegmatites penetrate the nappe structure discordantly (~580Ma, Rossetti et al., 2008), the influx of B bearing fluids triggers the observed formation of a 2nd generation corundum together with tourmaline.

4) Ongoing northwestward nappe stacking during D3 is related to the Kuunga-Malagasy Orogen and crosscuts the 2nd generation pegmatites by a penetrative foliation (Rossetti et al., 2008). This indicates deformation D3 to have developed after the emplacement of tonalitic dykes which are dated at ~580Ma by Rossetti et al. (2008). D3 related M3 metamorphism is found to be too low in terms of metamorphic conditions to be responsible for the 2nd ruby generation to form (greenschist facies). This again indicates an upper time limit for the ruby formation encountered in the marble-hosted deposits of the Morogoro Region, Tanzania.

The observed time restrictions narrow down the time frame for the two corundum formations to have taken place between ~620 and ~580Ma. They are therefore related to M1 and M2 metamorphic events during the East African Orogeny which are further in close relationships with the deformation periods D1 and D2. Consequently, the emplacement of anorthosite bodies in the Uluguru as well as the Mahenge Mts can be ruled out as a potential cause for the ruby formation due to unfavourable time relations (intrusion age of Uluguru anorthosite, 880-820Ma, Tenczer et al., 2006).

On a deposit scale the position of mineralised boudins confined to subsidiary folds of D1 fold structures in the Uluguru and Mahenge nappe stacks indicate a structurally controlled formation of ruby deposits for marble-hosted ruby deposits in the Morogoro Region, Tanzania. Mineralised lense-shaped nodules were found near D1 fold hinges where permeability was increased and fluids were channelled parallel to the fold axis (Fig. 7.3).

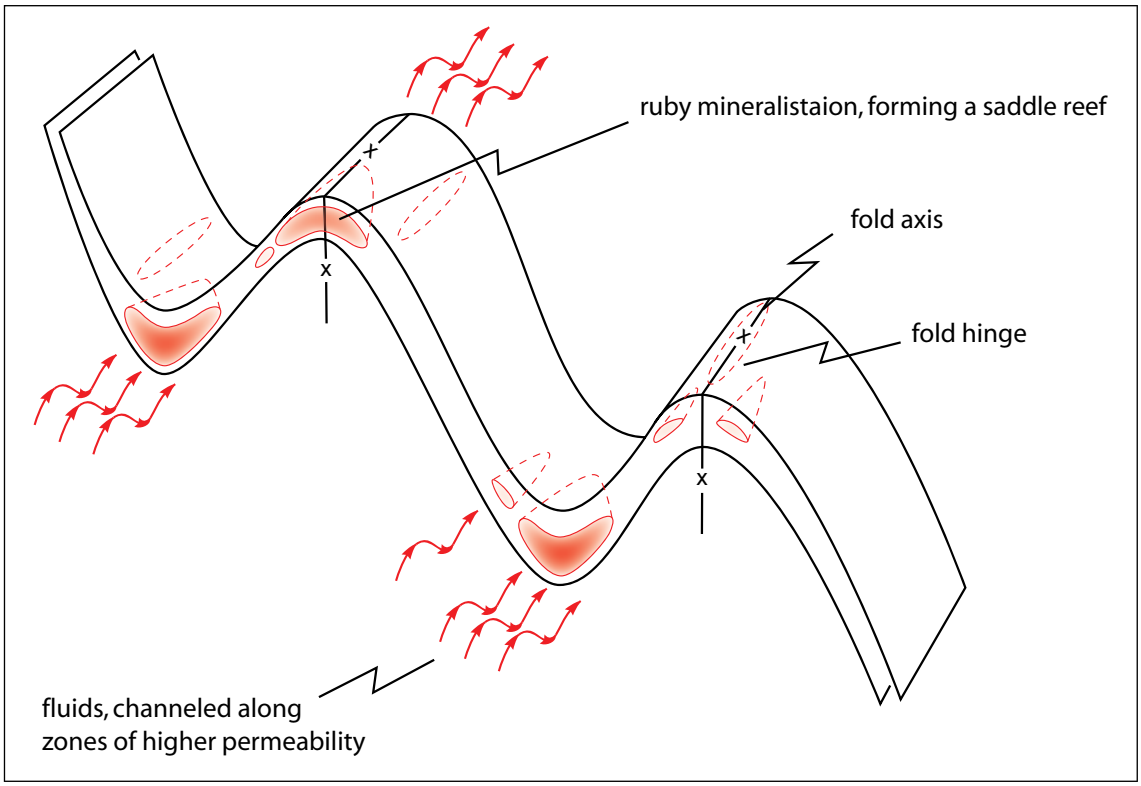

Fig. 7.3: Deposit scale fold structures as observed in the field indicate that the ruby mineralisation is confined to fold hinges of D1 fold structures and therefore being structurally controlled. The ruby formation is focused on zones with increased permeability at fold hinge areas where fluids where channelled during infiltration related to intrusion episodes as well as M1 and M2 metamorphism.

Finally, thermodynamic phase diagram calculations confirmed the proposed genetic model indicating an anticlockwise P-T-t path characterised by isobaric cooling between M1 and M2 as well as isothermal decompression related to M3 metamorphism (Fig. 7.4). Peak metamorphic conditions were indicated at conditions of granulite facies where as M2 metamorphism is representing upper amphibolite facies thermodynamic parameters. Finally, M3 is recorded as a chloritisation in the marbles of the Morogoro Region at greenschist facies conditions and responsible for a recrystallistion eliminating structural information in the examined rock samples most likely.

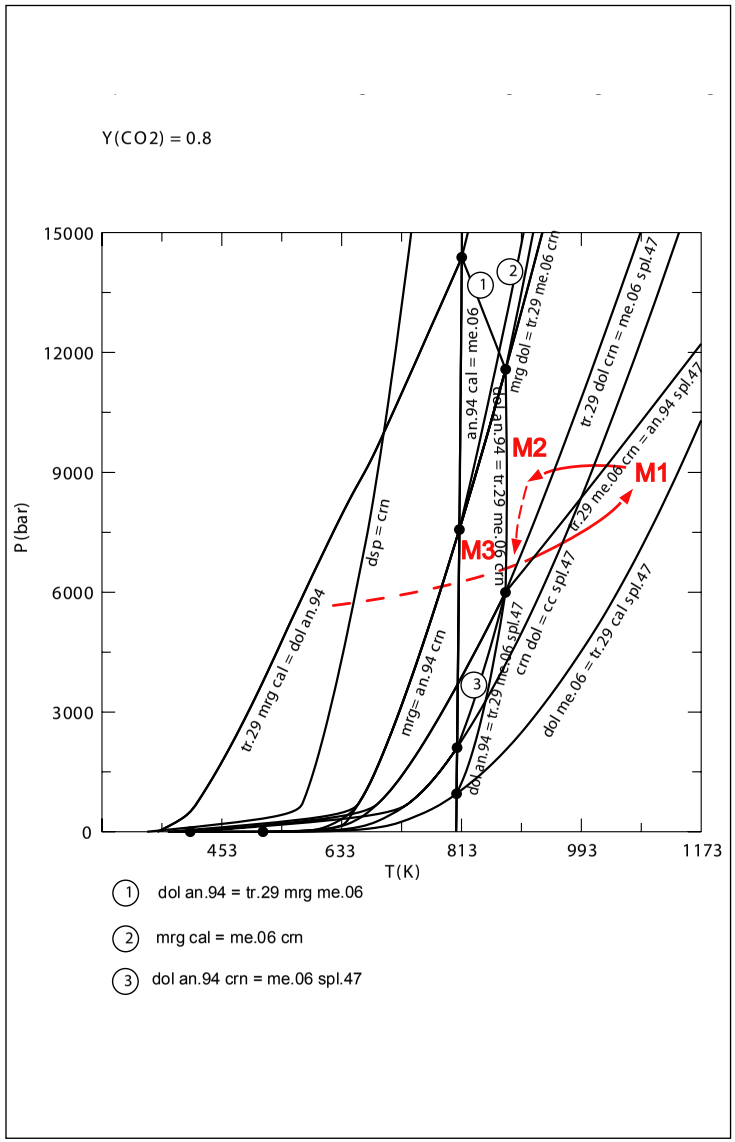

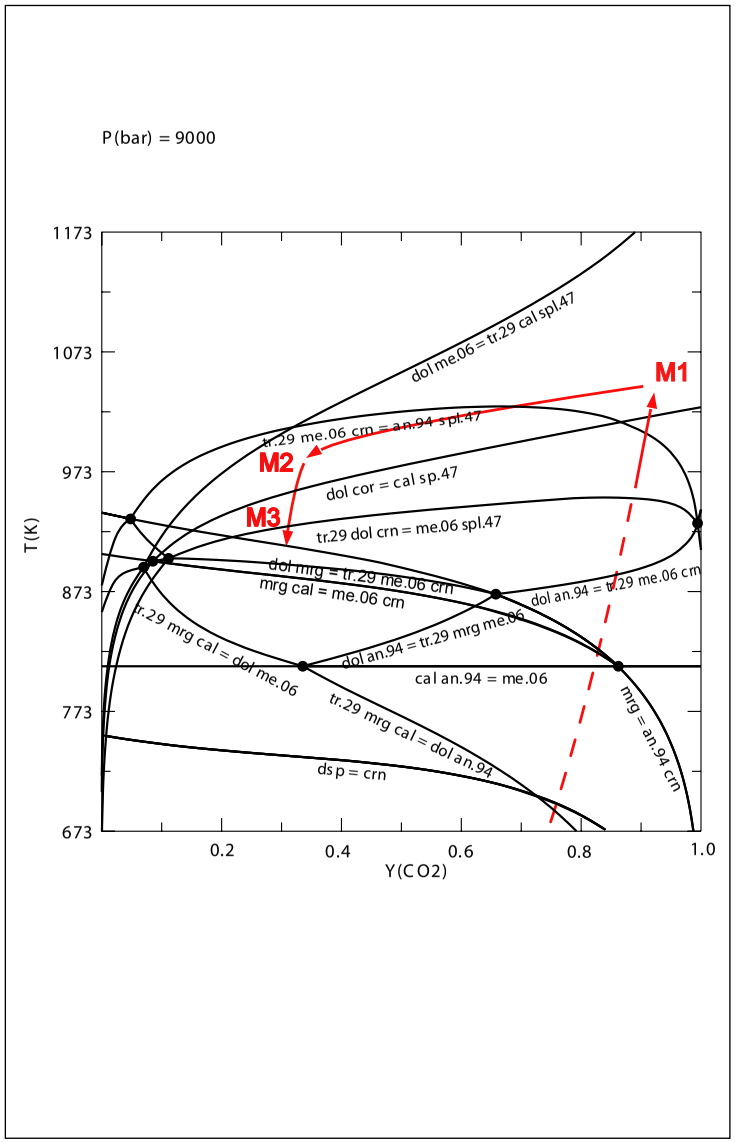

Fig. 7.4: Mineral assemblages observed in the marble-hosted ruby mineralisations of the Morogoro Region describe an anticlockwise P-T-t path with peak conditions at granulite facies for M1 and upper amphibolite facies for M2. A last metamorphic event took place under greenschist facies conditions and is documented by chloritisation mainly.

As an example sample WB1, Visakazi Mine II, Uluguru Mts, Tanzania is shown above. From the X_{CO2} phase diagram it can be seen that a change in fluid composition during retrograde metamorphism is indicated. As metamorphic textures imply a rapid and drastic change in thermodynamic conditions, in this case mainly the fluid composition, forced a symplectite of corundum and scapolite to form instantly. On the right hand side a P-T phase diagram is shown where minimal pressure conditions can be concluded at ~8.5kbar based on relative time relationships documented by conclusive mineral assemblage sequences.

7.5 Comparison of Marble-Hosted Ruby Deposits

Taking the publication by Garnier et al. (2008) into account a comparison between the marble-hosted ruby deposits of Luc Yen, Vietnam and the Morogoro Region, Tanzania can be made. Not only are these two deposits geographically far apart but also very different in thermodynamic conditions, tectonic settings as well as age. The differences characterising these two marble-hosted ruby deposits are displayed in Tab.7.1.

The differences of the two marble-hosted ruby deposits are mainly due to a different position within the orogen they are related to. A deeper crustal depth results in higher pressure and therefore different deformation style as observed for the compared deposits. Further, the Morogoro Region deposits are found within the orogenic front zone while the deposit in Luc Yen is located on an extrusion wedge off the orogenic front. Linked to this position is most likely also the time of ruby formation. While the two ruby generations in the Morogoro Region formed during the orogeny itself it seems that the mineralisation in Luc Yen, Vietnam is late compared to the orogeny. After all, differences between the two compared deposits are smallest in terms of temperature and both deposits seem to be closely related to dominant regional structures. Finally, fluids are recognised as key conditions for the formation in both of the compared marble-hosted ruby deposits. Finally, relative time relationships indicate, as observed during this study, the marble-hosted ruby deposits in the Morogoro Region, Tanzania to be the oldest one known of its kind.

	Luc Yen Vietnam (Garnier et al., 2002) (Garnier et al., 2008)	**Morogoro** Tanzania (this study)
related orogen	Himalayan	East African
ruby formation age	40 - 35Ma	620 - 580Ma
temperature (peak conditions)	~650°C	~750°C
pressure (peak conditions)	2.5 - 3kbar	8 - 9kbar
crustal depth	shallow	deep
position related to orogen	extrusion wedge	orogenic front
dominant structures	shear zone faults	nappes folds

Tab. 7.1: Based on literature and data collected in this study striking differences in geologic parameters could be recognised characterising the two compared marble-hosted ruby deposits. Only in temperature the marble-hosted ruby deposit in Luc Yen, Vietnam and deposits in the Morogoro Region, Tanzania seem to share a similarity.

CHAPTER VIII

RECOMMENDATIONS

8.1 Future Research Targets

During whole rock analysis carried out at Department of Mineral Resources, Bangkok, Thailand it was neglected analysis Cr_2O_3. It was realised in the course of this research, however, that this left an analytical gap which did not allow further investigations regarding the source of Cr_2O_3. Due to the fact that Cr_2O_3 is the essential chromophore of rubies this information is still of a certain importance. It is therefore recommended to make sure that Cr_2O_3 is included into future whole rock analysis related to marble-hosted ruby deposits. As a further consequence, it is planned to carry out Cr_2O_3 trace-element composition analysis subsequent to the completion of this research project.

Isotopic analysis of B in tourmaline, O in corundum, and S in sulphides may reveal further information about the sources of these three elements. This may lead to confirmation or falsification of the proposed genetic model where fluids are related to migmatisation of the Eastern Granulite basement. With the suggested isotopic investigation it may also be possible to clarify whether organic matter was indeed sedimented within the marbles of the Uluguru and Mahenge Mts being responsible for an elevated SO_3 content in specific localities.

Regarding differences in mineral chemistry of the two ruby generations observed in the Morogoro Region further trace-element analysis by LA-ICP-MS has still to be carried out. This may reveals further information to support the suggested genetic model regarding the involvment of fluids during ruby formation.

To take origin determination of marble-hosted rubies based on trace-element composition to the next level, blind testing of several batches with samples from different marble-hosted deposits would be necessary. Subsequently, this data would be plotted in the suggested binary and ternary diagrams. To further verify the distinctive power of the suggested diagrams rubies from other deposit types also would have to be considered. A more comprehensive picture of the trace-element composition of rubies in general would be obtained from such an investigation. Despite of the 10 elements which were defined to be distinctive for origin determination on marble-hosted rubies it is still suggested to use the full range of 50 elements for research projects when ever possible. This because it might still be possible to detect elements which were found not conclusive in this project to be detected with a satisfying reproducibility in other ruby deposit types.

To allow a more conclusive data interpretation by PCA it is recommended to create projections from a multi-dimensional data space into 3D instead of 2D. As it can be

expected from Fig. 6.13 this would increase the possibility to separate the data clusters related to different deposits more clearly. The software package applied in this study did not allow such projections, however, and might be carried out in a consecutive project.

In terms of advanced gemmological testing it would be interesting to investigate whether rubies from other deposit types could be separated by the application of UV-vis spectrum analysis. This additional investigation could be carried out in combination with LA-ICP-MS and PCA analysis which were recommended above. As a last step, blind testing would also be indicated for UV-vis spectrum analysis as well.

Finally, the spinel occurrences in the Mahenge and Uluguru Mts were not addressed during this study. To arrive with a complete picture about the gemstone mineralisation present in the marbles of the Uluguru and Mahenge Mts a future project could focus on related spinel mines. Especially since the Ipangko Spinel Mine opened its production, spinels from the Mahenge Mts became famous and have therefore a certain economic importance. A study of these spinel occurrences would also be interesting in relationship to the ruby mines investigated in this study. The assumption that these two mineralisations are linked could finally be examined.

8.2 Potential Sites for Economic Gem Resources in Tanzania

As Malisa & Muhongo (1990) described, major gemstone occurrences are related to similar structures throughout the Eastern Granulites. Based on their work which was mainly related to the tanzanite occurrence in the Merelani Hills and compared with the results presented in this study a similar deformation style as well as structural controlled mineralisation can be recognised. In both cases precious minerals are found in combination with mineralised, boudin-shaped lenses and were created during fluid-rock interactions after D1 deformation structures were formed. As Fritz et al. (2009) indicate (Fig.8.1) there are additional areas in the Eastern Granulites

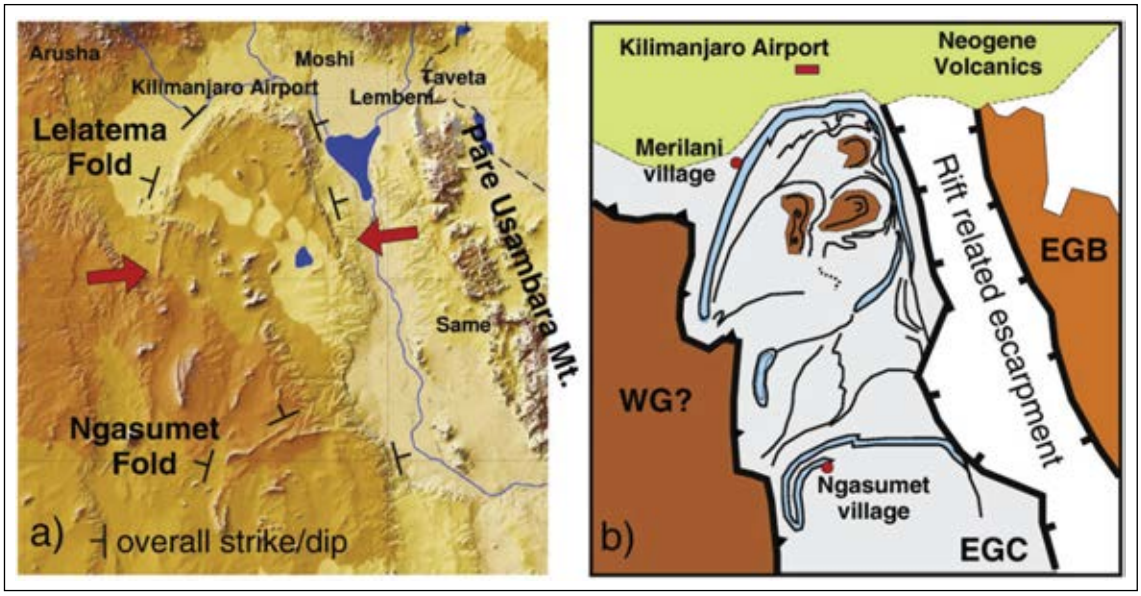

Fig. 8.1: It is possible to recognise further major fold structures within the Eastern Granulite cover sequence which potentially contain additional gemstone mineralisations (after Fritz et al., 2009).

which contain similar structure features as the ones found in the Merelani Hills or the Morogoro Region.

It is therefore recommended to focus future gemstone explorations in zones where Eastern Granulite cover sequences combined with pronounced fold structures related to D1 and D2 deformation are exposed. Such areas may be found either to the north or the south of the Uluguru Mts where occasional gemstone findings were reported in the past already.

References

Abduriyim, A., Kitawaki, H. 2006. Application of laser ablation-inductively coupled plasma-mass spectrometry (LA-ICP-MS) to gemology. **Gems & Gemology** 42(2): 98-118.

Abduriyim, A., Kitawaki, H. 2006. Determination of the origin of blue sapphires using Laser Ablation Inductively Coupled Plasma Mass Spectrometry (LA-ICP-MS). **Journal of Gemmology** 30(1 /2): 23-36.

Abduriyim, A., Kitawaki, H. 2006. Application of LA-ICP-MS (laser ablation-inductively coupled plasma-mass spectrometry) to the gemological field. **Gems & Gemology** 42(3): 87-88.

Altherr, R., Okrusch, M., Bank, H. 1982. Corundum and kyanite-bearing anatexites from the Precambrian of Tanzania. **Lithos** 15: 191-197.

Appel, P., Möller, A., Schenk, V. 1998. High-pressure granulite facies metamorphism in the Pan-African belt of eastern Tanzania: P-T-t evidence against granulite formation by continent collision. **Journal of Metamorphic Geology** 16(4): 491-509.

Baker, J., Newton, C.C. 1995. Experimentally determined activity-composition relations for Ca-rich scapolite in the system $CaAl_2Si_2O_8$-$NaAlSi_3O_8$-$CaCO_3$, at 7kbar. **American Mineralogist** 80: 744-751.

Balan, E., Saitta, A. M., Mauri, F., Calas, G. 2001. First-principles modeling of the infrared spectrum of kaolinite. **American Mineralogist** 86: 1321–1330.

Balan, E., Lazzeri, M., Morin, G., Mauri, F. 2006. First-principle study of the OH-strechting modes of gibbsite. **American Mineralogist** 91: 115-119.

Balan, E., Lazzeri, M., Mauri, F. 2006. Infrared spectrum of hydrous minerals from first-principle calculations. **Psi-K Electronic Structure Calculation of Solids and Surfaces**, Newsletter 75: 143-150. Available from: http://www.psi-k.org [2008, November]

Balmer, W.A., Sutthirat, C., Hauzenberger, Ch.A., Pettke, T., Atichat, W., Krzemnicki, M. 2009. The marble-hosted ruby deposits of Morogoro,Tanzania: a current research report. **Proceedings of the 31st international gemmological conference (IGC).** Arusha, Tanzania.

Balmer, W.A. 2009. Empirical Determination of Cleaning Agents Applied During the Preparation Procedure of Corundum Rough for Heat Treatments. **Proceedings of the 2nd International Gem and Jewelry Conference.** Bangkok, Thailand.

Balmer, W.A., Susawee, N., Sutthirat, C., Hauzenberger, Ch., Pettke, Th., Coldham, T.C. 2010. The marble-hosted ruby deposit near Yuan Jiang, Ailao Shan Moutains, Yunnan Province, China: Is there a genetic linkage to the marble-hosted ruby deposits in Luc Yen, Vietnam ? **Proceedings of the 5th international Workshop on Provenance and Properties of Gems and Geo-Materials (Pro-Gem-Geo).** Hanoi, Vietnam.

Balmer, W.A., Bosshart, G., Sutthirat, C., Hauzenberger, C.A., Pettke, Th. 2011. Reassessment of UV-vis Spectra Characterisation for Rubies from Marble-hosted Deposits. **Proceedings of the 32nd international gemmological conference (IGC).** Interlaken, Switzerland.

Bank, H., Henn, U. 1989. Schleifwürdige Korunde von Ngoronghoro, Tanzania. **Zeitschrift der Deutschen Gemmologischen Gesellschaft** 38(1): 44-49.

Beaumont, C., Nguyen, M.H., Jamieson, R.A., Ellis, S. 2006. Crustal flow modes in large hot orogens. In Law, R.D., Searle, M.P., Godin, L. (Eds.), **Channel Flow, Ductile Extrusion and Exhumation in Continental Collision Zones**, pp.91–145. London: Geological Society, Special Publications.

Bell, V.A., Citro, V.R., Hodge, G.D. 1991. Effect of Pellet Pressing on the Infrared Spectrum of Kaolinite. **Clays and Clay Minerals** 39(3): 290-292.

Beran, A., Rossman, G.R. 2006. OH in naturally occurring corundum. **European Journal of Mineralogy** 18(4): 441-447.

Bingen et al. 2011. Geological Evolution of Northeastern Mozambique, in the Context of the Pan-African Gondwana Assembly. **Abstracts Volume, 23rd Colloquium of African Geology (CAG23).** University of Johannisburg, South Africa.

Birch, R.L., Stephens, E.A. 1962. **Quarter Degree Sheet 251, Mahenge**. Dodoma, Tanzania: Geological Survey of Tanzania.

Bosshart, G. 1982. Distinction of Natural and Synthetic Rubies by Ultraviolet Spectrophotometry. **Journal of Gemmology** 18(2): 145-160.

Bowersox, G.W., Foord, E.E., Laurs, B.M., Shigley, J.E., Smith, C.P. 2000. Ruby and Sapphire from Jegdalek, Afghanistan. **Gems & Gemology** 36(2): 110-126.

Brown, G. 1992. Vietnamese Ruby: A Discriminatory Problem for Gemmologists. **Australian Gemmologist** 18(2): 43-46.

Connolly, J.A.D 1990. Mulitvariable Phase Diagrams: An Algorithm Base on Generalized Thermodynamics. **American Journal of Science** 290: 660-718.

Connolly, J.A.D, Petrini, K. 2002. An automated strategy for calculation of phase diagram sections and retrieval of rock properties as a function of physical conditions. **Journal of Metamorphic Petrology** 20: 697-708.

Collins, A.S., Pisarevsky, S.A. 2005. Amalgamating eastern Gondwana: The evolution of the Circum-Indian Orogens. **Earth-Science Reviews** 71: 229–270.

Dachs, E. 1998. PET: petrological elementary tools for matematica. **Computers & Geosciences** 24(3): 219-235.

Deer, W.A., Howie, R.A., Zussman, J. 1996. **An Introduction to the Rock Forming Minerals**. Essex, England: Longman Group Ltd.

Droop, G.T.R. 1987. A general equation for estimating $Fe3^{+}$ in ferromagnesian silicates and oxides from microprobe analysis, using stoichiometric criteria. **Mineralogical Magazine** 51: 431-437.

Dirlam, D.M., Misiorowski, E.B., Tozer, R., Stark, K.B., Bassett, A.M. 1992. Gem wealth of Tanzania. **Gems & Gemology** 28: 80-134.

Emmett et al. 2003. Beryllium Diffusion of Ruby and Sapphire. **Gems & Gemology** 39(2): 84-135.

Farmer, V.C. 1974. **The infrared spectra of minerals**. London, Canada: Mineralogical Society Monograph 4.

Fritsch, E., Stockton, C.M. 1987. Infrared spectrometry in gem identification. **Gems & Gemology** 23(1): 18-26.

Fritz et al. 2005. Central Tanzanian tectonic map: A step forward to decipher Proterozoic structural events in the East African Orogen. **Tectonics** 24(TC6013): 26.

Fritz, H., Tenczer, V., Hauzenberger, Ch., Wallbrecher, E., Muhongo, S. 2009. Hot granulite nappes -Tectonic styles and thermal evolution of the Proterozoic granulite belts in East Africa. **Tectonophysics** 477: 160–173.

Fryer, B.J., Jackson, S.E., Longerich, H.P. 1995. Design, operation and role of the laser-ablation microprobe coupled with an inductively-coupled plasma-mass-spectrometer (LAM-ICP-MS) in the earth-sciences. **Canadian Mineralogist** 85(1): 78-88.

Garnier et al. 2002. Ar-Ar ages in phlogopites from the marble-hosted ruby deposits in northern Vietnam: Evidence for Cenozoic ruby formation. **Chemical Geology** 188: 33-49.

Garnier et al. 2005. Les gisements de rubis du Pakistan et du Vietnam. **Revue de Gemmologie** 151: 6-12.

Garnier et al. 2008. Marble-hosted ruby deposits from Central and Southeast Asia: Towards a new genetic model. **Ore Geology Reviews** 34: 169–191.

Giuliani et al. 2003: CO2-H2S-COS-S8-AlO(OH)-bearing fluid inclusions in ruby from marble-hosted deposits in Luc Yen area, North Vietnam. **Chemical Geology** 194: 67-185.

Giuliani, G., Ohnenstetter, D., Garnier, V., Fallick, A.E., Rakotondrazafiny, M., and Schwarz, D. 2007. The geology and genesis of gem corundum deposits. In Groat, L.A. (ed.), **Geology of Gem Deposits**, pp.23-78. Mineralogical Association of Canada: Short Course Series ,Volume 37.

Gübelin, E.J. 1973. **Innenwelt der Edelsteine**. Zürich, Switzerland: ABC Verlag.

Gübelin, E.J. 1982. Gemstones of Pakistan: Emerald, Ruby, and Spinel. **Gems & Gemology** 28(3): 123-139.

Gübelin, E.J. 1983. Genetische Aspekte der Mineraleinschlüsse in Farbsteinen. **Zeitschrift der Deutschen Gemmologischen Gesellschaft** 32(1): 10-27.

Gübelin Gem Lab 2006. The roots of origin determination. **Jewellery News Asia** July: 66-71.

Gübelin Gem Lab 2006. The limitations of origin determination. **Jewellery News Asia** August: 52-62.

Gübelin Gem Lab 2006. A holistic method of determining gem origin. **Jewellery News Asia** September: 118-126.

Gübelin, E.J., Koivula, J.I. 1986. **Photoatlas of Inclusions in Gemstones Vol.1**. Zürich, Switzerland: ABC Editions.

Gübelin, E.J., Koivula, J.I. 2008. **Photoatlas of Inclusions in Gemstones Vol.3**. Basel, Switzerland: Opinio Verlag.

Guillong, M., Günther, D. 2001. Quasi 'non-destructive' laser ablation-inductively coupled plasma-mass spectrometry fingerprinting of sapphires. **Spectrochimica Acta Part B** 56: 1219-1231.

Guillong, M. and Heinrich, C.A. 2007. Sensitivity enhancement in laser ablation ICP-MS using small amounts of hydrogen in carrier gas. **Journal of Analytical Atomic Spectrometry** 22: 1488–1494.

Guillong, M., Meier, D.L., Allan, M.M., Heinrich, C.A., Yardley, B.W.D. 2008. SILLS: A MATLAB-based program for the reduction of Laser-ablation ICP-MS data of homogenous materials and inclusions. In Sylvester, P. (ed.), **Laser ablation ICP-MS in the Earth Sciences: Current practices and outstanding issues**, pp.328-333. Mineralogical Association of Canada: Short Course Series, Volume 40.

Günther, D., Heinrich, C.H. 1999. Enhanced sensitivity in laser ablation-ICP mass spectrometry using helium-argon mixtures as aerosol carrier. **Journal of Analytical Atomic Spectrometry** 14: 1363-1368.

Guo, J.F., O'Reilly, S.Y., and Griffin, W.L. 1996. Corundum from basaltic terrains: a mineral inclusion approach to the enigma. **Contributions to Mineralogy and Petrology** 122: 368-386.

Hamid, G., Kelly, S.M.B., Brown, G. 1999. Ruby from Tunduru-Songea, East Africa, **Australian Gemmologist** 20: 326-330.

Hänni, H.A. 1986. Korunde aus dem Umba-Tal. **Zeitschrift der Deutschen Gemmologischen Gesellschaft** 35(1/2): 1-13.

Hänni, H.A. 1987. On corundum from Umba Valley Tanzania. **Journal of Gemmolgy** 20(5): 278-284.

Hänni, H.A. 1994. Origin determination for gemstones: possibilities, restrictions and reliability. **Journal of Gemmology** 24(3): 139-148.

Hänni, H.A., Kiefert, L., Chalain, J.-P., Wilcock, I.C. 1997. A Raman microscope in the gemmological laboratory: first experienced of application. **Journal of Gemmology** 25(6): 394-406.

Hänni, H.A., Schmetzer, K. 1991. New rubies from the Morogoro area, Tanzania. **Gems & Gemology** 27 (3): 156-167.

Hänni, H.A., Pettke, T. 2002. Eine neue Diffusionsbehandlung liefert orangefarbene und gelbe Saphire. **Zeitschrift der Deutschen Gemmologischen Gesellschaft** 51(4): 137-152.

Harding, R.R., Scarratt, K. 1986. A description of ruby from Nepal. **Journal of Gemmology** 20(1): 3-10.

Hauzenberger, C.A., Robl, J., Stüwe, K., 2005. Garnet zoning in high pressure granulite-facies metapelites, Mozambique belt, SE-Kenya: constraints on the cooling history. **European Journal of Mineralogy** 17: 43-55.

Heinrich et al. 2003. Quantitative multi-element analysis of minerals, fluid and melt inclusions by laser-ablation inductively-coupled-plasma mass-spectrometry. **Geochimica et Cosmochimica Acta** (18): 3473–3496.

Holland, T. J. B., Powell, R., 1998. An internally consistent thermodynamic data set for phases of petrological interest. **Journal of Metamorphic Geology** 16(3): 309-343.

Hughes, R.W. 1994. The rubies and spinels of Afghanistan – a brief history. **Journal of Gemmology** 24(4): 256-267.

Hughes, R.W. 1997. **Ruby and Sapphire**. Boulder, Colorado: RWH Publishing.

Hunstiger, C. 1990: Rubinvorkommen in metamorphen Muttergesteinen, **Zeitschrift der Deutschen Gemmologischen Gesellschaft**, 39(2/3), p.121-145.

Jackson, S. E., Longerich, H. P., Dunning, G. R., and Fryer, B. J. 1992. The Application of Laser-Ablation Microprobe - Inductively Coupled Plasma - Mass-Spectrometry (Lam-Icp-Ms) to In situ Trace-Element Determinations in Minerals. **Canadian Mineralogist** 30: 1049-1064.

Jackson, S. 2008. LAMTRACE data reduction software for LA-ICP-MS. In Sylvester, P. (ed.), **Laser ablation ICP-MS in the Earth Sciences: Current practices and outstanding issues**, pp.305-307. Mineralogical Association of Canada: Short Course Series, Volume 40.

Jochum et al. 2011. Determination of reference values for NIST SRM 610-617 glasses following ISO guidelines. **Geostandard and Geoanalytical Research** doi: 10.1111/j.1751-908X.2011.00120.x.

Kammerling, R.C., Keller, A.S., Scaratt, K.V., Repetto, S. 1994. Update on mining rubies and fancy sapphires in northern Vietnam. **Gems & Gemology** 30(2): 109-114.

Kammerling, R.C., Scarratt, K., Bosshart, G., Jobbins, E.A., Kane, R.E., Gübelin, E.J., and Levinson, A.A. 1994. Myanmar and its gems – an update. **Journal of Gemmology** 24(1): 3-40.

Kane, R.E., McClure, S.F., Kammerling, R.C., Nguyen, D.K., Mora, C., Repetto, S., Nguyen, D.K., Koivula, J.I 1991. Ruby from Vietnam. **Gems & Gemology** 27(3): 136-155.

Kane, R.E., and Kammerling, R.C. 1992. Status of ruby and sapphire mining in the Mogok Stone Tract. **Gems & Gemology** 28(3): 152-174.

Keller, P.C. 1992. **Gemstones of East Africa**. Tucson, Arizona: Geoscience Press Inc.

Key, R.M., and Ochieng, J.O. 1991. The growth of rubies in south-east Kenya. **Journal of Gemmology** 22(8): 484-496.

Kloprogge, J.T., Ruan, H.D., Frost, R.L. 2002. Thermal decomposition of bauxite minerals: infrared emission spectroscopy of gibbsite, boehmite, and diaspore. **Journal of Material Science** 37: 1121-1129.

Koivula, J.I., Kammerling, R.C., Fritsch, E. 1993. Ruby mining near Mahenge, Tanzania. **Gems & Gemology** 29(2): 136.

Krzemnicki, M.S. 2007. Determining the orgin of gemstones: Challenges and perspectives. **InColor Magazine** Spring: 31-34.

Kretz, R. 1983. Symbols for rock-forming minerals. **American Mineralogist** 68: 277-279.

Leake et al. 1997. Nomenclature of amphiboles. **European Journal of Mineralogy** 9(3): 623-651.

Levinson, A.A., Cook, F.A., 1994. Gem Corundum in alkali basalt: origin and occurrence. **Gems & Gemmolgy** 30(4): 253-262.

Long et al. 2004. Gem corundum deposits in Vietnam. **Journal of Gemmology** 29: 129-147.

Longerich, H.P., Jackson, S.E., Günther, D. 1996. Laser Ablation Inductively Coupled Plasma Mass Spectrometric Transient Signal Data Acquisition and Analyte Concentration Calculation. **Journal of Analytical Atomic Spectrometry** 11: 899-904.

Marthaler M. 2005. **Das Matterhorn aus Afrika - Die Entstehung der Alpen in der Erdgeschichte**. Bern, Switzerland: Ott Verlag.

Malisa, E., Muhongo, S. 1990. Tectonic setting of gemstone mineralization in the Proterozoic metamorphic terrain of the Mozambique Belt in Tanzania. **Precambrian Research** 46: 167-176.

Mc Clure, S.F. 2006. Source type classification of gem corundum. **Gems & Gemology** 42(3): 102.

Mercier, A., Debat, P., Saul, J.M. 1999. Exotic origin of the ruby deposits of the Mangari area in SE Kenya. **Ore Geology Reviews** 14: 83–104.

Meixner, H. 1977. Rubin von Longido Tansania. **Lapis** 2(8): 12.

Möller, A., Mezger, K., Schenk, V., 2000. U-Pb dating of metamorphic minerals: Pan-African metamorphism and prolonged slow cooling of high pressure granulites in Tanzania, East Africa. **Precambrian Research** 104: 123-146.

Msolo, A.P.B. 1992. **Geology of Matombo ruby prospect, Morogoro region, Eastern Tanzania**, Master's Thesis, University of Dar es Salaam, Tanzania.

Muhlmeister, S., Fritsch, E., Shigley, J.E., Devouard, B., Laurs, B.M. 1998. Separating natural and synthetic rubies on the basis of trace-element chemistry. **Gems & Gemology** 34(2): 80-101.

Muhongo, S., Errera, M. 1993. Gemmological characteristics of rubies in Eastern Uluguru Mountains, Tanzania: A reconnaissance study, Museum royale Africe de centre, Tervuren (Belgium). **Départment de Géologie et des Minereaux, Rapport annuel** 1991-1992: 201-206.

Okrusch, M., Bunch, T.E., Bank, H. 1976. Paragenesis and Petrogenesis of a Corundum-Bearing Marble at Hunza (Kashmir). **Mineralium Deposita** 11: 278-297.

Pardieu, V., Thanachakaphad, J., Jacquat, St., Senoble, J.-B., Bryl, L.-P. 2009. **Rubies from the Niassa and Cabo Delgado region of Northern Mozambique**. Available from : http://www.giathai.net [2010 January]

Pardieu, V., Thirangoon, K., Lomthong, P., Saeseaw, S., Thanachakaphad, J., Du Toit, G. 2009. **Sapphires Reportedly from Batakundi/Basil area : A preliminary examination and a comparison with rubies and pink sapphires from other deposits in Central Asia**. Available from : http://www.giathai.net [2010 January]

Pettke, Th. 2006. Laser ablation ICP-MS in the Earth Sciences: Current practices and outstanding issues. In Sylvester, P. (ed.), **Melt Inclusions in Plutonic Rocks**, pp.51-80. Mineralogical Association of Canada: Short Course Series, Volume 36.

Pettke, Th. 2008. Analytical Protocols for Element Concentration and Isotope Ratio Measurements in Fluid Inclusions by LA–(MC–)ICP–MS. In Sylvester, P. (ed.), **Laser ablation ICP-MS in the Earth Sciences: Current practices and outstanding issues**, pp.189-217. Mineralogical Association of Canada: Short Course Series, Volume 40.

Peretti, A., Schmetzer, K., Bernhardt, H.-J., Mouawad, F. 1995. Rubies from Mong Hsu. **Gems & Gemology** 31(1): 2-26.

Peretti, A., Mullis, J., Mouawad, F. 1996. The role of fluorine in the formation of colour zoning in rubies from Mong Hsu, Myanmar. **Journal of Gemmology** 25(1): 3-19.

Peucat, J.J., Ruffault, P., Fritsch, E., Bouhnik-Le Coz, M., Simonet, C., Lasnier, B. 2007. Ga/Mg ratio as a new geochemical tool to differentiate magamatic from metamorphic blue sapphires. **Lithos** 98(1-4): 261-274.

Pohl, W., and Horkel, A. 1980. Notes on the geology and mineral resources of the Mitito Andei-Taita area (southern Kenya). **Mitteilungen Österreichische Geologische Gesellschaft** 73: 135-152.

Pohl, W., and Niedermayr, G. 1979. **Geology of the Mwatate Quadrangle and the Vanadium Grossularite Deposits of the area**, Report 101. Nairobi, Kenya: Geological Surveyof Kenya.

Rankin, A.H., Greenwood, J., Hargreaves, D. 2003. Chemical Fingerprinting of some East African Gem Rubies by Laser Ablation ICP-MS. **Journal of Gemmology** 28 (8): 473-482.

Rossetti, F., Cozzupoli, D., Phillips, D. 2008. Compressional reworking of the East African Orogen in the Uluguru Mountains of eastern Tanzania at c. 550 Ma: implications for the final assembly of Gondwana. **Terra Nova** 20: 59–67.

RRUFF Sample Data [Online] (n.d.): Available from : http://rruff.info [2010 January]

Saminpanya, S., Manning, D.A.C., Droop, G.T.R., Henderson, C.M.B. 2003. Trace elements in Thai gem corundums. **Journal of Gemmology** 28(7): 399-415.

Sampson, D.N., Spence, J. 1959. **Quarter Degree Sheet 201, Uluguru**. Dodoma, Tanzania: Geological Survey of Tanzania.

Sampson, D.N., Wright, A.E. 1961. **Quarter Degree Sheet 183**, **Morogoro**. Dodoma, Tanzania: Geological Survey of Tanzania.

Sampson, D.N., Wright, A.E. 1964. **The Geology of the Uluguru Mountains**, Bulletin No.37. Dodoma, Tanzania: Geological Survey of Tanzania.

Schlüssel, R. 2002. **Mogok Myanmar, eine Reise durch Burma zu den schönsten Rubinen und Saphiren der Welt**. Munich, Germany: Christian Weise Verlag.

Schlüter, T. 1997. **Geology of East Africa**. Berlin, Germany: Verlag Gebrüder Borntraeger.

Schmetzer, K., Bank, H. 1981. The colour of natural corundum. **Neues Jahrbuch für Mineralogie** 140: 59-68.

Schmetzer, K., Bosshart, G., Hänni, H.A. 1983. Naturally-coloured and treated yellow and orange-brown sapphires. **Journal of Gemmology** 18 (7): 607-622.

Schubert, W. 1996. Mineraleinschlüsse - Indikatioren metamorpher Reaktionen. **Zeitschrift der Deutschen Gemmologischen Gesellschaft** 45(1): 5-12.

Schwarz, D., Pardieu, V., Saul, J. M., Schmetzer, K., Laurs, B. M., Giuliani, G., Klemm, L., Malsy, A.-K., Erel, E., Hauzenberger, Ch., Du Toit, G., Fallick, A.E., Ohnenstetter, D. 2008. Rubies and sapphires from Winza, Central Tanzania. **Gems & Gemology** 44(4): 322-347.

Simonet, C. 2000. **Geology of Sapphire and Ruby Deposits -The example of the John Saul Ruby Mine, Mangare area, Southern Kenya**. Ph.D. Thesis, University of Nantes.

Simonet, C., Fritsch, E., Lasnier, B. 2008. A classification of gem corundum deposits aimed towards gem exploration. **Ore Geology Reviews** 34: 127–133.

Siripaisarnpipat, S., Pattharakorn, T., Pattharakorn, S., Sanguangruang, S., Koonsaeng, N., Achiwawanich, S., Promsurin, M., Hanmungthum, P. 2002. Spectroscopic properties of Möng Hsu ruby. **Australian Gemmologist** 21: 236-241.

Smith, C.P., and Surdez, N. 1994. The Mong Hsu ruby: A new type of Burmese ruby. **Jewel Siam** 4(6): 82-98.

Smith, C.P. 1995. A contribution to understanding the infrared spectra of rubies from Mong Hsu, Myanmar. **Journal of Gemmology** 24(5): 321-335.

Smith, C.P., Gübelin, E.J., Bassett, A.M., Manandhar, M.N. 1997. Rubies and fancy-color sapphires from Nepal. **Gems & Gemology** 33(1): 24-41.

Smith, C.P. 1998. Rubies and pink sapphires from the Pamir Mountain Range in Tajikistan, former USSR. **Journal of Gemology** 26(2): 103-109.

Solesbury, F.W. 1967. Gem corundum pegmatites in NE Tanganyika. **Econonimca Geologica** 62: 983-991.

Stern, W.B., Hänni, H.A. 1982. Energy-dispersive X-ray spectrometry: A non-destructive tool in gemmology. **Journal of Gemmology** 18(4): 285-296.

Suhner, B. 1979. Infrarot-Spektren in der Gemmologie. **Zeitschrift der Deutschen Gemmologischen Gesellschaft** 28(2): 55-68.

Sutherland, F.L., Schwarz, D., Jobbins, E.A., Coenraads, R.R., and Webb, G. 1998. Distinctive gem corundum suites from discrete basalt fields; a comparative study of Barrington, Australia, and West Pailin, Cambodia, gemfields. **Journal of Gemmology** 26(2): 65-85.

Sutherland, L.F., Hoskin, P.W.O, Fanning, M.C., Coenraads, R.R 1998. Models of corundum origin from alkali basaltic terrains; a reappraisal. **Contributions to Mineralogy and Petrology** 133(4): 356-372.

Sutherland, L.F., Coenraads, R.R., Schwarz, D., Raynor, L.R., Barron, B.J., Webb, G.B. 2003. Al-rich diopside in alluvial ruby and corundum-bearing xenoliths, Australian and SE Asian basalt fields. **Mineralogical Magazine** 67(4): 717-732.

Sutthirat, C., Saminpanya, S., Droop, G.T.R., Henderson, C.M.B., Manning, D.A.C., 2001. Clinopyroxene-corundum assemblage from alkali basalt and alluvium, eastern Thailand: constraints on the origin of Thai rubies. **Mineralogical Magazine** 65(2): 277-295.

Tenczer et al. 2006. Anorthosites in the Eastern Granulites of Tanzania—New SIMS zircon U–Pb age data, petrography and geochemistry. **Precambrian Research** 148(1-2): 85-114.

Tenczer, V., Hauzenberger, C.A., Fritz, H., Hoinkes, G., Muhongo, S., Klötzli, U., 2011. The P-T-$X_{(fluid)}$ evolution of meta-anorthosites in the Eastern Granulites, Tanzania. **Journal of Metamorphic Geology** 29: 537-560.

Wang, W., Hall, M., Shen, A.H., Breeding, C.M. 2006. Developing Corundum Standards for LA-ICP-MS Trace-Element Analaysis. **Gems & Gemology** 42(3): 105.

Webster, R. 1994. **Gems: their sources, descriptions, and identification**. London, England: Butterworth- Heinemann Ltd.

Zwaan, P.C. 1974. Garnet, corundum and other gem materials from Umba Tanzania. **Scripta Geologica** 20: 1-41.

Biography

Captain Walter Adrian Balmer was born on the 21st of December 1973 in Luzern, Switzerland. He obtained his Master of Science degree in 2001 form the Department of Earth Sciences at the Swiss Federal Institute of Technology Zürich (ETH Zürich), Switzerland. After the completion of his initial studies and the graduation from the officer's academy of the Swiss Armed Forces he attended an on-campus graduate gemmologist course with the Gemmological Institute of America, Carlsbad, California, United States of America. Immediately after, in 2002, Walter Adrian Balmer got the opportunity to work with the Gübelin Gem Lab in Luzern, Switzerland. During the time with the Gübelin Gem Lab which is specialised in origin determination of gemstones he gained the position of a senior staff gemmologist. In 2006, Walter Adrian Balmer decided to move to Bangkok, Thailand where he worked as a research consultant at the Gems & Jewelry Institute of Thailand and as a lecturer at the Kasetsart University first, before he started his Ph.D. project at the Department of Geology, Faculty of Science, Chulalongkorn University in the same year.